Design of a high intensity magnetic force field source and studies of its impact on electrochemical reaction at the liquid-solid interface

Jinu Kurian

UNIVERSITÉ DE STRASBOURG

ÉCOLE DOCTORALE de Physique et Chimie-Physique – ED 182

Institut de Physique et Chimie des matériaux de Strasbourg

THÈSE présentée par :

Jinu KURIAN

soutenue le : **06 Julliet 2022**

pour obtenir le grade de : **Docteur de l'université de Strasbourg**

Discipline/ Spécialité : Physique de la matière condensée

Design of a high intensity magnetic force field source and studies of its impact on electrochemical reaction at the liquid-solid interface.

THÈSE dirigée par :

M. Bernard DOUDIN Professeur, Université de Strasbourg

RAPPORTEURS :

M. Jean-Philippe ANSERMET Professeur, Ecole Polytechnique Fédérale de Lausanne

M. Vincent VIVIER Professeur, Sorbonne Université

AUTRES MEMBRES DU JURY :

Ms. Salia CHERIFI-HERTEL Chargé de recherches, CNRS (IPCMS)

Résumé

Introduction

Bien que les études relatives à l'influence du champ magnétique sur les processus électrochimiques remontent à Faraday, un intérêt croissant pour la compréhension du mécanisme physique et l'exploration des possibilités d'applications dans le domaine de l'énergie et de l'électrodéposition est notable depuis ces dernières années [1, 2]. Un champ magnétique peut avoir un impact sur l'électrochimie sous deux aspects distincts, l'électrodéposition et le processus électrochimique, principalement par le biais de la force de Lorentz et de la force du gradient de champ, ou force de Kelvin [3, 4]. La force de Lorentz induit une magnétoconvection si le champ est non colinéaire à la densité de courant. D'autre part, la force de Kelvin sera active dans un champ non uniforme lorsqu'il existe un gradient de concentration orthogonal au gradient de champ. Indépendamment de la nature des forces impliquées, dans la plupart des cas, l'influence d'un champ magnétique sur le système électrochimique peut être expliquée par les effets convectifs induits par le champ sur la couche de diffusion.

L'influence du champ magnétique à l'interface solide/liquide est un sujet controversé. Les estimations d'ordres de grandeur des énergies révèlent que l'énergie magnétique des espèces est négligeable par rapport à l'énergie thermique qui régit la diffusion et l'énergie potentielle électrostatique qui régit le transfert d'électrons. On pourrait donc s'attendre à ce que le champ magnétique n'ait aucun impact sur la double couche électrochimique et la cinétique des réactions à l'électrode. Les études de Koehler [5] et Devos [6] basées sur la magnéto-impédance et la voltampérométrie à balayage linéaire ainsi que les données de Tafel [7] confirment ce point de vue. Cependant, des études récentes ont montré que le magnétisme de l'électrode peut en fait avoir une influence surprenante sur la polarisation de spin des radicaux intermédiaires, favorisant ainsi la formation de triplet O_2 [8]. Sambalova [9] a utilisé des électrodes Co/Pt pour étudier la réaction d'évolution de l'hydrogène et a observé les effets du champ sur la double couche, mesurée au moyen de la réponse magnéto-optique. Il a également été montré que le film d'alliage PtCo avec une anisotropie magnétique perpendiculaire présente une activité plus élevée pour la réaction de réduction de l'oxygène par rapport à l'aimantation dans le plan et l'amélioration est attribuée à l'ordre chimique du [10]. En outre, Dunne et Coey [11] ont récemment signalé une augmentation de la capacité de la double couche et de la constante de vitesse de réaction due à la contrainte

de Maxwell lorsqu'un champ de 0.5 T est appliqué parallèle à la surface de l'électrode. Il est donc nécessaire d'étudier en détail l'influence du champ magnétique sur l'interface électrochimique.

Afin d'étudier les effets du champ à l'interface solide-liquide, il faudrait idéalement que la force magnétique soit maximale à proximité immédiate de l'électrode mais minimale ailleurs. Une telle configuration de champ peut séparer l'influence du champ de la région de la couche de double de celle de la région de la diffusion couche. Si l'on considère la force du gradient de champ de Kelvin, la diminution de la taille du système entraîne une augmentation du champ de forces magnétique. Les structures magnétiques définies à l'échelle nano permettent donc d'atteindre ou de dépasser les forces magnétiques les plus élevées rapportées dans la littérature [12]. En particulier, les films minces magnétiques présentant une anisotropie magnétique perpendiculaire (PMA) sont d'un grand intérêt en raison de leur fabrication optimisée bien connue et de leur surface plane et stable. Le rapport d'aspect est un paramètre important à prendre en compte pour la génération du gradient de champ requis. Dans un film magnétique, les sources du champ magnétique sont les bords des domaines magnétiques. Par conséquent, un film mono-domaine avec des bords minimaux ne générerait que des gradients de champ plus faibles par rapport au grand gradient de champ près de la surface générée par les films magnétiques multi-domaines (Figure 1). Ainsi, les films PMA multi-domaines ayant un rapport d'aspect approprié peuvent être considérés comme une source de champ primaire pour générer un grand gradient de champ sur une distance de quelques dizaines de nm.

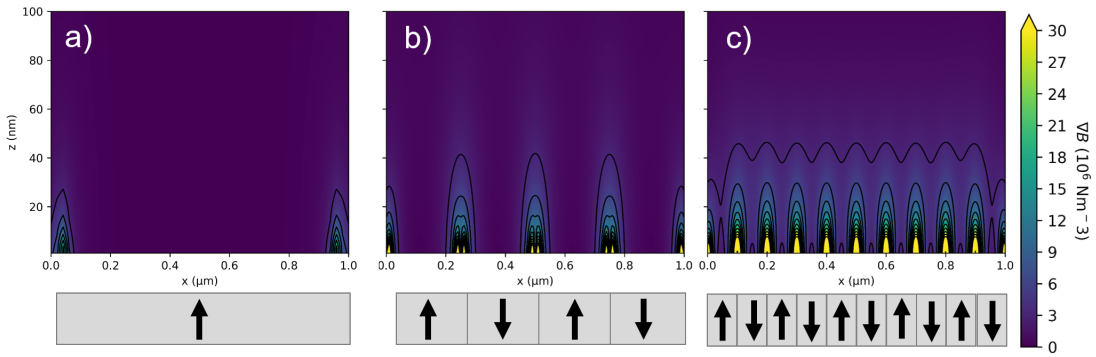

FIGURE 1: Courbe de niveau du gradient de champ magnétique généré par des films PMA avec différentes tailles de domaine : a) un seul domaine de 1.0 µm de largeur, b) quatre domaines de 0.25 µm de largeur et c) plusieurs domaines de 0.1 µm de largeur. Les valeurs de champ sont estimées en utilisant un modèle 2D. Les paramètres utilisés sont les suivants : magnétisation = 1.4 T, surface de la couche morte = 10 %, épaisseur de la couche magnétique = 20.0 nm, orientation = hors du plan.

L'influence du champ magnétique sur la couche de diffusion est bien documentée alors que les effets du champ sur la double couche électrochimique sont rarement rapportés. Toutes les réactions de l'électrode se produisent dans la région interfaciale d'une épaisseur d'environ 10 nm, où la tension de surface et la distribution des charges excédentaires deviennent plus importantes [11, 13]. Notre motivation est de voir comment de grandes forces magnétiques imposées à une interface électrode/électrolyte peuvent avoir un impact sur la réaction électrochimique. Pour générer les conditions de gradient de champ requises, des films minces magnétiques ayant une propriété PMA ont été fabriqués et étudiés. Deux stratégies ont été suivies pour créer une configuration magnétique multi-domaines où le champ de force peut être activé ou désactivé par des stimuli externes. Dans la première approche, des multicouches de Co/Pt ayant un nombre différent de répétitions ont été fabriquées et l'état PMA multi-domaines a été obtenu à l'état déposé. Ces domaines ont été manipulés à l'aide d'un champ externe qui a permis de réaliser un paysage de champ de forces contrôlable magnétiquement. Une autre approche consiste à manipuler les domaines magnétiques par des moyens électriques. Des hétérostructures à base de Pt/Co/W à ont été fabriquées. Nous avons combiné la technologie de commutation d'aimantation basée sur le coupl spin-orbite (SOT) induit par le courant avec la technologie d'irradiation ionique focalisée afin de concevoir un réseau magnétique reprogrammable électriquement. Cela permet un contrôle temporel des bits magnétiques individuels, ce qui ouvre la porte à des expériences où l'évolution temporelle des effets du champ de gradient peut être explorée.

Influence du champ magnétique à grand gradient sur la réaction électrochimique

Afin de générer un gradient de champ important à proximité immédiate de l'électrode, des couches multiples de $[Co/Pt]_N$ avec différentes épaisseurs de Co et différents nombres de répétitions N sont fabriquées. L'épaisseur et la qualité des films sont confirmées par la réflectivité des rayons X (XRR) et la microscopie électronique à transmission (TEM). Les propriétés magnétiques des multicouches sont déterminées à l'aide de magnétométrie SQUID, de la microscopie à force magnétique (MFM) et de l'imagerie basée sur l'effet Kerr magnéto-optique (MOKE) (Figure 2). L'état multi-domaines est observé à l'état rémanent, qui sature lorsque le champ appliqué est $>|250$ mT$|$. L'évolution des domaines magnétiques avec le champ perpendiculaire externe est similaire ce qui a été rapporté par plusieurs chercheurs [14, 15]. En combinaison avec les techniques de magnétométrie et d'imagerie

magnétique, à l'état rémanent, le modèle de calculs 2D a permis d'estimer un gradient de champ nanométrique intense de l'ordre de 10^7 T/m dans une région de < 10 nm près de la surface du film. Pour l'étude électrochimique, un système modèle de réaction ferri/ferrocyanure ($Fe(CN)6^{3-}$/($Fe(CN)6^{4-}$) (Equ. 1) est choisi comme sonde redox standard en raison de sa réversibilité électrochimique [16] et de sa stabilité. Dans cette réaction redox, les deux espèces sont solubles dans l'eau et restent sous forme d'ions solvatés, ce qui minimise les modifications de la surface de l'électrode pendant les mesures électrochimiques, contrairement à l'électrodéposition ou à la corrosion qui altèrent nécessairement la surface. Les propriétés interfaciales et en solution de la réaction sont pré-caractérisées pour l'électrode faite d'un film de Pt en utilisant des techniques comme la voltampérométrie cyclique (CV), la chronoampérométrie (CA) et la spectroscopie d'impédance (EIS).

$$[Fe(CN)_6]^{4-} \rightleftharpoons [Fe(CN)_6]^{3-} + e^- \tag{1}$$

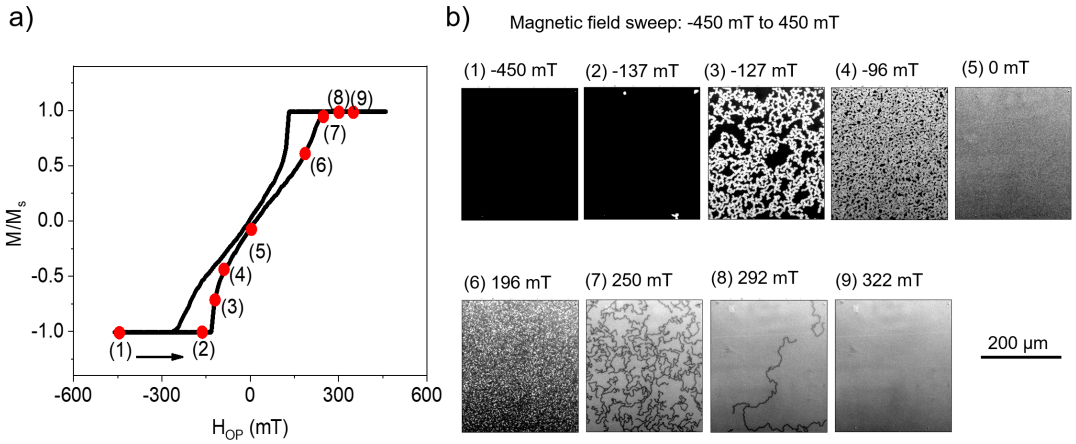

FIGURE 2: Boucle d'hystérésis Kerr d'un film mince répétitif TCD N=20 Co/Pt sous un champ appliqué hors du plan et (b) images Kerr de l'échantillon similaire sous différentes valeurs de champ marquées en (a). Le contraste sombre et clair représente les domaines aimantés dans des directions opposées.

Avant d'étudier les effets du gradient de champ à l'interface électrochimique, l'influence de l'épaisseur de la couche de Pt sur l'activité électrochimique du film multicouche Co/Pt est étudiée. La réactivité du film de Pt et des films de Co/Pt avec différentes épaisseurs de couche de Pt de couverture est obtenue en utilisant la voltampérométrie cyclique (CV) et est résumée dans le tableau 1. Comme on peut le voir, une dépendance claire de l'épaisseur de la couche de recouvrement sur la vitesse de réaction des films peut être observée. Un minimum de 5 nm de couche de Pt est nécessaire pour que le film Co/Pt présente un taux de réaction atteignant celui des films de Pt pur. Toutes les CV sont obtenus sous un champ

hors plan de 400 mT où les films de Co/Pt à l'état saturé peuvent être comparés au film de Pt. Les effets convectifs induits par la force de Lorentz peuvent affecter de manière significative l'estimation de la constante de vitesse en raison de sa dépendance au coefficient de diffusion. Par conséquent, les effets de la force de Lorentz sont examinés en détail dans la configuration de champ dans le plan et hors du plan. On observe que, lorsque le champ appliqué est orthogonal au courant normal à la surface, la force de Lorentz peut être considérée comme équivalente à une agitation mécanique de la solution. D'autre part, les effets convectifs sont plus faibles dans la configuration de champ hors du plan, et peuvent donc être négligés. Afin de comprendre l'influence de la couche de recouvrement sur le taux de réaction, la composition chimique de la surface est analysée à l'aide de la spectroscopie de photons X à résolution angulaire (ARXPS). Pour un film Co/Pt coiffé de 2.8 nm de Pt, l'ARXPS a montré des traces de Co à la surface, suggérant une couverture imparfaite de la surface par une fine couche de coiffe de Pt. La source de Co ou d'oxyde de Co dans le film est suggérée comme étant liée à la structure colonnaire révélée par TEM du film Co/Pt, où la rugosité accrue et la couverture partielle aux joints de grains peuvent laisser certaines parties de la couche supérieure de Co non protégées.

Sample	10^3 k_0 $\pm$ 0.2 cm/s	10^6 D_R $\pm$ 0.1 cm^2/s	10^6 D_O $\pm$ 0.1 cm^2/s	SR nm
HZDR samples				
$[Co/Pt]_{19}/Co/Pt(0.0)$	1.1	5.2	4.7	2.7 ± 0.4
$[Co/Pt]_{19}/Co/Pt(3.0)$	3.1	5.8	5.2	2.2 ± 0.3
$[Co/Pt]_{19}/Co/Pt(5.0)$	9.7	6.0	5.5	2.1 ± 0.3
$[Co/Pt]_{19}/Co/Pt(10.0)$	10.0	6.1	5.6	2.1 ± 0.3
Pt	13.0	6.4	5.9	2.2 ± 0.2
TCD samples				
$[Co/Pt]_{19}/Co/Pt(2.8)$	4.5	5.4	5.1	1.4 ± 0.3
Pt film	11.2	5.8	5.4	1.3 ± 0.2

TABLE 1: Résumé de la caractérisation électrochimique et de surface des différentes électrodes de travail. Les échantillons HZDR et TCD indiquent la laboratoire source des échantillons. Dans les échantillons HZDR, les couches de Co et de Pt ont une épaisseur de 1.0 nm alors qu'elle est de 0,8 pour les échantillons TCD. L'épaisseur de la couche de Pt est en nm. Le taux standard cinétique de réaction k_0, les coefficients de diffusion de réduction et d'oxydation, D_R et D_O, sont obtenus à partir de mesures CV sous un champ magnétique hors plan appliqué de 400 mT, et la rugosité de surface, SR est calculée à partir de la microscopie à force atomique.

Pour étudier l'influence du fort gradient de champ sur la réaction électrochimique, les mesures en régime permanent basées sur la chronoampérométrie sont choisies comme l'une des principales méthodes. La figure 3 montre la mesure de l'hystérésis du courant en régime permanent de la réduction du ferricyanure en utilisant un film de Pt et des films Co/Pt avec différentes épaisseurs de la couche externe de Pt comme électrode de travail. Une augmentation de la densité de courant avec un champ perpendiculaire appliqué est observée sur les films Co/Pt recouverts d'une couche de Pt de 5.0 nm. Lorsque le champ passe de ±400 mT à 0 mT, l'augmentation de la densité de courant est d'environ 8, 7 et 5 % pour les films Co/Pt avec une couche externe de Pt de 0.0, 3.0 et 5.0 nm d'épaisseur, respectivement. D'autre part, aucune dépendance du champ sur la densité de courant n'est observée ni pour le film de Pt ni pour le film Co/Pt recouvert de Pt de 10 nm d'épaisseur. Une estimation approximative des champs de force estime une densité de force de Lorentz faible de l'ordre de 25 N/m^3 alors que la densité de champ de gradient de Kelvin peut être aussi élevée que 10^7 N/m^3 à la surface de l'électrode sans couche de recouvrement de Pt. La force du gradient de champ peut inhiber la convection des espèces paramagnétiques et peut modifier localement le gradient de concentration. Une étude utilisant des nanofils de CoPt intégrés dans une membrane d'alumine a vait montré que le courant de réduction de l'oxygène peut être augmenté par l'inhibition convective des radicaux paramagnétiques à proximité de la surface de l'électrode grâce au gradient de champ magnétique [17, 18]. Par conséquent, le gradient de champ important créé par les films magnétiques multi-domaines à l'interface électrochimique est supposé être la force motrice des effets observés.

La spectroscopie d'impédance (EIS) est également utilisée pour étudier les effets du fort gradient de champ sur les propriétés de l'interface et de transport de masse du système. Dans le cas de l'EIS, la réponse de l'impédance à une petite perturbation en courant alternatif est enregistrée et modélisée à l'aide d'un circuit électrique équivalent afin d'extraire la résistance de transfert de charge R_{ct} et la capacité à double couche C_{dl} qui dépendent de l'interface, ainsi que l'élément de Warburg W qui dépend du transport de masse. Le résultat le plus frappant se produit dans la région des hautes fréquences où la résistance de transfert de charge et la capacité à double couche montrent une dépendance au champ magnétique appliqué (Figure 4c et d). Les deux quantités sont réduites de 5 à 6 % lorsque le champ appliqué passe de $\pm$ 400 mT à 0 mT. La réduction de Rct est en accord avec l'augmentation du courant observée dans les mesures de chronoampérométrie (Figure 3). Comme la tension de polarisation continue appliquée est proche du demi potentiel $E_{1/2}$, la capacité effective de la double couche peut être traitée comme un condensateur de Gouy-Chapman correspondant

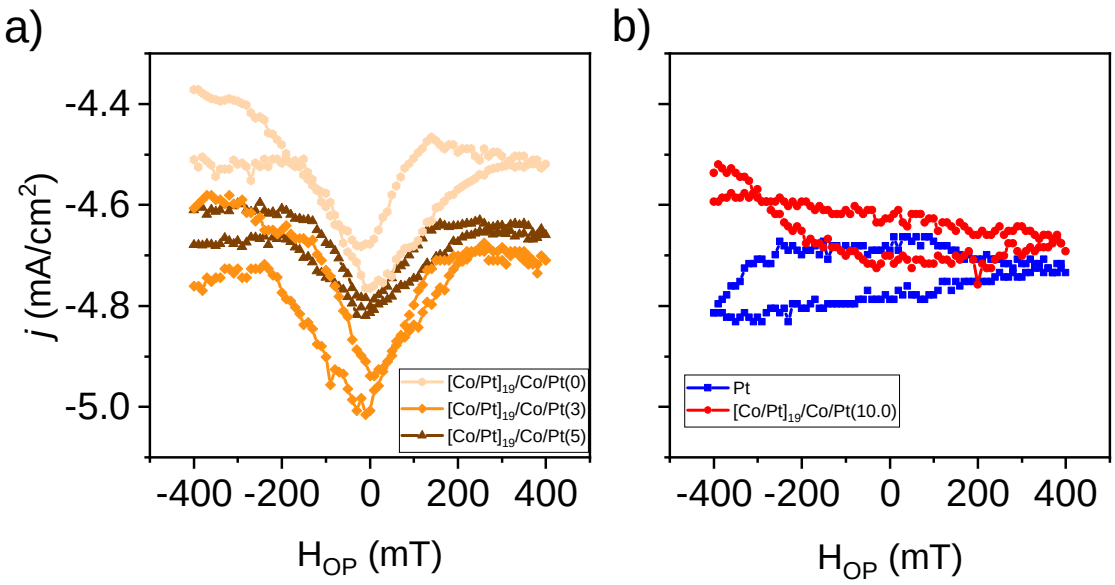

FIGURE 3: Densité de courant en régime permanent en fonction du champ magnétique hors du plan à une tension de 0.25 V (a) pour des films Co/Pt HZDR avec une couche de Pt externe de 0, 0.3 et 5.0 nm d'épaisseur, et (b) pour un film Pt(20.0) HZDR et un film Co/Pt avec une couche de Pt externe de 10 nm d'épaisseur.

à la région de la double couche diffusive. Un changement de C_{dl} avec le champ appliqué impliquerait alors un changement dans la concentration des ions dans la région de la double couche diffusive. Cela correspond à notre hypothèse de micro-convection entraînée par le gradient de champ comme origine de l'augmentation du courant dans les films Co/Pt. Cependant, aucune modification de la cinétique sous-jacente n'est observée.

Gradient de champ magnétique programmable électriquement à l'aide d'une irradiation par un faisceau He^+ focalisé

Afin de créer un paysage magnétique contrôlable électriquement, nous avons adopté une approche sophistiquée en combinant les phénomènes de SOT pour la commutation de magnétisation et la technologie d'irradiation ionique focalisée sans masque pour définir des domaines magnétiques. Nous discutons ici de la feuille de route pour la réalisation de la commutation sélective de magnétisation de la région magnétique prédéfinie, et de la tentative de créer un système modèle pour générer les champs de force magnétiques reprogrammables électriquement.

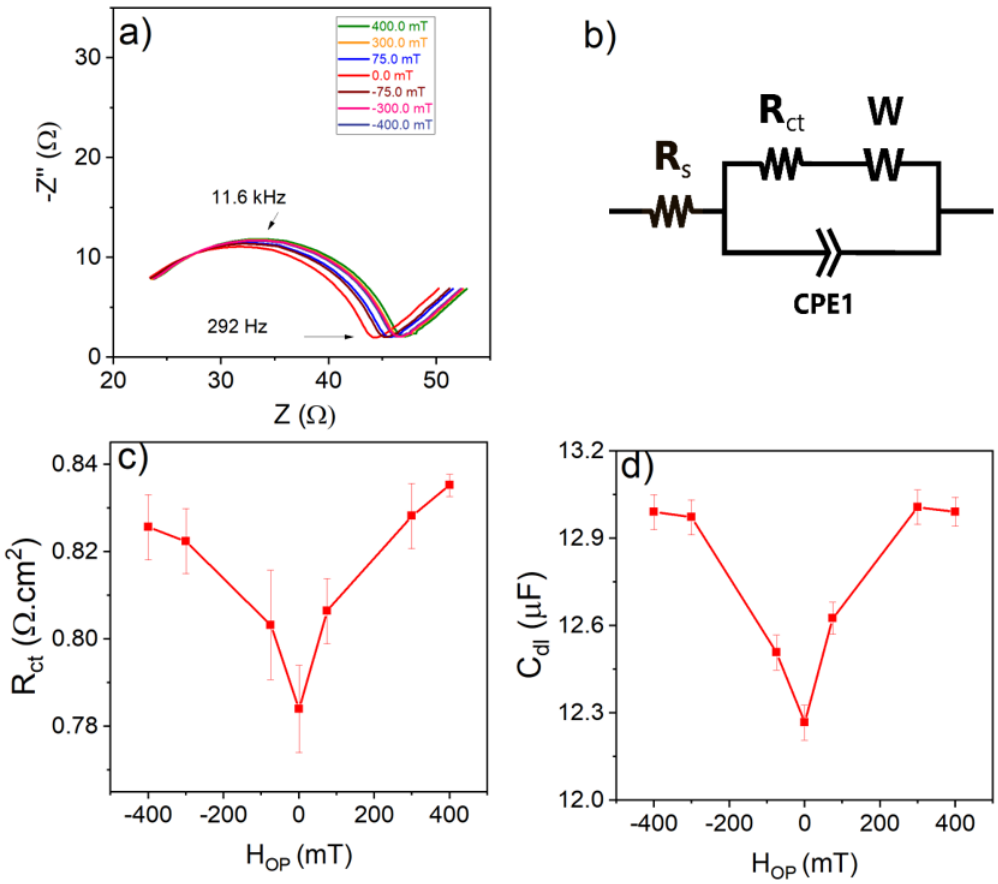

FIGURE 4: a) Spectres EIS à une tension de polarisation de 0.25 V sous différents champs magnétiques externes normaux à la surface. b) Circuit de Randles utilisé pour l'ajustement aux données EIS. c) Résistance normalisée de transfert de charge et d) capacité de la double couche en fonction du champ appliqué.

Le SOT est un moyen efficace de manipuler électriquement l'aimantation d'objets magnétiques à l'échelle nanométrique [19, 20]. Le courant nécessaire pour changer l'état magnétique ($\pm$ M_z) dépend de plusieurs paramètres, notamment l'aimantation à saturation et l'anisotropie magnétique du film mince [21], qui sont difficiles à modifier localement dans un film. L'irradiation ionique est connue pour provoquer le mélange des atomes de l'interface, ce qui augmente la rugosité interfaciale [22]. Cela permet de contrôler les propriétés magnétiques dépendant de l'interface, comme l'aimantation et l'anisotropie magnétique [23–25]. La formation de motifs magnétiques à l'aide d'une irradiation à faisceau large a été démontrée en utilisant des masques par lithographie [24], mais le plus petit bit magnétique formé est principalement déterminé par la résolution des étapes de lithographie plutôt que par le volume d'interaction du faisceau d'ions. Par contre, le faisceau d'ions d'hélium focalisé permet une définition de domaines à l'échelle nano sans masque où les dimensions latérales des structures magnétiques sont limitées uniquement par la taille de la

cascade de collision ($\leq$ 10 nm) [26]. En plus de la précision nanométrique, cette approche préserve également la topographie plane de l'empilement magnétique initial [24] qui est une condition préalable majeure pour les applications électrochimiques [27].

Des films minces à anisotropie magnétique perpendiculaire (PMA) dont la couche magnétique est prise en sandwich entre des métaux lourds à angle de Hall de spin opposé, Pt/Co/W et Pt/Co/Ta, sont fabriqués pour cette étude. Les mesures de magnétométrie et de magnéto-transport (figure 5a) ont confirmé la présence d'un PMA intact dans les films minces tels que déposés et structurés. La commutation SOT déterministe est réalisée dans les deux types de films sous champ magnétique de polarisation de rupture de symétrie appliqué de manière colinéaire au courant (Figure 5b). Nous avons utilisé la mesure de Hall harmonique pour estimer l'angle de Hall de spin effectif (SHE) du dispositif à base de Pt/Co/W, qui s'avère être de 0.4, en bon accord avec la valeur de la littérature [28]. Comme dans d'autres articles de la littérature [29], nous avons également trouvé un couple de type amortissement comme couple dominant dans la commutation de magnétisation induite par le courant du dispositif Pt/Co/W.

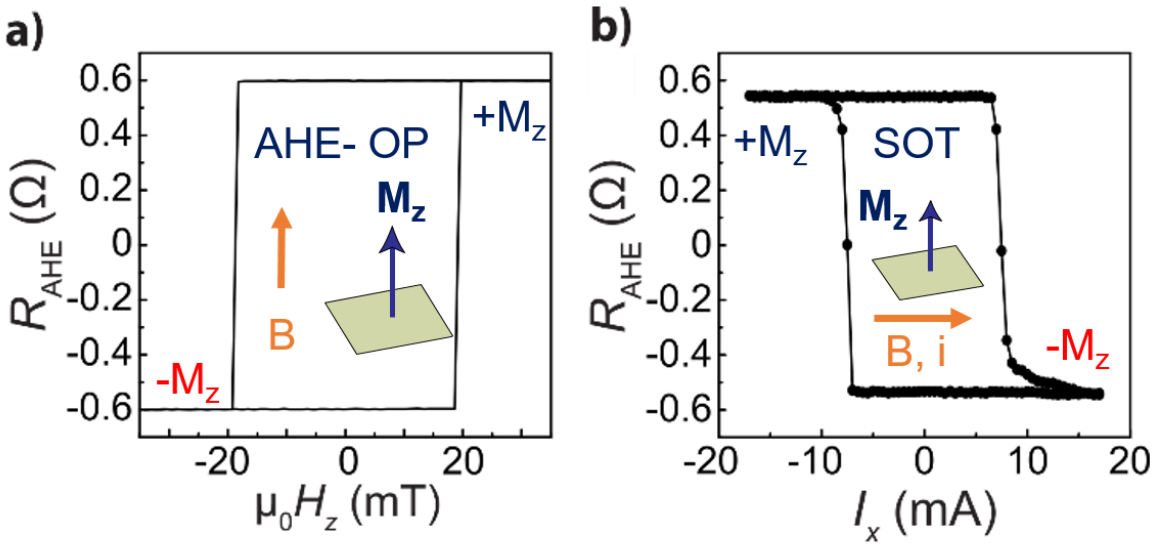

FIGURE 5: Mesures électriques basées sur l'effet Hall anormal sur des dispositifs à base de Pt/Co/W. a) Boucle d'hystérésis sous l'application d'un champ normal qui confirme la PMA du système. b) Commutation de magnétisation induite par le courant sous un champ de polarisation de 150 mT. Toutes les mesures sont effectuées avec des barres de Hall non irradiées.

Les films montrent une PMA façonnée localement sous irradiation He^+ focalisée sans masque. La mesure in-situ de la tension de Hall nous a permis de contrôler en temps réel l'évolution de l'anisotropie avec l'irradiation. Comme le montre la figure 6a, pour la barre de Hall Pt/Co/W, le signal de Hall diminue initialement avec la dose jusqu'à 38 ions/nm^2,

après quoi un changement notable est observé lorsque l'aimantation bascule dans le plan. Sur la base de la courbe d'irradiation, les barres de Hall sont irradiées avec différentes doses et sont caractérisées ex-situ pour obtenir leurs propriétés magnétiques et électriques. La figure 6b montre l'évolution de l'aimantation à saturation et du champ d'anisotropie en fonction de la dose d'irradiation. Après irradiation avec une dose presque critique de 35 ions/nm^2, la densité de courant de commutation SOT et le champ d'anisotropie magnétique sont réduits d'environ 70 % par rapport aux échantillons non irradiés. Aucun changement appréciable de l'angle de Hall de spin et de la résistivité longitudinale n'est noté avec l'irradiation, ce qui suggère l'insensibilité de l'irradiation aux propriétés globales. Ainsi, la commutation sélective de la croix irradiée par rapport au reste de la barre de Hall est réalisée et un état multi-domaine contrôlable électriquement est démontré (Figure 7a).

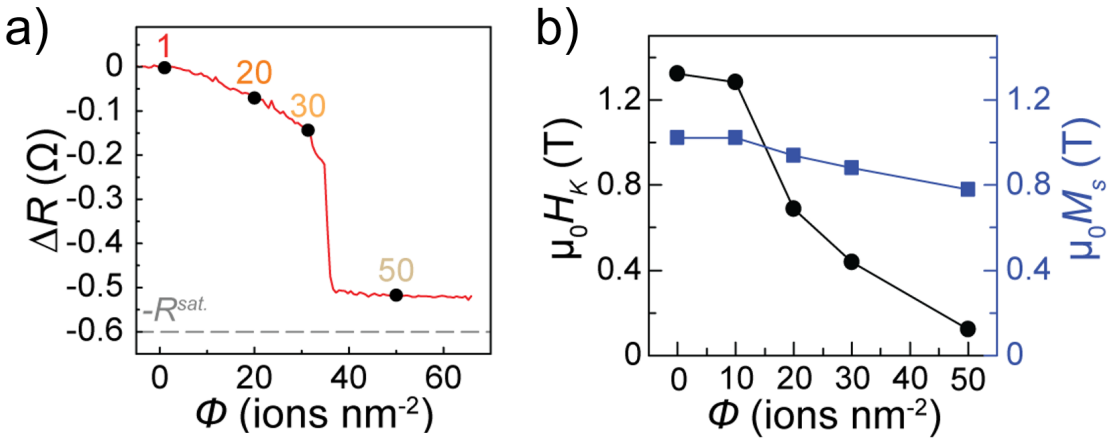

FIGURE 6: a) Évolution in situ en temps réel de la résistance de Hall anormale en fonction de la dose d'irradiation et b) champ d'anisotropie ex-situ H_k et aimantation à saturation Ms en fonction de la dose d'irradiation pour l'hétérostructure à base de Pt/Co/W.

Dans le but d'améliorer le volume magnétique (et donc la stabilité thermique), les effets de l'irradiation des films ayant une couche de Co unique sont comparés à ceux des films Pt/Co/W à trois couches de Co. Cependant, des états multi-domaines complexes qui ne sont plus entièrement commutables par le courant électrique sont observés dans l'échantillon à trois couches, et donc une optimisation supplémentaire pourrait être nécessaire en termes de designs de domaines d'irradiation et de nombre de couches. En outre, afin d'accéder à davantage d'états intermédiaires multi-domaines par le courant électrique, l'irradiation est modifiée en termes de zones d'irradiations et de dose. L'imagerie Kerr nous a permis de réaliser l'importance de séparation entre les régions irradiées pour une commutation multi-niveaux bien définie, attribuée au blocage de la paroi du domaine magétique

par le gradient d'anisotropie (figure 7b).

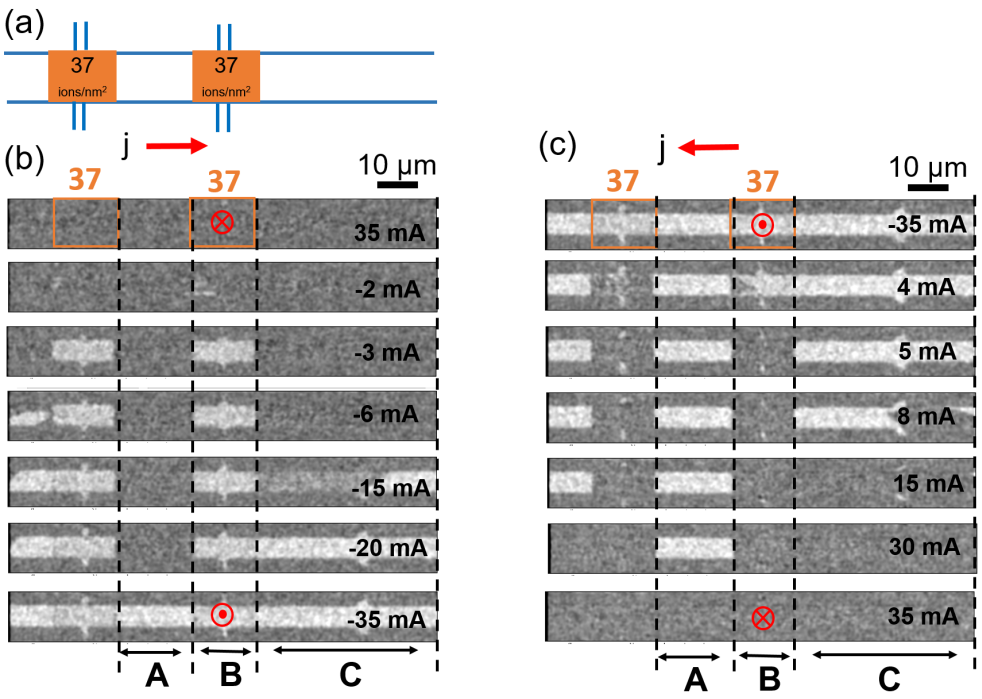

FIGURE 7: Figure 7 Démonstration du contrôle électrique de l'état multi-domaines magnétiques à l'aide de l'imagerie MOKE. a) Commutation sélective induite par le courant des régions irradiées lors du balayage du courant de -35 mA à +35 mA. Les régions marquées dans la boîte sont irradiées avec une dose de 37 ions/nm^2. b) Géométrie de l'irradiation et doses utilisée pour la commutation multi-niveaux. c) Commutation multi-niveaux à 4 états induite par le courant montrant l'importance de l'espace entre les régions irradiées pour la réalisation de la commutation partielle indépendante. Toutes les expériences SOT sont réalisées sous un champ de polarisation de 100 mT.

Conclusion

Les champs magnétiques ont souvent une influence surprenante sur les réactions électrochimiques. La plupart de ces effets peuvent être expliqués en termes d'effets convectifs sur la couche de diffusion entraînés par la force de Lorentz et/ou la force de Kelvin. L'influence du champ magnétique sur l'interface électrochimique est un sujet controversé. Nous avons étudié, en détail, comment un grand gradient de champ à une interface électrochimique peut influencer le mécanisme de réaction. Pour créer un grand gradient de champ concentré uniquement à l'interface solide/liquide, des films minces nanomagnétiques présentant une anisotropie magnétique perpendiculaire (PMA) ont été utilisés.

Des répétitions multiples de films Co/Pt ayant des domaines multiples ont été fabriquées et optimisées pour générer un gradient de champ maximal. Le couple redox ferri/ferrocyanure a été utilisé comme sonde redox pour l'investigation. L'influence de l'épaisseur de la couche de Pt sur l'activité des films Co/Pt a montré qu'une couche externe d'au moins 5 nm est nécessaire pour éviter complètement les effets des impuretés de surface. En utilisant la chronoampérométrie, une augmentation du courant a été observée avec le gradient de champ créé par les films de Co/Pt. La spectroscopie d'impédance a révélé comment les paramètres interfaciaux et de masse étaient affectés par la grande densité de force Kelvin à l'échelle nanométrique.

Dans un effort complémentaire afin de créer des configurations magnétiques électriquement reprogrammables, nous avons combiné le couplage spin orbite (SOT) et la technologie des ions hélium focalisés. L'anisotropie magnétique du film a été modifiée localement par irradiation. Des mesures électriques in-situ ont permis de suivre en temps réel le changement des propriétés magnétiques avec l'irradiation, ce qui a permis de déterminer avec précision la dose critique nécessaire pour atteindre l'état de transition d'aimantation hors du plan vers une aimantation dans le plan. La réduction correspondante du courant de commutation nous a permis de commuter sélectivement la région irradiée. Ainsi, un état magnétique multi-domaines piloté par un courant électrique a été démontré. En outre, la commutation multi-niveaux a également été démontrée avec une irradiation partielle et sous différentes doses de la barre de Hall.

Bibliography

[1]J. M. D. Coey, *Magnetism and magnetic materials* (Cambridge University Press, 2010).

[2]V. Gatard, J. Deseure, and M. Chatenet, "Use of magnetic fields in electrochemistry: a selected review", Current Opinion in Electrochemistry **23**, 96–105 (2020).

[3]L. M. A. Monzon and J. M. D. Coey, "Magnetic fields in electrochemistry: the lorentz force. a mini-review", Electrochemistry Communications **42**, 38–41 (2014).

[4]L. M. A. Monzon and J. M. D. Coey, "Magnetic fields in electrochemistry: the kelvin force. a mini-review", Electrochemistry Communications **42**, 42–45 (2014).

[5]S. Koehler and A. Bund, "Investigations on the kinetics of electron transfer reactions in magnetic fields", The Journal of Physical Chemistry B **110**, Publisher: American Chemical Society, 1485–1489 (2006).

[6]O. Devos, O. Aaboubi, J.-P. Chopart, A. Olivier, C. Gabrielli, and B. Tribollet, "Is there a magnetic field effect on electrochemical kinetics?", The Journal of Physical Chemistry A **104**, Publisher: American Chemical Society, 1544–1548 (2000).

[7]G. Hinds, F. E. Spada, J. M. D. Coey, T. R. Ní Mhíocháin, and M. E. G. Lyons, "Magnetic field effects on copper electrolysis", The Journal of Physical Chemistry B **105**, Publisher: American Chemical Society, 9487–9502 (2001).

[8]F. A. Garcés-Pineda, M. Blasco-Ahicart, D. Nieto-Castro, N. López, and J. R. Galán-Mascarós, "Direct magnetic enhancement of electrocatalytic water oxidation in alkaline media", Nature Energy **4**, Number: 6 Publisher: Nature Publishing Group, 519–525 (2019).

[9]O. Sambalova, E. Billeter, O. Yildirim, A. Sterzi, D. Bleiner, and A. Borgschulte, "Magnetic field enhancement of electrochemical hydrogen evolution reaction probed by magneto-optics", International Journal of Hydrogen Energy, `10.1016/j.ijhydene.2020.10.210` (2020).

[10]V. Lebedeva, V. Pierron-bohnes, C. Goyhenex, V. Papaefthimiou, S. Zafeiratos, R. Nazmutdinov, V. Da Costa, M. Acosta, L. Zosiak, R. Kozubski, D. Muller, and R. Savinova, "Effect of the chemical order on the electrocatalytic activity of model PtCo electrodes in the oxygen reduction reaction", Electrochimica Acta **108**, 605–616 (2013).

[11]P. Dunne and J. M. D. Coey, "Influence of a magnetic field on the electrochemical double layer", The Journal of Physical Chemistry C **123**, Publisher: American Chemical Society, 24181–24192 (2019).

[12]N. M. Dempsey, D. Le Roy, H. Marelli-Mathevon, G. Shaw, A. Dias, R. B. G. Kramer, L. Viet Cuong, M. Kustov, L. F. Zanini, C. Villard, K. Hasselbach, C. Tomba, and F. Dumas-Bouchiat, "Micro-magnetic imprinting of high field gradient magnetic flux sources", Applied Physics Letters **104**, Publisher: American Institute of Physics, 262401 (2014).

[13]Y. Zhang, C. Liang, J. Wu, H. Liu, B. Zhang, Z. Jiang, S. Li, and P. Xu, "Recent advances in magnetic field-enhanced electrocatalysis", ACS Applied Energy Materials, Publisher: American Chemical Society, 10.1021/acsaem.0c02104 (2020).

[14]O. Hellwig, A. Berger, J. B. Kortright, and E. E. Fullerton, "Domain structure and magnetization reversal of antiferromagnetically coupled perpendicular anisotropy films", Journal of Magnetism and Magnetic Materials **319**, 13–55 (2007).

[15]R. Salikhov, F. Samad, B. Böhm, S. Schneider, D. Pohl, B. Rellinghaus, A. Ullrich, M. Albrecht, J. Lindner, N. S. Kiselev, and O. Hellwig, "Control of stripe-domain-wall magnetization in multilayers featuring perpendicular magnetic anisotropy", Physical Review Applied **16**, Publisher: American Physical Society, 034016 (2021).

[16]P. H. Daum and C. G. Enke, "Electrochemical kinetics of the ferri-ferrocyanide couple on platinum", Analytical Chemistry **41**, Publisher: American Chemical Society, 653–656 (1969).

[17]N. B. Chaure and J. M. D. Coey, "Enhanced oxygen reduction at composite electrodes producing a large magnetic gradient", Journal of the Electrochemical Society **156**, Publisher: IOP Publishing, F39 (2009).

[18]N. B. Chaure, F. M. F. Rhen, J. Hilton, and J. M. D. Coey, "Design and application of a magnetic field gradient electrode", Electrochemistry Communications **9**, 155–158 (2007).

[19]I. M. Miron, T. Moore, H. Szambolics, L. D. Buda-Prejbeanu, S. Auffret, B. Rodmacq, S. Pizzini, J. Vogel, M. Bonfim, A. Schuhl, and G. Gaudin, "Fast current-induced domain-wall motion controlled by the rashba effect", Nature Materials **10**, Number: 6 Publisher: Nature Publishing Group, 419–423 (2011).

[20]L. Liu, O. J. Lee, T. J. Gudmundsen, D. C. Ralph, and R. A. Buhrman, "Current-induced switching of perpendicularly magnetized magnetic layers using spin torque from the spin

hall effect", Physical Review Letters **109**, Publisher: American Physical Society, 096602 (2012).

[21]K.-S. Lee, S.-W. Lee, B.-C. Min, and K.-J. Lee, "Threshold current for switching of a perpendicular magnetic layer induced by spin hall effect", Applied Physics Letters **102**, Publisher: American Institute of Physics, 112410 (2013).

[22]J. Fassbender, D. Ravelosona, and Y. Samson, "Tailoring magnetism by light-ion irradiation", Journal of Physics D: Applied Physics **37**, Publisher: IOP Publishing, R179–R196 (2004).

[23]J. H. Franken, M. Hoeijmakers, R. Lavrijsen, and H. J. M. Swagten, "Domain-wall pinning by local control of anisotropy in pt/co/pt strips", Journal of Physics: Condensed Matter **24**, Publisher: IOP Publishing, 024216 (2011).

[24]T. Devolder, C. Chappert, Y. Chen, E. Cambril, H. Bernas, J. P. Jamet, and J. Ferré, "Sub-50 nm planar magnetic nanostructures fabricated by ion irradiation", Applied Physics Letters **74**, Publisher: American Institute of Physics, 3383–3385 (1999).

[25]C. Fowley, Z. Diao, C. C. Faulkner, J. Kally, K. Ackland, G. Behan, H. Z. Zhang, A. M. Deac, and J. M. D. Coey, "Local modification of magnetic anisotropy and ion milling of Co/Pt multilayers using a He$\mathplus$ion beam microscope", Journal of Physics D: Applied Physics **46**, 195501 (2013).

[26]G. Hlawacek, V. Veligura, R. van Gastel, and B. Poelsema, "Helium ion microscopy", Journal of Vacuum Science & Technology B **32**, Publisher: American Vacuum Society, 020801 (2014).

[27]M. J. Gira, K. P. Tkacz, and J. R. Hampton, "Physical and electrochemical area determination of electrodeposited Ni, Co, and NiCo thin films", Nano Convergence **3**, 6 (2016).

[28]S. Woo, M. Mann, A. J. Tan, L. Caretta, and G. S. D. Beach, "Enhanced spin-orbit torques in pt/co/ta heterostructures", Applied Physics Letters **105**, Publisher: American Institute of Physics, 212404 (2014).

[29]Z. A. Bekele, K. Meng, J. Miao, X. Xu, and Y. Jiang, "The dominancy of damping like torque for the current induced magnetization switching in Pt/Co/W multilayers", Solid State Communications **274**, 41–45 (2018).

Acknowledgements

First and foremost, I would like to acknowledge my supervisor Prof. Bernard Doudin, not only for giving me the opportunity to work with him but also for his patient guidance, encouragement, advice and support throughout my PhD. I would like to thank him for all the fruitful discussions which helped me develop my critical thinking and scientific knowledge. I would like to thank Dr. Peter Dunne for his great support and motivation during my research. I express my sincere gratitude to him sharing his scientific knowledge and expertise which helped me widen my research in various perspectives.

I would like to thank MAMI, the Marie Curie Horizon 2020 ITN network EU for funding my PhD. I am honoured and proud to be a part of this interdisciplinary Marie Curie research network through which I got the opportunity to interact with many of the greatest minds in different fields. Conferences and workshops during the MAMI network meetings not only improved my scientific insight but also helped me to interact and collaborate with other scientists. I thank Dr. Anna Oleshkevych and Dr. Laura, our current and former project managers, for organizing the meetings and also for all the help and suuport throughout the project. I thank all my fellow PhD students in the network for their help and support.

I am deeply greatful to Prof. Michael Coey for the scientific discussions and advises during my secondment in Dublin. I would like to extend my heartful thanks to Dr. Venkatesan for helping me with the the SQUID measurements and and also for VISA related help. I thank Prof. P. Stamenov, Dr. Niclas Teichert, Dr. Gwenael Atcheson, Dr. Karsten Rode, Ajay Jha, Simon Lenne and Sruthy Poulose for their help with experiments related to sputtering and magneto-optical measurements.

I would like to acknowledge Dr. Ciaran Fowley for all his help and support during my secondment in Dresden. I thank him for the discussions related to irradiation and electrical measurements which helped me improve my understanding about the topics. I thank Dr. Gregor Hlawacek for his immense help and support with the helium irradiation. I thank Prof. Olav Hellwig and Dr. Ruslan Salikhov for the help with sample sputtering. Thanks to Dr. Serhii Sorokin and Dr. Lakshmi Ramasubramanian for their help and support during my secondment in Dresden.

I would like to thank Dr. Hicham Majjad, Sabine Seigwald and Romain Bernard for the constant help during the cleanroom nanofabrication process. I would like to express my sincere gratitude for helping me with all those endless wafer dicing.

I would like to thank my colleagues in the host institute for their aid and coorporation throughout my PhD. I would like to express my sincere thanks to our institute director Pierre Rabu, the Doctroral School (ED-182) director Aziz Dinia, the IPCMS secretary Catherine Bonnin, the IPCMS librarian Beatrice Masson, the head of department (DMONS) Yves Henry, the department secretary Veronique Wernher and all the other people in the IPCMS for hosting me for these years and all the administrative help. I thank Dr. Jerome Robert for helping me with the SQUID measurements. Our friendship started with just a piece of cake and now he is our group's official French-to-English translator. I thank Dr. Bohdan Kundys for his help and support to build my experimental setup for electrical measurements. I would like to thank Dr. Salia Cherifi-Hertel and Dr. Victor Da Costa for the magnetic domain imaging measurements. I thank Fabien for his technical help during the course of my work.

My colleagues and friends Aleena Joseph, Arvind Dev and Dr. Krishna Prasad Maity deserves a special mention. I can not ever forget the moments how I first met with each of you and spending these many years together. Without you guys, my PhD journey would have been way more difficult. The week-end cooking, biking, tennis and trips were all a wonderful experience. Our small talks in the office and during the coffee time were so stress-relieving and delightful. I also thank Niveditha, Raj, Cristeena, Deeksha, Anjana and Vineesha for their help and support.

I should not forget to mention the motivation and support from my bachelors teacher Dr.Biju K.P. I express my sincere gratitude to him for inspiring me to build a career in research. I am thankful for the love and encouragement from all my teachers since the beginning.

I am extremely thankful to my close friend Kavipriya Thangavel for always buoying me up and believing in me. I thank Alvin Joseph, Shintu Vargheese, Praveen Vijayan and Amrutha V. for their love and constant support.

Last, but most importantly, I would be nowhere around here without the endless love and care from my family. Words cannot express my gratitude to my father Kurian C.K, my mother Saly, my brother Dr. Manu and my sister-in-law Rini. I can't thank you enough for the continuous and unconditional support and for being there with me whenever I felt alone and weak.

Contents

List of Figures

List of Tables

List of Abbreviations

1D	1-**D**imensional
2D	2-**D**imensional
ac	**a**lternating **c**urrent
AFM	**A**tomic **F**orce **M**icroscope
AHE	**A**nomalous **H**all **E**ffect
CA	**C**hrono-**A**mperometry
CE	**C**ounter **E**lectrode
CISS	**C**hirality **I**nduced **S**pin **S**electivity
CV	**C**yclic **V**oltammety
dc	**d**irect **c**urrent
DMI	**D**zyaloshinskii–**M**oriya **I**nteraction
DW	**D**omain **W**all
EIS	**E**lectrochemical **I**mpedance **S**pectroscopy
FIB	**F**ocused **I**on **B**eam
FM	**F**erromagnetic **M**etal
HER	**H**ydrogen **E**volution **R**eaction
HH	**H**armonic **H**all
HIM	**H**elium **I**on **M**icroscope
HM	**H**eavy **M**etal
HZDR	**H**elmholtz-**Z**entrum-**D**resden-**R**ossendorf
IHP	**I**nner **H**elmholtz **P**lane
KK	**K**ramers **K**ronig
MFM	**M**agnetic **F**orce **M**icroscopy
MHD	**M**agneto-**H**ydro**D**ynamics
MOKE	**M**agneto-**O**ptical **K**err **E**ffcet
OCP	**O**pen **C**ircuit **P**otential
OER	**O**xyen **E**volution **R**eaction
OHP	**O**uter **H**elmholtz **P**lane

OOMMF	**O**bject **O**riented **M**icro**M**agnetic **F**ramework
ORR	**O**xygen **R**eduction **R**eaction
pH	**p**otential of **H**ydrogen
PHE	**P**lanar **H**all **E**ffect
PMA	**P**erpendicular **M**agnetic **A**niotropy
RDE	**R**otating **D**isk **E**lectrode
RE	**R**eference **E**lectrode
SHE	**S**pin **H**all **E**ffect
SOC	**S**pin **O**rbit **C**oupling
SOT	**S**pin **O**rbit **T**orque
SQUID	**S**uper-conducting **Q**uantum **I**nterference **D**evice
TCD	**T**rinity **C**ollege **D**ublin
TEM	**T**ransmission **E**lectron **M**icroscope
WE	**W**orking **E**lectrode
XPS	**X**-ray **P**hoton **S**pectroscopy
XRR	**X**-**R**ay **R**eflectivity

List of Publications

1. Peter Dunne, Ciaran Fowley, Gregor Hlawacek, **Jinu Kurian**, Gwenaël Atcheson, Silviu Colis, Niclas Teichert, Bohdan Kundys, M Venkatesan, Jürgen Lindner, Alina Maria Deac, Thomas M. Hermans, J. M. D. Coey and Bernard Doudin, *'Helium Ion Microscopy for Reduced Spin Orbit Torque Switching Currents'*, Nano Letters, 2020, 20, 10, 7036–7042, doi.org/10.1021/acs.nanolett.0c02060

2. **Jinu Kurian**, Aleena Joseph, Salia Cherifi-Hertal, Peter Dunne, Ciaran Fowley, Gregor Hlawacek, Gwenaël Atcheson, Michelangelo Romeo, Thomas M. Hermans, J. M. D. Coey, Bernard Doudin, *'Design of Multi-state Spin Orbit Torque Switching Device Using Helium Ion Microscopy'.* (to be submitted)

3. **Jinu Kurian**, Peter Dunne, Ruslan Salikhov, Olav Hellwig, Ciaran Fowley, Gwenaël Atcheson , J. M. D. Coey and Bernard Doudin *' Influence of Pt Cap Layer Thickness on the Electrochemical Activity of Co/Pt Mutlilayers'.* (under preparation)

4. **Jinu Kurian**, Peter Dunne, Ruslan Salikhov, Olav Hellwig, Ciaran Fowley, Gwenaël Atcheson , J. M. D. Coey and Bernard Doudin, *' Influence of High Intensity Nanoscale Magnetic Field Gradient on the Electrochemical Reaction'.* (under preparation)

About the Project

This PhD thesis is a part of Marie Curie Magnetics and Microhydrodynamics (MAMI) HORIZON 2020 ITN network funded by European Union[1]. This project entitled: "Magnetics and Microhydrodynamics - from guided transport to delivery" combines the expertise in the fields of magnetism and fluidics to solve the pressing challenges in the field of microfluidics. Taking advantage of magnetic forces in combination with the high susceptibility liquids, a liquid-in-liquid confined microfluidic channel without walls can be realised. These microns sized wall-less channels are attractive due to its unique non-fouling properties and no-slip boundary conditions, which find applications in the biological microfluidics. All early-stage-researchers involved in this multi-disciplinary project work towards the common goal which is to understand the fundamentals of the local fluid flow, and to develop and optimize the novel magnetic liquid confined wall-less microfluidic devices of industrial relevance.

Our group has recently achieved the stabilization of wall-less microchannel using the combination of magnetic quadrapole and ferrofluids [1]. This top-down approach is based on the special arrangement of macroscopic magnets to obtain the required magnetic field conditions for the realization of microscopic tubes. On the other hand, a bottom-up approach uses nanostructures to realize the similar goal. Owing to the scale invariance of the magnetic field, huge field gradient can be achieved in the immediate vicinity of the nanomagnets. Our motivation is to study how this intense nanoscale magnetic forces can impact local chemical reactions. For this purpose, we fabricated planar surfaces with high magnetic contrast at the nanoscale, creating the required large force field at the interface with the solution, and investigated its influence in water-based solutes.

[1] https://mami.u-strasbg.fr/

Bibliography

[1]P. Dunne, T. Adachi, A. A. Dev, A. Sorrenti, L. Giacchetti, A. Bonnin, C. Bourdon, P. H. Mangin, J. M. D. Coey, B. Doudin, and T. M. Hermans, "Liquid flow and control without solid walls", Nature **581**, Number: 7806 Publisher: Nature Publishing Group, 58–62 (2020).

Chapter 1

Introduction

1.1 Electrochemical Phenomena

Electrochemistry deals with relationships between electricity and chemical reactions. In this section, we will discuss the processes and factors affecting the charge transport between an electronic conductor (electrode) and an ionic conductor (electrolyte).

1.1.1 Electrochemical Cell

An electrochemical cell is a device than can convert chemical energy into electrical energy or vice versa . These are classified as either galvanic cells or electrolytic cells. In galvanic or Voltaic cells, spontaneous chemical reactions convert chemical energy into electrical energy. An example is the Daniel cell which consists of copper and zinc electrodes immersed in a solution of copper and zinc sulphate, respectively. Zinc oxidized at the anode and copper reduced at the cathode generate a cell emf around 1.1 V. An electrolytic cell in contrast requires external electrical energy to drive the chemical reaction. An example is the electrolysis of water where hydrogen and oxygen gas can be produced by supplying an external direct current to split the water.

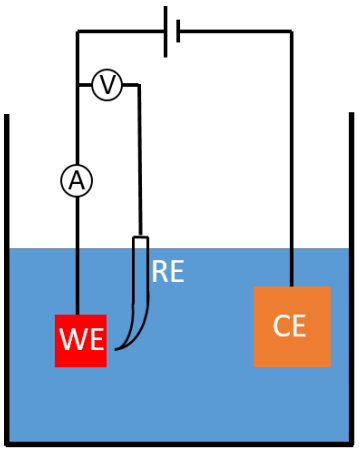

FIGURE 1.1: An electrochemical cell in three electrode configuration

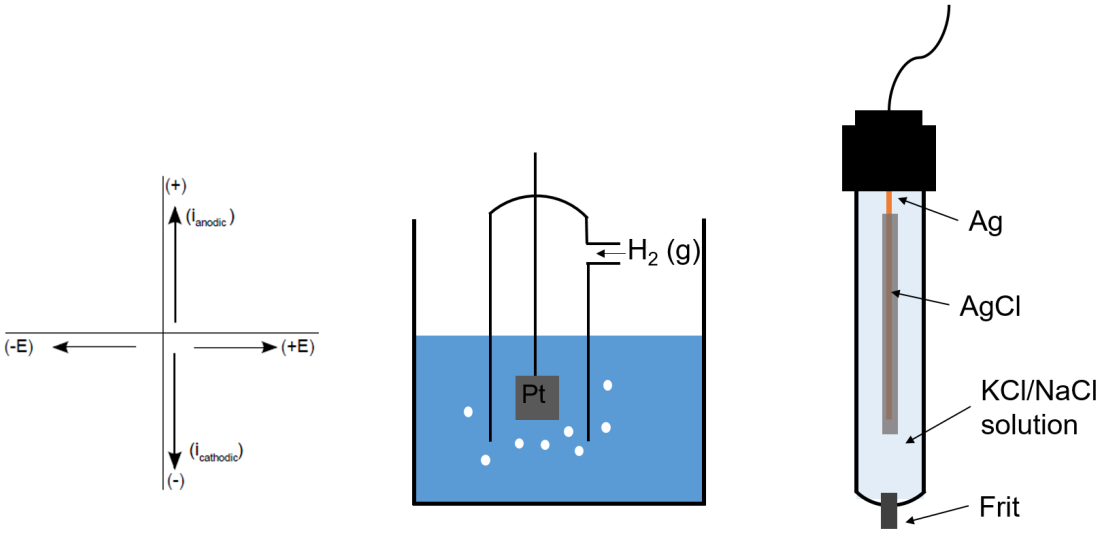

FIGURE 1.2: a) IUPAC voltammetry convection. Example of b) standard hydrogen electrode and c) Silver/silver chloride reference electrode.

A standard three-electrode configuration is commonly used in electrochemistry for a better control and measurement of current and potential in the cell [1, 2] (Fig. 1.1). It consists of a working electrode (WE) where the reaction of interest happens, a counter electrode (CE) which supplies the current, and a reference electrode (RE) with respect to which the potential of the WE is measured. The area of CE should always be greater than that of the WE so that the reaction near WE won't be limited by the CE supply. The purpose of RE is to provide a sTable potential reference for the controlled regulation of WE. Standard hydrogen electrode (SHE) is an internationally accepted primary choice for reference electrode (Fig. 1.2b). It consists of a redox half reaction:

$$2H^+(aq) + 2e \rightleftharpoons H_2(g) \tag{1.1}$$

and its standard potential is defined as E^0 = 0.0 V at all temperatures. Hydrogen electrodes are not very convenient to use in laboratory. Silver/silver chloride reference electrode is another practical choice due to its simplicity and non-toxicity (Fig. 1.2c). The redox reaction in saturated KCl/NaCl solution follows as:

$$AgCl + e^- \rightleftharpoons Ag + Cl^- \tag{1.2}$$

where $E^0_{Ag/AgCl}$ = 0.197 V versus SHE (25^0C). It is also worthwhile to note that, through out the present work, the European polarity convention adopted by IUPAC is followed, where anodic (positive) potentials are plotted to the right of the origin and anodic currents are

taken as positive (Fig. 1.2a).

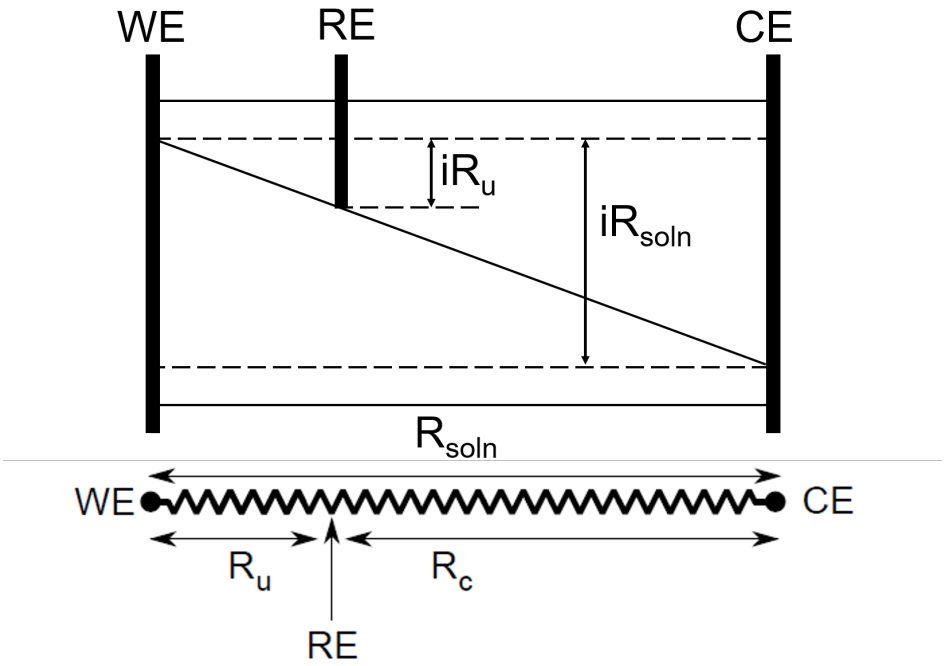

FIGURE 1.3: Schematic of uncompensated resistance between working electrode and reference electrode.

The relative position of the reference electrode with respect to the working electrode is also critical in the electrochemical system. In a three electrode configuration, the potential of WE is measured with respect to the reference electrode RE and any measuring current flowing in this circuit is reduced using a high impedance voltmeter. However, a small but finite current can pass through the reference electrode which can shift the potential from the true value. More generally, as a current always flow in a solution that possess an intrinsic resistance, there will always be a difference in the effective potential experienced by the WE when compared to the measured potential between RE and WE (Fig. 1.3). Hence, it is important to correct for this so-called iR drop as it can significantly affect the measurement and analysis.

The main approaches dealing with iR compensation are (i) impedance spectroscopy, (ii) current-interrupt method and (iii) positive feedback method. Using impedance spectroscopy, R_u can be estimated and the potential is post-corrected for iR drop. But, it is a relatively time consuming process and also demands a prior knowledge of equivalent circuit model for the EIS fit. In current-interrupt method, R_u is determined by switching off the current and measuring the cell potential decay. When the current is switched off quickly, the potential difference due to the uncompensated resistance drops to zero and R_u can be estimated. Last but not least is the positive feedback method where solution resistance is

compensated electronically using op-amps based feedback circuits. The measured potential is made match with the applied voltage by adjusting the feedback resistance R_f. A higher R_f will drive the electronics into oscillations. R_f is adjusted to a value corresponding to the threshold of the oscillations.

Consider a general electrochemical reaction of the type

$$O + ne^- \rightleftharpoons R \tag{1.3}$$

where O is reduced to R in an n electron transfer reaction. When an electrode is placed in an electrolyte, thermodynamic equilibrium is achieved between the electrode and the solution. In this condition, both forward and reverse reactions are balanced, and the interface is in dynamic equilibrium. This equilibrium is characterised by the Nernst equation

$$E = E^{0'} + \frac{RT}{nF} \ln \frac{C_O}{C_R} \tag{1.4}$$

where E is the electrode potential, $E^{0'}$ is the formal potential and C_O, C_R are the concentration of oxidised and reduced species, respectively. The Nernst equation thus provides the interrelation between the solute concentration and the cell potential in a system under equilibrium. To illustrate this, the open circuit potential (OCP) is considered. OCP is the potential established between WE and RE when the circuit is open. In the case of ferri/ferrocyanide redox couple in electrolyte containing 0.2 M potassium ferricyanide and 1 M KCl, corresponding to experiments presented in chapter 3,

$$[Fe(CN)_6]^{3-} + e^- \rightleftharpoons [Fe(CN)_6]^{4-} \tag{1.5}$$

the OCP of the system is experimentally measured as 0.41 V. Using a value E^0 = 0.26 V obtained from cyclic voltammetry, the ratio of oxidized to reduced species can then be calculated as

$$0.41V = 0.26V + 0.0257V \ln \left(\frac{[Fe(CN)_6]^{3-}}{[Fe(CN)_6]^{4-}} \right) \tag{1.6}$$

which gives the ratio of $Fe(CN)_6^{3-}$ to $Fe(CN)_6^{4-}$ as 12.6:1.0. Therefore, the solution contains approximately 93% (0.185 M) $Fe(CN)_6^{3-}$ and 7% (0.015 M) $Fe(CN)_6^{4-}$. OCP also indicates the stability of the system. It has been reported that the magnetic field can shift the OCP of metallic electrodes in Nitric acid solutions which is ascribed to the Lorentz force enhanced corrosion current [3]. In the case of ferri/ferrocyanide, we observed sTable OCP for long time which hints to the good stability of the redox system under study (Fig.1.4).

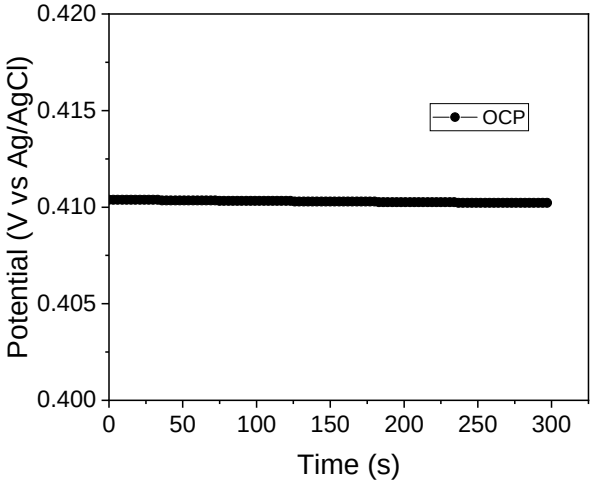

FIGURE 1.4: Open-circuit potential of Pt thin film working electrode in 0.2 M potassium ferricyanide and 1 M KCl.

1.1.2 Electrode Kinetics

Processes occurring at electrodes can be classified as faradaic and nonfaradaic in nature. Faradaic process are those which are governed by Faraday's law which states that the amount of chemical reaction caused by the flow of current is proportional to the amount of electricity passed. On the other hand, nonfaradaic process involves transient currents due to the specific adsorption and desorption at the solid-liquid interface. Here, we limit the discussion to electron transfer mechanism that are faradaic processes without chemical transformation. Ferri/ferrocyanide redox reaction is an example of such a reaction. A simple description of the mechanism follows [2] as (Fig. 1.5):

1. Diffusion of species from bulk solution to electrode interface.
2. Rearrangement of the ionic atmosphere (10^{-8} s).
3. Reorientation of the solvent dipoles (10^{-11} s).
4. Alterations in the distances between the central ion and the ligands (10^{-14} s).
5. Electron transfer (10^{-16} s).
6.. Relaxation.

For any electrode reaction in solution, the Arrhenius expression relates the activation energy E_A and temperature of the system to the kinetic rate constant as,

$$k = A \exp[-E_A/RT] \tag{1.7}$$

We consider a standard redox reaction with k_a, k_c are the forward and reverse reaction rate respectively. From eqn.1.7, we obtain

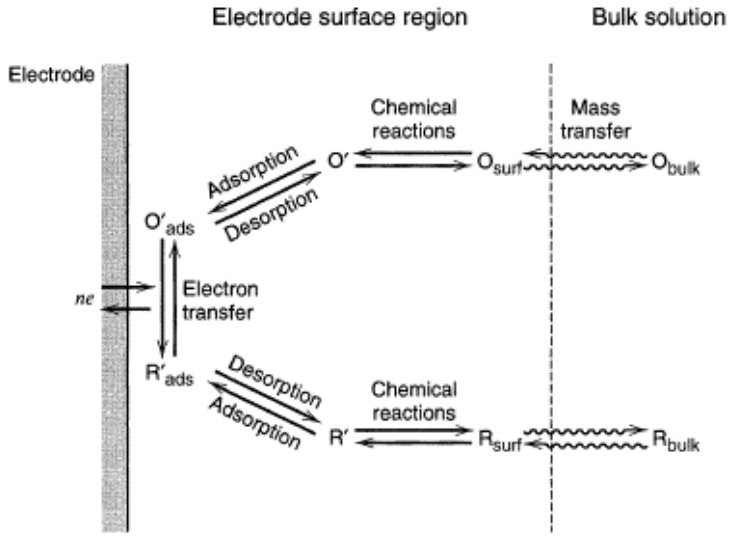

FIGURE 1.5: Schematic representation of electron transfer at electrode surface [1].

$$k_a = k_0 \exp[\alpha_a n F(E - E^0)/RT] \tag{1.8}$$

$$k_c = k_0 \exp[-\alpha_c n F(E - E^0)/RT] \tag{1.9}$$

where k_0 is the standard rate constant at equilibrium, and α_a, α_c are the charge transfer coefficients of the oxidation and reduction steps respectively. For a reversible one electron transfer system $\alpha_a + \alpha_c = 1$. α_a, α_c represents the symmetry of the activation barrier for oxidation and reduction, and can take values from 0 to 1 where 0.5 corresponds to a symmetric barrier. In a first order reaction, the rate of reaction is proportional to the concentration of reactants and the net current flow is given as

$$I = nFA(k_a[R]_* - k_b[O]_*) \tag{1.10}$$

At equilibrium, there is no net current flow and $k_a[R]_* = k_c[O]_*$. In a special case if $[R]_* = [C]_*$, then $k_a = k_c = k_0$ and using eqn.1.8 and eqn.1.9 in eqn.1.10 we get

$$I = I_0 \left[\frac{[O]_*}{[O]_\infty} \exp\left(\frac{-\alpha_c n F \eta}{RT}\right) - \frac{[R]_*}{[R]_\infty} \exp\left(\frac{\alpha_a n F \eta}{RT}\right) \right] \tag{1.11}$$

where η = E - E^0 is the overpotential. At low overpotential or when the solution is stirred so that the surface concentration won't deviate much from the bulk concentration, the current-potential relation reduees to Bulter-Volmer (BV) equation,

$$I = I_0 \left[\exp\left(\frac{-\alpha_c n F \eta}{RT}\right) - \exp\left(\frac{\alpha_a n F \eta}{RT}\right) \right] \tag{1.12}$$

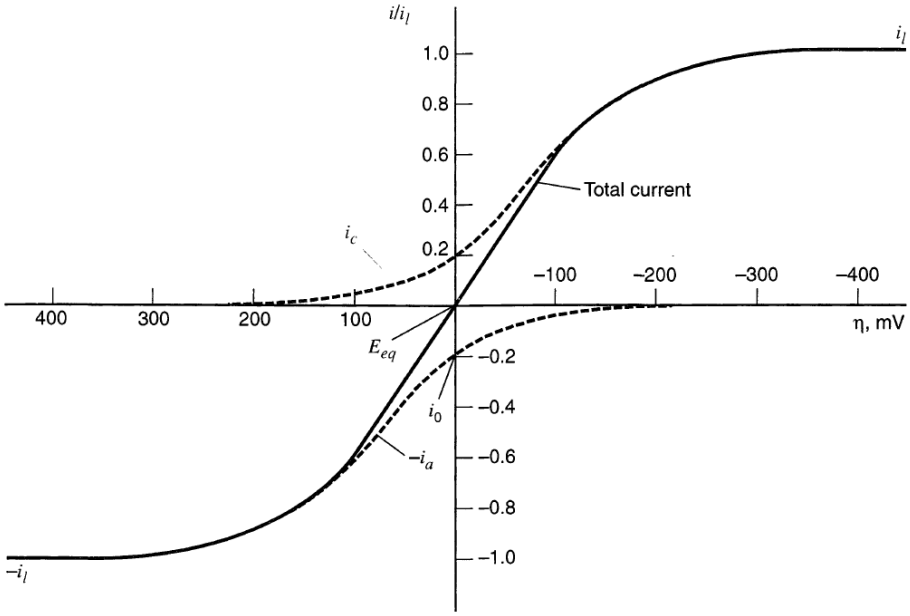

FIGURE 1.6: Current-overpotential curve for a reversible reaction. At low overpotential the current magnitude rises rapidly because of the exponential current dependence to voltage (Eqn. 1.12). At large overpotential, the current is limited by mass transfer [1] Note: American convection is used in this plot.

BV equations deals with the current-potential relation (Fig. 1.6). In a kinetically controlled reaction, it tells that the current changes exponentially with the applied voltage. On the other hand, it does not include any mass transport effects and assumes a infinite supply of reactants near the electrode surface.

Kinetic rate (k_0) is a measure of the kinetic facility of a redox couple. A system with large k_0 will achieve equilibrium on a shorter timescale compared to the one with lower k_0 value. Wide range of k_0 has been reported in electrochemistry with a minimum of 10^{-9} cm/s for irreversible methanol oxidation [4] to a maximum of 1-10 cm/s for reversible reactions involving hydrocarbons like anthracene and pyrene [5, 6]. For quasi-reversible ferri/ferrocyanide redox couple, k_0 value has been reported in the range of 0.01 to 0.4 cm/s depending on the nature of electrode and supporting electrolytes used [7–9].

In order for the kinetic theory to be accurate, the kinetic equations should reach the the thermodynamic relations in the limit of equilibrium. At equilibrium, the net current is zero and from Eqn.1.11 we get,

$$[O]_* \exp\left(\frac{-\alpha_c n F (E - E^0)}{RT}\right) = [R]_* \exp\left(\frac{(1-\alpha_c) n F (E - E^0)}{RT}\right) \tag{1.13}$$

Rewriting the equation yields,

$$E = E^0 + \frac{RT}{F} \ln \frac{[0]_*}{[R]_*} \tag{1.14}$$

which is the Nernst equation. Even though the net current is zero, the equilibrium is envisioned as a flow is equal amount of cathodic and anodic current defined as the exchange current.

1.1.3 Interfacial Region

In the previous section we discussed about the kinetics of the reaction but without considering the nature of solid-liquid interface. In fact, the interface plays a crucial role in determining the kinetic as well as the thermodynamic properties of the reaction. In this section, we will discuss about the various models which describes the electrode-electrolyte interface capacitance.

1.1.3.1 Double Layer Models

Experimentally, the double layer capacity at different potentials can be measured by impedance spectroscopy and electrocapillary. Several models have been developed to predict the evolution of the interfacial capacitance with the applied potential.

1.1.3.1.1 Helmholtz Model

The first model for interface capacitance was given by Helmholtz in 1879. He considered the charge separation at electrode-solution interface as single rigid layer of counter ions in the solution balancing the excess charge on the electrode surface.

In this model, the interfacial capacitance is treated as a parallel plate capacitor, giving rise to the designation double layer. The relation between stored charge density σ and the voltage drop V in a parallel plate capacitor placed at distance d is given by

$$\sigma = \frac{\epsilon_r \epsilon_0 A}{d} V \tag{1.15}$$

The differential capacitance is then given as,

$$C_H = \frac{\partial \sigma}{\partial V} = \frac{\epsilon_r \epsilon_0 A}{x_H} \tag{1.16}$$

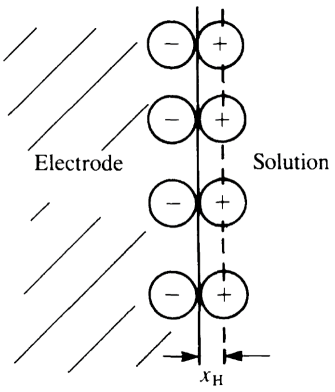

FIGURE 1.7: Helmholtz model of double layer with rigid arrangement of ions [2].

where x_H is the distance of closest approach of ions defined as the ionic radius even though the ions are treated as point charges. Helmholtz double layer capacitance is independent of applied voltage which is in contrast to the experimental observation. Furthermore, it neglects any adsorption effects as well as does not take into account any dependence on electrolyte concentration.

1.1.3.1.2 Gouy-Chapman Model

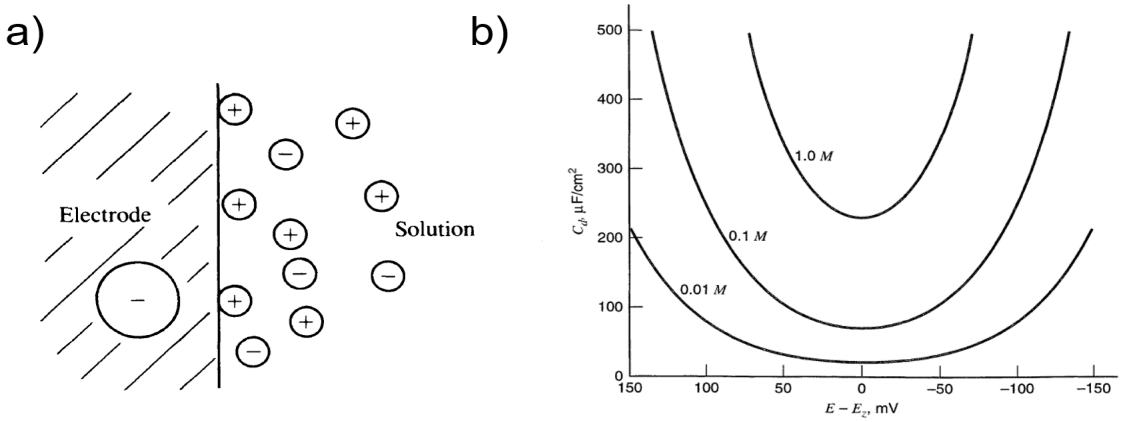

FIGURE 1.8: Gouy-Chapman model of double layer. a) Schematics of ions distribution in diffusive layer [2] and b) variation of diffusive double layer capacitance with potential at different electrolyte concentrations [1].

In order to include the influence of electrolyte concentration and applied potential, Gouy and Chapman independently proposed the diffusive double layer model where the ions in the solution side of the interface are considered distributed across a finite distance, in contrast to the rigid layer Helmholtz model. Such a distribution would arise due to the thermal energy as well as due to the electrostatic repulsion and attraction between ions. In their model, the solution side is subdivided into laminae, parallel to electrode, and the distribution of ions in any lamina is given by Boltzmann's law as

$$n_i = n_i^0 \exp\left(\frac{-z_i e \phi_\Delta}{kT}\right) \tag{1.17}$$

where n_i is the number concentration of ions i in bulk solution, z_i is the ion charge and $\phi_\Delta = \phi - \phi_s$ is the potential at the lamina. The total charge per unit volume in any lamina is

$$\rho(x) = \sum_i n_i z_i e = \sum_i n_i^0 z_i \exp\left(\frac{-z_i e \phi_\Delta}{k_B T}\right) \tag{1.18}$$

From electrostatics, $\rho(x)$ is related to potential by Poisson equation

$$\frac{\partial^2 \phi_\Delta}{\partial^2 x} = -\frac{\rho}{\epsilon_r \epsilon_o} \tag{1.19}$$

which leads to the Poisson-Boltzmann equation

$$\frac{\partial^2 \phi_\Delta}{\partial^2 x} = -\frac{e}{\epsilon_r \epsilon_o} \sum_i n_i^0 z_i \exp\left(\frac{-z_i e \phi_\Delta}{k_B T}\right) \tag{1.20}$$

Solving this equation and assuming a symmetric z:z electrolyte (one which has only one cation and anion, both of charge z), one would get the differential capacitance as

$$C_{d,GC} = \left(\frac{2z^2 e^2 \epsilon_r \epsilon_0 n_i^0}{k_B T}\right) \cosh\left(\frac{ze\phi_{\Delta,0}}{2k_B T}\right) \tag{1.21}$$

The cosh tern in the Gouy-Chapman contains the potential dependence of the capacitance. The minimum occurs at point of zero charge (E_{pzc}). Similar V-shaped capacitance function resembles the experimentally observed shape near E_{pzc} but deviates at larger potentials and also at higher electrolyte concentration.

1.1.3.1.3 Stern Model

The Gouy-Chapman capacitance will rise to an unlimited value when the potential is far from E_{pzc}. This is due to the fact that the ions are considered as point charges and are not restricted with respect to their location in the solution. Far from E_{pzc}, ions can be considered as arranged tightly attracted to the electrode surface with a separation equal to the ionic radius. Thus, Stern combines the diffuse double layer and rigid layer models which is mathematically equivalent to two capacitors connected in series. The effective capacitance is given as

$$\begin{aligned} \frac{1}{C_S} &= \frac{1}{C_H} + \frac{1}{C_{GC}} \\ &= \frac{x_H}{\epsilon_r \epsilon_0 A} + \frac{1}{\left(\frac{2z^2 e^2 \epsilon_r \epsilon_0 n_i^0}{k_B T}\right) \cosh\left(\frac{ze\phi_{\Delta,0}}{2k_B T}\right)} \end{aligned} \tag{1.22}$$

where C_H, C_{GC} represents the Helmholtz and Gouy-Chapman capacitance respectively. When two capacitors are connected in series, the smaller one dominates over other. As we have already seen, at potential far from E_{pzc}, C_{GC} rises to huge value which makes the C_H dominant term. On the other hand, close to E_{pzc}, $C_H >> C_{GC}$ and so $C_S \approx C_{GC}$. This is one of

the most accurate model so far to describe the interfacial capacitance dependence with the applied voltage.

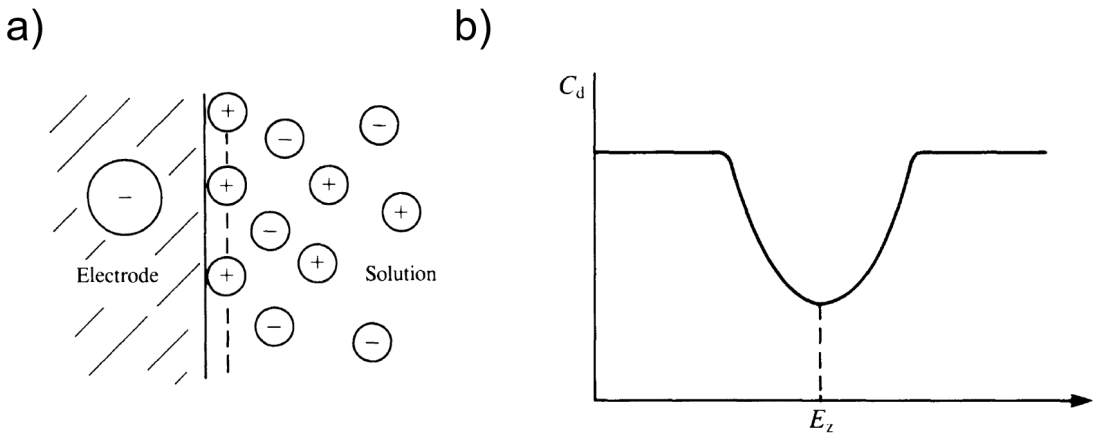

FIGURE 1.9: Stern's model of double layer [2]. a) Schematics of ions distribution at the interface and b) variation of Stern capacitance with potential [1].

1.1.3.1.4 Further Developments

In 1947, Grahame developed a double layer model which divides interfacial region into three regions: the inner Helmholtz plane (IHP), the outer Helmholtz plane (OHP) and the diffusive layer. The difference with the Stern model is the inclusion of the IHP which forms the plane of specifically adsorbed ions. In contrast to a non-specifically adsorbed ion, a specifically adsorbed ion can approach closer to the electrode surface by losing its solvation layer. Besides, there is no restriction in the charge of the ions involved. The effect of specific adsorption is more sensitive near E_{pzc} as the ions are more tightly bound at larger potentials. It causes a shift in the point of zero charge [10]. The extend of specific adsorption depends on the electrolyte concentration as well as on the electrode material.

1.1.4 Mass Transport

As we discussed in section 1.1.2, the net current flow in a kinetic limited system is given by Eqn. 1.10. The rate of charge transfer increases with the potential as the kinetic rate depends on the electrode potential. Regarding the surface concentration, so far we only considered reactions which have infinite supply of ions at the surface i.e, constant surface concentration irrespective of the applied voltage. Such an assumption is good when the kinetics of the reaction is very slow compared to the transport time of species to and from the solution (kinetically limited reaction). However, in electrochemistry, there are many reactions whose

kinetics are fast and the net reaction depends on the surface concentration under the application of a sufficiently high potential. Thus, it is important to discuss about the different means of mass transfer which are diffusion, migration and convection. Diffusion refers to the movement of ions due to concentration gradient while migration is caused by the movement of charged particle in an electric field. Whereas convection deals with the ion transport due to density gradient or mechanical stirring. The process of mass transport is described by the Nernst-Plank equation as

$$J_i = -D_i \nabla c_i - \frac{z_i F}{RT} D_i c_i \nabla \phi + c_i v \tag{1.23}$$

where J_i is the flux of the species i at a given position from the surface, D_i is the diffusion coefficient, ∇c_i is the concentration gradient, z_i is the charge of species i, $\nabla \phi$ is the electric potential gradient and v is the fluid velocity of a volume element in solution. Electrochemical analysis becomes complicated when all three modes of transport are present in the system. In most of the measurements, migratory effects are minimised by adding an excess of electroinactive species. The presence of this inert supporting electrolyte screens the electric field at the interface which makes the field effects concentrated near to the electrode surface. Furthermore, convection can be minimised by avoiding any stirring of solution, by adjusting the working electrode position to minimize the natural convection and by minimising the thermal gradient. Charge transfer and mass transport are two consecutive process, hence the slowest process determines the overall reaction of the system. It is possible to write the observed steady state current as

$$\frac{1}{i_s} = \frac{1}{i_k} + \frac{1}{i_m} \tag{1.24}$$

where i_k, i_m represents the kinetic and mass transport controlled currents respectively. At low over-potential, $i_k < i_m$ and a steady current increases with potential. At large over-potential, $i_m < i_k$ and the steady current will be independent of the applied potential irrespective of any improvement in the kinetic rate. Fig. 1.10 shows the example plot of the limiting current as a function of applied voltage for ferri/ferrocyanide redox reaction. When the potential is near OCP of 0.41 V, the system is kinetically limited, and becomes mass transport limited when the applied potential is < 0.2 V.

1.1.4.1 Diffusion

As mentioned earlier, diffusion refers to the natural movement of species due to the concentration gradient. Fick's first law of diffusion can be expressed as

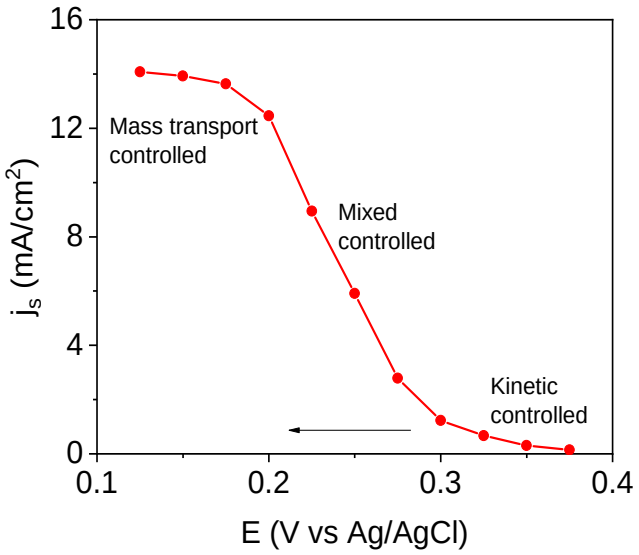

FIGURE 1.10: Steady state current density as a function of applied potential to the Pt film electrode in electrolyte consists of 0.2 M potassium ferricyanide and 1 M KCl. Steady state current measured 5 min after the application of potential.

$$J = -D\frac{\partial c}{\partial x} \tag{1.25}$$

where the proportionality constant between flux and concentration gradient is called the diffusion coefficient D. In dilute solutions, typical values of D range between 10^6 and 10^{-5} cm^2/s. The variation of concentration with time due to the diffusion is described by Fick's second law which can be expressed in a 1D simplest case as

$$\frac{\partial c}{\partial t} = D\frac{\partial^2 c}{\partial x^2} \tag{1.26}$$

At steady state, the concentration is constant and the left side of Eqn. 1.26 becomes zero which leads to the Laplace's equation (1D)

$$\frac{\partial^2 c}{\partial x^2} = 0 \tag{1.27}$$

1.1.4.1.1 Cottrellian system

Chronoamperometry is a commonly used technique to study the diffusion limited systems. In this technique, the WE potential is stepped from a value where no reaction occurs to a value where all the electroactive species react. Evolution of diffusion limited current (assuming no migration and convective effects) with time is recorded to find the diffusion coefficient of the system. Assuming semi-infinite linear diffusion for planar electrode, the

diffusion limited current can be expressed as

$$I_d = nFAD\left(\frac{\partial c}{\partial x}\right)_0 \tag{1.28}$$

as $I_d = nFAJ$. For simplicity, the oxidation with c = [R] is considered. We solve for the Fick's second law (Eqn. 1.26) with the following boundary conditions

$$t = 0, \qquad c_0 = c_\infty \qquad \text{no electrode reaction} \tag{1.29}$$

$$t \geq 0, \qquad \lim_{x\to\infty} c = c_\infty \qquad \text{bulk solution} \tag{1.30}$$

$$t < 0 \text{ and } x = 0, \qquad c_0 = 0 \qquad \text{diffusion limited current} \tag{1.31}$$

where c_0 is the surface concentration and c_∞ is the bulk concentration. Solving this using the Laplace transform and inverting it, we find the concentration gradient as

$$\left(\frac{\partial c}{\partial x}\right)_0 = \frac{1}{\delta} \tag{1.32}$$

where $\delta = (\pi Dt)^{1/2}$ is the diffusion layer thickness. This leads to the Cottrell equation

$$I(t) = I_d(t) = \frac{nFAD^{1/2}c_\infty}{(\pi t)^{1/2}} \tag{1.33}$$

It must be noted that any capacitive or convective effects are not considered in the Cottrellian system. At short times there can be contribution due to the charging of double layer and at long time, natural convection can perturbs the concentration gradients.

1.1.4.2 Convection

Convection is the motion of a fluid under the action of a force. It can be divided into natural convection which arises due to the thermal or density gradient, and forced convection due to mechanical or magnetohydrodynamic stirring. One of the relevant parameter is the hydrodynamic boundary layer δ_H within which all the velocity gradient occurs. It is related to the diffusion layer δ as

$$\delta_H = \left(\frac{v}{D}^{1/3}\right)\delta \tag{1.34}$$

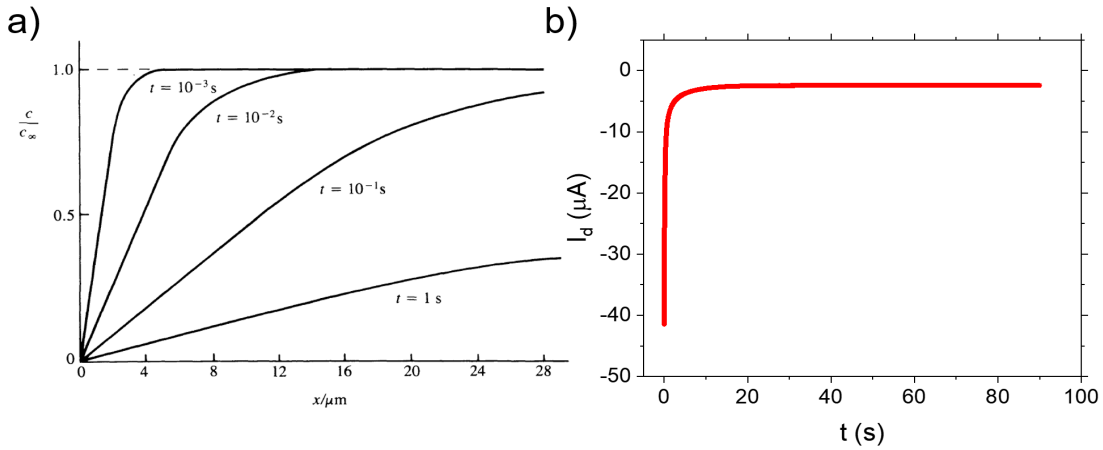

FIGURE 1.11: a)Variation of concentration with distance at planar electrode at different time after the application of potential step [1] and b) variation of current with time in during the reduction of ferricyanide to ferrocyanide in a solution of 0.2 M potassium ferricyanide and 1 M KCl (inset shows the linear nature of current with $t^{-1/2}$).

For a typical aqueous solution, a diffusion coefficient D $\approx 10^{-5}$ cm^2/s and a kinematic viscosity $v \approx 10^{-2}$ cm^2/s give $\delta_H = 10\delta$, which indicates that the hydrodynamic boundary layer is larger than diffusion layer thickness.

In a Cottrellian system, the natural convection plays role at larger time scale and balances the steady state. Natural convection can be minimised by adjusting the electrode position with respect to the gravity in an otherwise unstirred solution. For ferricyanide reduction reaction, it has been shown that the electrode at the bottom facing up is the position at which the convective effects are minimum [11]. On the other hand, forced convection in a diffusion limited system can be used to obtain a well-defined concentration profile with respect to time. A well-documented example of such a hydrodynamic electrode is the rotating disc electrode (RDE). In RDE, a disc electrode is rotated at a constant known rate around its vertical axis which generates a well defined steady state [12].

1.2 Magneto-electrochemistry

The coupling of a magnetic field to electrochemistry share an interesting history started with Faraday's famous failed experiment. He tried to demonstrate the phenomena of electromagnetic induction by measuring the potential difference across the Thames river but failed as his equipment was not sensitive enough and the river bed short circuited the signal. However, in later course of time, researchers found field induced effects on various electrochemical process as well as on electrodeposition. In this section, we summarizes the

various field effects and how they can influence the electrochemical reactions. A rough estimate of different force densities involved [13] are tabulated in Table 1.2. As can be seen, the Lorentz and Kelvin magnetic force densities are not comparable to the force driving the diffusion and migration. On the other hand, these forces are comparable in magnitude to the natural convection and can influence the convective effects.

[htp!]

Force	Expression	Typical Value[a] (N/m^3)
Diffusion	$RT\nabla c$	10^{10}
Migration	$zFc\nabla V$	10^{10}
Forced convection at RDE	$\rho(r\omega)^2/2\delta_0$	10^5
Natural convection	$\Delta\rho g$	10^2
Lorentz Force	$\mathbf{j}\times\mathbf{B}$	10^3
Kelvin force	$\mu_0\chi cH\nabla H$	10^2
Viscous drag	$\rho\nu\nabla^2 v$	10^2
Magnetic damping	$\sigma(\mathbf{v}\times\mathbf{B})\times\mathbf{B}$	10^1

[a] *Estimated for* $T = 298K, c = 10^3 mol/m^3, \delta = 10^{-4}m, z = 1, V = 1V, \rho = 10^3 kg/m^3, d = 10^{-2}m, \omega = 10^2 rad/s, \Delta\rho = 10kg/m^3, v = 10^{-1}m/s, B = 1T, \chi, = 10^{-8}m^3/mol, \nabla B = 10T/m, j = 10^3 A/m^2$, *and* $\sigma = 10^2/\omega m$.

1.2.1 The Lorentz Force

In an electrochemical reaction, the current density **j** interacts with a magnetic field **B** through the Lorentz force given by

$$\boldsymbol{F_L} = \boldsymbol{j}\times\boldsymbol{B} \tag{1.35}$$

The force is zero when **j** // **B**, and it is maximum when they are orthogonal. In a typical electrochemcial system with **B** = 1 T and **j**= 10^3 A/m^2, $\mathbf{F}_L$ = 10^3 N/m^3 which is comparable to the magnitude of buoyancy driven convective forces (Table 1.2). Thus, Lorentz force induced stirring modifies the convection and changes the ion concentration in the hydrodynamic layer. This subsequently leads to the thinning of the adjacent diffusion layer within which the concentration gradient is assumed to be linear. Under steady state (when sufficiently large potential is applied), the relation between limiting current and diffusion layer thickness δ_0 is

$$I_L = \frac{nFAD}{\delta_0} \tag{1.36}$$

Modifications of the limiting current with field strength and orientation has been reported by several researchers [13–17]. Aogaki *et al.* [18, 19] analytically derived a set of equations relating the limiting current density to the Lorentz force (for systems where mass transport is the rate determining step) as

$$j_L = j_0 + \alpha B^{\beta} c_0^{\gamma} \tag{1.37}$$

where j_0 is the zero field current density, c_0 is the ion concentration, α is constant that depends on the cell configuration, and β and γ depends on the flow profile. An Aogaki cell consists of two parallel plate placed at the wall of a tube with field applied perpendicular to the flow profile. For a narrow channel, $\beta = 1/2$, $\gamma = 3/2$ and for a wide channel $\beta = 1/3$ and $\gamma = 4/3$. A similar relationship was obtained experimentally for the ferri/ferrocyanide redox couple [20]. A much higher convective force on a larger scale can be achieved by mechanical stirring (Table 1.2), but the dependence of Lorentz force on the local current density makes it possible to induce flow patterns [21] magnetically as well as avoids the need of moving parts. When the applied field is perpendicular to the surface, vortexes can also be formed due to the edge effects [22] of the local current density (Fig. 1.12b). During metal electrodeposition, an applied magnetic field can influence the surface morphology [23–27], deposition rate [13, 14], crystal structure and orientation [28], and magnetic properties [28].

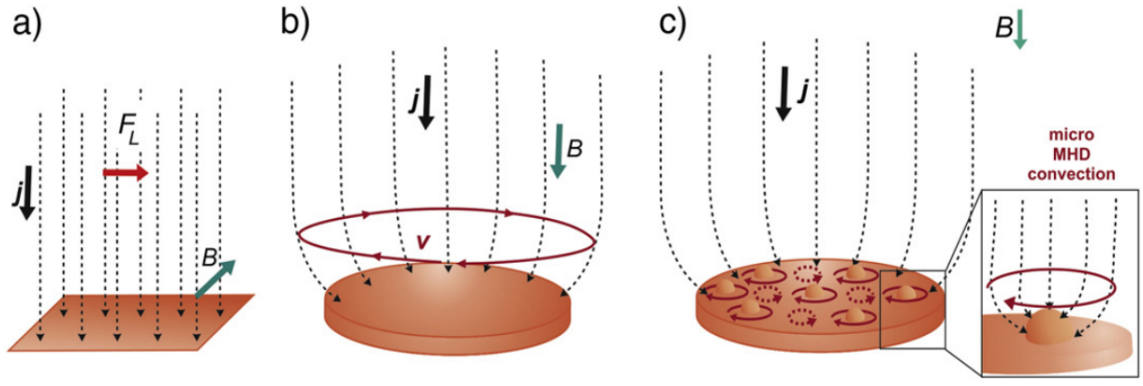

FIGURE 1.12: Magnetohydrodynamic effects. a) Primary MHD parallel to the electrode as field applied parallel to the surface, b) primary MHD flow and c)local MHD effect. [29].

Micro-MHD flow is another topic of interest (Fig. 1.12c) which results from the non-uniformity in the current density or an irregular electrode surface. Deformation in local current density has been reported in the case of bubble formation during the water electrolysis [30, 31]. Bubble release in microelectrodes [32] can be strongly influenced by the

direction and magnitude of the applied field. Other types of micro-MHD flows can be associated with electrodeposition during which physical quantities changes with location and time. Aogaki formulated a theory describing the MHD flows inside the diffusion layer [33], referred as micro-MHD effect. In this formalism, space-time dependence of physical properties during the electrodeposition results in non equilibrium fluctuations which in turn interacts with the magnetic field. This theory of micro-convection is used to explain the origin of the micro-mystery circles during copper deposition [34] under a magnetic field, and modifications of fractal the geometry of Zn and Cu deposits [15, 35]. Micro-MHD flows can affect the deposition even for an applied magnetic field parallel to the surface through symmetric and asymmetric fluctuations [33]. Asymmetric fluctuations arises from the electrical double layer and controls 2D nucleation while the symmetric fluctuations affects the diffusion layer properties and controls 3D nucleation.

1.2.2 The Kelvin Force

The magnetostatic energy stored per unit volume in an electrolyte [36] is given by

$$E_m = \frac{1}{2}\mu_0 MH \; or \; = \frac{1}{2}\mu_0 \chi H^2 \tag{1.38}$$

where **M** = χ**H** is the magnetization induced by the field **H**. The molar magnetic susceptibility χ_m of the species in the aqueous solution is given by Curie-law

$$\chi_m = \frac{\mu_0 N_A g^2 \mu_B^2 J(J+1)}{3k_B T} \tag{1.39}$$

where N_A is the Avogadro's number, g is the g-factor, μ_B is the Bohr magneton, J is the appropriate quantum number , and k_B is the Boltzmann's constant. It is related to the total dimensionless susceptibility χ of the electrolyte as

$$\chi = \chi^{water} + \chi_m c \tag{1.40}$$

where χ^{water} = -9 $\times$ 10^{-6} is the diamagnetic susceptibility for an aqueous solution and c is the molar concentration of paramagnetic species in solution. Typical values of χ at room temperature ranges from 16 $\times$ 10^{-6} for 1 M Cu^{2+} to 594 $\times$ 10^{-6} for 1 M Dy^{3+}. This also implies that the magnetization of an electrolyte induced by the applied field is very small.

The relation between **H**-field and the fundamental **B**-field follows as

$$\boldsymbol{B} = \mu_0(\boldsymbol{H} + \boldsymbol{M}) \tag{1.41}$$

In electrochemistry, with negligible induced magnetization **M**, the relation between **B**-field and **H**-field reduces to $\mathbf{B} = \mu_0\mathbf{H}$.

The force density acting on the electrolyte can be calculated from the energy density using the relation $\mathbf{F}_m$ = -∇E_m which gives

$$\boldsymbol{F_m} = \mu_0\chi_m cH\nabla H + \frac{1}{2}\mu_0\chi_m H^2\nabla^2 c \tag{1.42}$$

The first term is the Kelvin field gradient force,

$$\boldsymbol{F_{\nabla H}} = \mu_0\chi_m cH\nabla H \tag{1.43}$$

and the second term referred as the magnetic concentration gradient force or paramagnetic force,

$$\boldsymbol{F_{\nabla C}} = \frac{1}{2}\mu_0\chi_m H^2\nabla c \tag{1.44}$$

which is expected to be present in a uniform field. The paramagnetic concentration gradient was introduced by Waskaas and Kharkats [37, 38] to explain the magneto-convective effects in systems where other field effects are assumed negligible. However, Coey *et al.* [39] showed that this force can be ignored in aqueous solution where the demagnetising field is small. A simple explanation follows the magnetic charge model, with imaginary positive and negative magnetic charges q_m introduced to represent the positive and negative poles. Magnetic charge will arise whenever the magnetization is non-uniform, with charge density ρ= -∇ . **M**. The force acting on the charge q_m is $\mu_o q_m$**H** and thus the force density can be expressed as

$$\boldsymbol{F_m} = -\mu_0(\nabla.\boldsymbol{M})\boldsymbol{H} \tag{1.45}$$

Using Eqn.1.41 and Maxwell's equation ∇. B = 0 (no current), we get $\mathbf{F}_m = \mu_0(\nabla.\ \mathbf{H})\mathbf{H}$ which is zero when **H** is uniform. Therefore, there is no "magnetic concentration gradient force" across the interface of a dilute system.

The Kelvin force, is a body force which acts on the volume of the electrolyte. When the ion concentration is constant, it will be a potential force as $\nabla \times \mathbf{F}_{\nabla H} = 0$. The Quincke method best illustrates the effect of the potential part (constant concentration and so conservative)

of the Kelvin force: a thin U-pipe filled with a solution is exposed to a field gradient that can be switched on and off. When the field gradient is present, the potential part of the force acts against gravity and changes the height. Magnetic susceptibility can be estimated from this height difference. If the same experiment is performed in a closed pipe, the potential part of the force will be balanced by the wall pressure and no fluid motion will occur [40].

A force field is said to be conservative when $\nabla \times \mathbf{F} = 0$, meaning it cannot induce convection. In the case of field gradient force, $\nabla \times \mathbf{F}_{\nabla H} = \nabla \times \left(\frac{1}{2\mu_0}\chi_m c \nabla B^2\right)$ which can be expressed as

$$\nabla \times \boldsymbol{F}_{\nabla B} = (1/2\mu_0)\chi_m(\nabla c \times \nabla B^2) \tag{1.46}$$

This tells that the field gradient force can influence convection only if there is a concentration gradient component orthogonal to the field gradient. Hence, in bulk solution, the effect of this force can be neglected as there is no concentration gradient. However, near to the electrode where the concentration gradient exists in the diffusion layer, the field gradient force induce local convective effects when both are orthogonal. In an electrolyte with paramagnetic concentration c = 1 M, $\chi_m = 10^{-8}$ m^3 mol^{-1}, B = 1.25 T, ∇B = 100 Tm^{-1}, we obtain $\mathbf{F}_{\nabla H}$ = 10^3 N m^{-3} which is similar in magnitude to the natural convection driven force. On the other hand, one should not consider that the magnetic field gradient can pull paramagnetic ions near to the region of larger B∇B. This is because, in aqueous solution, the magnetic energy of ions is always far less than the thermal energy driving diffusion. For example, the magnetic energy of Co^{2+} (J = 3/2) under 1 T field can be estimated as 7×10^{-7} eV which is considerably less than the thermal energy $k_BT \sim 1/40$ eV. Hence, the non-uniformity in the field hardly affect the equilibrium concentration of the ions in solution. Stabilization of paramagnetic liquid tubes along a ferromagnetic track in the presence of a magnetic field has shown that the field gradient can influence convection but not diffusion [41, 42]. Likewise, magnetic field gradient cannot compete with electrostatic forces driving migration as the latter is orders of magnitude higher than the former force (Table 1.2).

Fig.1.13 summarizes the different situations that arise in an electrochemical cell with uniform or nonuniform field and diffusive or sharp boundary. In a) field is uniform and the interface is sharp, hence the field effects cane be ignored. In b) the interface is diffusive but the field gradient effects will be minimum in this case as the field is uniform. In case c) the field is non-uniform but there is no concentration and susceptibility difference. As the magnetic energy is very small compared to the thermal energy of ions, there won't be

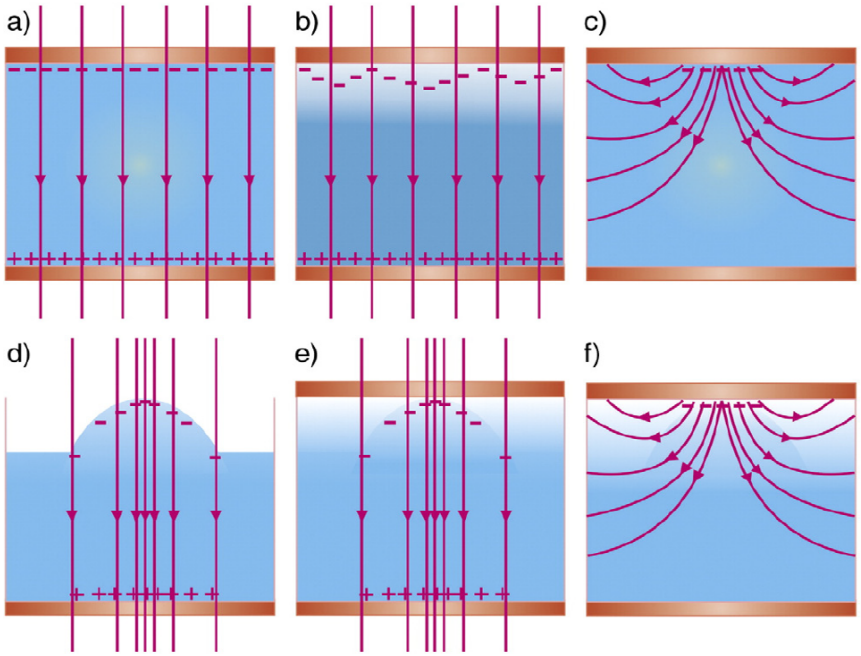

FIGURE 1.13: Schematics of various concentration profile of paramagnetic species under various magnetic field distribution. a-c) situations where field has no effect on paramagnetic interface, and d-f) where the paramagnetic liquid is influenced by the field [43].

any redistribution of ions due to magnetic field. The magnetic charge at the bottom is zero as there is no field reaching the bottom of the cell. Hence, in the first three situations, the field gradient has no effect in the electrochemical system. However, in case d) a nonuniform field is applied to the solution with a free upper surface. Paramagnetic species are attracted towards the high field region. If the liquid is diamagnetic, solution will be depleted at the high field region, referred as Moses effect [44]. The effect arises due to the potential part of the force as the ion concentrations are constant and the system is open. In e) and f), the kelvin force will act as the field gradient and concentration gradient are noncollinear.

Several reviews discuss the influence of field gradient force on the electrochemical process [30, 43, 45]. Henry white and co-workers investigated the effect of Lorentz and Kelvin force in paramagnetic solution, and decoupled the effects by the variation of field homogeneity and electrode orientation [46]. Later, they stimulated the interest of magnetic field gradient force by showing that the paramagnetic species can be focused near to the ferromagnetic microelectrodes [47, 48]. They observed that the convective flow of the paramagnetic nitrobenzene species can be minimized by the field gradient, but not diffusion. Recently, it has been illustrated that the paramagnetic solution in a diamagnetic medium can be stabilized near ferromagnetic track in the presence of a magnetic field [41, 42] and is further extended to create frictionless microfluidic channels [49]. The convective effects of

the Kelvin force were used to pattern the deposits involving paramagnetic species [25, 50, 51]. Magnetic arrays can be arranged to create regions of non-homogeneous field gradient. The paramagnetic ions (Cu^{2+}, Zn^{2+}) get deposited in the region where the field is concentrated. Inverse patterning is also possible when a strongly paramagnetic electroinactive species like Dy^{3+} is added to the solution [50]. Another technologically relevant reaction where magnetic field gradient force plays a relevant role is the oxygen reduction reaction (ORR). In fuel cell, ORR is one of the major rate-limiting step that affects the efficiency of the device. It has been reported that the paramagnetic O_2 gas can be influenced by the field gradient force [52]. Furthermore, the field gradient enhancement of oxygen reaction rates have been reported using a permanent magnet placed behind a Pt working electrode [53], using a superconducting magnet [54].

The Kelvin gradient force can be enhanced by reducing the size of the magnetic structures which generates the field. Reducing the system size increases the field gradient which in turn enhances the kelvin force density. Thus huge field gradient can be achieved in micro- or nano- magnetic structures [55, 56]. Enhancement of ORR in acid media has been reported in electrodeposited magnetic nanowires embedded in porous alumina membrane [57, 58]. Field effects on hydrogen evolution reaction (HER) has been reported recently in Co/Pt multilayer thin film electrode [59]. Nowicka *et al.* [60] showed the possibility of magnetic-nanoparticle modified electrodes to improve the efficiency of fuel cells. Studies using model ferri/ferrocyandie redox reaction reported an increase in the limiting current using similar kind of surface modified electrode [61]. Artificial magnetic stay field surfaces created in exchange-biased magnetic film has shown selective adsorption based on the field gradient landscape [62]. Huge field gradient by micro- and nanomagnets find application not only in surface chemistry [62] but also in biological field [63].

1.2.3 Other Related Effects

In addition to Lorentz and Kelvin force effects, it has been reported that magnetic stress can also have substantial influence on the electrochemical reactions (Fig. 1.14a) [10]. It arises from the interaction between a magnetic field and magnetic dipoles. For a paramagnetic droplet surrounded by a diamagnetic medium, this stress can cause lateral or transverse deformation depending on the direction of the magnetic field [41]. Dunne and Coey [10] recently found that Maxwell stress can impact the shape of paramagentic ionic cloud near the electrochemical double layer, modifying its capacitance and charge transfer resistance. Such an effect can be explained by the shift in the outer-Helmholtz plane (OHP) potential

due to the stretching/elongation of the paramagentic species at the electrode/electrolyte interface. The effect of a magnetic field on the diffusion layer have been extensively studied [29, 43] whereas its effects on the double layer is rarely reported [64, 65].

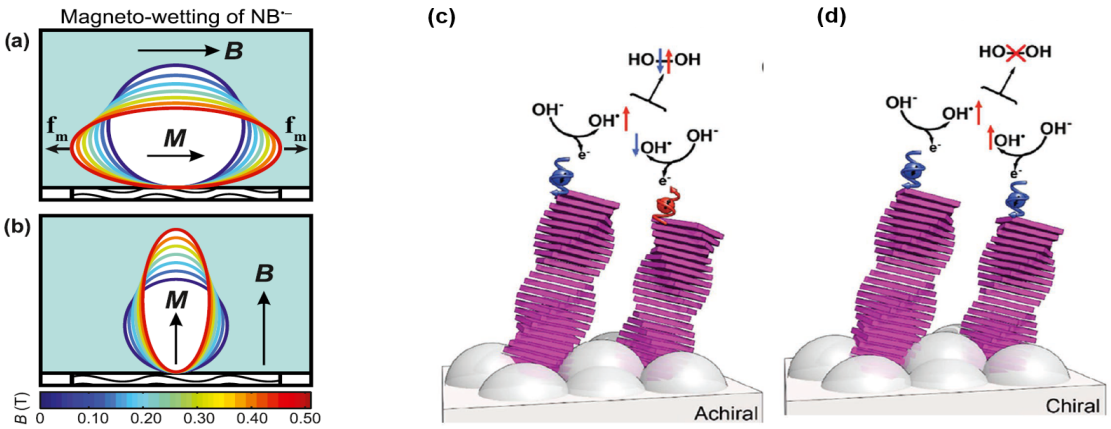

FIGURE 1.14: Schematics Maxwell stress [10] and chirality-induced spin selectivity CISS effect [66]. a) Magnetic field parallel to the surface where paramagnetic droplet stretches and improves wetting, and b) field normal to surface causing the elongation of droplet. c) possible and d) hindered formation of hydrogen peroxide in relation to the spin or two reacting hydroxyl radicals.

Spin dependent electrochemistry is another branch of growing interest which shows potential application in the oxygen evolution reaction(OER) [30, 67–69]. The pathway mechanism of OER is highly dependent on the pH of the solution [70]. At low pH (acidic), both oxygen and hydroxyl radicals are crucial in the reaction pathway while at high pH (alkaline), the interaction of adsorbed oxygen at the electrode surface becomes relevant. The initial reports on spin selectivity effect dates back to the discovery finding that the chiral molecules can be explored as spin filters (referred as chiral-induced spin selectivity effect CISS) (Fig. 1.14b) [71]. Subsequently, the application of CISS to oxygen reaction kinetics showed promising enhancement in the OER activity [68]. In addition, Garces-Pineda *et al.* [67] reported an enhancement in the OER efficiency in alkaline conditions using the ferromagnetic mixed oxide based electrodes. By applying a 450 mT field using a standard NdFeB cube magnet, they have shown that the current density can be improved as high as 100 %. The observed effects were explained by the influence of external parameters on the spin polarization of the intermediate radicals which then promote or obstruct the evolution of ground state triplet O_2 [67, 72].

1.3 Magnetic Thin Films

For the electrochemical experiments planned in this thesis, we are in need of a magnetic source which generates a large field gradient at the immediate vicinity of the electrode surface. In order to create such a field source, we take advantage of the scale invariance of the magnetic field. For a cube magnet magnetized along z-axis, the field above the magnet along z- axis (Fig. 1.15a) is given by [73],

$$\boldsymbol{B}(z) = \frac{\mu_0 \boldsymbol{M}}{\pi}\left[\tan^{-1}\left(\frac{(z+a)\sqrt{2a^2+(z+a)^2}}{a^2}\right) - \tan^{-1}\left(\frac{z\sqrt{2a^2+z^2}}{a^2}\right)\right] \tag{1.47}$$

where a is the size of the cubical magnet and the $\mathbf{M}$ is the magnetization of the material. From Eqn. 1.47, we can see that the field generated by a 1 cm^3 magnet at 1 cm away is same as that of the field generated by a 10 nm^3 magnet at 1 nm away, ie. the magnetic field is independent of the scale. To discuss the consequence of this, we consider two magnets of different dimensions as shown in Fig. 1.15 b and c. In case a) we assume a 1.0 T field at a distance z_1 = 1 cm away from the center of a 1 cm^3 (a_1 = 1 cm) cubical magnet. The field gradient at point p $\nabla \mathbf{B}_p$ would then be 10^2 T/m. In case b) the size of the magnet is reduced from 1 cm to 10 nm. As the magnetization (moment per unit volume) is an intrinsic property of the material, it is independent of the material size and hence $\mathbf{M}_1 = \mathbf{M}_2$. Furthermore, it can be found that the field generated at the point p will be 1.0 T, same as in case a), as the additional factors cancels out in Eqn. 1.47. As a consequence, the field gradient generated at the immediate vicinity of the nanomagnet would be as large as 10^8 T/m! Thus, scale independent property of the magnetic field can be explored to create large field gradient by reducing the system size.

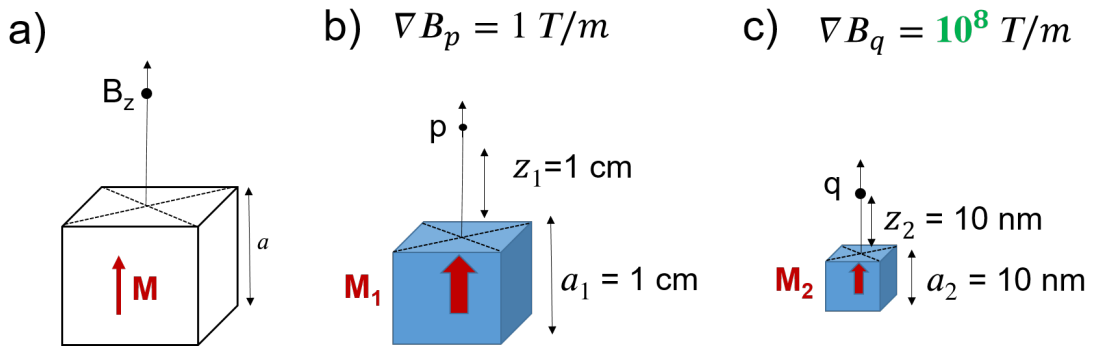

FIGURE 1.15: a) Schematics of the cubical magnet representing the magnetization axis and field direction. Demonstration of scale independency of magnetic field by comparing the field gradient of magnet with size a) 1 cm and b) 10 nm.

Enhanced mass transport was reported in systems using magnetic nanoparticle modified electrodes [61]. But, these studies can be complicated by the agglomeration or non-uniform distribution of nanoparticles which impact the distribution field gradient and its range. Studies were also reported on exploring the magnetic nanowires embedded membranes [57, 58] to improve the local field gradient but the leakage of solution through the membrane and the subsequent corrosion of nanowires can adversely affected the stability of the system. Here, we propose to use Pt coated magnetic thin films as the magnetic source to study the field influence at the solid/liquid interface. Pt cap layer protects the bottom magnetic layer from oxidation and ensures a surface exposed to the liquid which is a standard for sTable eletrochemcial behavior. The flat surface and long-term stability of the film promises a reproducible electrochemical response. Moreover, the fabrication of these films are well documented [74, 75] due to its application in the field of memory and data storage [36].

A magnetic thin film is a layer or layers of materials (magnetic or combination of magnetic and non-magnetic) having nanometers to several micrometers thickness deposited on a flat substrate. These structures are particularly interesting as the small dimension is of the order of the characteristic magnetic or electrical length scales. For example, the mean free path and spin-diffusion length of electron in magnetic metals are in the range of 1 - 100 nm [36]. Recent advances in microfabrication technology and micromagnetic simulation along with the interface effects such as spin-dependent scattering opens a new era for the application of thin films in the field of magnetic sensors, memory and data storage. In this section, some of the fundamental concepts on magnetic thin films are discussed.

1.3.1 Micromagnetic Energy

The magnetic configuration and domain structure at equilibrium state is a result of the the minimisation of the total magnetic energy, expressed as

$$E_{tot} = E_{ex} + E_{Zee} + E_{an} + E_{mag} \tag{1.48}$$

where E_{ex} is the exchange energy, E_{Zee} is the Zeeman energy, E_{an} is the anisotropy energy, and E_{mag} is the magnetostatic energy.

The exchange energy arises from the exchange coupling between two neighbouring spins. In the continuum picture, it can be written as

$$E_{ex} = \int \mathbf{A} \, (\nabla \mathbf{e_M})^2 \, d^3r \tag{1.49}$$

where $\mathbf{e_M} = \mathbf{M}(\mathbf{r})/M_s$ is the unit vector in the local direction of magnetization. $\mathbf{A}$ is the exchange stiffness which is related to the Curie temperature T_C and exchange constant J. This exchange energy will be minimum when all the spins are aligned with each other for ferromagnetic interactions.

The Zeeman energy arises from the interaction of magnetic moments with the external magnetic field $\mathbf{H}_{ext}$. It favours the alignment of moments parallel to the field. The associated energy is

$$E_{Zee} = -\int \mathbf{M(r)}.\mathbf{H}_{ext} \, d^3r \tag{1.50}$$

The magnetic anisotropy deals with the directional dependence of magnetic properties of a ferromagnet. The uniaxial anisotropy energy can be decribed as

$$E_{an} = \int K_u \left[1 - \left(\frac{M_{ea}}{M_s}\right)^2\right] d^3r \tag{1.51}$$

where K_u is the anisotropy constant and M_{ea} is the magnetization component along easy axis. This anisotropy energy favours a magnetization alignment along the direction of the easy axis, directly related to the asymmetry of the atomic environment. This magnetocrystalline anisotropy is an intrinsic property which originates from the spin-orbit coupling within the material. Due to this anisotropy, the easy magnetization axis depends on the crystal symmetry. For example, in hexagonal YCo_5 shown in Fig. 1.16, the magnetic easy axis is along the c-axis. The c/a ratio is a key measure to obtain high anisotropy values.
Magneto-elastic anisotropy arises when a magnetic film is exposed to stress. During the growth of a thin film heterostructure, the lattice mismatch between the different layer can deform the interface atoms and act as a source of magneto-elastic anisotropy. Other types of anisotropy can also be developed at the interface where the continuum of atoms is limited. Néel pointed out the possibility of band structure modification at the interface symmetry breaking, which can even stabilize the out-of-plane magnetization in ultrathin films (section 1.3.4).

Lastly, the magnetostatic energy emerges from the shape anisotropy of the material which results from the long range dipole-dipole interaction. This interaction give rise to

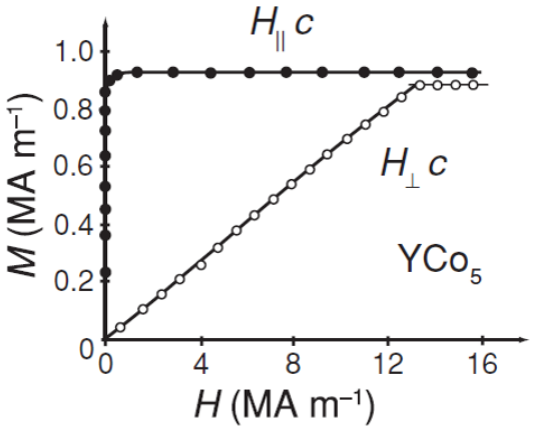

FIGURE 1.16: Magnetization as a function of applied field in single crystal YCo_5 [36]

a demagnetising field $\mathbf{H}_d$, given by

$$\mathbf{H}_d = -N_d\mathbf{M} \tag{1.52}$$

where N_d is the demagnetising tensor which is dependent on the geometry of the object. The corresponding energy can be expressed as

$$E_{mag} = \int \mathbf{M(r)}.\mathbf{H}_d \, d^3r \tag{1.53}$$

For a thin film, the principle components of N_d are N_x = N_y = 0, N_z =1. Hence, to minimize the demagnetising energy, the shape anisotropy favours the magnetization in the plane of the film.

The magnetic state of the ferromagnetic object can be simulated by several micromagnetic software packages like object oriented micromagnetic framework (OOMMF) [76]. A length scale of importance here is the characteristic exchange length $l_{ex} = \sqrt{\frac{A}{\mu_0 M_s^2}}$ which defines the competition between exchange energy and the dipolar energy. A typical value of l_{ex} is 3 - 5 nm. Hence, in micromagnetic simulation, while the FM sample is discretized into small cells, the size of each cell must be smaller than the exchange length.

1.3.2 Macro-spin model

The micromagnetic approach is capable to simulate the spatial distribution of magnetization of many systems at equilibrium. But, the process is time consuming, mathematically complex and can even be sensitive to simulation parameters. The macro-spin model, on the other hand, is an attempt to explain the experimental observations with reduced complexity.

We use this model to explain the spin orbit torque effects which will be discussed later in this chapter.

The macro-spin model can successfully explain the hysteresis behaviour of the single domain magnetic particles. If a coherent magnetization response to the applied field $\mathbf{H}_{ext}$ is assumed, the free energy of the FM upon the application of external field $\mathbf{H}_{ext}$ can be written as the sum of anisotropy and Zeeman energy,

$$E = -\mathbf{M}.\boldsymbol{H}_{ex} - K_{eff}\cos^2\theta \tag{1.54}$$

Solving for the energy minimization, the hysteresis behaviour of single domain magnetic entities can be obtained.

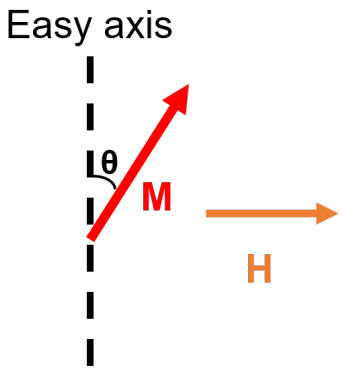

FIGURE 1.17: Schematics showing the anisotropy easy axis, and the direction of magnetization and applied field.

1.3.3 Domain theory

Domains constitute a fundamental concept in magnetism. Domain theory postulates the existence of large regions of uniform magnetization in a macroscopic sample separated by regions called domain walls. The domain formation reduces the magnetostatic energy but it comes with the expense of the wall energy. Within a domain wall, the magnetization rotates from one easy axis to another (Fig. 1.18a). In a 180^0 magnetization rotation, the exchange energy makes the wall wider so that moments changes direction gradually over a long distance (or thickness) keeping the neighbouring spins almost parallel to each other. On the other hand, as the spins within the wall are no longer aligned along an easy axis, this creates an anisotropy energy. Hence, the domain wall thickness results from a balance between the exchange energy and the anisotropy energy. The typical range of wall thickness range 10 - 100 nm.

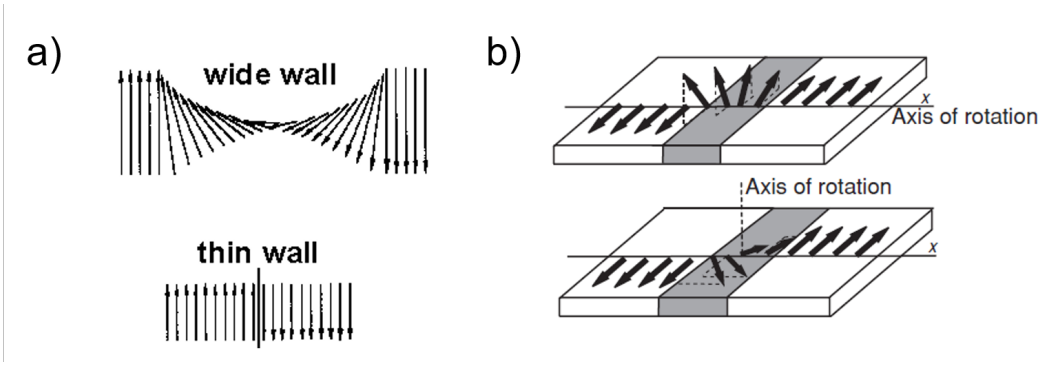

FIGURE 1.18: a)A wide and a thin domain wall and b) a Bloch and Néel domain wall [77]

Furthermore, depending on the plane of magnetization rotation within the wall, two types of domain walls exist: the Bloch wall and the Néel Wall (Fig. 1.18b). In Bloch wall, the magnetization rotates in the plane of the wall. As it creates no divergence of the magnetisation due to the absence of volume charge, the demagnetising energy due to volume charge does not contribute.

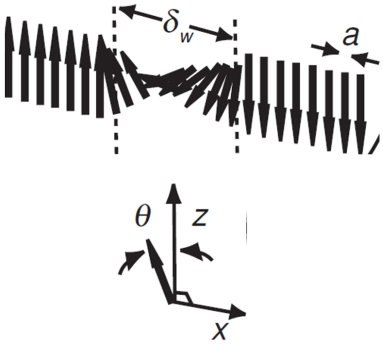

FIGURE 1.19: A 180^0 Bloch domain wall [77].

The total energy can thus be expressed in terms of exchange and anisotropy energy as

$$E_{tot} = \int \left[\mathbf{A} \left(\partial\theta / \partial x \right)^2 + K_u \sin^2 \theta \right] \, dx \tag{1.55}$$

Here K_u is assumed positive so that θ = 0 and π are easy axis. Magnetization is confined to the plane $\phi = \pi/2$ and the only variation is θ along the x-axis. Solving for the energy minimization, the Bloch wall width can be estimated as

$$\delta_w = \pi \sqrt{\frac{A}{K_u}} \tag{1.56}$$

which reflects the role of exchange and anisotropy energy for a finite domain wall width. This type of domain walls are commonly found in bulk materials and thin films with perpendicular magnetic anisotropy (detailed discussion in next section 1.3.4). On the other hand, in a Néel wall, the magnetization rotates along the plane of the magnetization. This creates volume charges and resultant magnetostatic energy makes it energetically less favourable. These types of domain walls can be stabilized in thin films magnetized along the film plane.

1.3.4 Perpendicular Magnetic Anisotropy (PMA)

The magnetic anisotropy can have volume and interface components. The volume contribution results from the shape anisotropy and the bulk magneto-crystalline anisotropy. On the other hand, the interfacial or surface magnetic anisotropy have multiple origins. The magnetocrystalline anisotropy from the interface can be different from bulk and the magnetoelastic anisotropy resulting from the stress. The effective anisotropy K_{eff} in a thin film can be discussed in terms of volume anisotropy K_v and surface anisotropy K_s as

$$K_{eff} = K_v + 2K_s / t_f \tag{1.57}$$

where t_f is the film thickness. The factor 2 is due to the fact that there are two interfaces on either side of the film. Typical values of K_v and K_s are 1 MJ/m^3 and 1 mJ/m^3.

The most technologically relevant consequence of surface anisotropy arises when K_s stabilize magnetization normal to the film surface. This is called ***perpendicular magnetic anisotropy (PMA)***. Interfaces that generate PMA are found in combination of 3*d* based ferromagnets with heavy metals. Examples are Co/Pt, Co/Pd and Co/Au multilayers. Heterostructures based on 3*d* metals and oxides like Co/Mgo have also reported to exhibit perpendicular magnetization. The typical thickness value where the surface term in Eqn. 1.57 dominates and can result in PMA is of the order of 2.0 nm.

We deposited cobalt Co based magnetic thin films having thickness no more than 1.5 nm to obtain PMA single domain films. The relevant properties are discussed in chapter 4. Upon increasing the magnetic layer thickness above 2.0 nm, the system will loose the PMA property as the magnetization orientation turns in-plane due to the shape anisotropy. One way to increase the magnetic layer thickness keeping the PMA of the film would be by increasing the number of repeats N. As the number of interfaces (or the interfacial anisotropy) scales with N, it has been observed that the PMA can be preserved even when N is as large as 100 [78]. One of the consequence is the multi-domain formation, to minimize the shape anisotropy. The properties of these alternating domains are well-documented (detailed discussion in Appendix A.1). We fabricated Co/Pt based mutlilayers with various N and results are discussed in chapter 3.

In a perpendicularly magnetized media where the width of the film is greater than the domain width, a Bloch wall is expected to be the ground state due to the magnetostatic energy minimization. Nevertheless, the energy barrier between the Bloch and Néel wall is lower in thin films and can be easily altered by the application of a small external magnetic field of the order of a few mT or by interface engineering of the stacks [79]. Dzyaloshinskii-Moriya interaction (DMI) can stabilize Néel walls of fixed chirality without the presence of an external field [80–82]. DMI is a form of exchange energy that makes the neighbouring moments lightly canted [83, 84]. This antisymmertic DMI field is related to the Hamiltonian

$$H_{DMI} = -\boldsymbol{D}_{12}.(\boldsymbol{S}_1 \times \boldsymbol{S}_2) \tag{1.58}$$

where $\mathbf{D}_{12}$ is the DMI vector, and $\mathbf{S}_1$ and $\mathbf{S}_2$ are the interacting spins of atoms. The cross product in the H_{DMI} favours the orthogonal alignment of adjacent spins. The sign of $\mathbf{D}$ give rise to preferential chirality to the system. The DMI is a negligible effect in most of the cases.

But, in special cases like in an ultrathin film of 3d ferromagnetic metals deposited on heavy metals, the strong DMI can leads to interesting magnetic configurations such as magnetic skyrmions [85] and chiral domain walls [86].

1.4 Current Induced Magnetization Switching Via Spin-Orbit Torque (SOT)

The magnetization of a thin film can be manipulated by an external magnetic field as well as by an electric current. The influence of a magnetic field on the magnetic configuration of thin film is well documented, with some aspect already summarized in the previous section. On the other hand, the current induced effects on the thin film magnetism is a relatively new topic with great technological importance due to its application in the field of memory and logic devices. It has been recently observed that, upon passing a charge current across a non-magnetic conductor having large spin-orbit coupling (SOC), an appreciable spin accumulation polarised transverse to the electric field can be generated around the lateral interface of the conductor due to the spin-orbit torques (SOT) effect [87, 88]. The effective SOT fields have been shown to influence the switching [89, 90], precession [91] and domain wall motion of the adjacent ferromagnetic layer [86]. In this section, the fundamental understanding related to the current induced phenomena and different models of SOT switching are discussed.

1.4.1 Theory of Spin-Orbit Torque

The SOT effects are attributed to the spin accumulation at the ferromagnetic/non-magnetic (FM/NM) interface. The origin of this transverse spin accumulation is treated mainly with two main SOC phenomena: the spin Hall effect (SHE) and the interface Rashba effect. They are discussed in recent reviews by Manchon *et al.* [92, 93] and Ramaswamy *et al.* [94].

1.4.1.1 The Spin Hall Effect

The SHE was theoretically predicted by Dyakonov and Perel in 1971 [88], later discussed by Hirsch in 1999 [87], and observed using Kerr microscopy in 2004 [95]. In the SHE picture, when an unpolarized charge current flows through a spin Hall metal, it gets polarised and give rise to a pure spin current due to the bulk SOC effects. In a non-magnetic layer, the bulk SOC effects can arise either due to the intrinsic band structure [96, 97] or due to extrinsic impurities [87, 88]. Fig. 1.20a illustrates the spin accumulation generated at the FM/NM

interface due to bulk SHE in the NM layer. As can be seen, the polarisation of the accumulated spins, σ, the spin current, $\mathbf{j}_s$, and the charge current, $\mathbf{j}_c$, are mutually orthogonal to each other:

$$j_s = \frac{\hbar\theta_{SH}}{2e}(j_c \times \sigma) \tag{1.59}$$

where θ_{SH} is the intrinsic property of NM called the spin Hall angle. θ_{SH} is a measure of the spin current density that can be generated from a given charge current density and the sign of it defines the direction of the spin accumulation at the NM/FM interface. These accumulated spins or pure spin current further diffuse into the FM layer and exerts a torque on the magnetization of FM layer.

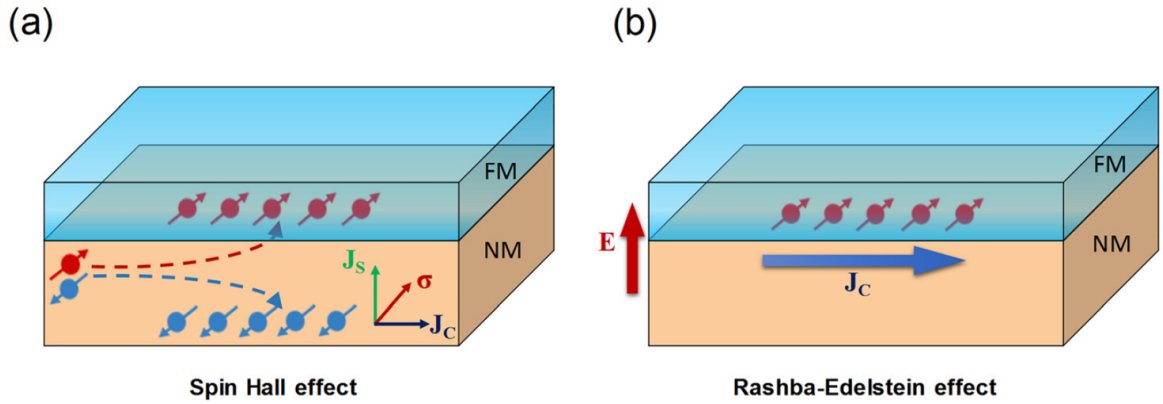

FIGURE 1.20: a) Spin Hall effect (SHE) and b) Rashaba effect in NM/FM bilayer system [94]

1.4.1.2 The Rashba Effect

In another spin torque mechanism, the possibility of spin accumulation due to an interfacial SOC phenomenon that arises in structures with broken inversion symmetry is considered[98, 99]. This is referred as Rashba effect or inverse spin galvanic effect (Fig. 1.20b). It was initially proposed in the context of semiconductors [99] and two dimensional electron gas [100], further extended to the FM/NM bilayers [101–103]. In this picture, an internal electric field, **E** is generated at the interface along the direction of symmetry breaking. When electrons with momentum **p** flow near to this interface having nonzero **E**, it experience an effective magnetic field in the direction $\mathbf{E} \times \mathbf{p}$. This magnetic field interact with the spin magnetic moment of the conduction electrons and polarizes their spin moment along $\mathbf{E} \times \mathbf{p}$. This non-equillibrium spin density can exert a torque on the magnetization of the adjacent layer via exchange coupling. The Rashba SOC is modelled using the Hamiltonian,

$$H_R = \frac{\alpha_R}{\hbar}(\mathbf{E} \times \mathbf{p}).\sigma \tag{1.60}$$

where α_R is the Rashba parameter.

1.4.2 Theory of SOT-induced magnetization reversal

1.4.2.1 Torque Decomposition of SOT

A promising and technologically relevant application of SOT is the deterministic magnetization switching of nanomagnetic objects [104, 105]. SOT can be used to switch in-plane and out-of plane magnetized multilayers [106]. However, as we mostly deal with the perpendicular magnetic anisotropy (PMA) system throughout this thesis, the discussion is limited to the current induced magnetization switching of a PMA system. Irrespective of the underlying origin of the transverse spin accumulation at the NM/FM interface, the torque exerted by the spin current on the magnetization of the adjacent magnetic layer **M** can be expressed in terms of two effective fields namely, damping like- and field like- fields, $\mathbf{B}_{DL}$ and $\mathbf{B}_{FL}$ respectively. They corresponds to the torque $\mathbf{T}_{DL,FL} = \mathbf{M} \times \mathbf{B}_{DL,FL}$ [107–110]. The advantage of this effective field formulation is that the SOT induced effective fields can be compared to the the external field of known magnitude and direction. The torques acting on the magnetization (Fig. 1.21) can be expressed as

$$\boldsymbol{T}_{DL} \sim \boldsymbol{M} \times (\boldsymbol{\sigma} \times \boldsymbol{M}) \tag{1.61}$$

$$\boldsymbol{T}_{FL} \sim \boldsymbol{M} \times \boldsymbol{\sigma} \tag{1.62}$$

In this work, harmonic Hall measurement is used to quantify the effective field. Typical values of $\mathbf{B}_{DL,FL}$ are in the range of 0.1 - 10 mT for a current density of $j_c = 10^{10}$ A/m^2 (Table 1.4.3). $\mathbf{T}_{DL}$ can be considered as the Slonczewski spin-trasnfer torque which acts on the magnetization of a FM due to the injected spin current with the polarization σ [111]. Therefore, intuitively $\mathbf{T}_{DL}$ is attributed to the spin currents generated from bulk SOC effects like SHE. On the other hand, the effect of $\mathbf{T}_{FL}$ on **M** is similar to that of a magnetic field which makes **M** precess around σ. Thus, $\mathbf{T}_{FL}$ can be attributed to the interfacial SOC phenomena like the Rashba effect where the polarized spins at the NM/FM interface acts on the **M** via an exchange interaction. The origin of SOT can be understood by comparing the SOT effective fields. Quantifying the effective fields as a function of non magnetic layer thickness

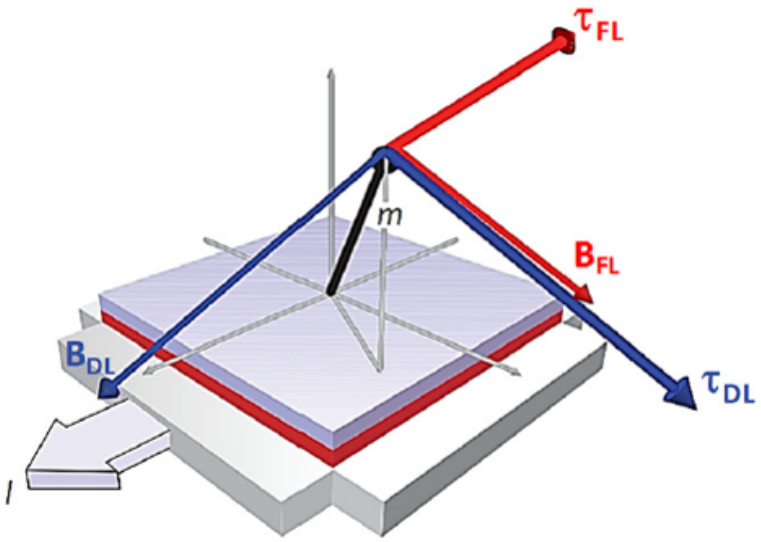

FIGURE 1.21: Illustration of two spin torque components and their effective magnetic fields [107]

is another approach for distinguishing between the bulk and interfacial origin of SOT. In the simplest model, one would expect no thickness dependence to the $\mathbf{T}_{FL}$ whereas effects emerging from bulk SHE should monotonically increase up to saturation [112]. An increase in $\mathbf{T}_{DL}$ with non-magnetic layer thickness is observed in Ta [113], W [114], and Pt [115] based multilayers, which agrees with the SHE model assuming a spin-diffusion length of the order of 1.5 nm for all metals [92]. However, recent works have pointed out that both bulk and interfacial SOC effects can contribute and hence the thickness dependence study can't be taken as indicative to the origin of SOT [116, 117]. Consequently, the identification between the bulk and interfacial contributions to the SOTs is not straightforward.

The SOT switching of a ferromagnetic entity with PMA is less trivial due to the fact that the polarisation σ (along y) and the two sTable magnetization states (along z) are orthogonal to each other. This would imply that no deterministic switching can be achieved as the current induced torques will continuously switch the magnetization from one state (lets say z) to another ($-z$). In order to break the symmetry, an external magnetic field along the direction of current has to be applied. This bias magnetic field allows the deterministic switching of the magnetization of ferromagnetic entity via SOT. This need of external magnetic field for deterministic switching is a bottleneck in a technological viewpoint [92, 94]. Recent studies have explored the possibilities of interlayer exchange coupling [118] and tilted magnetic anisotropy [119] to achieve deterministic SOT switching without the need of external magnetic field.

1.4.2.2 The Macro-spin Model of SOT switching

The switching of PMA layer can be qualitatively explained using the macrospin model by considering the damping like torque and the in-plane bias field B_x [120]. It assumes the coherent switching of magnetization in a uniform manner upon the application of current induced torques. In this model, a positive current of appropriate magnitude induces B_{DL} and subsequently switches the magnetization if B_{DL} is initially parallel to the bias field. The magnetic state when B_{DL} opposes the bias field is the sTable one (Fig. 1.22). Upon reversal of the current applied, a reversible switching can be achieved. Under a macrospin

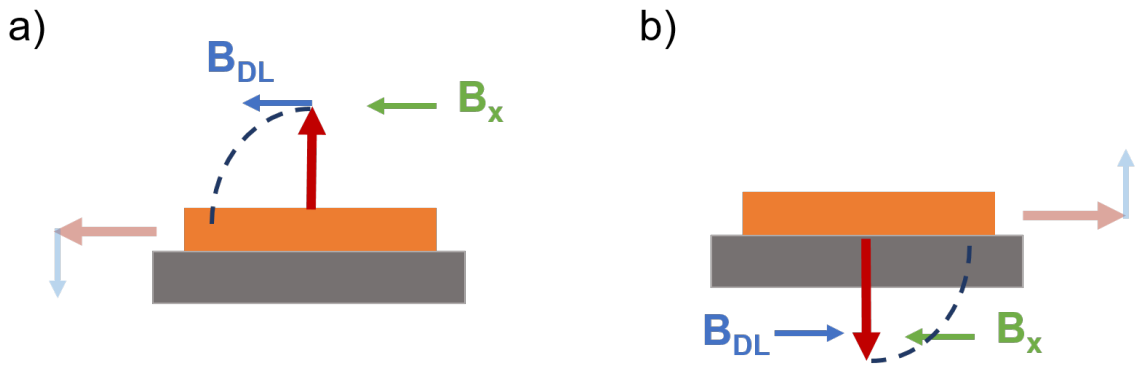

FIGURE 1.22: Macrospin model showing a) unsTable and b) sTable magnetic configurations depending on the sign of B_{DL} relative to B_x.

approximation with the condition where bias field << anisotropy field ($B_x << B_k$), the threhold current density for switching of a PMA layer is given by [120],

$$j_c = \frac{2eM_s t_f}{\hbar\theta_{SH}} \left(\frac{B_k}{2} - \frac{B_x}{\sqrt{2}} \right) \tag{1.63}$$

where e is the electron charge, $\hbar$ is the reduced Planck's constant, t_f is the ferromagnetic layer thickness, and B_k is the anisotropy field. When the applied field is comparable to the anisotropy, the critical current density can be instead written as [120]

$$j_c = \frac{2eM_s t_f}{\hbar\theta_{SH}} \left(\sqrt{\frac{B_k^2}{32}[8 + 20b^2 - b^4 - b(8 + b^2)^{3/2}} \right) \tag{1.64}$$

where $b = B_x/B_k$. The macrospin model assumes that the in-plane spin competes with the anisotropy field. This model qualitatively explains the ferromagnetic layer thickness dependence on switching current and the requirement of bias/assisted field for the deterministic switching. However, the switching current estimated using this model is 10 - 100 times

higher than that of the experimentally observed values [121], which hinted the role of domain nucleation and expansion in the realisation of SOT switching.

1.4.2.3 SOT Switching via Domain wall motion

As discussed on the previous section, the macrospin coherent rotation model failed to qualitatively estimate the SOT switching current density of a ferromagnetic PMA layer. Lee *et al.* [122] pointed out the possibility of using SOT induced domain wall motion to describe the current induced magnetization switching of the PMA film. In this picture, the domain nucleation and the damping like torque acting on the domain wall plays an important role in the realisation of SOT switching. The action of SOT on the magnetic film strongly depends on the internal structure of the domain wall (DW). A simple one dimensional model of domain wall is considered with the chain of magnetic moment along the x axis and the easy axis along the z axis. Based on the relative switching axis of the moments in the domain wall, two wall types such as Bloch and Néel types (section 1.3.3) are illustrated in Fig. 1.23. When current is applied along x, a spin polarisation along y will exert a damping like torque on local moments. Without the presence of a bias field, a Bloch wall with its moments aligned along y cannot be moved using damping like torque.

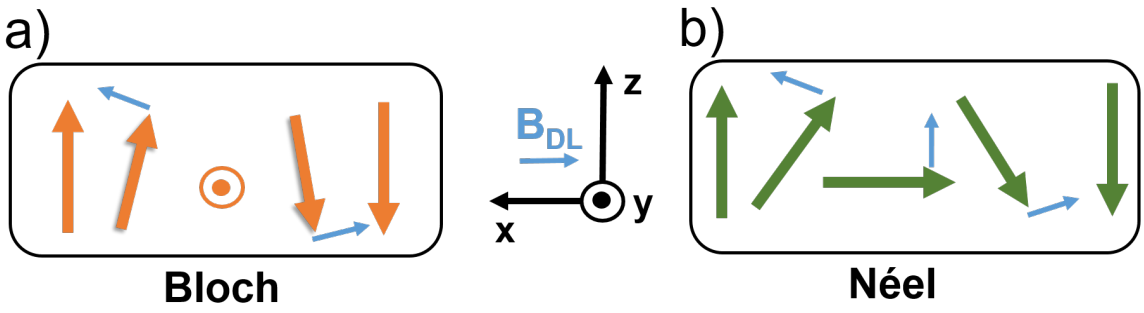

FIGURE 1.23: Illustration of a) Bloch wall with internal structure pointing to y axis and b) Néel wall with internal structure pointing to x axis. The spin polarisation is along y axis and the damping like effective field is represented by blue arrows. The effective field is expected to deform the Bloch wall, while it drives a Néel domain wall.

The influence of current induced field on the Néel wall depends on the chirality of DW [123]. Depending on the DW internal structure, the SOT field can either results in the DW motion or expansion. Chirality, which deals with the magnetization rotation of DW internal structure, can be altered using an external magnetic field or by interface induced DMI engineering (section 1.3.4). The presence of a bias/assisted magnetic field is attributed to breaking the chirality imposed by the DMI field [122]. This is illustrated in Fig. 1.24 (initial

-blue and reversed state -red) in which the presence of DMI leads to stabilization of chiral Néel walls (Fig. 1.24a). Without an assisted field, the SOT effective field due to the damping like torque acts in opposite direction on the two sides of the reversed domain, which results in the domain displacement. In the presence of a bias field larger than the DMI field, all the moments at the domain wall points along the field direction and a deterministic switching can be realised.

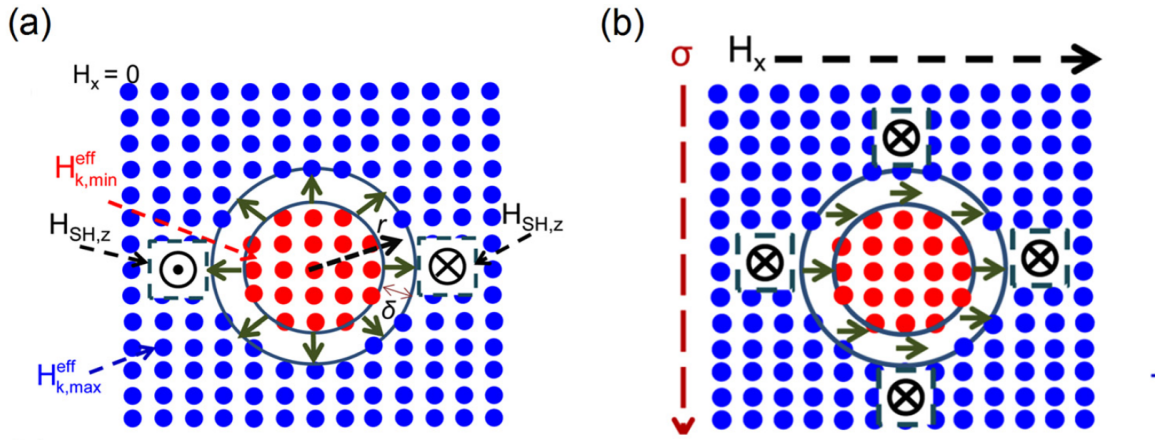

FIGURE 1.24: (a) Schematic of a reversed domain with chiral Néel domain wall stabilized by DMI at zero external bias field. The SOT effective field due to damping like torque ($H_{SH,z}$) causes the domain wall motion. (b) Illustration of a reversed domain in the presence of an assisted bias field strong enough to overcome the DMI field. Moments at the domain wall are aligned along the field direction which causes the domain expansion [122]

1.4.2.4 Spatial and Time Resolution of SOT Switching

Spin orbit torque switching has been studied in detail to understand the spatial and temporal resolution of current induced magnetization switching. A recent study on 500 nm diameter Pt/Co/AlO_x dots has used a 25 nm spatial resolution and 100 ps temporal resolution X-rays to study the dynamics of SOT switching [124]. Fig. 1.25a shows the spatial evolution of SOT switching process at every 100 ps for a 2 ns current pulse with different direction of bias magnetic field. As can be seen, the switching proceeds via domain nucleation and propagation, which is determined by the combined action of DMI, bias field, and damping like and field like SOT fields. The evolution of j_c as a function of dot size has been investigated for CoFeB based dots and j_c was found to be increased by one order of magnitude when the device size was reduced from a few micron down to 30 nm [125]. This increase was attributed to the single domain nature where the j_c is expected to be large compared to the domain expansion based switching.

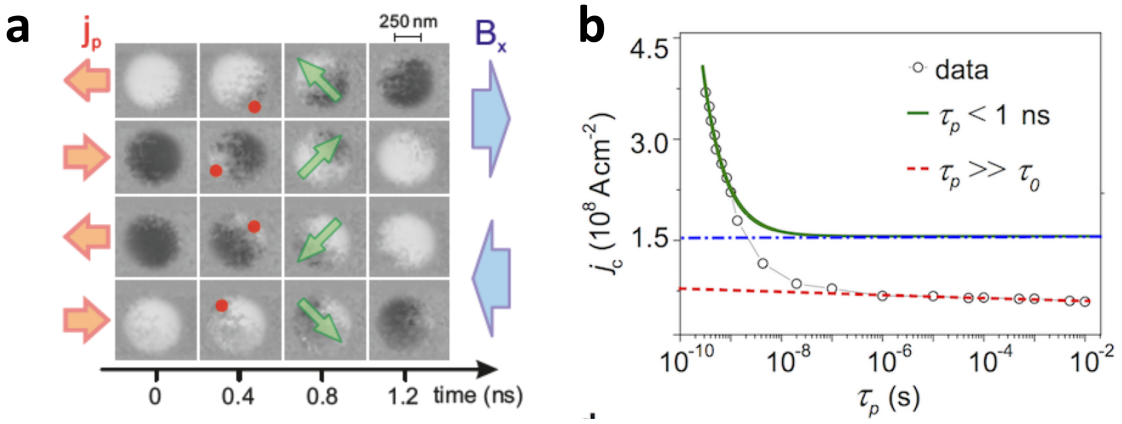

FIGURE 1.25: a) Images of the reversal process of a Pt/Co/Alo$_x$ circular dot (500 nm diameter) of for different configurations of bias field and the current measured by time-resolved X-ray microscopy [124] b) Critical current density as a function of pulse duration for Pt/Co/AlO$_x$ dot (90 nm diameter). The green solid line fit corresponds to the short time regime (< 1 ns), and the red dashed line fit in the thermally activated regime ($> 1\mu$s). The blue dash-dotted line represents the intrinsic critical current. [125]

The timescale of the magnetization switching is one of the salient features of the SOT switching. Sub-ns switching was demonstrated in 90 nm sized Pt/Co/AlO$_x$ nanodots [125]. The threshold switching current was characterized for long and short timescale regimes as shown in Fig. 1.25b [125]. Above 10 ns, j_c weakly depended on pulse duration τ_p, as expected for a thermally-assisted switching process. However, τ_p^{-1} scaled linearly with time in region below 1 ns, which indicates the strongly dependence of switching dynamics on the current induced torques. An additional feature that adds to the fast switching dynamics of SOT is its negligible incubation time ($\sim 10^{-20}$) []. In a related current induced switching technique called spin transfer torque (STT), the switching time is delayed by several ns due to the dependence of thermal fluctuations to trigger the reversal [126, 127]. On the other hand, in SOT geometry, damping like torque acts immediately on the magnetization, leading to ultra-fast switching. Recent studies on Pt/Co/Cu/Ta based PMA film reports a deterministic current induced magnetization switching of a nanometer thick cobalt layer using a single electrical pulse of of width as small as 6 ps and of magnitude $\approx 600 \times$ MA/cm^2 [128, 129].

1.4.3 Material Survey

A large number of different materials have been studied for the purpose of generating spin currents from charge current flowing through them. The spin Hall angle θ_{SH}, which gives the measure of the spin current generated, is used to quantify the spin Hall effect (SHE) in the materials. In SHE, the spin current is generated through the spin orbit coupling (SOC)

effects where the conduction electrons undergo asymmetric scattering with opposite spins of the material. Consequently, the magnitude of SHE can be enhanced by increasing the strength of SOC and it is natural to expect high SHE in heavy metals as the SOC is proportional to Z^4 (atomic number). In addition, the strength of SOC also increase with the product of angular momentum and spin momentum **L**.**S**. These conditions are satisfied by 5*d* heavy metals in particular Ta ($5d^3 6s^2$) [104], W ($5d^4 6s^2$) [130] and Pt ($5d^9 6s^1$) [131, 132]. Among these heavy metals, W in β-phase shows the largest spin Hall angle of -0.3. On the other hand, elements with half filled or full filled valence shell (e.g. Re, Ag, Au) shows negligible SOC as in this case **L** = 0. From Table 1.4.3, one can observe not only the magnitude but also a sign dependence of θ_{SH} to the heavy metal, which can be explained using the SOC. For example, in the case of Pt which has positive θ_{SH}, the *d* orbit is greater than half filled ($3d^9$) and resultant **L** = +2. Whereas, for W having negative a θ_{SH}, the **L** = -2 as the *d* orbital is less than half filled.

Samples	$\lvert B_{DL}/j \rvert$ mT/(MA/cm^2)	θ_{SH}	Comment	Ref.
Pt(3.0)/CoFe(0.6)/MgO(1.8)	0.5	0.06	Pt based	[86]
Ta(4.0)/CoFeB(1.0)/MgO(1.6)	0.35	-0.12	Ta based	[104]
W(6.0)/CoFeB(5.0)	-	-0.3	W based	[130]
Pt(5.0)/Co(0.8)/W(3.0)	0.8	0.24	FM layer sandwiched between NM of opposite θ_{SH}	[133]
Bi_2Se_3(7.4)/CoTb(4.6)/SiN_x(3.0)	0.6	0.16	Topological insulator based	[134]

Another approach to boost the SHE would be to enhance the scattering events by means of extrinsic scattering [135, 136], which is proportional to the SOC contrast between host and impurity elements. To probe this effect, SOT studies have been performed on metal alloys like Ir-doped Cu [137], Bi-doped Cu [138] and W-doped Au [139]. Notably, $Cu_{99.5}Bi_{0.5}$ shows a large θ_{SH} of -0.24, which is larger than the reported θ_{SH} value of heavy metals like Pt and Ta. Furthermore, it has been recently found that sandwiching a ferromagnetic layer between two nonmagnetic layers having opposite θ_{SH} would improve the SOT efficiency as parallel damping like torques acts at both interfaces [133, 140, 141].

It should also be noted that SOT have been reported in other class of materials including anitiferromagnets [142] and topological insulators [143]. A detailed discussion is beyond the scope of this thesis.

1.5 Light Ion Irradiation on Magnetic Thin Films

Ion irradiation is an advanced technology that can be used to manipulate the interface dependent magnetic properties of ultrathin magnetic films and multilayers[144, 145]. As we discussed in section 1.4.2, the spin orbit torque (SOT) induced magnetization switching of the magnetic multilayer depends on several properties of the magnetic film such as magnetization and anisotropy field, which are intrinsic to the material. In addition, the perpendicular magnetic anisotropy (PMA) of the magnetic thin film (e.g. Co/Pt multilayer) strongly depends on the magnetic layer thickness and the interface quality. Hence, ion irradiation, which can modify the interfaces of magnetic films, is a suiTable method to gain spatial control over the PMA and therefore SOT switching properties.

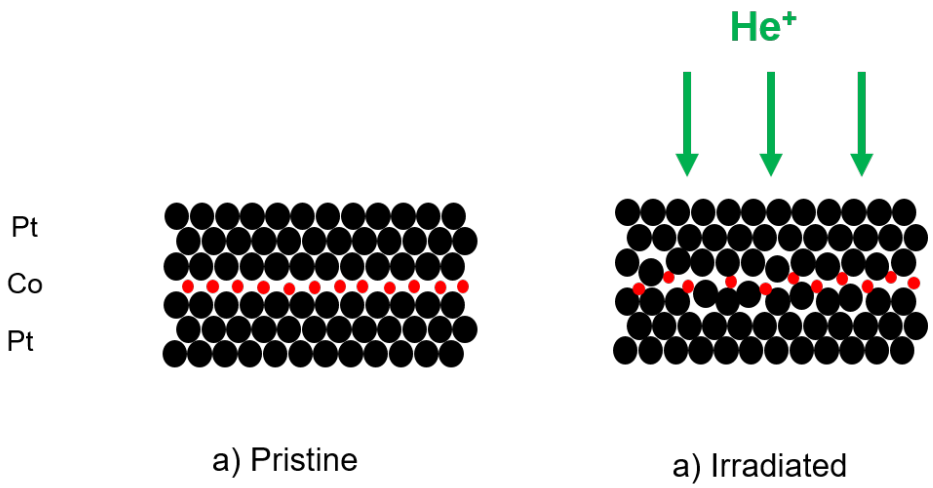

FIGURE 1.26: Graphical representation of the ion beam induced intermixing of a single Co layer in a Pt/Co/Pt sandwich

When a magnetic thin film is subjected to an energetic ion beam, intermixing will be promoted at the interface (Fig. 1.26). It has been reported that, upon irradiating a film with He ions with suiTable energy range, in average an energy of 100 – 500 eV is transferred by the ions, which is sufficient enough for the small atomic displacement of the atoms (1-2 inter atom shifts) [146]. This interfacial intermixing is large enough to influence the interfacial anisotropy supported PMA in Co/Pt multilayers [145, 147]. Depending on the beam energy

and the external parameters, the irradiation can influence chemical composition [148] and interface modification [144, 149, 150].

An ion beam passing through a material will have an interaction volume associated with it. The interaction volume depends on the beam energy and the mass of ions. Fig. 1.27 schematically represents the interaction volume of different beams. For a similar beam energy, Ga+ ion beam has a larger interaction volume as compared to the He+ beam due to the larger scattering cross section of former ions. For a low energy electron beam -needed to get the similar resolution and surface sensitivity- the penetration depth is limited due to the electron-electron scattering. He+ ions are also subjected to scattering due to the nuclei of the sample atoms but, the smaller cross-section of helium effectively reduces the scattering compared to that of the Ga ions which results in the minimal beam divergence inside the sample.

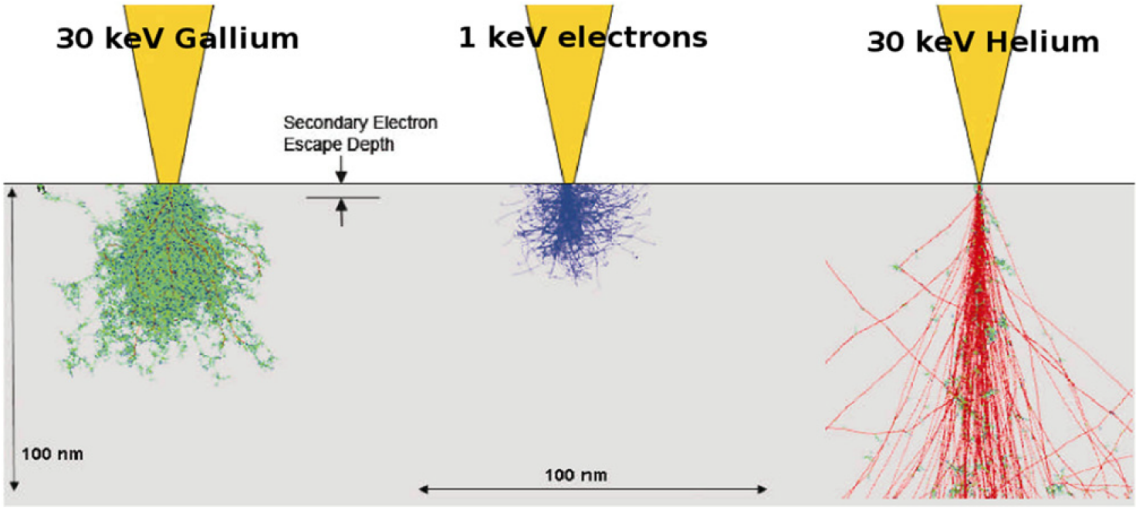

FIGURE 1.27: Monte-Carlo simulation showing the interaction volume with silicon for different beams [151]

Most of the studies using light-ion irradiation to tailor the magnetic properties of ultrathin films have been performed using *broad beam* of He+ ions [144, 152, 153]. In this method, magnetic patterning is achieved with the help of photoresist mask. The area which is covered by mask effectively stops the ions interacting with the sample while the exposed region of film interacts with the beam. Sub 50 nm magnetic Co/Pt arrays have been patterned using broad beam He+ ions combined with high resolution lithography[154]. However, this mask based exposure can result in over irradiated regions between irradiated and non-irradiated area due to ions escaping from mask edges and can act as pinning sites [152].

In order to avoid the limitations set by photoresist mask and lithography patterning, a

focused helium ion beam (FIB) can be used to locally tailor the interface dependent properties of the thin film [147, 151]. In this method, a focused helium beam having a spot size no larger than 2 nm raster multiple times through a predefined region on the sample surface, with a resulting uniformly irradiated region over a predefined area. The focused helium beam also allows one to pattern much smaller features as compared to the traditional focused Ga+ beam and photoresist assisted patterning whose resolution is limited by the beam size and lithography process.

1.6 My PhD project

The aim of my PhD project is twofold. The first aim is to design a large intensity magnetic field gradient source where the field effect can be confined within a region of a few nm (< 10 nm). The second aim is to investigate the influence of a large field gradient on the electrochemical reactions at the solid/liquid interface. In order to achieve this goal, two approaches have been taken and the results are organised in two chapters of the thesis.

In chapter 2, the experimental techniques used for the realization of the present work are discussed. Various electrochemical characterization techniques along with the magnetic thin film fabrication and characterization methods are detailed.

In chapter 3, the influence of a large gradient magnetic field on the electrochemical reaction is presented. In order to generate such field gradient at the immediate vicinity of the electrode, $[Co/Pt]_N$ multilayers with different Co thickness and various number of repeats N are fabricated. Thickness and quality of the films are confirmed using X-ray reflectivity (XRR) and transmission electron microscopy (TEM). Magnetic properties of the multilayers are determined using super-conducting quantum interference device (SQUID), magnetic force microscopy (MFM) and magneto-optical Kerr effect (MOKE) based imaging. Using a simplified 2D magnetized sheet model, it is estimated that a gradient field of order of magnitude 10^7 T/m can be reached within a region of < 10 nm next to the film surface. For electrochemical investigation, an electrochemically reversible and sTable ferri/ferrocyanide reaction is chosen as a standard probe. Interfacial and bulk properties of the reaction are pre-characterized on Pt film electrode using cyclic voltammetry (CV), chronoamperometry (CA), and impedance spectroscopy (EIS) techniques. Prior to the investigation of field gradient effects at the electrochemical interface, the influence of the Pt cap layer thickness on the electrochemical activity of the Co/Pt multilayer film and the Lorentz force effects are

studied in detail. To investigate the large field gradient influence on electrochemical reactions, steady state measurements based on chronoamperometry is opted as one of the key method. Impedance spectroscopy measurements also confirmed the field gradient effects observed using chronoamperometry.

In chapter 4, we discuss a more sophisticated approach to create a model system with an electrically controllable magnetic landscape, with related force field. We combine the spin orbit torque phenomena for magnetization switching and the maskless focused light ion irradiation technology for magnetic patterning. Perpendicular magnetic anisotropy thin films having magnetic layer sandwiched between heavy metals of opposite spin Hall angle, Pt/Co/W and Pt/Co/Ta, are fabricated for the study. Magnetic and magneto-transport measurements confirm an intact PMA in the as-deposited and the patterned thin films. Deterministic SOT switching is realized in both films with the help of a symmetry breaking bias field applied collinear to a current. Harmonic Hall measurement is used to estimate the effective spin Hall angle (SHE) of the Pt/Co/W based device. PMA films are locally patterned using maskless focused He+ irradiation. Selective switching of the irradiated region is achieved and are characterized using the magneto-transport and the Kerr imaging techniques. In an attempt to improve the magnetic volume and thus by the field gradient, the irradiation effects are studied in heterostructures with more than single Pt/Co/W repeat. Furthermore, in order to access more intermediate multi-domain states by electric current, partial junction irradiation with improved irradiation design is explored.

In chapter 5, the thesis is concluded by summarizing the research outcomes of my PhD and proposing perspectives of the work.

Bibliography

[1]A. J. Bard and L. R. Faulkner., "Electrochemical methods: fundamentals and applications.", 2nd edn. Wiley (2000).

[2]C. M. A. Brett and A. M. Oliveira-Brett., "Electrochemistry: principles, methods, and applications", Oxford University Press, Oxford, New York, Tokyo (2000).

[3]F. Rhen, P. Dunne, and J. M. D. Coey, "Magnetic field induced rest potential shift of metallic electrodes in nitric acid solution", Magnetohydrodynamics **42**, 395–401 (2006).

[4]W. Xu, T. Lu, C. Liu, and W. Xing, "Supplement to the theory of normal pulse voltammetry and its application to the kinetic study of methanol oxidation on a polycrystalline platinum electrode", The Journal of Physical Chemistry. B **109**, 7872–7877 (2005).

[5]H. Kojima and A. J. Bard, "Determination of rate constants for the electroreduction of aromatic compounds and their correlation with homogeneous electron transfer rates", Journal of the American Chemical Society **97**, Publisher: American Chemical Society, 6317–6324 (1975).

[6]M. E. Peover and B. S. White, "The electro-oxidation of polycyclic aromatic hydrocarbons in acetonitrile studied by cyclic voltammetry", Journal of Electroanalytical Chemistry and Interfacial Electrochemistry **13**, 93–99 (1967).

[7]I.-F. Hu, D. H. Karweik, and T. Kuwana, "Activation and deactivation of glassy carbon electrodes", Journal of Electroanalytical Chemistry and Interfacial Electrochemistry **188**, 59–72 (1985).

[8]M. Stieble and K. Jüttner, "Surface blocking in the redox system pt/[fe(CN)6]3,[fe(CN)6]4: an ac impedance study", Journal of Electroanalytical Chemistry and Interfacial Electrochemistry **290**, 163–180 (1990).

[9]G. P. Rao and S. K. Rangarajan, "A new relaxation method for studying electrode reactions", Journal of Electroanalytical Chemistry and Interfacial Electrochemistry **41**, 473–489 (1973).

[10]P. Dunne and J. M. D. Coey, "Influence of a magnetic field on the electrochemical double layer", The Journal of Physical Chemistry C **123**, Publisher: American Chemical Society, 24181–24192 (2019).

[11]X. Gao, J. Lee, and H. S. White, "Natural convection at microelectrodes", Analytical Chemistry **67**, Publisher: American Chemical Society, 1541–1545 (1995).

[12]G. Denuault, M. Sosna, and K.-J. Williams, "11 - classical experiments", in *Handbook of electrochemistry*, edited by C. G. Zoski (Elsevier, Amsterdam, Jan. 1, 2007), pp. 431–469.

[13]G. Hinds, F. E. Spada, J. M. D. Coey, T. R. Ní Mhíocháin, and M. E. G. Lyons, "Magnetic field effects on copper electrolysis", The Journal of Physical Chemistry B **105**, Publisher: American Chemical Society, 9487–9502 (2001).

[14]A. Bund, S. Koehler, H. H. Kuehnlein, and W. Plieth, "Magnetic field effects in electrochemical reactions", Electrochimica Acta, New Developments in Electrode Kinetics:Selection of Papers from the 2nd Gerischer Symposium **49**, 147–152 (2003).

[15]G. Hinds, J. M. D. Coey, and M. E. G. Lyons, "Influence of magnetic forces on electrochemical mass transport", Electrochemistry Communications **3**, 215–218 (2001).

[16]M. Uhlemann, A. Gebert, M. Herrich, A. Krause, A. Cziraki, and L. Schultz, "Electrochemical deposition and modification of cu/co–cu multilayer", Electrochimica Acta **48**, 3005–3011 (2003).

[17]A. Krause, M. Uhlemann, A. Gebert, and L. Schultz, "The effect of magnetic fields on the electrodeposition of cobalt", Electrochimica Acta **49**, 4127–4134 (2004).

[18]R. Aogaki, K. Fueki, and T. Mukaibo, "Application of magnetohydrodynamic effect to the analysis of electrochemical reactions 1MHD flow of an electrolyte solution in an electrodecell with a short rectangular channel", Denki Kagaku oyobi Kogyo Butsuri Kagaku **43**, 504–508 (1975).

[19]R. Aogaki, K. Fueki, and T. Mukaibo, "Diffusion process in viscous flow of electrolyte solution in magnetohydrodynamic pump electrodes", Denki Kagaku oyobi Kogyo Butsuri Kagaku **44**, 89–94 (1976).

[20]O. Aaboubi, J. P. Chopart, J. Douglade, A. Olivier, C. Gabrielli, and B. Tribollet, "Magnetic field effects on mass transport", Journal of The Electrochemical Society **137**, Publisher: IOP Publishing, 1796 (1990).

[21]T. Weier, J. Hüller, G. Gerbeth, and F.-P. Weiss, "Lorentz force influence on momentum and mass transfer in natural convection copper electrolysis", Chemical Engineering Science **60**, 293–298 (2005).

[22]D. Fernández and J. M. D. Coey, "Inhomogeneous electrodeposition of copper in a magnetic field", Electrochemistry Communications **11**, 379–382 (2009).

[23]T. Z. Fahidy, "Characteristics of surfaces produced via magnetoelectrolytic deposition", Progress in Surface Science **68**, 155–188 (2001).

[24]P. Dunne, L. Mazza, and J. M. D. Coey, "Magnetic structuring of electrodeposits", Physical Review Letters **107**, Publisher: American Physical Society, 024501 (2011).

[25]P. Dunne, R. Soucaille, K. Ackland, and J. M. D. Coey, "Magnetic structuring of linear copper electrodeposits", Journal of Applied Physics **111**, Publisher: American Institute of Physics, 07B915 (2012).

[26]P. Dunne and J. M. D. Coey, "Patterning metallic electrodeposits with magnet arrays", Physical Review B **85**, Publisher: American Physical Society, 224411 (2012).

[27]P. Dunne, R. Soucaille, K. Ackland, and J. M. D. Coey, "Structuring of electrodeposits with permanent magnet arrays", Magnetohydrodynamics **48**, 331–341 (2012).

[28]I. Tabakovic, S. Riemer, V. Vas'ko, V. Sapozhnikov, and M. Kief, "Effect of magnetic field on electrode reactions and properties of electrodeposited NiFe films", Journal of The Electrochemical Society **150**, Publisher: IOP Publishing, C635 (2003).

[29]L. M. A. Monzon and J. M. D. Coey, "Magnetic fields in electrochemistry: the lorentz force. a mini-review", Electrochemistry Communications **42**, 38–41 (2014).

[30]Y. Zhang, C. Liang, J. Wu, H. Liu, B. Zhang, Z. Jiang, S. Li, and P. Xu, "Recent advances in magnetic field-enhanced electrocatalysis", ACS Applied Energy Materials, Publisher: American Chemical Society, `10.1021/acsaem.0c02104` (2020).

[31]H. Matsushima, T. Iida, and Y. Fukunaka, "Observation of bubble layer formed on hydrogen and oxygen gas-evolving electrode in a magnetic field", Journal of Solid State Electrochemistry **16**, 617–623 (2012).

[32]H. Liu, L.-m. Pan, H. Huang, Q. Qin, P. Li, and J. Wen, "Hydrogen bubble growth at micro-electrode under magnetic field", Journal of Electroanalytical Chemistry **754**, 22–29 (2015).

[33]R. Aogaki and R. Morimoto, *Nonequilibrium fluctuations in micro-MHD effects on electrodeposition*, Publication Title: Heat and Mass Transfer - Modeling and Simulation (IntechOpen, Sept. 22, 2011).

[34]A. Sugiyama, M. Hashiride, R. Morimoto, Y. Nagai, and R. Aogaki, "Application of vertical micro-disk MHD electrode to the analysis of heterogeneous magneto-convection", Electrochimica Acta **28**, 5115–5124 (2004).

[35]I. Mogi and M. Kamiko, "Striking effects of magnetic field on the growth morphology of electrochemical deposits", Journal of Crystal Growth, Crystal Growth 1995 **166**, 276–280 (1996).

[36]J. M. D. Coey, "Magnetism and magnetic materials (cambridge university press)",

[37]M. Waskaas and Y. I. Kharkats, "Effect of magnetic fields on convection in solutions containing paramagnetic ions", Journal of Electroanalytical Chemistry **502**, 51–57 (2001).

[38]M. Waskaas, "Short-term effects of magnetic fields on diffusion in stirred and unstirred paramagnetic solutions", The Journal of Physical Chemistry **97**, Publisher: American Chemical Society, 6470–6476 (1993).

[39]J. M. D. Coey, F. M. F. Rhen, P. Dunne, and S. McMurry, "The magnetic concentration gradient force—is it real?", Journal of Solid State Electrochemistry **11**, 711–717 (2007).

[40]G. Mutschke, K. Tschulik, T. Weier, M. Uhlemann, A. Bund, and J. Fröhlich, "On the action of magnetic gradient forces in micro-structured copper deposition", Electrochimica Acta **55**, 9060–9066 (2010).

[41]J. M. D. Coey, R. Aogaki, F. Byrne, and P. Stamenov, "Magnetic stabilization and vorticity in submillimeter paramagnetic liquid tubes", Proceedings of the National Academy of Sciences **106**, Publisher: Proceedings of the National Academy of Sciences, 8811–8817 (2009).

[42]R. Aogaki, E. Ito, and M. Ogata, "A new flow-type cell by the application of magnetic microfluidic chip", Journal of Solid State Electrochemistry **11**, 757–762 (2007).

[43]L. M. A. Monzon and J. M. D. Coey, "Magnetic fields in electrochemistry: the kelvin force. a mini-review", Electrochemistry Communications **42**, 42–45 (2014).

[44]E. Bormashenko, "Moses effect: physics and applications", Advances in Colloid and Interface Science **269**, 1–6 (2019).

[45]V. Gatard, J. Deseure, and M. Chatenet, "Use of magnetic fields in electrochemistry: a selected review", Current Opinion in Electrochemistry **23**, 96–105 (2020).

[46]S. R. Ragsdale, K. M. Grant, and H. S. White, "Electrochemically generated magnetic forces. enhanced transport of a paramagnetic redox species in large, nonuniform magnetic fields", Journal of the American Chemical Society **120**, Publisher: American Chemical Society, 13461–13468 (1998).

[47]M. D. Pullins, K. M. Grant, and H. S. White, "Microscale confinement of paramagnetic molecules in magnetic field gradients surrounding ferromagnetic microelectrodes", The Journal of Physical Chemistry B **105**, Publisher: American Chemical Society, 8989–8994 (2001).

[48]K. M. Grant, J. W. Hemmert, and H. S. White, "Magnetic focusing of redox molecules at ferromagnetic microelectrodes", Electrochemistry Communications **1**, 319–323 (1999).

[49]P. Dunne, T. Adachi, A. A. Dev, A. Sorrenti, L. Giacchetti, A. Bonnin, C. Bourdon, P. H. Mangin, J. M. D. Coey, B. Doudin, and T. M. Hermans, "Liquid flow and control without solid walls", Nature **581**, Number: 7806 Publisher: Nature Publishing Group, 58–62 (2020).

[50]P. Dunne, L. Mazza, and J. M. D. Coey, "Magnetic structuring of electrodeposits", Physical Review Letters **107**, Publisher: American Physical Society, 024501 (2011).

[51]P. Dunne and J. M. D. Coey, "Patterning metallic electrodeposits with magnet arrays", Physical Review B **85**, Publisher: American Physical Society, 224411 (2012).

[52]N. I. Wakayama, "Behavior of gas flow under gradient magnetic fields", Journal of Applied Physics **69**, Publisher: American Institute of Physics, 2734–2736 (1991).

[53]N. I. Wakayama, T. Okada, J.-i. Okano, and T. Ozawa, "Magnetic promotion of oxygen reduction reaction with pt catalyst in sulfuric acid solutions", Japanese Journal of Applied Physics **40**, Publisher: IOP Publishing, L269 (2001).

[54]S.-y. Kishioka, A. Yamada, and R. Aogaki, "Electrochemical detection of magnetic convection: effect of high magnetic fields on o2/o2 electrode reaction in acetonitrile", Electroanalysis **13**, _eprint: https://onlinelibrary.wiley.com/doi/pdf/10.1002/1521-4109%28200110%2913%ELAN1161%3E3.0.CO%3B2-S, 1161–1164 (2001).

[55]N. M. Dempsey, D. Le Roy, H. Marelli-Mathevon, G. Shaw, A. Dias, R. B. G. Kramer, L. Viet Cuong, M. Kustov, L. F. Zanini, C. Villard, K. Hasselbach, C. Tomba, and F. Dumas-Bouchiat, "Micro-magnetic imprinting of high field gradient magnetic flux sources", Applied Physics Letters **104**, Publisher: American Institute of Physics, 262401 (2014).

[56]Y. P. Ivanov, J. Leliaert, A. Crespo, M. Pancaldi, C. Tollan, J. Kosel, A. Chuvilin, and P. Vavassori, "Design of intense nanoscale stray fields and gradients at magnetic nanorod interfaces", ACS Applied Materials & Interfaces **11**, Publisher: American Chemical Society, 4678–4685 (2019).

[57]N. B. Chaure, F. M. F. Rhen, J. Hilton, and J. M. D. Coey, "Design and application of a magnetic field gradient electrode", Electrochemistry Communications **9**, 155–158 (2007).

[58]N. B. Chaure and J. M. D. Coey, "Enhanced oxygen reduction at composite electrodes producing a large magnetic gradient", Journal of the Electrochemical Society **156**, Publisher: IOP Publishing, F39 (2009).

[59]O. Sambalova, E. Billeter, O. Yildirim, A. Sterzi, D. Bleiner, and A. Borgschulte, "Magnetic field enhancement of electrochemical hydrogen evolution reaction probed by magneto-optics", International Journal of Hydrogen Energy, 10.1016/j.ijhydene.2020.10.210 (2020).

[60]A. M. Nowicka, A. Kowalczyk, M. L. Donten, M. Donten, M. Bystrzejewski, and Z. Stojek, "Carbon-encapsulated iron nanoparticles as ferromagnetic matrix for oxygen reduction in absence and presence of immobilized laccase", Electrochimica Acta, BIOELECTROCHEMISTRY 2013 **126**, 115–121 (2014).

[61]K. Ngamchuea, K. Tschulik, and R. G. Compton, "Magnetic control: switchable ultrahigh magnetic gradients at fe3o4 nanoparticles to enhance solution-phase mass transport", Nano Research **8**, 3293–3306 (2015).

[62]F. Ahrend, U. Glebe, L. Árnadóttir, J. E. Baio, D. A. Fischer, C. Jaye, B. O. Leung, A. P. Hitchcock, T. Weidner, U. Siemeling, and A. Ehresmann, "Magnetic field landscapes guiding the chemisorption of diamagnetic molecules", Langmuir **32**, Publisher: American Chemical Society, 10491–10496 (2016).

[63]B. Lim, P. Vavassori, R. Sooryakumar, and C. Kim, "Nano/micro-scale magnetophoretic devices for biomedical applications", Journal of Physics D: Applied Physics **50**, 033002 (2017).

[64]S. Koehler and A. Bund, "Investigations on the kinetics of electron transfer reactions in magnetic fields", The Journal of Physical Chemistry B **110**, Publisher: American Chemical Society, 1485–1489 (2006).

[65]O. Devos, O. Aaboubi, J.-P. Chopart, A. Olivier, C. Gabrielli, and B. Tribollet, "Is there a magnetic field effect on electrochemical kinetics?", The Journal of Physical Chemistry A **104**, Publisher: American Chemical Society, 1544–1548 (2000).

[66]W. Mtangi, F. Tassinari, K. Vankayala, A. Vargas Jentzsch, B. Adelizzi, A. R. A. Palmans, C. Fontanesi, E. W. Meijer, and R. Naaman, "Control of electrons' spin eliminates hydrogen peroxide formation during water splitting", Journal of the American Chemical Society **139**, Publisher: American Chemical Society, 2794–2798 (2017).

[67]F. A. Garcés-Pineda, M. Blasco-Ahicart, D. Nieto-Castro, N. López, and J. R. Galán-Mascarós, "Direct magnetic enhancement of electrocatalytic water oxidation in alkaline media", Nature Energy **4**, Number: 6 Publisher: Nature Publishing Group, 519–525 (2019).

[68]P. C. Mondal, W. Mtangi, and C. Fontanesi, "Chiro-spintronics: spin-dependent electrochemistry and water splitting using chiral molecular films", Small Methods **2**, _eprint: https://onlinelibrary.wiley.com/doi/pdf/10.1002/smtd.201700313, 1700313 (2018).

[69]V. Gatard, J. Deseure, and M. Chatenet, "Use of magnetic fields in electrochemistry: a selected review", Current Opinion in Electrochemistry **23**, 96–105 (2020).

[70]Y. Nakabayashi and Y. Nosaka, "The pH dependence of OH radical formation in photoelectrochemical water oxidation with rutile TiO2 single crystals", Physical Chemistry Chemical Physics **17**, Publisher: The Royal Society of Chemistry, 30570–30576 (2015).

[71]K. Ray, S. P. Ananthavel, D. H. Waldeck, and R. Naaman, "Asymmetric scattering of polarized electrons by organized organic films of chiral molecules", Science **283**, Publisher: American Association for the Advancement of Science, 814–816 (1999).

[72]S. Ghosh, B. P. Bloom, Y. Lu, D. Lamont, and D. H. Waldeck, "Increasing the efficiency of water splitting through spin polarization using cobalt oxide thin film catalysts", The Journal of Physical Chemistry C **124**, Publisher: American Chemical Society, 22610–22618 (2020).

[73]E. P. Furlani, "Permanent magnet and electromechanical devices (academic press, san diego, 2001)",

[74]P. He, W. A. McGahan, S. Nafis, J. A. Woollam, Z. S. Shan, S. H. Liou, F. Sequeda, T. McDaniel, and H. Do, "Sputtering pressure effect on microstructure of surface and interface, and on coercivity of co/pt multilayers", Journal of Applied Physics **70**, Publisher: American Institute of Physics, 6044–6046 (1991).

[75]M. S. Pierce, J. E. Davies, J. J. Turner, K. Chesnel, E. E. Fullerton, J. Nam, R. Hailstone, S. D. Kevan, J. B. Kortright, K. Liu, L. B. Sorensen, B. R. York, and O. Hellwig, "Influence of structural disorder on magnetic domain formation in perpendicular anisotropy thin films", Physical Review B **87**, Publisher: American Physical Society, 184428 (2013).

[76]M. Donahue, *Oommf user's guide, version 1.0*, en, 1999-09-01 1999.

[77]J. M. D. Coey, *Magnetism and magnetic materials* (Cambridge University Press, 2010).

[78]O. Hellwig, A. Berger, J. B. Kortright, and E. E. Fullerton, "Domain structure and magnetization reversal of antiferromagnetically coupled perpendicular anisotropy films", Journal of Magnetism and Magnetic Materials **319**, 13–55 (2007).

[79]P. P. J. Haazen, E. Murè, J. H. Franken, R. Lavrijsen, H. J. M. Swagten, and B. Koopmans, "Domain wall depinning governed by the spin hall effect", Nature Materials **12**, Number: 4 Publisher: Nature Publishing Group, 299–303 (2013).

[80]M. Heide, G. Bihlmayer, and S. Blügel, "Dzyaloshinskii-moriya interaction accounting for the orientation of magnetic domains in ultrathin films: fe/w(110)", Physical Review B **78**, Publisher: American Physical Society, 140403 (2008).

[81]O. A. Tretiakov and A. Abanov, "Current driven magnetization dynamics in ferromagnetic nanowires with a dzyaloshinskii-moriya interaction", Physical Review Letters **105**, Publisher: American Physical Society, 157201 (2010).

[82]A. Thiaville, S. Rohart, É. Jué, V. Cros, and A. Fert, "Dynamics of dzyaloshinskii domain walls in ultrathin magnetic films", EPL (Europhysics Letters) **100**, Publisher: IOP Publishing, 57002 (2012).

[83]I. Dzyaloshinsky, "A thermodynamic theory of "weak" ferromagnetism of antiferromagnetics", Journal of Physics and Chemistry of Solids **4**, 241–255 (1958).

[84]T. Moriya, "Anisotropic superexchange interaction and weak ferromagnetism", Physical Review **120**, Publisher: American Physical Society, 91–98 (1960).

[85]S. Mühlbauer, B. Binz, F. Jonietz, C. Pfleiderer, A. Rosch, A. Neubauer, R. Georgii, and P. Böni, "Skyrmion lattice in a chiral magnet", Science **323**, Publisher: American Association for the Advancement of Science, 915–919 (2009).

[86]S. Emori, U. Bauer, S.-M. Ahn, E. Martinez, and G. S. D. Beach, "Current-driven dynamics of chiral ferromagnetic domain walls", Nature Materials **12**, 611–616 (2013).

[87]J. E. Hirsch, "Spin hall effect", Physical Review Letters **83**, Publisher: American Physical Society, 1834–1837 (1999).

[88]M. I. Dyakonov and V. I. Perel, "Current-induced spin orientation of electrons in semiconductors", Physics Letters A **35**, 459–460 (1971).

[89]I. M. Miron, K. Garello, G. Gaudin, P.-J. Zermatten, M. V. Costache, S. Auffret, S. Bandiera, B. Rodmacq, A. Schuhl, and P. Gambardella, "Perpendicular switching of a single ferromagnetic layer induced by in-plane current injection", Nature **476**, 189–193 (2011).

[90]L. Liu, T. Moriyama, D. C. Ralph, and R. A. Buhrman, "Spin-Torque Ferromagnetic Resonance Induced by the Spin Hall Effect", Physical Review Letters **106**, 036601 (2011).

[91]L. Liu, C.-F. Pai, D. C. Ralph, and R. A. Buhrman, "Magnetic oscillations driven by the spin hall effect in 3-terminal magnetic tunnel junction devices", Physical Review Letters **109**, Publisher: American Physical Society, 186602 (2012).

[92]A. Manchon, J. Železný, I. M. Miron, T. Jungwirth, J. Sinova, A. Thiaville, K. Garello, and P. Gambardella, "Current-induced spin-orbit torques in ferromagnetic and antiferromagnetic systems", Reviews of Modern Physics **91**, Publisher: American Physical Society, 035004 (2019).

[93]A. Manchon, H. C. Koo, J. Nitta, S. M. Frolov, and R. A. Duine, "New perspectives for rashba spin–orbit coupling", Nature Materials **14**, Number: 9 Publisher: Nature Publishing Group, 871–882 (2015).

[94]R. Ramaswamy, J. M. Lee, K. Cai, and H. Yang, "Recent advances in spin-orbit torques: moving towards device applications", Applied Physics Reviews **5**, Publisher: American Institute of Physics, 031107 (2018).

[95]Y. K. Kato, R. C. Myers, A. C. Gossard, and D. D. Awschalom, "Observation of the spin hall effect in semiconductors", Science **306**, Publisher: American Association for the Advancement of Science, 1910–1913 (2004).

[96]J. Sinova, D. Culcer, Q. Niu, N. A. Sinitsyn, T. Jungwirth, and A. H. MacDonald, "Universal intrinsic spin hall effect", Physical Review Letters **92**, Publisher: American Physical Society, 126603 (2004).

[97]S. Murakami, N. Nagaosa, and S.-C. Zhang, "Dissipationless quantum spin current at room temperature", Science **301**, Publisher: American Association for the Advancement of Science, 1348–1351 (2003).

[98]V. M. Edelstein, "Spin polarization of conduction electrons induced by electric current in two-dimensional asymmetric electron systems", Solid State Communications **73**, 233–235 (1990).

[99]G. Dresselhaus, "Spin-orbit coupling effects in zinc blende structures", Physical Review **100**, Publisher: American Physical Society, 580–586 (1955).

[100]Y. A. Bychkov and E. I. Rashba, "Properties of a 2d electron gas with lifted spectral degeneracy", in (1984).

[101]I. Mihai Miron, G. Gaudin, S. Auffret, B. Rodmacq, A. Schuhl, S. Pizzini, J. Vogel, and P. Gambardella, "Current-driven spin torque induced by the rashba effect in a ferromagnetic metal layer", Nature Materials **9**, Number: 3 Publisher: Nature Publishing Group, 230–234 (2010).

[102]I. M. Miron, T. Moore, H. Szambolics, L. D. Buda-Prejbeanu, S. Auffret, B. Rodmacq, S. Pizzini, J. Vogel, M. Bonfim, A. Schuhl, and G. Gaudin, "Fast current-induced domain-wall motion controlled by the rashba effect", Nature Materials **10**, Number: 6 Publisher: Nature Publishing Group, 419–423 (2011).

[103]A. Manchon and S. Zhang, "Theory of spin torque due to spin-orbit coupling", Physical Review B **79**, Publisher: American Physical Society, 094422 (2009).

[104]L. Liu, C.-F. Pai, Y. Li, H. W. Tseng, D. C. Ralph, and R. A. Buhrman, "Spin-Torque Switching with the Giant Spin Hall Effect of Tantalum", Science, 10.1126/science.1218197 (2012).

[105]I. Mihai Miron, G. Gaudin, S. Auffret, B. Rodmacq, A. Schuhl, S. Pizzini, J. Vogel, and P. Gambardella, "Current-driven spin torque induced by the Rashba effect in a ferromagnetic metal layer", Nature Materials **9**, 230–234 (2010).

[106]M. Aoki, E. Shigematsu, M. Matsushima, R. Ohshima, S. Honda, T. Shinjo, M. Shiraishi, and Y. Ando, "In-plane spin-orbit torque magnetization switching and its detection using the spin rectification effect at subgigahertz frequencies", Physical Review B **102**, Publisher: American Physical Society, 174442 (2020).

[107]K. Garello, I. M. Miron, C. O. Avci, F. Freimuth, Y. Mokrousov, S. Blügel, S. Auffret, O. Boulle, G. Gaudin, and P. Gambardella, "Symmetry and magnitude of spin–orbit torques in ferromagnetic heterostructures", Nature Nanotechnology **8**, Number: 8 Publisher: Nature Publishing Group, 587–593 (2013).

[108]J. Kim, J. Sinha, M. Hayashi, M. Yamanouchi, S. Fukami, T. Suzuki, S. Mitani, and H. Ohno, "Layer thickness dependence of the current-induced effective field vector in ta | CoFeB | MgO", Nature Materials **12**, Number: 3 Publisher: Nature Publishing Group, 240–245 (2013).

[109]M. Hayashi, J. Kim, M. Yamanouchi, and H. Ohno, "Quantitative characterization of the spin-orbit torque using harmonic hall voltage measurements", Physical Review B **89**, Publisher: American Physical Society, 144425 (2014).

[110]X. Qiu, K. Narayanapillai, Y. Wu, P. Deorani, D.-H. Yang, W.-S. Noh, J.-H. Park, K.-J. Lee, H.-W. Lee, and H. Yang, "Spin–orbit-torque engineering via oxygen manipulation", Nature Nanotechnology **10**, Number: 4 Publisher: Nature Publishing Group, 333–338 (2015).

[111]J. C. Slonczewski, "Current-driven excitation of magnetic multilayers", Journal of Magnetism and Magnetic Materials **159**, L1–L7 (1996).

[112]Z. Liu, R. Brandt, O. Hellwig, S. Florez, T. Thomson, B. Terris, and H. Schmidt, "Thickness dependent magnetization dynamics of perpendicular anisotropy co/pd multilayer films", Journal of Magnetism and Magnetic Materials **323**, 1623–1626 (2011).

[113]J. Torrejon, J. Kim, J. Sinha, S. Mitani, M. Hayashi, M. Yamanouchi, and H. Ohno, "Interface control of the magnetic chirality in CoFeB/MgO heterostructures with heavy-metal underlayers", Nature Communications **5**, Number: 1 Publisher: Nature Publishing Group, 4655 (2014).

[114]Q. Hao and G. Xiao, "Giant spin hall effect and switching induced by spin-transfer torque in a $\mathrm{w}/{\mathrm{co}}_{40}{\mathrm{fe}}_{40}{\mathrm{b}}_{20}/\mathrm{MgO}$ structure with perpendicular magnetic anisotropy", Physical Review Applied **3**, Publisher: American Physical Society, 034009 (2015).

[115]M.-H. Nguyen, D. C. Ralph, and R. A. Buhrman, "Spin torque study of the spin hall conductivity and spin diffusion length in platinum thin films with varying resistivity", Physical Review Letters **116**, Publisher: American Physical Society, 126601 (2016).

[116]V. P. Amin and M. D. Stiles, "Spin transport at interfaces with spin-orbit coupling: formalism", Physical Review B **94**, Publisher: American Physical Society, 104419 (2016).

[117]P. M. Haney, H.-W. Lee, K.-J. Lee, A. Manchon, and M. D. Stiles, "Current induced torques and interfacial spin-orbit coupling: semiclassical modeling", Physical Review B **87**, Publisher: American Physical Society, 174411 (2013).

[118]Y.-C. Lau, D. Betto, K. Rode, J. M. D. Coey, and P. Stamenov, "Spin–orbit torque switching without an external field using interlayer exchange coupling", Nature Nanotechnology **11**, Number: 9 Publisher: Nature Publishing Group, 758–762 (2016).

[119]L. You, O. Lee, D. Bhowmik, D. Labanowski, J. Hong, J. Bokor, and S. Salahuddin, "Switching of perpendicularly polarized nanomagnets with spin orbit torque without an external magnetic field by engineering a tilted anisotropy", Proceedings of the National Academy of Sciences **112**, Publisher: Proceedings of the National Academy of Sciences, 10310–10315 (2015).

[120]K.-S. Lee, S.-W. Lee, B.-C. Min, and K.-J. Lee, "Threshold current for switching of a perpendicular magnetic layer induced by spin hall effect", Applied Physics Letters **102**, Publisher: American Institute of Physics, 112410 (2013).

[121]P. Dunne, C. Fowley, G. Hlawacek, J. Kurian, G. Atcheson, S. Colis, N. Teichert, B. Kundys, M. Venkatesan, J. Lindner, A. M. Deac, T. M. Hermans, J. M. D. Coey, and B. Doudin, "Helium ion microscopy for reduced spin orbit torque switching currents", Nano Letters **20**, Publisher: American Chemical Society, 7036–7042 (2020).

[122]O. J. Lee, L. Q. Liu, C. F. Pai, Y. Li, H. W. Tseng, P. G. Gowtham, J. P. Park, D. C. Ralph, and R. A. Buhrman, "Central role of domain wall depinning for perpendicular magnetization switching driven by spin torque from the spin hall effect", Physical Review B **89**, Publisher: American Physical Society, 024418 (2014).

[123]M. Hayashi, L. Thomas, C. Rettner, R. Moriya, X. Jiang, and S. S. P. Parkin, "Dependence of current and field driven depinning of domain walls on their structure and chirality in permalloy nanowires", Physical Review Letters **97**, Publisher: American Physical Society, 207205 (2006).

[124]M. Baumgartner, K. Garello, J. Mendil, C. O. Avci, E. Grimaldi, C. Murer, J. Feng, M. Gabureac, C. Stamm, Y. Acremann, S. Finizio, S. Wintz, J. Raabe, and P. Gambardella, "Spatially and time-resolved magnetization dynamics driven by spin–orbit torques", Nature Nanotechnology **12**, Number: 10 Publisher: Nature Publishing Group, 980–986 (2017).

[125]K. Garello, C. O. Avci, I. M. Miron, M. Baumgartner, A. Ghosh, S. Auffret, O. Boulle, G. Gaudin, and P. Gambardella, "Ultrafast magnetization switching by spin-orbit torques", Applied Physics Letters **105**, Publisher: American Institute of Physics, 212402 (2014).

[126]T. Devolder, J. Hayakawa, K. Ito, H. Takahashi, S. Ikeda, P. Crozat, N. Zerounian, J.-V. Kim, C. Chappert, and H. Ohno, "Single-shot time-resolved measurements of nanosecond-scale spin-transfer induced switching: stochastic versus deterministic aspects", Physical Review Letters **100**, Publisher: American Physical Society, 057206 (2008).

[127]C. Hahn, G. Wolf, B. Kardasz, S. Watts, M. Pinarbasi, and A. D. Kent, "Time-resolved studies of the spin-transfer reversal mechanism in perpendicularly magnetized magnetic tunnel junctions", Physical Review B **94**, Publisher: American Physical Society, 214432 (2016).

[128]K. Jhuria, J. Hohlfeld, A. Pattabi, E. Martin, A. Y. Arriola Córdova, X. Shi, R. Lo Conte, S. Petit-Watelot, J. C. Rojas-Sanchez, G. Malinowski, S. Mangin, A. Lemaître, M. Hehn, J. Bokor, R. B. Wilson, and J. Gorchon, "Spin–orbit torque switching of a ferromagnet with picosecond electrical pulses", Nature Electronics, Publisher: Nature Publishing Group, 1–7 (2020).

[129]C. O. Avci, "Picosecond switching in a ferromagnet", Nature Electronics **3**, 660–661 (2020).

[130]C.-F. Pai, L. Liu, Y. Li, H. W. Tseng, D. C. Ralph, and R. A. Buhrman, "Spin transfer torque devices utilizing the giant spin hall effect of tungsten", Applied Physics Letters **101**, Publisher: American Institute of Physics, 122404 (2012).

[131]L. Liu, O. J. Lee, T. J. Gudmundsen, D. C. Ralph, and R. A. Buhrman, "Current-induced switching of perpendicularly magnetized magnetic layers using spin torque from the spin hall effect", Physical Review Letters **109**, Publisher: American Physical Society, 096602 (2012).

[132]O. Mosendz, J. E. Pearson, F. Y. Fradin, G. E. W. Bauer, S. D. Bader, and A. Hoffmann, "Quantifying spin hall angles from spin pumping: experiments and theory", Physical Review Letters **104**, Publisher: American Physical Society, 046601 (2010).

[133]X. Zhang, J. Mao, M. Chang, Z. Yan, Y. Zuo, and L. Xi, "Current-induced magnetization switching in Pt/Co/W and Pt/Co/W0.82Pt0.18 structures with perpendicular magnetic anisotropy", Journal of Physics D: Applied Physics **53**, 225003 (2020).

[134]J. Han, A. Richardella, S. A. Siddiqui, J. Finley, N. Samarth, and L. Liu, "Room-temperature spin-orbit torque switching induced by a topological insulator", Physical Review Letters **119**, Publisher: American Physical Society, 077702 (2017).

[135]M. Gradhand, D. V. Fedorov, P. Zahn, and I. Mertig, "Extrinsic spin hall effect from first principles", Physical Review Letters **104**, Publisher: American Physical Society, 186403 (2010).

[136]A. Fert and P. M. Levy, "Spin hall effect induced by resonant scattering on impurities in metals", Physical Review Letters **106**, Publisher: American Physical Society, 157208 (2011).

[137]Y. Niimi, M. Morota, D. H. Wei, C. Deranlot, M. Basletic, A. Hamzic, A. Fert, and Y. Otani, "Extrinsic spin hall effect induced by iridium impurities in copper", Physical Review Letters **106**, Publisher: American Physical Society, 126601 (2011).

[138]Y. Niimi, Y. Kawanishi, D. H. Wei, C. Deranlot, H. X. Yang, M. Chshiev, T. Valet, A. Fert, and Y. Otani, "Giant spin hall effect induced by skew scattering from bismuth impurities inside thin film CuBi alloys", Physical Review Letters **109**, Publisher: American Physical Society, 156602 (2012).

[139]P. Laczkowski, J.-C. Rojas-Sánchez, W. Savero-Torres, H. Jaffrès, N. Reyren, C. Deranlot, L. Notin, C. Beigné, A. Marty, J.-P. Attané, L. Vila, J.-M. George, and A. Fert, "Experimental evidences of a large extrinsic spin hall effect in AuW alloy", Applied Physics Letters **104**, Publisher: American Institute of Physics, 142403 (2014).

[140]S. Woo, M. Mann, A. J. Tan, L. Caretta, and G. S. D. Beach, "Enhanced spin-orbit torques in pt/co/ta heterostructures", Applied Physics Letters **105**, Publisher: American Institute of Physics, 212404 (2014).

[141]Z. A. Bekele, K. Meng, J. Miao, X. Xu, and Y. Jiang, "The dominancy of damping like torque for the current induced magnetization switching in Pt/Co/W multilayers", Solid State Communications **274**, 41–45 (2018).

[142]W. Zhang, M. B. Jungfleisch, W. Jiang, J. E. Pearson, A. Hoffmann, F. Freimuth, and Y. Mokrousov, "Spin hall effects in metallic antiferromagnets", Physical Review Letters **113**, Publisher: American Physical Society, 196602 (2014).

[143]A. R. Mellnik, J. S. Lee, A. Richardella, J. L. Grab, P. J. Mintun, M. H. Fischer, A. Vaezi, A. Manchon, E.-A. Kim, N. Samarth, and D. C. Ralph, "Spin-transfer torque generated by a topological insulator", Nature **511**, Number: 7510 Publisher: Nature Publishing Group, 449–451 (2014).

[144]C. Chappert, H. Bernas, J. Ferré, V. Kottler, J.-P. Jamet, Y. Chen, E. Cambril, T. Devolder, F. Rousseaux, V. Mathet, and H. Launois, "Planar patterned magnetic media obtained by ion irradiation", Science **280**, 1919–1922 (1998).

[145]T. Devolder, J. Ferré, C. Chappert, H. Bernas, J.-P. Jamet, and V. Mathet, "Magnetic properties of He^+-irradiated pt/co/pt ultrathin films", Phys. Rev. B **64**, 064415 (2001).

[146]M. G. L. Boite, A. Traverse, H. Bernas, C. Janot, and J. Chevrier, "Study of ion beam mixed multilayers via neutron scattering", Materials Letters **6**, 173 (1988).

[147]C. Fowley, Z. Diao, C. C. Faulkner, J. Kally, K. Ackland, G. Behan, H. Z. Zhang, A. M. Deac, and J. M. D. Coey, "Local modification of magnetic anisotropy and ion milling of Co/Pt multilayers using a He$\mathplus$ion beam microscope", Journal of Physics D: Applied Physics **46**, 195501 (2013).

[148]H. Bernas, J.-P. Attané, K.-H. Heinig, D. Halley, D. Ravelosona, A. Marty, P. Auric, C. Chappert, and Y. Samson, "Ordering intermetallic alloys by ion irradiation: a way to tailor magnetic media", Phys. Rev. Lett. **91**, 077203 (2003).

[149]H. Bernas and A. Traverse, "Atomic displacements in metals due to low-energy light ion implantation", Applied Physics Letters **41**, 245–246 (1982).

[150]J. Fassbender, D. Ravelosona, and Y. Samson, "Tailoring magnetism by light-ion irradiation", Journal of Physics D: Applied Physics **37**, Publisher: IOP Publishing, R179–R196 (2004).

[151]G. Hlawacek, V. Veligura, R. van Gastel, and B. Poelsema, "Helium ion microscopy", Journal of Vacuum Science & Technology B **32**, 020801 (2014).

[152]X. Zhao, Y. Liu, D. Zhu, M. Sall, X. Zhang, H. Ma, J. Langer, B. Ocker, S. Jaiswal, G. Jakob, M. Kläui, W. Zhao, and D. Ravelosona, "Spin–orbit torque driven multi-level switching in he+ irradiated w–CoFeB–MgO hall bars with perpendicular anisotropy", Applied Physics Letters **116**, Publisher: American Institute of Physics, 242401 (2020).

[153]T. Devolder, C. Chappert, Y. Chen, E. Cambril, H. Bernas, J. P. Jamet, and J. Ferré, "Sub-50 nm planar magnetic nanostructures fabricated by ion irradiation", Applied Physics Letters **74**, Publisher: American Institute of Physics, 3383–3385 (1999).

[154]T. Devolder, C. Chappert, Y. Chen, E. Cambril, H. Bernas, J. P. Jamet, and J. Ferré, "Sub-50 nm planar magnetic nanostructures fabricated by ion irradiation", Applied Physics Letters **74**, 3383–3385 (1999).

Chapter 2

Experimental Methods

In this chapter, we discuss about experimental methods and techniques used in this research work. The initial section discuss about the well known electrochemical experiments like cyclic voltammetry, chronoamperometry and impedance spectroscopy. Later, the magnetic thin film preparation technique and lithography based patterning are discussed. After introducing the helium beam irradiation source, the final section of the chapter talks about various magnetic and magneto-transport measurements, magnetic domain imaging methods and surface analysis techniques.

2.1 Electrochemical Measurements

2.1.1 Cyclic Voltammetry

Cyclic voltammetry (CV) is the most commonly used potential sweep method to get insight into the mechanics of governing electrochemical reactions. It is useful to identify the number of electrons transfer in a reaction, as well as to determine the kinetic and diffusion parameters of the reaction [1]. In this method, the current is monitored while sweeping the working electrode potential under defined constant rate in the specific range of interest. Fig. 2.1 shows the potential waveform and the resultant cyclic voltammogram corresponding to the ferri/ferrocyanide redox reaction. The shape can be understood with the help of the Nernst equation and diffusion mediated mass transport. As we discussed in section 1.1.1, the Nernst equation relates concentration of species to the applied and formal potential E^0 of the reaction. E^0 is specific to the experimental conditions. Using CV one can estimate E^0 which is related to the CV half potential $E_{1/2}$ as

$$E_{1/2} = E^0 - \frac{RT}{nF} \ln\left(\frac{D_O}{D_R}\right) \tag{2.1}$$

where D_O and D_R represents the diffusion coefficient of oxidised and reduced species, and $E_{1/2}$ is the halfway potential between the two observed peaks. In the case of ferri/ferrocyanide redox reaction used in the current study, $D_O/D_R = 1.08$ which implies $E_{1/2} \approx E^0$.

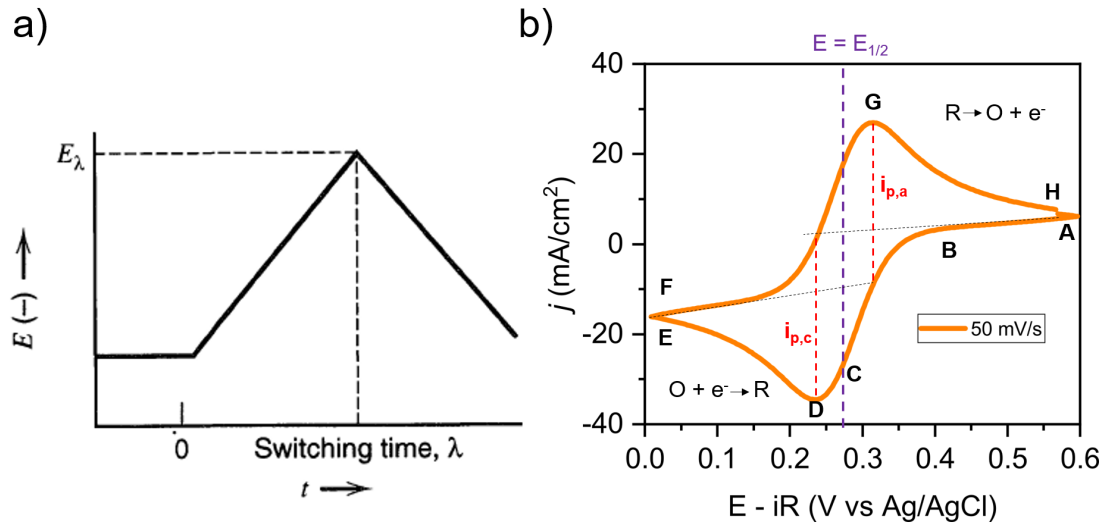

FIGURE 2.1: a) Cyclic potential sweep [2] and b) a typical CV of Pt film electrode in solution consists of 0.2 M potassium ferricyanide and 1 M potassium chloride.

Fig. 2.1 can be used to qualitatively understand the evolution of the electrochemical system with respect to the applied potential. When electrode potential is scanned from A to E, the O species are reduced to R species locally at the electrode, resulting in the depletion of O species concentration and a current flow. In the region A to B, the flat region corresponds to the capacitive contribution arises due to the potential sweep. With further advance in potential (B-D), the current increases as the system is in kinetically limited region. At point D, where the peak cathodic current is observed, the rate of reduction of O species equals the rate of its replacement by the mass transport. With further increase in the potential from D to E, the current decreases with potential as the current in this region is more dependent on the mass transport compared to the kinetic rate. The diffusion layer thickness grows in this region as the potential increases, which reduces the concentration of O species near electrode surface. Upon changing the potential sweep direction (F to H), the R species near the electrode surface oxidises to O species completing the curve.

Electrochemical reversibility describes the rate of electron transfer. If the kinetic rate is fast enough, the system will attain thermodynamic conditions immediately after the application of the potential. Thus electrochemically reversible systems are also referred as nerstian systems as it obeys the Nernst equation.For a reaction to be reversible, the conditions required to obey are:

- the peak current I_p and the scan rate v are related $I_p \propto v^{1/2}$
- the peak potential E_p independent of v
- the peaks potential difference $|E_{p,a} - E_{p,c}| = 57.0/n$ mV
- the peak current ratio $|I_{p,a}/I_{p,c}| = 1$

The evolution of the peak current would be then given by Randles-Sevcik equation

$$i_p = 2.69 \times 10^5 n^{3/2} A D_0^{1/2} [O]_\infty v^{1/2} \tag{2.2}$$

where n is the number of electrons transferred, A is the area of electrode, and D_0 and $[O]_\infty$ are the diffusion coefficient and bulk concentration of oxidized species respectively. Plotting peak current as a function of $v^{1/2}$, one can find the diffusion constant of the reaction.

Scan rate is an important parameter in cyclic voltammetry. Faster scan rate implies thinner diffusion layer which then increases the current flow. Reversibility can also be influenced by the scan rate. By increasing the scan rate, it is possible to drive a reversible system to quasi-reversible (rate constant in the range of 10^{-4} - 10^{-2} cm/s [3]). Kinetic rate constant of such a quasi-reversible system can be estimated using Nicholson approach [4] based on the relation,

$$\psi = k^0 [\pi D n F v / RT]^{-1/2} \tag{2.3}$$

where ψ can be obtained in terms of $X = \Delta E_p \times n$ using the empirical relation,

$$\psi = (-0.6288 + 0.0021X)/(1 - 0.017X) \tag{2.4}$$

2.1.2 Chronoamperometry

Chronoamperometry is a potential step method which refers to the study of the current response with time under potentiostatic control. The potential is stepped from a value where there is no reaction to one corresponding to a mass transport limited region (Fig. 2.2) . The current response with time for a planar electrode can be expressed by Cottrell equation as

$$I(t) = \frac{nFAD^{1/2}c_\infty}{(\pi t)^{1/2}} \tag{2.5}$$

At shorter timescale: Under the application of a potential, the solid-liquid interfacial region can be modelled as a parallel capacitor-resistor circuit. The resistor denotes the charge

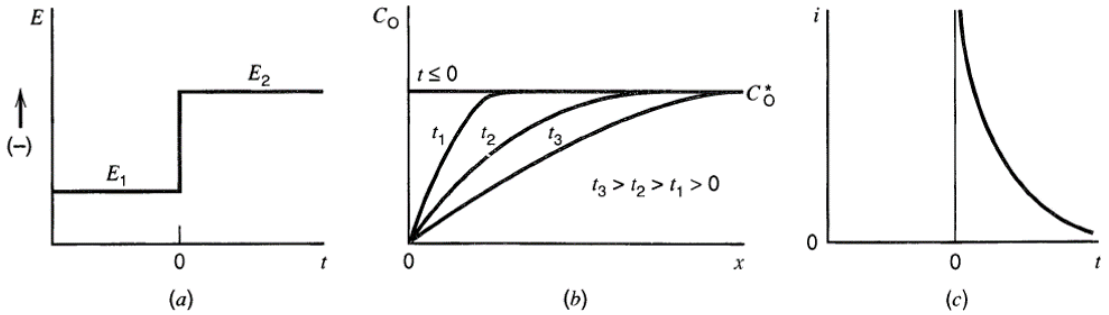

FIGURE 2.2: a) Waveform for a step experiment in which species O is electroinactive at E_1, but is reduced at a diffusion-limited rate at E_2. b) Concentration profiles for various times into the experiment. (c) Current flow vs. time. [2]

transfer resistance of a reaction while the capacitive part is referred as the double layer capacitance. Complications can occur at shorter timescale due to the double layer charging current. For a potential step of ΔE, the capacitive current in an RC circuit follows as $I_c = \Delta E/R \exp(-t/R_s C_{dl})$ where R_s represents the electrode area independent solution resistance and C_{dl} the area dependent double layer capacitance. At smaller timescale, the capacitive current can significantly contribute to the total current but will dies off quickly with time. Another complication might be related to the compliance of the potentiostat as the current can initially rise to large values.

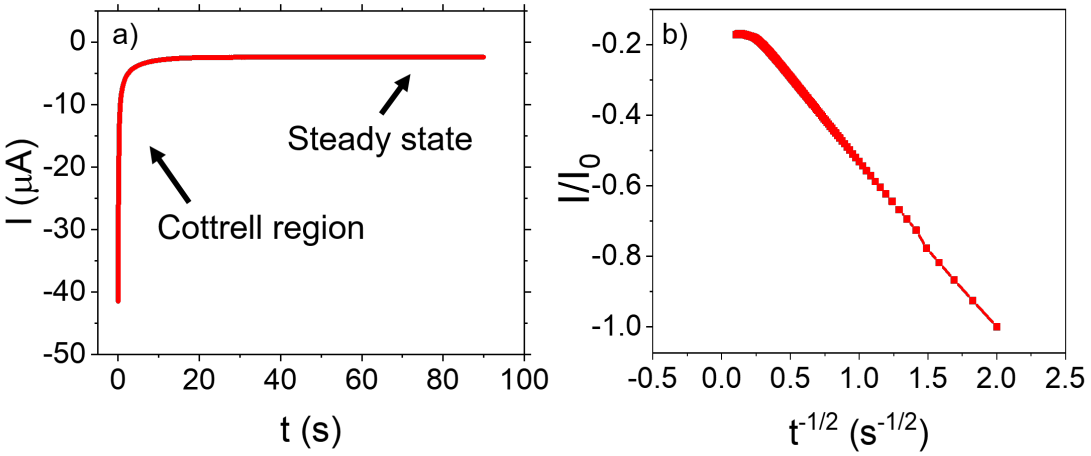

FIGURE 2.3: a) Current response to the potential step from OCP 0.41 V to diffusion limited region 0.15 V applied to planar Pt film electrode in solution containing 0.2 M potassium ferricyanide and 1 M potassium chloride and b) normalised current vs $t^{-1/2}$

At longer timescale: Natural convection can disturb the growth of the diffusion layer. This invalidates the assumptions of the Cottrell equation and the current decrease will no longer follow $t^{1/2}$. At long enough time, the system will reach a steady state where the further development of the diffusion layer will be restricted by the density gradient driven

convective motion. Fig. 2.3 shows the current response with time highlighting the Cottrell region and the steady state region corresponding to ferricyanide reduction.

2.1.3 Electrochemical Impedance Spectroscopy

Impedance spectroscopy is an ac technique which can be used to investigate the properties of the electrochemical reactions. In this method, the impedance response corresponding to a perturbation with a small amplitude alternating signal is measured when the system is at equilibrium or steady state. The perturbation can be an applied current or given electrode potential .

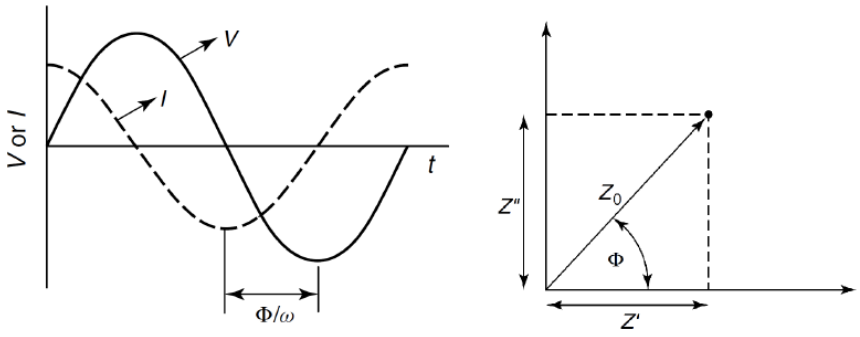

FIGURE 2.4: a)A sinusoidal voltage perturbation and the current response and b) the impedance representation in the complex plane

Consider a sinusoidal ac voltage signal which has the form

$$E_t = E_0 \sin(\omega t) \tag{2.6}$$

where $\omega = 2\pi f$. In a linear system, the current response will be shifted in phase ϕ and can be represented (Fig. 2.4a) as

$$I_t = I_0 \sin(\omega t + \phi) \tag{2.7}$$

Analogous to Ohm's law, the impedance can be defined as,

$$Z = \frac{E_t}{I_t} \tag{2.8}$$

Euler's relation allows to express impedance as amplitude and phase of a complex number. From the potential $E = E_0 \exp(j\omega t)$ and current response $I_t = I_o \exp(j\omega t - \phi)$, the

impedance can be represented (Fig. 2.4b) as

$$Z = Z_0(\cos\phi + j\sin\phi) = Z_0\exp(j\phi) = Z^{'} + jZ^{''} \tag{2.9}$$

Element	Impedance
R	R
L	$j\omega L$
C	$-\frac{1}{j\omega C}$
CPE	$-\frac{1}{(j\omega C)^{\alpha}}$
Series RC	R - $\frac{1}{j\omega C}$
Parallel RC	$\frac{1}{Z} = \frac{1}{R} - j\omega C$
Warburg	Z = $\frac{W}{\sqrt{\omega}} + \frac{W}{j\sqrt{\omega}}$

TABLE 2.1: Common circuit elements and corresponding impedance

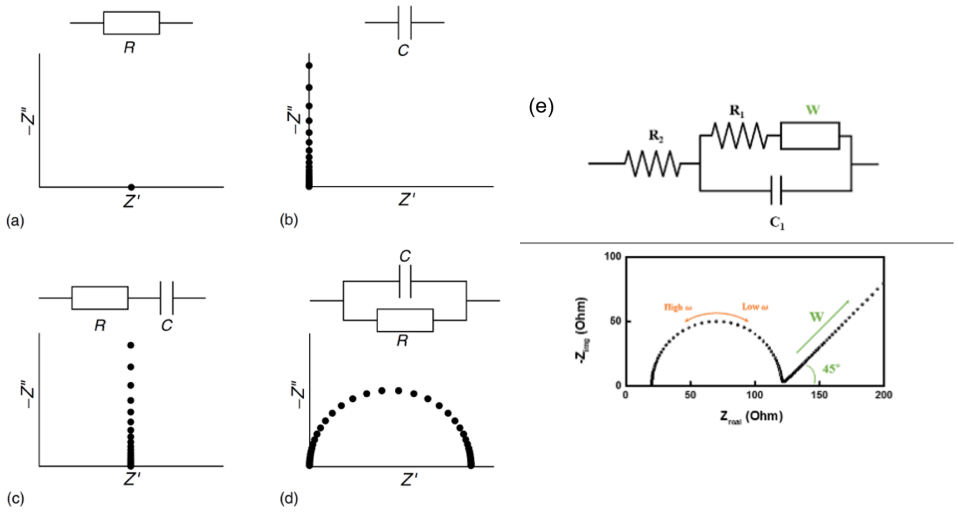

FIGURE 2.5: Nyquist plots for some circuit elements [5]

2.1.3.1 Equivalent Circuits

An electrochemical cell can be modelled as a network of electrical circuit elements (Table 2.1). Such a network is called an equivalent circuit. In an EIS measurement, the measured

impedance of the electrochemical cell at different frequencies is compared to the response of the equivalent circuit. Hence, a prior knowledge of the reaction will be always useful to design the equivalent circuit. All the elements in the circuit should have some specific activity in the electrode reaction. The Randles circuit is one of the commonly used circuit which consists of charge transfer resistance R_{ct} in series with the Warbug diffusion resistance Z_W, both in parallel with double layer capacitance C_{DL} and all three elements in series with solution resistance R_s (Fig. 2.5e). At very high frequency, capacitor act as short and solution resistance can be extracted. By reducing the frequency, the parallel R_{ct} and C_{DL} forms a semicircle. Warburg impedance dominates at low frequency range with a signature curve of 45^0 slanted straight line in Nyquist plot representation. Thus, a single wide frequency impedance spectra gives information not only about the reaction kinetics but also about the mass transport properties. EIS is normally represented as Bode plot or Nyquist plot (Fig. 2.5).

In Nyquist plot, the high frequency region is commonly characterised by a depressed arc instead of a semi-circle corresponding to parallel resistance R_{ct} and an ideal capacitor C_{DL}. One approach to model this behaviour in experimental data is to replace the double layer capacitor C_{DL} with a constant phase element CPE. The impedance of CPE is given by

$$Z = -\frac{1}{(j\omega C)^{\alpha}} \tag{2.10}$$

where α is the distribution factor and can vary between 0 to 1.0. CPE can be thought of as an effective impedance of the distribution of capacitance over the electrode surface. Even though a particular theory may not give exactly CPE behaviour, several explanations were put forward such as surface roughness [6] and non-uniform current distribution [7].

2.1.3.2 Kramers-Kronig Relations

The Kramers-Kronig (KK) test is used to check the validity of the EIS data. Electrochemical impedance spectroscopy (EIS) is built on linear systems theory which requires that the system satisfy conditions of linearity, causality, and stability. A system is defined linear when its response to a sum of input signal is a sum of individual responses. Causality will be satisfied if the measured system response is entirely caused by the applied perturbation signal. Stability implies the equilibrium state of the system unless excited by an external perturbation. These requirements can be validated using KK relations which consist of a set of

transformations that can be used to predict one component of the impedance from the other over the wide frequency range. The imaginary component is related to real component as

$$Z''(\omega) = -\frac{2\omega}{\pi}\int_0^\infty \frac{Z'(x) - Z'(\omega)}{x^2 - \omega^2}\, dx \tag{2.11}$$

and the real component from the imaginary component as

$$Z'(\omega) = Z''(\omega) + \frac{2}{\pi}\int_0^\infty \frac{xZ''(x) - \omega Z''(\omega)}{x^2 - \omega^2}\, dx \tag{2.12}$$

Any deviation from the measured component and the KK transformed component is due to the non-linearities in the system either due to the non-stationary behaviour of reaction or by instrument artefacts. In the case of ferricyanide reduction reaction discussed in this thesis, a good agreement with the measured EIS spectra and KK transformed data is obtained which confirms the validity of the measurement(Fig. 2.6).

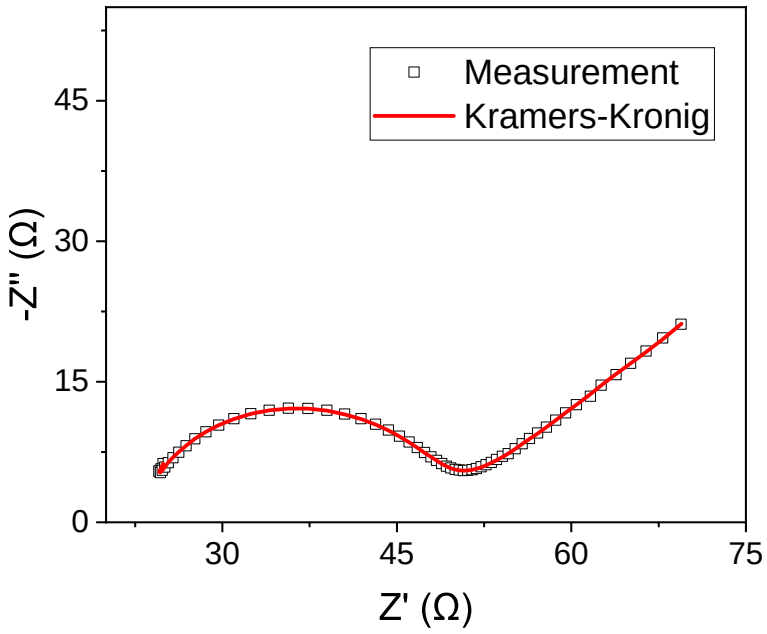

FIGURE 2.6: EIS spectra measured and calculated with the Kramers-Kronig relations in a solution of 0.2 M potassium ferricyanide and 1 M KCl at bias voltage 0.175 V applied to a Pt film working electrode (Vs Ag/AgCl)

2.2 Magnetic thin film deposition and device fabrication

2.2.1 DC Magnetron Sputtering

Sputtering is a physical vapour deposition technique for depositing thin films. Because of its ability to produce high quality films with uniform thickness, it is a preferred industrial deposition technique. The mechanism mainly consisted of the ejection of surface atoms from a source material (target) when exposed to an energetic atoms (usually Ar) bombardment, which deposits on the substrate placed in the path of ejected atoms or cluster of atoms (Fig. 2.7). Prior to the deposition, high vacuum of the order of 10^{-8} Torr should be achieved in the deposition chamber to avoid any contamination. The chamber will be then filled with noble gas (typically Ar) with the pressure maintained in the range of 1 - 100 $\times$ 10^{-8} Torr. Upon the application of a large potential difference between target (-ve) and substrate (+ve), the Ar gas get ionized creating plasma in the chamber. The positively charged Ar^{+} ions are accelerated towards negatively biased target which results in the ejection of atoms from the surface of target material. These neutral atoms land on the substrate and the chamber walls.

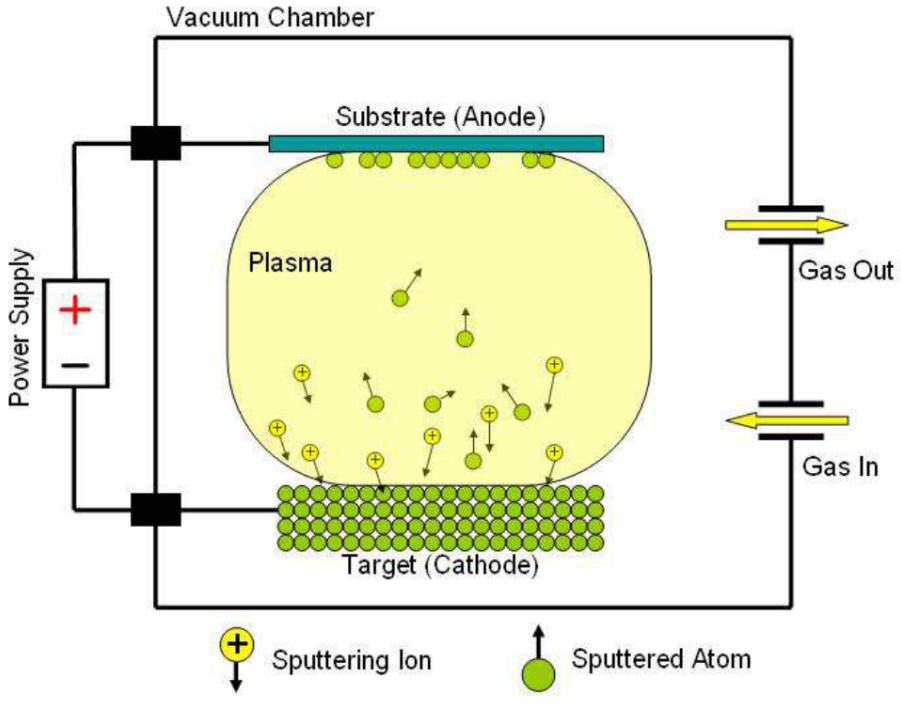

FIGURE 2.7: Schematic representation of the sputtering process. Atoms ejected from the target material when subject to ion bombardment are deposited on the substrate.

In order to improve the efficiency of the process, a magnetron sputtering technique has been developed. In this technique, permanent magnets are placed behind the target which not only traps the electrons involved in sputtering but also helps to concentrate the plasma

near to the target. Under the presence of the magnetic field, the cycloid-like motion of electrons near the target surface results in an enhancement of the ionisation rate. The deposition parameters like pressure, power and sputter rate can significantly influence the quality and magnetic properties of the thin films [8]. Adjusting these parameters will affect the mean free path, and control the energy of the deposited atoms which influence the degree of reorganisation of the atoms when deposited. This in effect can influence the interfacial roughness, dead layer formation, anisotropy, coercivity, to name a few.

During the course of the present work, two sputtering machines are used to fabricate magnetic heterostructures. Initial samples are sputter deposited using a Shamrock chamber A machine in the CRANN cleanroom, TCD[1]. The sputtering of samples are done at a base pressure of 2×10^{-8} Torr and an Ar pressure in the range of a few 10^{-3} Torr. Later, more samples are fabricated using ATC 2200 from AJA International, located at HZDR[2]. The deposition is done at base pressure of 4×10^{-8} Torr and an Ar pressure 3×10^{-3} Torr.

2.2.2 Hall Bar Patterning

For electrical measurements, thin films are patterned into Hall bars using the combination of the laser lithography and ion etching tools [3]. Laser lithography allows patterning of devices down to sub-μm sizes. A standard procedure for the lithography is illustrated in Fig. 2.8.

Clean and flat wafer surface is an important requirement for accomplishing high resolution lithography. In general, before the pattering process, the substrate (thin films deposited on Si or glass wafer) is rinsed in acetone and ethanol followed by isopropanol. N_2 is blown on the wafer for drying purposes. Once a cleaned wafer is obtained, a suitable photoresist (positive or negative) is spread uniformly over the film surface using a spin coater. The film has to have a minimum size (5 mm $\times$ 5 mm but depends on the size of pattern structure too) for the photoresist to spread uniformly over the surface. Non-uniformity in resist distribution can results in over and under exposed regions. After spin coating, the substrate is baked at high temperature (around 100^0 C) to drive out excess solvent from the photoresist. This process is called soft baking. One should be careful with the baking time as any excess solvent in the resist can interfere with the exposure of photoresist eventually affecting the lithographic patterns. The sample is then loaded into the Heidelberg μPG 101 laser lithography machine. The alignment of the sample can be done with the help of the -inbuilt

[1]Thanks to Prof. Michael Coey and Dr. Gwenael Atcheson

[2]Thanks to Prof. Olav Hellwig, Dr. Ruslan Salikhov and Aleena Joseph

[3]Thanks to STnano for the cleanroom facility, and also to Dr. Hicham Majjad, Romain Bernard and Sabine Siegwald for the help and support with the cleanroom equipment

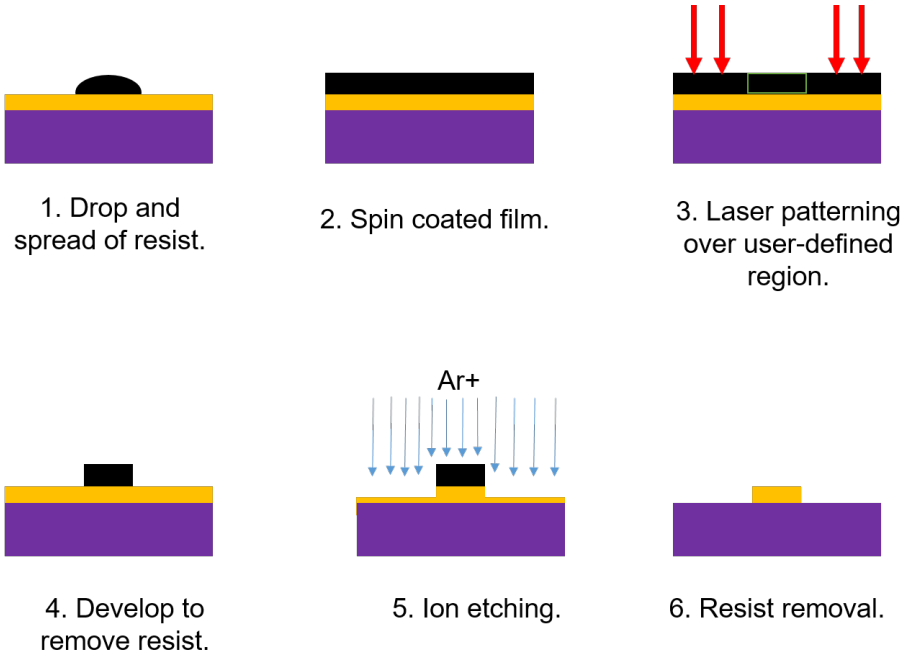

FIGURE 2.8: Lithography process

microscope. The machine can automatically correct for the spatial offset. The lithography pattern designed using software like Klayout is now uploaded to the system. After optimizing the parameters (exposure dose, direct or invert, humidity check), the laser will raster over the specified area. After exposure, the substrate is then placed in a solvent solution for development. During the development, the laser exposed area of the positive resist will be dissolved. The exposed region of the sample can be then etched using Ar+ ions to obtain specific patterns.

In this work, a combination of positive and negative resists are used during different steps of lithography. Fig. 2.9a shows the Klayout design of the Hall bar used in this work. In order to pattern the Hall bar structure from the film, a negative resist (AZ5214) is used. The structure is obtained after Ar+ etching the unwanted region in the sample. Ti(3.0)/Au(47.0) (numbers in nm) is deposited for electrical contact followed by the patterning using positive resist - AZ1505.

2.2.3 Helium ion microscope (HIM)

We employed a state-of-the-art Carl Zeiss Helium-Ion Microscope (HIM) facility at HZDR[4] for magnetic patterning of multilayer systems [9]. It is based on the gas field ion source

[4]Thanks to Dr. Gregor Hlawacek and Dr. Ciaran Fowley

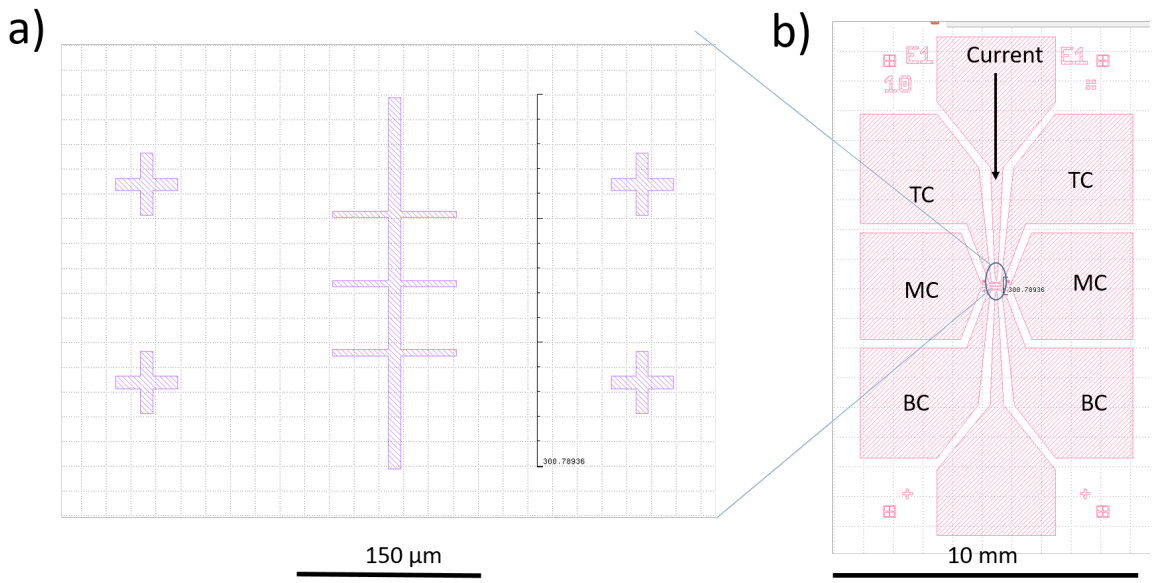

FIGURE 2.9: Klayout design of a) Hall bar having transverse length 10 μm and longitudinal length 300 μm and b) electrical contact used to pattern the thin film.

technology which can generate focused ion beams for ultrahigh resolution and nanofabrication applications [10]. HIM uses the apex of tungsten tip to ionize the helium gas. The control over the tip sharpness allows one to use only the last three of the apex atoms for the purpose of extremely focused beam production. As a result, a beam spot size of diameter of only 0.5 nm can be achieved. The beam can be rastered over a predetermined region over the specimen. The microscope is also equipped with 4 Kleindiek MM3A micromanipulators which in our case can be used to perform Hall resistance measurements *in situ* with the irradiation. We used the focused beam of ions to study the effect of local irradiation effects on the perpendicular magnetic anisotropy of Pt/Co/W based multilayers. The results are discussed in chapter 4.

2.3 Characterisation of magnetic thin films

2.3.1 SQUID magnetometry

Superconducting QUantum Interference Device (SQUID) is a non-destructive and high sensitivity technique to measure the absolute magnetic moment of a magnetic sample [11]. The operational principle of SQUID is based on the Josephson junction and flux quantization in superconducting ring. A Josephson junction consists of two superconducting rings separated by an insulator. The current density across the junction is sensitively influenced by the magnetic flux through the ring. In SQUID magnetometer, the sample is moved along

the vertical axis of the pick up coil which is forming a second order gradiometer as shown in Fig. 2.10. The current passing through the pick up coil is detected by the SQUID and converts it into voltage. The voltage measured by the SQUID depends also on the sample position in the gradiometer. After mounting a new magnetic specimen, the center position is determined using a long scan to properly adjust the sample position with respect to the pickup coils.

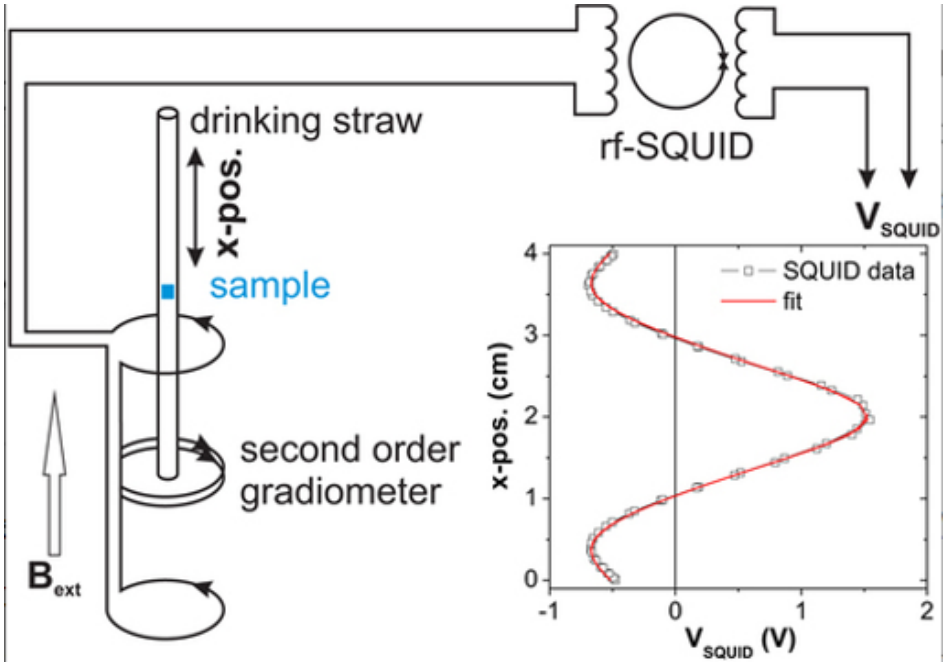

FIGURE 2.10: Schematics showing the setup of SQUID magnetometer. A second order gradiometer is used to limit the external disturbances. Inset shows the voltage response of the specimen to the vertical position in the gradiometer.

In this work, SQUID measurments are mostly performed at TCD [5] and at IPCMS[6]. Non-magnetic straws are used for holding the thin film samples during the measurement. Samples are diced into ≈ 4 mm $\times$ 4 mm for both in-plane and out-of-plane magnetic measurements. Even though a maximum of 5 T can be achieved, most of the measurements are performed only up to 2 T as the magnetization of all samples are saturated well below this field value.

2.3.2 X-ray Reflectivity (XRR)

Grazing-incidence X-ray reflectivity (XRR) is a non-destructive thin film characterization technique which can be used to evaluate the surface roughness, film thickness and structure of the thin film multilayers [12]. The technique is based on the analysis of reflection intensity

[5] Thanks to Prof. Michael Coey and Dr. M. Venkatesan
[6] Thanks to Dr. Jérome Robert

and pattern of a grazing-incidence X-ray beam. XRR can measure a film thickness ranging from several hundred of nm to as small as a few angstroms (A^0).

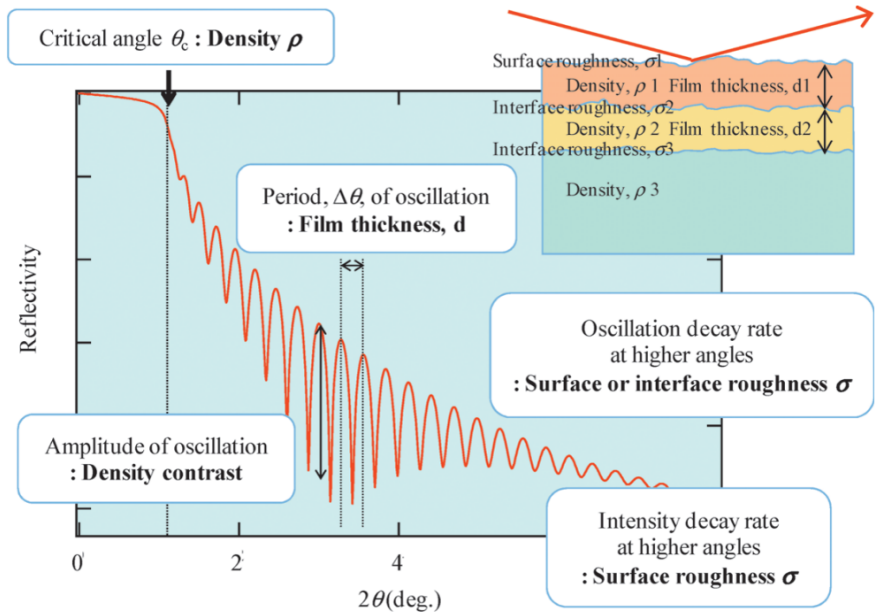

FIGURE 2.11: A summary of information provided by an XRR profile [12].

When an X-ray beam incident on an ideal flat surface at a small angle θ lower than the total internal reflection angle θ_c, the intensity of reflected beam will be larger as shown in Fig. 2.11. When $\theta \approx \theta_c$, the intensity of reflectivity started reducing and with further increase in θ the reflected intensity decreases proportional to θ^4. In XRR, the obtained spectra is the sum of the reflected beam from all the interface. The oscillations, which are inversely proportional to the layer thickness, are the result of the interference of the reflected beam from multiple interfaces. The decay rate of the reflected signal is related to the interfacial roughness. Rougher the interface, faster will be the decay of XRR.

2.3.3 X-ray Photoelectron Spectroscopy (XPS)

X-ray photoelectron spectroscopy (XPS) is one of the commonly used surface sensitive technique which allows the quantitative determination of the elemental composition, chemical specificity (oxidation state) and film thickness [13]. The working principle of XPS is based on the photoelectric effect. When an X-ray beam of known energy energy $h\nu$ falls on the specimen, the energy is absorbed by a core of valence electron. If the incident energy is larger than the binding energy BE of the electron, then the electron is emitted from the sample with a kinetic energy KE which will be related to other energies involved as

$$BE = h\nu - KE - \phi \tag{2.13}$$

where ϕ is a correction factor to the detector which is related to the threshold energy for the electron emission (work function). The emitted electrons are analysed by the spectrometer to obtain the XPS spectra. Since each element exhibits a characteristic peak in XPS spectra, the chemical composition of the surface can be determined qualitatively. Even though X-rays can penetrate into the sample op to hundreds of nanometer or more, the scattering of photoeletrons limit the probe depth to a maximum of a few nanometers over the typical kinetic energy range of 10 - 1000 eV used in XPS studies. As the emitted photoelectrons can also undergo scattering along its way to the detector, XPS is mostly performed under ultrahigh vacuum conditions. The XPS measurements on Co/Pt multilayers are done using Al source with 1486.6 eV energy and step size 0.1 eV, under an ultrahigh pressure range 1.0 - 4.8 $\times$ 10^{-9} Torr [7].

2.3.4 Magneto-Optical Kerr Effect (MOKE) Imaging

Magneto-Optical Kerr Effect (MOKE) can be used to characterize and image the magnetic properties of the thin films using polarized light. This method is based on the rotation of the polarization plane of the incoming light during the reflection from a magnetic sample [14]. The incident light is normally a linearly polarized light i.e, the plane of polarization is similar to the plane of electric field of the light. With such a light incident on a specimen, the oscillating electric field of the incident light interacts with the sample magnetization via the Lorentz force and results in the rotation of the polarization plane of the reflected light. This rotation, or Kerr rotation, can be analysed to image the magnetic state of the sample.

According to the magnetization direction of the specimen with respect to the plane of the incident light, the MOKE geometry is divided into three geometries: the polar, longitudinal and transverse, as shown in Fig. 2.12. In polar geometry, the magnetization of sample is perpendicular to the sample surface but in the plane of polarization of incident light. While in longitudinal geometry, the magnetization lies in the plane of incident light as well as in the plane of sample surface. Whereas in transverse geometry, the magnetization of the sample will be in the plane of sample surface but perpendicular to the plane of polarization of incident light. Since thin films having perpendicular magnetic anisotropy are presented in this research, polar MOKE is used as main imaging technique[8].

[7] Thanks to Prof. Peter A. Dowben, Thilini Kumari Ekanayaka, Gauthami Viswan and Archit Dhingra
[8] Thanks to Dr. Salia cherifi-Hertel

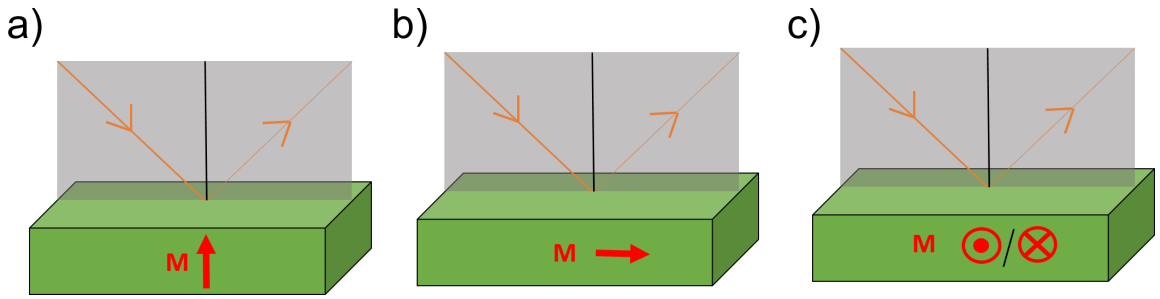

FIGURE 2.12: Different geometries of MOKE. (a) Polar MOKE, (b) longitudinal MOKE and (c) transverse MOKE.

2.3.5 Magnetotransport Measurement

Local magnetic properties of the thin film can be determined using electrical transport measurements. In a magnetic thin film, the transverse resistivity ρ_{xy} can be empirically expressed as

$$\rho_{xy} = R_0 H_z + R_s M_z \tag{2.14}$$

where R_0 is the ordinary Hall coefficient, R_s is the anomalous Hall coefficient, and H_z, M_z are film normal magnetic field and $z-$ component of the magnetization. Ordinary Hall effect (OHE) is due to the Lorentz force acting on charge carriers and is quite small in metals due to its high carrier concentration. On the other hand, in transition metal ferromagnets, the anomalous Hall resistance (AHE) has been reported to be an order of magnitude higher than the OHE [15]. Unlike OHE, AHE will be present even in the absence of external magnetic field.

The anomalous behaviour of Hall effect in ferromagnetic metals has been explained in relation to the intrinsic and extrinsic origins. The intrinsic mechanism is related to the band structure of the conducting material, and is still controversially discussed. Here, the Hall resistivity will scale with the longitudinal resistivity ρ_{xx} as $\rho_{xy} = \rho_{xx}^2$. On the other hand, extrinsic mechanism (skew scattering) is related to the asymmetric scattering of conduction electrons due to spin orbit coupling (SOC) . If the scattering is due to the SOC with the impurity, it is referred as side jump mechanism. In skew scattering, $\rho_{xy} = \rho_{xx}$, whereas the side jump results in $\rho_{xy} = \rho_{xx}^2$.

In this research, we measure the transverse voltage evolution with respect to the magnetic field to characterize the magnetic state of the perpendicular magnetic anisotropy (PMA) thin films. Films are patterned into specific geometry structures called Hall bar for the purpose of R_{xx} and R_{xy} electrical measurement (Fig. 2.13). The current is applied along the long

axis of the Hall bar, while the voltage is measured across three different junctions marked TC, MC and BC. For the magnetic hysteresis loop, the transverse voltage corresponding to 1 mA dc current is obtained by sweeping the magnetic field both in-plane and perpendicular to the sample surface. For spin orbit torque (SOT) switching measurements, the Hall voltage is measured after applying electric current pulses of various amplitude.

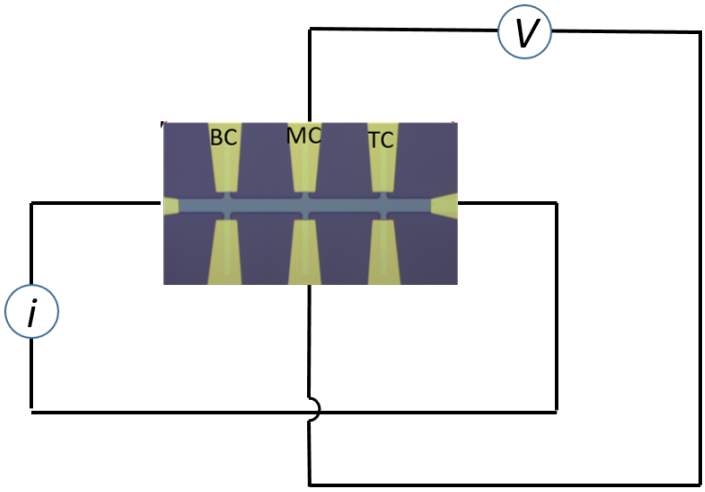

FIGURE 2.13: Hall bar pattern and the schematics of measurement setup of R_{xy}

2.3.6 Harmonic Hall Measurement (HH)

Recently, it has been shown that the current induced spin orbit torques in magnetic multilayers can be characterized by quantifying the effective fields [16, 17]. In this section, we will discuss how the SOT effective field can be obtained using harmonic Hall (HH) measurement.

2.3.6.1 Magnetization modulation due to current induced fields

We consider an out-of-plane magnetic system (magnetized along z) made of a heavy metal-ferromagnetic metal bilayer system. The current is applied along the longitudinal direction x of the Hall bar. The direction of the external field in polar and azimuthal angles can be expressed as $\mathbf{H} = \mathrm{H}\,(\sin\theta_H\cos\theta_H, \sin\theta_H\sin\psi_H, \cos\theta_H)$. The magnetization can be defined as $\mathbf{M} = \mathrm{M}_s\,(\sin\theta\cos\theta, \sin\theta\sin\psi, \cos\theta)$. Based on the macrospin model (section 1.3.2), the magnetic energy of the system, neglecting in-plane anisotropy, can be written as

$$E = -K_{eff}\cos^2\theta - \boldsymbol{M}.\mu_0\boldsymbol{H} \tag{2.15}$$

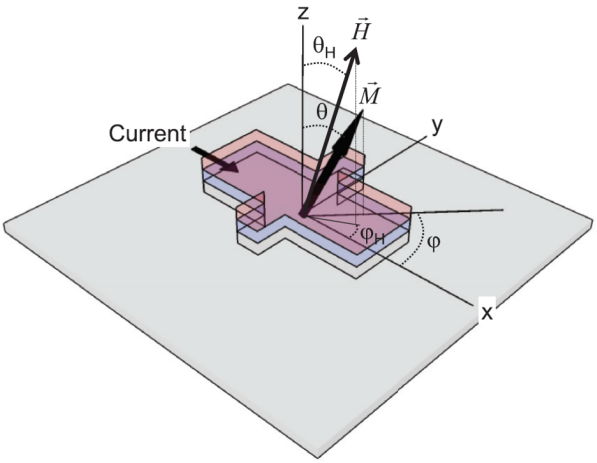

FIGURE 2.14: Schematic illustration of the experimental setup. Patterned Hall bar consists of a magnetic layer (middle) sandwiched between a non magnetic metal layer (bottom) and an insulating oxide layer (top). Coordinate systems of the magnetization **M**, current and external field **H** are illustrated.[16]

If we apply a sinusoidal excitation current $I(t) = I_0 \sin \omega t$ along x, the spin Hall effect results into the bottom heavy metal generating an oscillating spin current. The consequence is that this spin current diffuses through the interface and gives rise to time dependent SOT effective fields, $\Delta\mathbf{H}(t)$, which modulates the magnetization **M** $(\Delta\theta(t), \Delta\psi(t))$ around its equilibrium position. Note that the frequency of the applied current is small enough (a few kHz, in our case it is 1234.56 Hz) so that the phase difference between the effective fields and magnetization modulation can be ignored. The effect of the ac applied current can be summarised as,

$$\Delta\mathbf{H}(t) = \Delta\mathbf{H}_i \sin \omega t \text{ (where } i = x, y, z) \tag{2.16}$$

$$\Delta\theta(t) = \Delta\theta \sin \omega t \; ; \; \Delta\psi(t) = \Delta\psi \sin \omega t \tag{2.17}$$

2.3.6.2 Expression for Hall voltage

The Hall voltage can contains contributions from anomalous Hall effect (AHE) and planar Hall effect (PHE). When the current is applied along x, the Hall resistance R_{xy} can be expressed as,

$$R_{xy} = \frac{1}{2}\Delta R_A \cos\theta + \frac{1}{2}\Delta R_P \sin^2\theta \sin 2\psi \tag{2.18}$$

where ΔR_A and ΔR_P represents the Hall resistance change due to AHE and PHE. If we assume that the SOT fields are small perturbations to the system,*i.e.* Δ **H** « $\mathbf{H}_k$ (anisotropy field), then $\Delta\theta << 1$ and $\Delta\psi << 1$. Eqn. 2.18 can be now written as

$$R_{xy} \approx \frac{1}{2}\Delta R_A(\cos\theta_0 - \Delta\theta\sin\theta_0) + \frac{1}{2}\Delta R_P(\sin^2\theta_0 + \Delta\theta\sin 2\theta_0)(\sin 2\psi_0 + 2\Delta\psi\cos 2\psi_0) \quad (2.19)$$

In the presence of an ac excitation current $I = I_0 \sin\omega t$, replacing $\Delta\theta$ and $\Delta\psi$ with $\Delta\theta\sin\omega t$ and $\Delta\psi\sin\omega t$ in Eqn. 2.19, the measured Hall voltage can be expressed as

$$V_{xy} = R_{xy}(t)I_0\sin\omega t = V_0 + V_\omega\sin\omega t + V_{2\omega}\cos 2\omega t + ... \quad (2.20)$$

Combining Eqn. 2.19 and Eqn. 2.20, the Hall voltage harmonics can be written as

$$\begin{aligned} V_\omega &= AI_0 \\ V_{2\omega} &= -\frac{B_\theta + B_\psi}{2}I_0 \end{aligned} \quad (2.21)$$

where

$$\begin{aligned} A &= \frac{1}{2}\Delta R_A\cos\theta_0 + \frac{1}{2}\Delta R_P\sin^2\theta_0\sin 2psi_0 \\ B_\theta &= \frac{1}{2}\Delta\theta(\Delta R_A\sin\theta_0 + \frac{1}{2}\Delta R_P\sin 2\theta_0\sin 2\psi_0) \\ B_\psi &= \Delta R_P\Delta\psi\sin^2\theta_0\cos 2\psi_0 \end{aligned} \quad (2.22)$$

Note that V_ω, which is the in-phase first harmonic, is the ac analogue of the dc Hall voltage. Terms that are linear with $\Delta\theta$ and $\Delta\psi$ will give rise to the out-of-plane second harmonics

2.3.6.3 SOT effective field quantification

When an electric current is applied to the HM/FM heterostructure, spin accumulation at the interface exerts field like and damping like fields on the perpendicularly magnetized adjacent layer. Slonczewski-like field (H_{SL}) acts along the direction of $\sigma\times$ **M** while the field like (H_{FL}) acts alongσ. These effective fields can be quantified by monitoring the evolution of first and second harmonic Hall resistance as a function of applied field along x and y.

In the limit, when the applied field is small compared to the perpendicular anisotropy field and when the PHE can be neglected, the effective fields can be estimated as

$$\Delta\mu_0 H_{SL} \approx -2\left(\frac{\partial V_{2\omega}}{\partial H_x}/\frac{\partial V_\omega^2}{\partial H_x^2}\right) \; ; \; \Delta\mu_0 H_{FL} \approx -2\left(\frac{\partial V_{2\omega}}{\partial H_y}/\frac{\partial V_\omega^2}{\partial H_y^2}\right) \tag{2.23}$$

where $H_{x(y)}$ is the field swept along $x(y)$ direction. However, when the contribution of Hall resistance to the Hall resistance is comparable to AHE, the SOT field equation will be modified as

$$\Delta\mu_0 H'_{SL} \approx -2\frac{B_x \pm 2\zeta B_y}{1-4\zeta^2} \; ; \; \Delta\mu_0 H'_{FL} \approx -2\frac{B_y \pm 2\zeta B_x}{1-4\zeta^2} \; ; \; B_{i=x,y} = \left(\frac{\partial V_{2\omega}}{\partial H_i}/\frac{\partial V_\omega^2}{\partial H_i^2}\right) \tag{2.24}$$

where $\zeta = \Delta R_P/\Delta R_A$ and $\pm$ denotes the magnetization pointing $+z$ or $-z$ respectively. In the limit where the spin transport at the heavy metal / ferromagnetic metal interface is transparent and the spin current from the heavy metal will be entirely converted into Slonczewski-like effective field, the spin Hall angle θ_{SH} can be estimated as

$$\theta_{SH} = \frac{2e}{\hbar}\frac{\mu_0 H_{SL} M_s t_f}{j} \tag{2.25}$$

where t_f and j are the ferromagnetic layer thickness and the current density through the Hall bar respectively. Other relevant parameters (like the spin diffusion length) can be obtained by studying the thickness dependence of spin Hall angle [18].

Bibliography

[1]N. Elgrishi, K. J. Rountree, B. D. McCarthy, E. S. Rountree, T. T. Eisenhart, and J. L. Dempsey, "A practical beginner's guide to cyclic voltammetry", Journal of Chemical Education **95**, 197–206 (2018).

[2]A. J. Bard and L. R. Faulkner., "Electrochemical methods: fundamentals and applications.", 2nd edn. Wiley (2000).

[3]C.-y. Liu, Z.-y. Liu, R. Peng, and Z.-c. Zhong, "Quasireversible process of dopamine on copper-nickel hydroxide composite/nitrogen doped graphene/nafion modified GCE and its electrochemical application", Journal of Analytical Methods in Chemistry **2014**, 724538 (2014).

[4]R. S. Nicholson, "Theory and application of cyclic voltammetry for measurement of electrode reaction kinetics.", Analytical Chemistry **37**, Publisher: American Chemical Society, 1351–1355 (1965).

[5]W. Choi, H.-C. Shin, J. M. Kim, J.-Y. Choi, and W. Yoon, "Modeling and applications of electrochemical impedance spectroscopy (EIS) for lithium-ion batteries", `10.33961/jecst.2019.00528` (2020).

[6]M. W. H, S. J. H, P. T, and N. L, "Tafel current at fractal electrodes. connection with admittance spectra.", Journal of Electroanalytical Chemistry and Interfacial Electrochemistry **285**, 103–115 (1990).

[7]J.-B. Jorcin, M. E. Orazem, N. Pébère, and B. Tribollet, "CPE analysis by local electrochemical impedance spectroscopy", Electrochimica Acta, Electrochemical Impedance Spectroscopy **51**, 1473–1479 (2006).

[8]P. He, W. A. McGahan, S. Nafis, J. A. Woollam, Z. S. Shan, S. H. Liou, F. Sequeda, T. McDaniel, and H. Do, "Sputtering pressure effect on microstructure of surface and interface, and on coercivity of co/pt multilayers", Journal of Applied Physics **70**, Publisher: American Institute of Physics, 6044–6046 (1991).

[9]*Helium ions put magnetic skyrmions on the track | nano letters*, `https://pubs.acs.org/doi/abs/10.1021/acs.nanolett.1c00136` (visited on 04/06/2021).

[10]G. Hlawacek, V. Veligura, R. van Gastel, and B. Poelsema, "Helium ion microscopy", Journal of Vacuum Science & Technology B **32**, Publisher: American Vacuum Society, 020801 (2014).

[11]M. Buchner, K. Höfler, B. Henne, V. Ney, and A. Ney, "Tutorial: basic principles, limits of detection, and pitfalls of highly sensitive SQUID magnetometry for nanomagnetism and spintronics", Journal of Applied Physics **124**, Publisher: American Institute of Physics, 161101 (2018).

[12]M. Yasaka, "X-ray thin- lm measurement techniques v. x-ray refectivity measurement", Rigaku journal **26**, 1–9.

[13]H. Bluhm, "X-ray photoelectron spectroscopy (XPS) for in situ characterization of thin film growth", in *In situ characterization of thin film growth* (Elsevier, 2011), pp. 75–98.

[14]P. N. Argyres, "Theory of the faraday and kerr effects in ferromagnetics", Physical Review **97**, Publisher: American Physical Society, 334–345 (1955).

[15]E. Hall, "XVIII. on the "rotational coefficient" in nickel and cobalt", The London, Edinburgh, and Dublin Philosophical Magazine and Journal of Science **12**, Publisher: Taylor & Francis _eprint: https://doi.org/10.1080/14786448108627086, 157–172 (1881).

[16]M. Hayashi, J. Kim, M. Yamanouchi, and H. Ohno, "Quantitative characterization of the spin-orbit torque using harmonic hall voltage measurements", Physical Review B **89**, Publisher: American Physical Society, 144425 (2014).

[17]K. Garello, I. M. Miron, C. O. Avci, F. Freimuth, Y. Mokrousov, S. Blügel, S. Auffret, O. Boulle, G. Gaudin, and P. Gambardella, "Symmetry and magnitude of spin–orbit torques in ferromagnetic heterostructures", Nature Nanotechnology **8**, Number: 8 Publisher: Nature Publishing Group, 587–593 (2013).

[18]L. Liu, T. Moriyama, D. C. Ralph, and R. A. Buhrman, "Spin-Torque Ferromagnetic Resonance Induced by the Spin Hall Effect", Physical Review Letters **106**, 036601 (2011).

Chapter 3

Influence of Large-Gradient Magnetic Field on the Electrochemical Reaction

In this chapter, we will discuss the influence a of large magnetic field gradient applied at the electrochemical interface. Our study aims to find an answer to the controversial question: can a magnetic field influence the interfacial properties of electrochemical reactions. Decreasing the magnet size enhances the field gradient. Hence, nanomagnetic thin films made of Co/Pt repeats are used as the source for extreme field gradient. Thin films with perpendicular magnetic anisotropy (PMA) are fabricated to generate large field gradient near to the film surface of magnitude estimated assuming PMA films as magnetised 2D sheets. Ferri/ferrocyanide redox couple is used as a model system to study the field gradient effects at the electrode/electrolyte interface. In order to better understand the redox system and reveal unambiguously the influence of a magnetic field source, the reaction is characterised initially using non-magnetic Pt film electrodes. Prior to the field effect studies, the influence of the Pt capping layer thickness on the activity of Co/Pt multirepeats is discussed. Then, the Lorentz force effects on the mass transport limited reaction is explored, and its the equivalence to the mechanical stirring is illustrated. Finally, the influence of extreme field gradient at the electrochemical interface is studied in greater detail.

3.1 Introduction

Although studies related to magnetic field influence on electrochemical process date back to Faraday, the growing interest in understanding the physical mechanism and exploring the possibilities for application has increased since 40 years [1–3]. Magnetic field can impact electrochemistry in two distinct aspects, electrodeposition and electrochemical process, by means of mainly the Lorentz force and the Kelvin field gradient force [4]. In most of the cases, the effect of a magnetic field on the electrochemical system can be explained by the

field effects on the diffusion layer. The Lorentz force will be active when current density and magnetic field have orthogonal components. This magnetohydrodynamic (MHD) force induces an electrolyte flow perpendicular to the electrode surface and results in thinning of the diffusion layer. MHD effect is complex in nature and can generate vorticity due to edge effects [5], generate patterns in deposits [6] and can even affect the bubble formation due to micro-MHD flows induced by local change in current density [7]. On the other hand, the Kelvin force acts in a non-uniform field when there exists a concentration gradient orthogonal to the field gradient. Unlike Lorentz force, this force can be enhanced by reducing the magnetic source size. The different applications of the field gradient force includes levitation of diamagnetic materials in paramagnetic media [8], direct and inverse patterning of deposits using magnetic arrays [9, 10], enhancing efficiency of oxygen reduction reaction [11, 12], and even in microfluidics stabilizing frictionless flow tubes [13].

The influence of a magnetic field at the solid/liquid interface is a controversial topic. Energy estimates reveal that the magnetic energy of species is negligible when compared to the thermal energy driving diffusion and the electrostatic potential energy driving electron transfer. Hence, one would expect no effect of magnetic field on the electrochemical double layer and electrode kinetics. Magneto-impedance and linear sweep voltammetry based investigations by Koehler *et al.* [14], Devos *et al.* [15] along with the Tafel data [6] supports this view. However, recent studies have shown that the magnetism of a working electrode can in fact influence the spin polarisation of intermediate radicals enhancing the formation of triplet O_2 [16]. Sambalova *et al.* [17] used Co/Pt electrodes to study hydrogen evolution reaction and has observed field effects on the double layer measured by means of magneto-optic response. It has also been reported that PtCo alloy film with perpendicular magnetic anisotropy shows higher activity towards oxygen reduction reaction compared to the in-plane magnetization and the enhancement is attributed to the chemical ordering of the PMA film [18]. Dunne and Coey [19] have reported an enhancement in both the double layer capacitance and the rate constant due to Maxwell stress when a field of 0.5 T is applied parallel to the electrode surface. The effects are ascribed to the shift in outer Helmholtz plane and no true shift in kinetics is observed.

Decreasing the system size makes the magnetic force field density increase. Nanopatterned magnetic structures therefore make possible to achieve or exceed the highest reported magnetic forces in literature [20]. In particular, we use magnetic thin films having perpendicular magnetic anisotropy (PMA) as the large field gradient source. Aspect ratio is an important parameter to be considered for the required field generation. In a magnetic film,

the sources of the magnetic field are the edges of the magnetic domains. Hence, a mono-domain film with minimum edges would generate smaller field gradient compared to the large near surface field gradient generated by the multi-domain magnetic films (Fig. 3.1). Co/Pt multilayer stack is a well known and well studied heterostructure which exhibits PMA property under appropriate growth conditions [21–23]. Incorporation of Pt not only ensure the proper magnetic anisotropy but also protects the stack from oxidation. Magnetic layer thickness and number of repeats can be optimized to tune the magnetic domain size so that maximum field gradient can be obtained at the film surface (Fig. 3.2). Moreover, relative size and orientation of 'up' and 'down' domains can be manipulated using external magnetic field which helps to realise a magnetically controllable force field landscape.

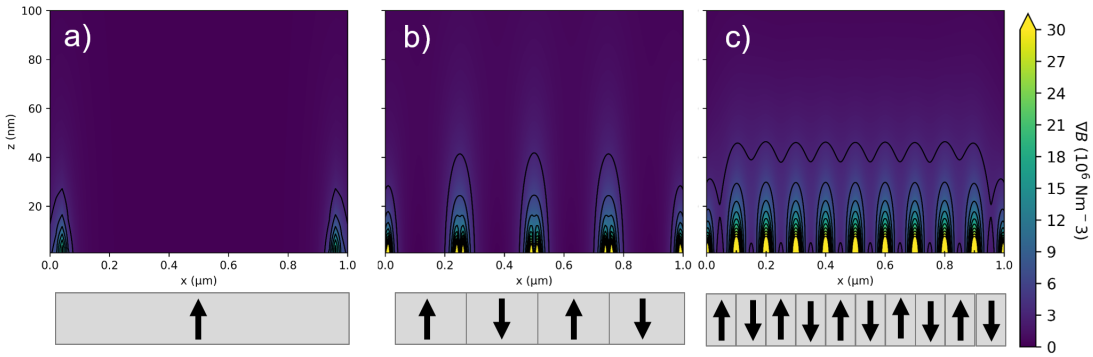

FIGURE 3.1: Contour plot of magnetic field gradient generated by magnetic films with different domain sizes a) mono-domain of width 1.0 μm b) four domains of width 0.25 μm and c) multi-domain of width 0.1 μm. Field values are estimated using 2D model (section 3.2.3). Parameters used are magnetization = 1.4 T, dead layer area = 10 %, magnetic layer thickness = 20.0 nm, orientation = out-of-plane.

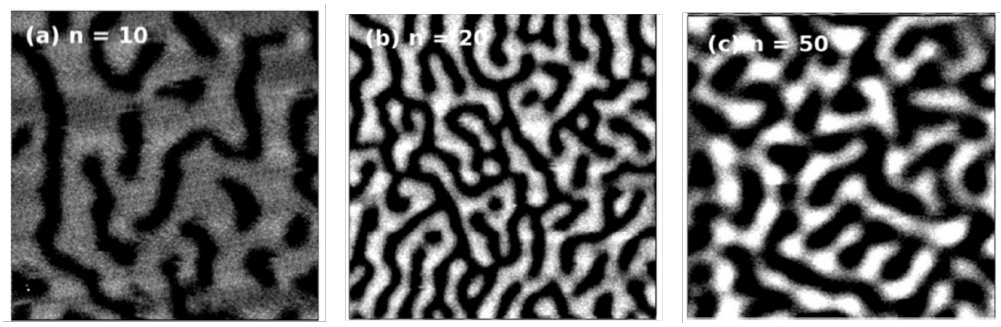

FIGURE 3.2: MFM images (2.5 μm × 2.5 μm) of $(Co_{90}Fe_{10}/Pt)_n$ multilayer stacks showing the variation of domain size with the number of repeats n [24].

The influence of a magnetic field on the diffusion layer is well documented whereas the field effects at the electrochemical double layer is rarely reported. All electrode reactions happen within a 10 nm thickness of interfacial region (Fig. 3.3) where the surface tension

and excess charge distribution becomes more relevant [19, 25]. Our motivation is to see how extreme magnetic forces imposed at this electrode/electrolyte interface can impact the electrochemical reaction (Fig. 3.3). Ferri/ferrocyanide redox couple is used as a chemical redox probe to investigate how chemical reactions can be impacted at these interfaces. The reasons for choosing this particular reaction will be discussed in a section below (section 3.3). Information about the field effects are extracted using various experimental methods like chronoamperometry, cyclic voltammetry and impedance spectroscopy.

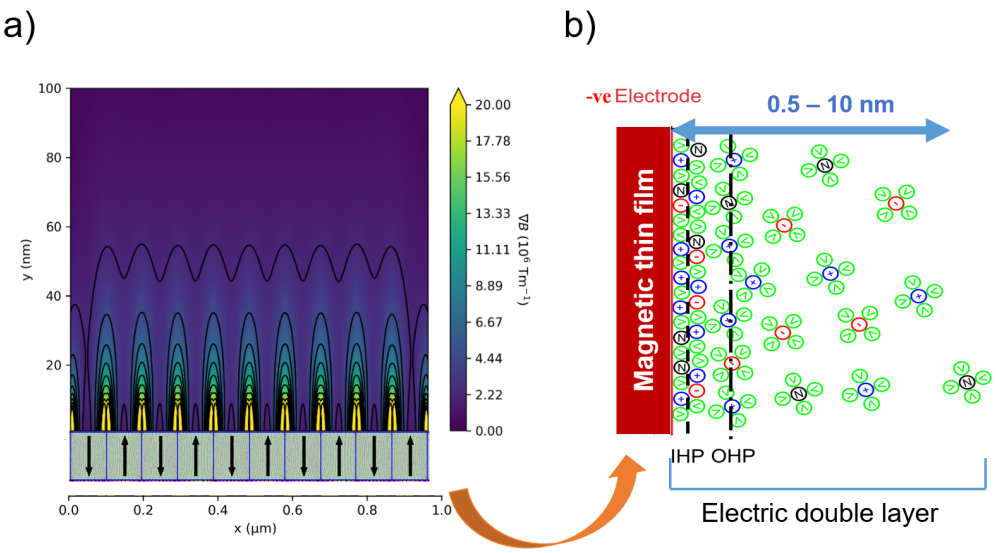

FIGURE 3.3: (a) Contour plot of field gradient above the multi-domain magnetic film with magnetic layer thickness of 20 nm and domain width 0.13 μm. Field gradient as high as $\sim 10^7$ T/m can be achieved in a region of < 10 nm near to surface. (b) schematic showing the concept of using multi-domain magnetic thin film as the source of large force field to study the influence of magnetic field at the electrode/electrolyte interface.

3.2 Fabrication and Characterization of large Field Gradient Source

Thin films are deposited using DCA magnetron sputtering. The quality of surface and interface plays a crucial role in determining the magnetic properties of thin films [26]. Hence, techniques based on atomic force microscopy (AFM) and grazing angle X-ray reflectivity (XRR) are utilised to check the surface and interface quality of films. Magnetic properties are characterized using superconducting quantum interference device (SQUID) magnetometry, magneto-optical Kerr effect (MOKE) based imaging technique and magnetic force microscopy (MFM). Magnetic field and the field gradient magnitudes near the film surface are also estimated.

3.2.1 Sample Fabrication

Multi-repeats of Co/Pt thin film samples were fabricated from TCD [1] and HZDR[2]. In TCD, high vacuum sputtering technique is used to deposit Ta, Pt and Co on thermally oxidised Si wafer at a rate of 0.012, 0.016 and 0.014 nm/s respectively. The structure of TCD thin film is:

- $Si/SiO_2//Ta(5.0)/Pt(2.0)/[Co(0.8)/Pt(0.8)]_N/Co(0.8)/Pt(2.8)$
- $Si/SiO_2//Ta(2.0)/Pt(20.0)$ (all thickness in nm)

where N = 9, 19 and 49. A Ta/Pt layer is used as a buffer layer to grow Co/Pt repeats, followed by a capping Pt layer to avoid oxidation. It has been reported that changing the thickness of individual Co layer will change the interfacial properties [27]. Thus, our approach has the advantage that we do not change the interface induced PMA of the system. On the other hand, N can be optimised to enhance the field gradient by adjusting the domain width and magnetic volume.

Similar Co/Pt multilayers were grown in HZDR, but with N fixed to an optimum value of 20, in order to study the influence of the Pt capping layer thickness on the electrochemical activity. Thermally oxidised Si wafer is used as substrate on which Ta, Pt and Co are deposited at a rate of 0.476, 0.116 and 0.075 nm/s respectively. It is worthwhile to note that HZDR deposition rates are higher than the TCD deposition rates. The HZDR film structure with t_{Pt} = 0.0, 3.0, 5.0 and 10.0 nm follows as:

- $Si/SiO_2//Ta(1.5)/Pt(5.0)/[Co(1.0)/Pt(1.0)]_{19}/Co(1.0)/Pt(t_{Pt})$
- $Si/SiO_2//Ti(2.0)/Pt(20.0)$ (all thickness in nm)

To characterize the surface and interfacial roughness, X-ray reflectivity (XRR) measurements were performed in TCD Co/Pt sample with $N = 20$ repeats (Fig. 3.4). We observed short wavelength oscillations in the low incident angle region and long wavelength oscillations at high angles. At low incident angles, the period of oscillation is inversely proportional to the number of Co/Pt repetitions N [21]. In wider angle range, the high wavelength oscillations corresponds to the Ta/Pt buffer whose layer thickness are comparatively larger than the individual Co and Pt layer in the superlattice. A slightly higher interface roughness is obtained from the XRR fit (3.4b). It is worthwhile to note that fitting of XRR data can be error-prone in our system due to the complexity of the multilayer stack. However, XRR

[1] Thanks to Prof. Michael Coey and Dr. Gwenael Atcheson
[2] Thanks to Prof. Olav Hellwig and Dr. Ruslan Salikhov

measurements provided an initial indication of multilayer growth in Co/Pt film and also approximates the surface and interface quality of the the film.

a)

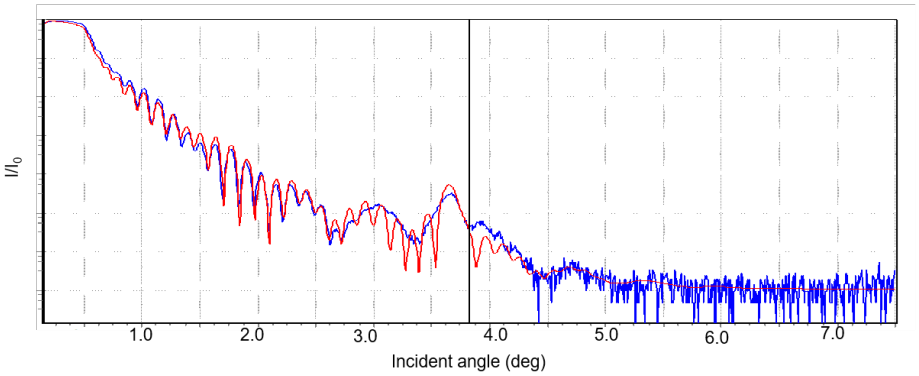

b)

Layer	Layer Description	Expected thickness (nm)	Fitted thickness (nm) ± 0.1	Roughness (nm)
4	Pt	2.0	1.5	0.54 ± 0.07
3	***Superlattice, Number of repeats= 20***			
3. 1	**Pt**	**0.8**	**0.8**	**0.32 ± 0.14**
3. 0	**Co**	**0.8**	**0.8**	**0.39 ± 0.13**
2	Pt	2.0	1.9	0.33 ± 0.06
1	Ta	5.0	5.1	0.25 ± 0.14
Substrate	SiO_2		xx	0.255 ± 0.05

FIGURE 3.4: (a) XRR of TCD Co/Pt thin film with N=20. Blue line represents the data and red line is the fitted curve. (b) relevant parameters obtained from the XRR fit.

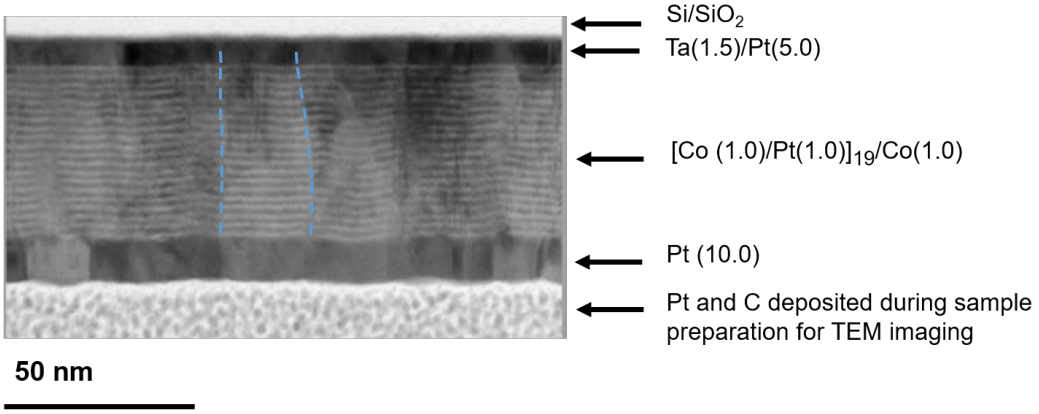

FIGURE 3.5: Cross sectional high resolution TEM image of the HZDR Co/Pt multilayer (N = 20) with 10.0 nm Pt cap layer thickness. The blue dashed lines indicate the columnar structure.

The thin film multilayer is also imaged using a high resolution transmission electron microscopy (TEM). Fig. 3.5 shows the cross-sectional bright field TEM image of the HZDR Co/Pt film having Pt cap layer thickness 10.0 nm[3]. The focused ion beam (FIB) technology is used to prepare the lamella for the TEM imaging. In bright field TEM mode, elements with

[3]Thanks to Dr. Corinne Bouillet for her help with TEM imaging of the multilayer sample

high atomic number (Z) appear darker (such as Ta and Pt) whereas lighter elements (such as Co) appear lighter. We can clearly see the stacking of both Co and Pt layers having 1.0 nm thickness each. Columnar grains, originating from the Ta/Pt seed layer and extending to the Co/Pt multilayers, are also visible from the images. One such pattern is highlighted in blue lines. These columnar grains promotes the interface roughness and its effect increases with the number of repeats. Similar observations of columnar grains have been reported in synthetic anitiferromagnetic (SAF) based multilayers [28] and Co/Pt multilayers [29].

3.2.2 Magnetic Thin Film Characterization

Both TCD and HZDR samples are characterized using SQUID magnetometry. Volume magnetization of sample is measured by applying field in-plane and perpendicular to the sample surface. Fig. 3.6 confirms the perpendicular magnetic anisotropy (PMA) in all thin films as perpendicular field easily saturates the film magnetization as compared to the parallel field. For example, N=10 TCD Co/Pt film saturates along surface normal under an out-of-plane field of < 0.15 T while the same film needs about 0.7 T to saturate when the field is applied in-plane. HZDR samples are also characterized using SQUID and the extracted parameters are listed in table 3.1. Magnetic dead layer thickness is quantified using the linearized M_s plot as shown in Fig. 3.7. The dead layer thickness is determined to be negligible from the x-intercept of the linear fit, while the slope corresponds to a saturation magnetization of 1.47 MA/m, larger than 1.44 MA/m expected for bulk Co. This suggests a partial magnetization of the neighbouring Pt layers is induced by the Co layers. Presence of PMA and absence of magnetic dead layer indicates a high quality Co/Pt interface in our Co/Pt repeats. Similar results on Co/Pt repeats has already been reported by other groups [24, 27].

Magnetic force microscopy (MFM) is used to image the magnetic domains of the thin films at remanent state. Fig. 3.8 shows the MFM images of multi-state maze like domain patterns of TCD samples with different number of repeats. The multi-domain formation and the change of domain width with the number of repeats can be well understood within the model of periodic stripe domains with uniaxial magnetic anisotropy developed by Kittel [30] [31] and further extended by Kooy and Enz [32]. According to this model, the total magnetic energy of film at remanent state can be expressed in terms of magnetostatic energy as well as domain wall energy. Upon increasing the number of repeats, the demagnetising energy increases. To reduce the total energy, the uniformly magnetized film breaks into multi-domain at the expense of introducing domain wall energy. In order to estimate the domain width, the contrast difference across stripes at different positions are fitted using

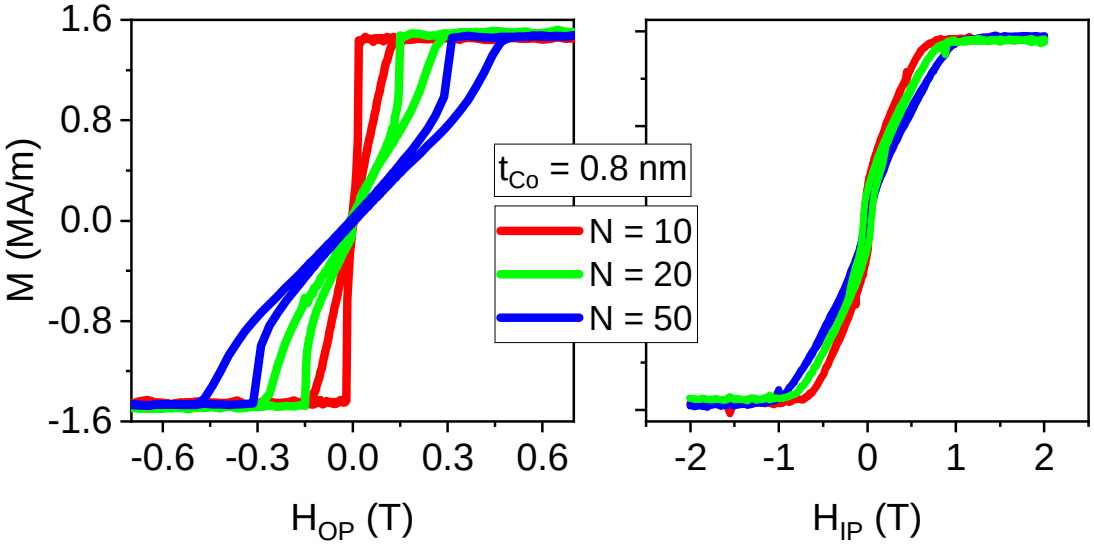

FIGURE 3.6: SQUID data of TCD samples with different number of Co/Pt repeats when field is applied (a) perpendicular and (b) in-plane to the sample surface

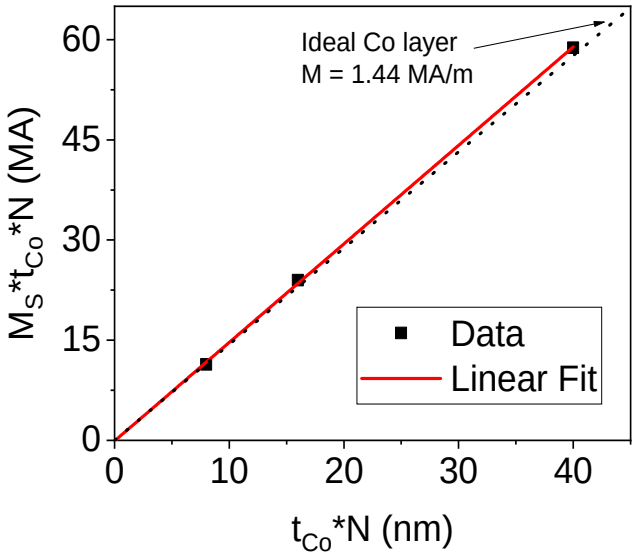

FIGURE 3.7: Saturation magnetization times the total Co thickness vs total Co thickness of TCD Co/Pt samples. Symbols corresponds to SQUID-VSM data and solid line is the linear fit.

a Gaussian function and the FWHM of the fit is taken as the average domain size. In our case, as can be seen in Fig. 3.8, a minimum of domain width of 130 $\pm$ 25 nm is observed when $N = 20$ (Table 3.1). Similar observation has been reported by Diao and Coey *et al.* for $Co_{90}Fe_{10}$/Pt based multilayer stacks [24].

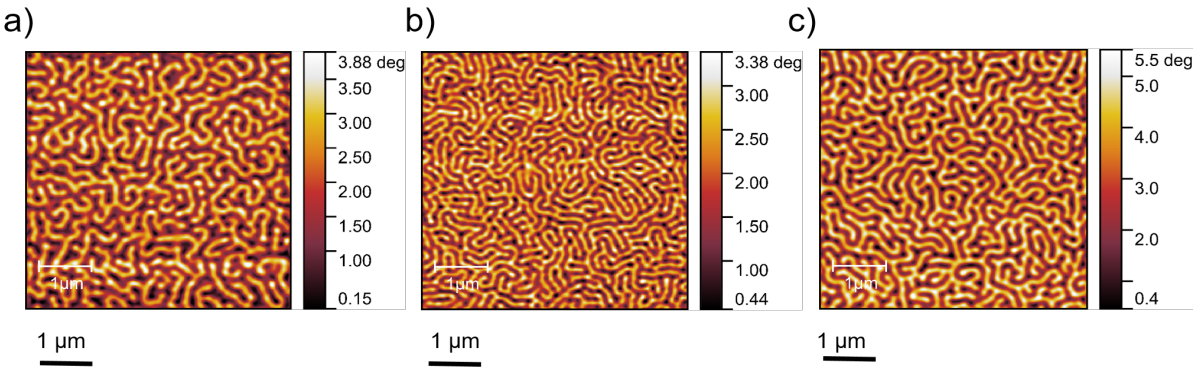

FIGURE 3.8: MFM images (5.0 μm $\times$ 5.0 μm) of TCD samples at tip lift height 50 nm with (a) N=10, (b) N=20 and (c) N=50 Co/Pt repeats at the remanent state.

Table 3.1 summarises the relevant parameters of the TCD and HZDR Co/Pt thin films. Anisotropy field, H_K, is defined as the field required to saturate the sample along its hard axis. As all the mentioned Co/Pt samples have PMA, the H_K can be considered as the in-plane field required to saturate the magnetization parallel to the film surface. The effective anisotropy can be found using the relation,

$$K_{eff} = \frac{M_s H_k}{2} \tag{3.1}$$

In terms of shape anisotropy K_v and surface anisotropy K_s,

$$K_{eff} = K_v + \frac{2K_s}{t} \tag{3.2}$$

Using Kittel's magnetic domain model, the Bloch wall width can be estimated using the relation $\lambda_w = \pi\sqrt{A/K_u}$ (section 1.3.3) where A is the exchange stiffness taken to be of the order of 10 pJ/m [33] and K_u is related to surface anisotropy as $K_u = K_s/t_{Co}$. Thus the domain wall thickness is found to be about 5 – 10 % of the domain width, depending on the number of Co/Pt repeats N. These values will be relevant in the estimation of field and field gradient, which will be discussed detail in the next section (section 3.2.3)

To further understand the evolution of magnetic domains with the applied out-of-plane field, magnetoptical Kerr microscope is used (thanks to Dr. Salia Cherifi-Hertel). Hysteresis loops are acquired using Kerr imaging (Fig. 3.9a) and corresponding magnetic states under

N	Total t_{Co} nm	M_s $\pm$ 0.03 MA/m	H_K $\pm$ 0.03 T	K_{eff} kJm^{-3}	λ_w nm	D nm
10*	8.0	1.53	0.7	535 ± 14	12.5	250 ± 40
20*	16.0	1.52	0.79	600 ± 17	12.1	130 ± 25
50*	32.0	1.54	0.97	746 ± 23	11.5	200 ± 25
20†	40.0	1.5	0.9	675 ± 19	11.8	150 ± 30

TABLE 3.1: *TCD Co/Pt samples, †HZDR Co/Pt sample with 3 nm Pt cap layer. Relevant parameters are saturation magnetization, M_s, anisotropy field, H_K, effective anisotropy, K_{eff}, Bloch domain wall width, λ_w, are calculated based on SQUID data, and domain width, D, estimated from MFM images.

different magnetic field are imaged (Fig. 3.9b). The dark and bright contrast represents the domains magnetised in opposite directions. Under -450 mT, the film's magnetization is saturated along the field direction (state 1). When the field is reduced to -137 mT (state 2), isolated nucleation of a few domains with opposite polarity can be observed. These domains are initially observed as bubble like which further becomes small stripes when the field is reduced. SQUID or MOKE-obtained hysteresis loop are not sensitive to this small domain formation as the macroscopic magnetization change due to these domains is negligible. With further decrease of reversal field to -127 mT (state 3), a sudden expansion originating from the nucleation points results in the formation of labyrinth stripe domains. A further decrease in the field causes reversed domain expansion (state 4) and the magnetic configuration of film reaches a minimum domain size near to 0 mT (state 5) where up and down domains have almost equal width and the net magnetic contrast difference will be zero. With further increase in field to +196 mT (state 6), the reversed domains expands. Near to the out-of-plane saturation field of +250 mT, a few stripes of reversed domains are still visible suggesting that the macroscopic saturation state is not equal to the real magnetic state of the film. At +292 mT, number of reversed domain stripe reduces and true saturation is achieved at +322 mT. These observations are similar to the well documented Co/Pt switching pathway that has been reported by several researchers [23, 32, 34, 35].

3.2.3 Magnetic Field Calculation

Estimation of magnetic field and field gradient as a function of distance from the film surface is key for understanding the field effects on the electrochemical reaction. To calculate the magnetic field, thin films are considered as 2D sheets magnetised along z (Fig. 3.10). Considering a single magnetic domain, it can be assumed as an infinitely long rectangular

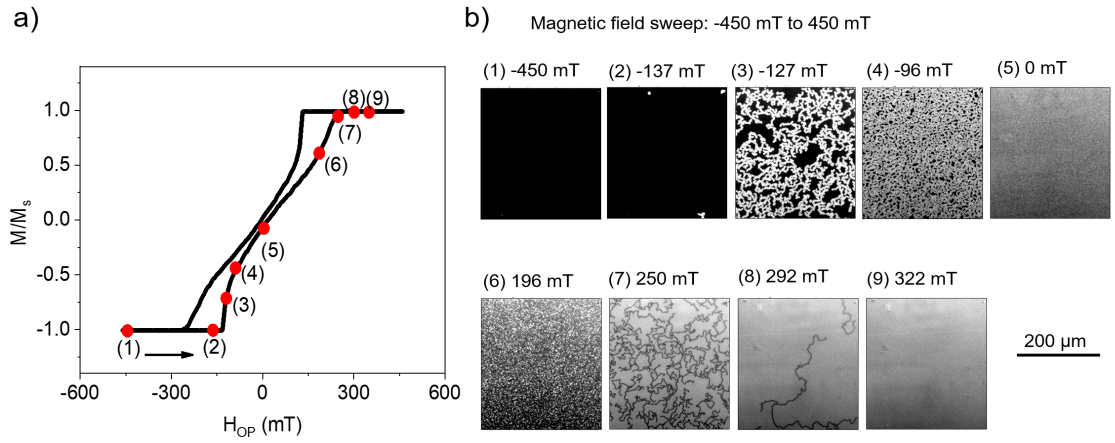

FIGURE 3.9: (a) Kerr hysteresis loop of TCD N=20 Co/Pt repeat thin film under out-of-plane applied field and (b) Kerr images of the similar sample under similar field conditions marked in (a).

magnet as the domain width ($\sim 0.1\ \mu$m) is comparatively smaller than its length ($\sim 0.5 - 1\ \mu$m) as shown in Fig. 3.10. Using the Amperian current model, the field components can be

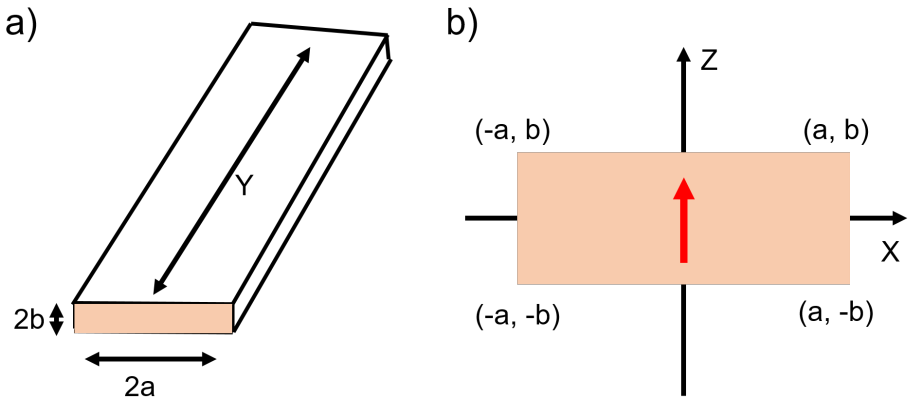

FIGURE 3.10: (a) Rectangular magnet and (b) cross-sectional view with reference frame

estimated using the equations [36]:

$$B = B_x\hat{x} + B_z\hat{z} \tag{3.3}$$

$$B_x = \frac{\mu_0 M_r}{4\pi}\left[\ln\left(\frac{(x+a)^2+(z-b)^2}{(x+a)^2+(z+b)^2}\right) - \ln\left(\frac{(x-a)^2+(z-b)^2}{(x-a)^2+(z+b)^2}\right)\right] \tag{3.4}$$

$$B_z = \frac{\mu_0 M_r}{2\pi}\left[\tan^{-1}\left(\frac{2b(x+a)}{z^2-b^2+(x+a)^2}\right) - \tan^{-1}\left(\frac{2b(x-a)}{z^2-b^2+(x-a)^2}\right)\right] \tag{3.5}$$

where $2a$ is the width of domain and 2b is the thickness of magnetic layer.

Fig. 3.11 illustrates the average field and the average field gradient variation near the perpendicular magnetic anisotropy thin film surface obtained using the parameters M_s = 1.44 T, domain size = 0.12 μm, t_{Co} = 20.0 nm and magnetic dead layer = 16 %. The python code for the calculation is available in ref [37]. It is worthwhile to note that the field gradient values can have local maxima and minima compared to the plotted average values. When the perpendicular magnetised film is in mono-domain state, the field outside the film is zero as the demagnetising field is maximum. On the other hand, in multi-domain state, a large field gradient of the order of 10^7 T/m can be achieved near the film surface. At the film surface, field gradient is maximum near to the domain wall where the magnetization changes its direction from up to down or vice versa. It is worthwhile to note that this field calculation is based on assumptions such as (1) domain wall region with tilted magnetization is considered to be a magnetically dead region, (2) equal width for domains which in real case consists of the distribution of widths, and (3) perfect interface and flat surface.

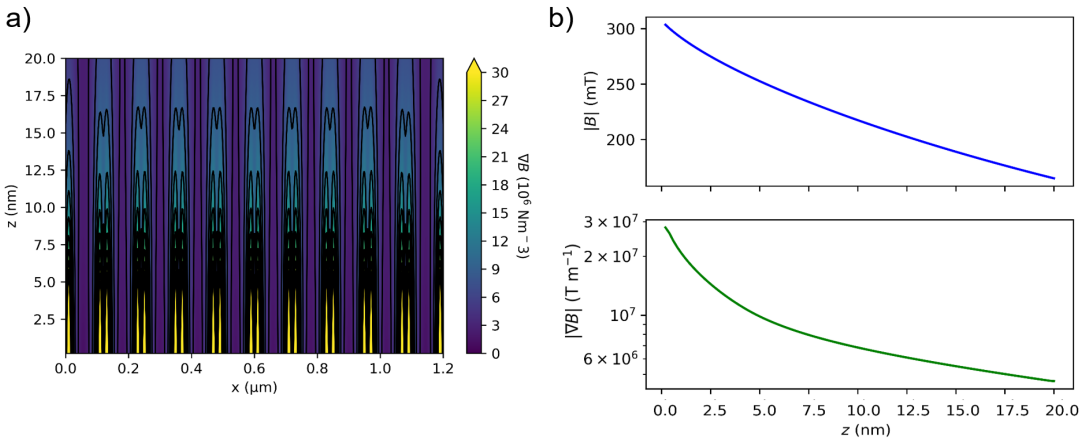

FIGURE 3.11: Example of (a) magnetic field gradient contour plot and (b) line plot of the average field and the average field gradient magnitude as a function of distance from film surface. Relevant parameters: magnet thickness = 20.0 nm, domain size = 0.13 μm, magnetization = 1.44 T, dead layer = 16 %

3.3 Standard Ferri-ferrocyanide Redox System

In order to study the large field gradient effects in the electrochemical reaction, the one-electron transfer outer sphere ferri/ferrocyanide redox couple [38, 39] is chosen as model system. It is commonly used as a standard redox probe [40, 41] due to its electrochemical reversibility [42], well-known structure [43], and electrochemical stability [44, 45]. In

this redox reaction, both species are soluble in water and remain as solvated ions, minimizing the changes to the electrode surface during electrochemical measurements, unlike electrodeposition or corrosion. The reactions redox potential ensures that gas generation due to water splitting (hydrogen or oxygen evolution) is negligible during electrochemical measurements, thus suppressing micro-convective effects due to bubble formation [7, 16]. The reaction follows:

$$[Fe(CN)_6]^{4-} \rightleftharpoons [Fe(CN)_6]^{3-} + e^- \tag{3.6}$$

where the ferrocyanide anion, $[Fe(CN)_6]^{4-}$, is reversibly reduced to form the ferricyanide anion, $[Fe(CN)_6]^{3-}$. Ferrocyanide is diamagnetic species having low spin ferrous (Fe^{2+}) ion while ferricyanide is paramagnetic ion with iron in high spin ferric (Fe^{3+}) state. Both the oxidized and reduced forms of the complex are well soluble in water based solvents. Compared to main group cyanides like potassium cyanide (KCN), ferricyanides are much less toxic because of the strong bond between the cyanide ion (CN^-) and the Fe^{3+} ion [46]. Table 3.2 lists the magnetic susceptibility (χ_{mol}) of the relevant ions.

Compound	χ_{mol} 10^{-9} m^3/mol	Magnetism
Potassium ferricyanide	+28.8	paramagnetic
Potassium ferrocyanide	-2.2	diamagnetic

TABLE 3.2: Magnetic properties of ferri-ferrocyanides

3.3.1 Experimental setup

A three electrode system is used in the entire experiments to characterize the electrochemical redox reaction. The electrochemical cell is specially designed and 3D printed using a Formlabs Form 3 (design shown in Fig. 3.12). Either Pt or Co/Pt films are used as working electrode (WE), Pt mesh as counter electrode (CE), and Ag/AgCl electrode in 3 M KCl as reference electrode (RE). The standard potential of this RE is 0.197 V versus the normal hydrogen electrode (NHE). The WE area is typically 1 – 10 mm^2 in a cell having 5 mL volume. The WE area is defined using electroinactive epoxy used to mask the sides of the thin film sample to avoid any oxidation and magnetic fringe field effects. The geometric area is determined from the analysis of microscopy images in ImageJ [47].

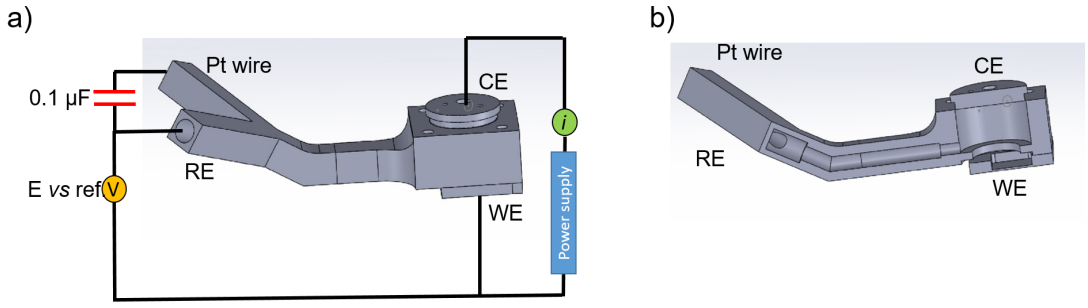

FIGURE 3.12: (a) Schematic diagram of the electrochemical cell setup. (b) Cross-section view of the cell

The electrolyte consists of 0.2 M potassium ferricyanide ($K_3[Fe(CN)_6]$, 98+ % purity) as electroactive species and 1 M potassium chloride (KCl, 99 % purity) as supporting electrolyte, and is freshly prepared each day of measurements. For all experiments, we used the same high concentration of supporting electrolyte as the measured kinetic rates are sensitive to the supporting electrolyte concentration [48–50], to increase the conductivity, and to reduce the migration effects. All chemicals are used as delivered without any further processing.

Natural convective effects can arise due to the electrochemically generated density differences [51] and thermal gradients. Reduction of $[Fe(CN)_6]^{3-}$ results in a solution near the electrode with a higher density due to increase in the concentration of charge-balancing K^+ cations [52]. This means the diffusion layer has a higher density compared to the bulk solution. Without proper positioning of WE, the convective flow can be significant at macroelectrodes and can affect the stability of long timescale measurements. These effects can also be enhanced or depressed in the presence of nonhomogenous magnetic field [53]. In our system, in order to minimize the convective effect during ferricyanide reduction [52], WE is positioned at the bottom of the cell so that a stable condition can be achieved for the measurements.

3.3.2 Electrochemical system

In order to understand the diffusion and double layer properties, it is important to characterize the redox reaction under no magnetic field conditions using non-magnetic working electrode. This section discusses the ferri/ferrocyanide redox reaction near Pt film electrodes and the reaction characterisation using sweep, pulse and AC techniques. All experiments in this section are performed at room temperature (confirmed by thermocouple) and under zero applied magnetic field. Measurements are performed using a Metrohm Autolab

potentiostat PGSTAT 302.

3.3.2.1 Cyclic Voltammograms

Prior the redox system characterization, it is important to clean the WE surface to avoid any possible surface related effects. It is known that the gold electrodes are not the best choice to study the ferri/ferrocyanide redox couple due to the possible adsorption and corrosion on the electrode surface [54]. Hence, we used Pt thin films as the WE to characterize the redox system. The kinetics of $[Fe(CN)_6]^{3-}/[Fe(CN)_6]^{4-}$ electrode process is known to be highly dependent on the cleanliness of electrode [48]. In the current set of experiments, the redox peaks in cyclic voltammogram are found absent when an uncleaned film is used as working electrode (Fig. 3.14a). Thus, the pre-treatment of thin film WE plays a critical role in the reproducibility and the kinetics of the reaction under study. Various cleaning procedures have been reported in the literature to improve the electrode activity [55]. We followed the procedure discussed in [48]. The procedure starts with sonication of thin film in acetone for 2 min followed by a rinse using ethanol and isopropanol. For the electrochemical cleaning, the electrode is kept in a solution of 0.1 M KCl solution and the potential is swept between -1.0 V and +1.3 V at scan rate 100 mV/s until a steady state response is observed (Fig. 3.13). Peaks corresponding to the formation and oxidation of both adsorbed hydrogen and adsorbed oxygen can be observed in the current-potential curve [56]. The potential range is chosen such that Pt surface undergo both oxidation and reduction which is known to improve the reaction rate and surface cleanliness [48].

After the pretreatment, the ferri/ferrocyanide redox reaction is characterized using cyclic voltammetry. The potential is swept between 0.0 V and 0.6 V (Fig. 3.14b), chosen based on the pretreatment i-V curve (Fig. 3.13) where no active species are present. The solution resistance, R_s, is found to be 21.5 Ω using both positive feedback method and electrochemical impedance spectroscopy. iR compensation is applied prior to the measurements. Open circuit potential, OCP, of the system is measured as 0.41 V. When the potential is swept from 0.6 V to 0.0 V, reduction of ferricyanide occurs while oxidation of the reduced species occurs in the reverse sweep. According to the Randles-Sevcik equation for a reversible system of the type $O + ne^- \rightarrow R$ as discussed in section 2.1.1 , the peak current at room temperature is

$$i_{p,c} = -2.69 \times 10^5 n^{3/2} A D_0^{1/2} [O]_\infty v^{1/2} \tag{3.7}$$

where v is the scan rate in V/s, A is electrode area in cm^2, D is analyte diffusion coefficient

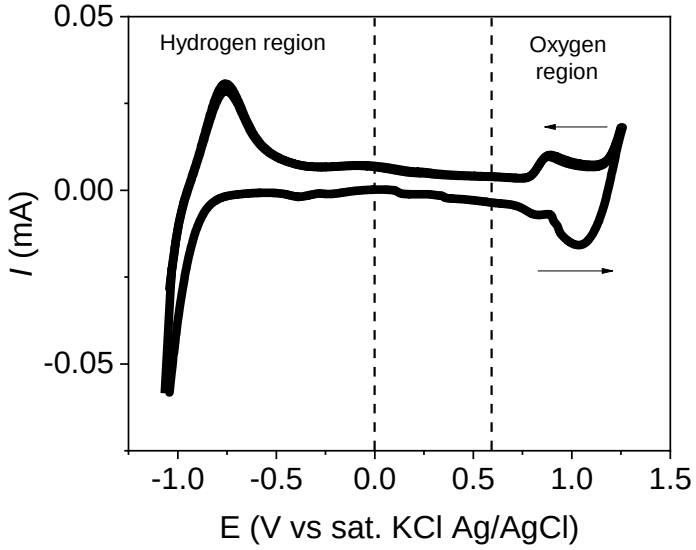

FIGURE 3.13: Cyclic voltammogram of Pt thin film electrode in 0.1 M KCl solution: potential scan rate = 0.1 V/s; temperature 298 K

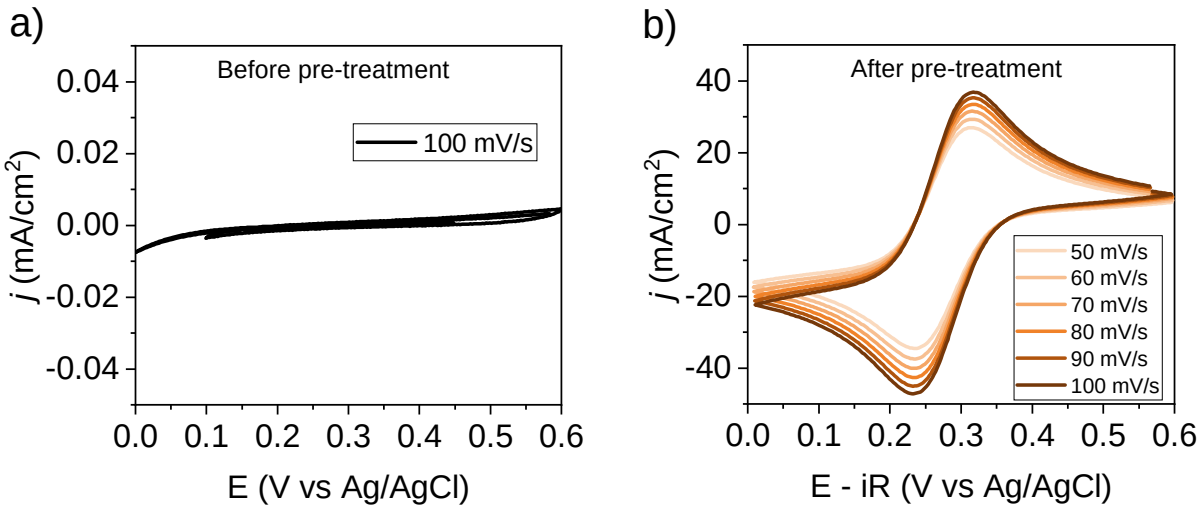

FIGURE 3.14: Cyclic voltammogram of Pt thin film electrode in solution containing 0.2 M $K_3[Fe(CN)_6]$ and 1 M KCl (a) before pre-treatment and (b) after pre-treatment of electrode.

in cm^2/s, $[O]_\infty$ is the bulk analyte concentration in mol/cm^3, and n is number of electrons transferred in the redox reaction.
The other characteristics of a reversible reaction includes:

1. $i_p \propto v^{1/2}$
2. redox peak potential independent of scan rate, $E_p \neq E_p(v)$
3. $|E_p - E_{p/2}| = 56.6/n$ mV
4. $|E_{p,a} - E_{p,c}| = 57.0/n$ mV (Vs Ag/AgCl)

In the case of a quasi-reversible system, the individual peaks will be widely separated. Irreversible systems are characterized by a shift in the peak potential with the scan rate and the characteristics follows:

1. $i_p \propto v^{1/2}$
2. $|E_p - E_{p/2}| = 47.7/(\alpha n^{'})$ mV
3. redox peak potential dependent of scan rate,$E_p = E_p(v)$

and the peak current is now given by

$$i_{p,c} = -2.99 \times 10^5 n(\alpha n^{'})^{1/2} A D^{1/2} [O]_\infty v^{1/2} \tag{3.8}$$

As can be seen in Fig. 3.15a, $|i_{p,a}/i_{p,b}| \neq 1$ can be due to quasi-reversibility, loss of reactant to adsorption, or follow up chemical steps. Furthermore, the peak separation ΔE_p increases from 77 mV at scan rate 50 mV/s to 88 mV at 100 mV/s. A higher ΔE_p value compared to the 57 mV separation for a reversible reaction might be related to the slow kinetics [57], electrode surface purity [58], or the influence of the supporting electrolyte concentration [49, 50] in the ferri/ferrocyanide system. The dependence of ΔE_p on the scan rate v further indicates the quasi-reversibility of the system. In order to find the diffusion coefficient, i_p is plotted against $v^{1/2}$ and is fitted assuming a linear relation (Eqn. 3.8). The diffusion coefficient of the ferricyanide reduction reaction is found to be 6.4×10^{-6} cm^2/s and that of ferrocyanide oxidation is 5.9×10^{-6} cm^2/s. As the diffusion coefficient indicates the amount of diffused particles per unit time, the observed difference is ascribed to the lower density of ferricyanide compared to that of the ferrocyanide [52]. The obtained values are comparable to the literature values $5 - 7.2 \times 10^{-6}$ cm^2/s for ferricyanide and $4.5 - 6.4 \times 10^{-6}$ cm^2/s for ferrocyanide [59, 60].

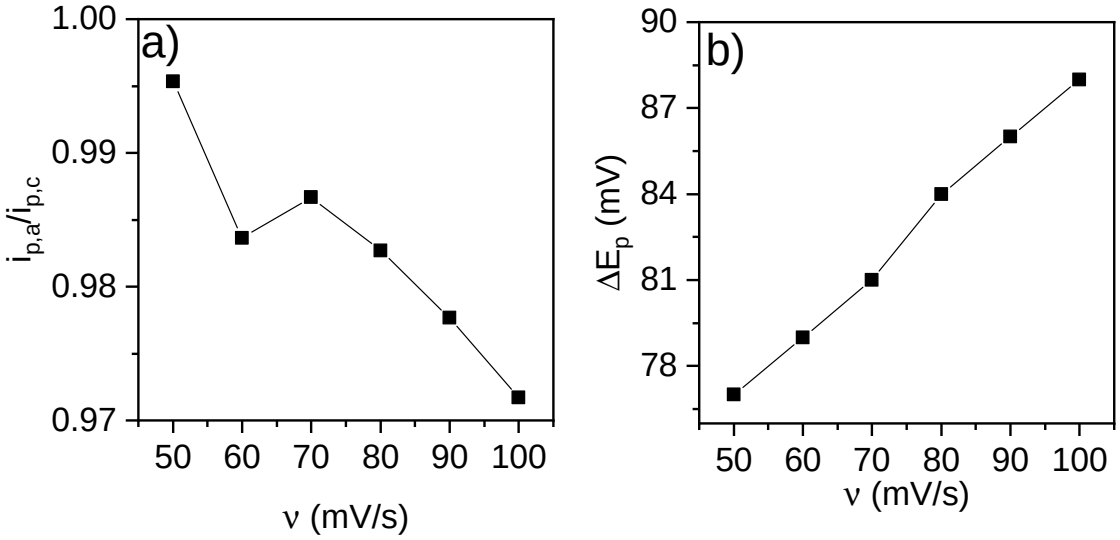

FIGURE 3.15: a) The ratio of anodic to cathodic peak current $i_{p,a}/i_{p,c}$ and b) peak potential separation ΔE_p versus scan rate v

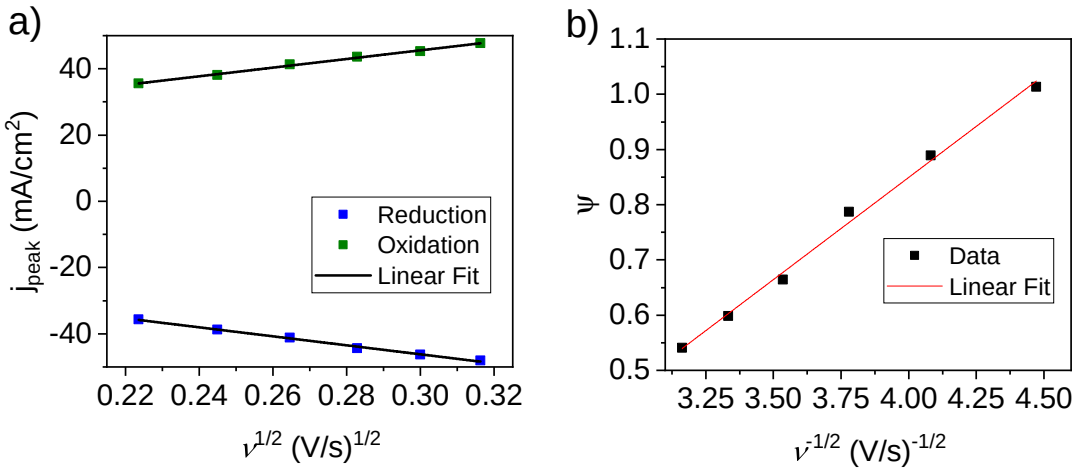

FIGURE 3.16: (a)CV peak current as a function of square root of scan rate for diffusion coefficient calculation, and (b) dimensionless parameter ψ obtained from Eqn. 3.9 as a function of inverse square root of scan rate for kinetic rate constant calculation.

The heterogeneous standard kinetic rate constant for a quasi-reversible system can also be extracted from the CV curves [57], using the empirical equation

$$\psi = (-0.6288 + 0.0021X)/(1 - 0.017X) \tag{3.9}$$

where $X = \Delta E_p \times n$, the rate constant k^0 can be obtained using the Nicholson approach [57] where ψ is given by

$$\psi = k^0[\pi DnFv/RT]^{-1/2} \tag{3.10}$$

To estimate the standard rate constant, ψ is calculated using Eqn. 3.9 and is plotted against $v^{-1/2}$ (Fig. 3.16b). Fitting the plot with a linear function and using Eqn. 3.10, k_0 is obtained as 0.013 cm/s. This result is within the wide range of k_0 values 0.01 – 0.4 cm/s reported for ferri/ferrocyanide systems [58, 61, 62].

3.3.2.2 Chrono-amperometry

Chronoamperometry can be used to measure the diffusion coefficient of the reaction. Recalling the Cottrell equation for reactions limited by mass transfer, the decay of current after the application of a potential step is

$$i = \frac{nFAD_0^{1/2}c_0}{\pi^{1/2}t^{1/2}} \tag{3.11}$$

In order to perform the measurement, a step voltage of 0.15 V is applied from the OCP 0.41 V. At this potential, the reaction will be in the diffusion limited as evidenced from the CV measurements (Fig. 3.14b). The resulting current is plotted against $t^{-1/2}$ as shown in Fig. 3.17. Fitting the curve using the linear equation, the diffusion coefficient for ferricyanide reduction, D_R, is found to be 6.2×10^{-6} cm^2/s. The obtained D_R is in good agreement with the value found using CV measurements and the literature [59] [60].

3.3.2.3 Electrochemical Impedance Spectroscopy

Impedance spectroscopy is further used to quantify the diffusion and kinetic properties of the ferri-/ferro-cyanide redox system. Measurements are performed under potentiostatic control in frequency range 100 kHz to 10 Hz. A Pt wire is coupled to the reference electrode through a 0.1 μF capacitor (Fig. 3.12a) to avoid the high frequency artifacts of reference electrode [63, 64]. Fig. 3.18b shows the Nyquist plot for the reduction of ferricyanide at the

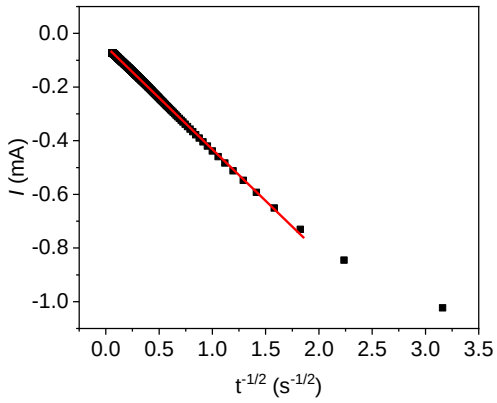

FIGURE 3.17: Chronoamperometry of Pt thin film electrode in electrolyte with 0.2 M $K_3[Fe(CN)_6]$ and 1 M KCl when a step potential from OCP 0.41 V to 0.15 V is applied.

potential of 0.25 V indicated by the red line in CV curve Fig. 3.18a. As expected for a standard redox reaction, the Nyquist plot consists of a semi-circle in the high frequency region and a slanted straight line in the low frequency region. Impedance data is fitted with a Randles circuit of a charge transfer resistance (R_{ct}) in series with a semi-infinite Warburg diffusion resistance (Z_w), both in parallel with the double layer capacitance expressed as a constant phase element (CPE), and all in series with the solution resistance which includes uncompensated as well as cable resistances (Fig. 3.18b inset). Fitted parameters are tabulated in Table 3.3. Prior to Randles fit, all impedance spectra are checked for linearity using the Kramers-Kronig transformations.

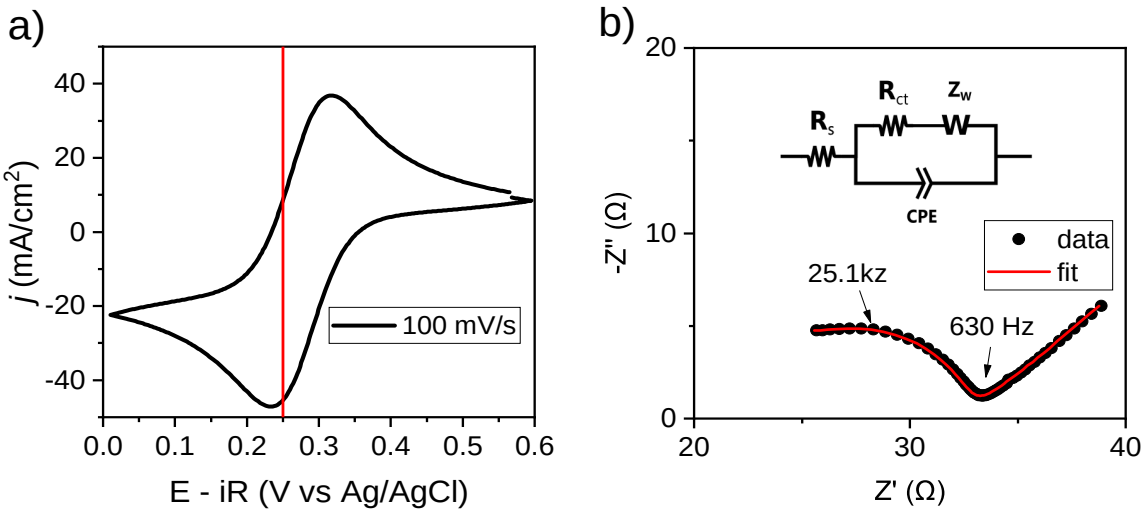

FIGURE 3.18: (a) cyclic voltammogram of Pt thin film electrode in electrolyte consists of 0.2 M $K_3[Fe(CN)_6]$ and 1 M KCl and (b) impedance spectrum at potential 0.25 V shown in (a)

In order to characterize the bulk and double layer properties of the redox system, impedance

R_s Ω	R_{ct} Ω	C_{dl} μF	Z_W $\Omega/s^{1/2}$
21.5	11.7	0.54	48.1

TABLE 3.3: Randles circuit fitted parameters of impedance spectra at potential 0.25 V

spectra are recorded at different dc bias voltage (Fig. 3.19a). At 0.41 V (OCP) there is no significant reduction of ferricyanide, and the majority of the impedance is dominated by diffusion, shown by a near 45° slope, with a small high frequency semi-circle related to the charge transfer kinetics and double layer capacitance. As the DC bias voltage is reduced, the semi-circle gradually dominates the impedance response, as expected when driven to reduction conditions. Assuming a reversible reaction that can be described by Nernst equation, the Warburg coefficient W can be written as [65]

$$W(E) = \frac{RT}{n^2F^2\sqrt{2}}\left[\frac{1}{\sqrt{D_o}C_0} + \frac{1}{\sqrt{D_R}C_R}\right] \tag{3.12}$$

which is related to Warburg impedance as $Z_w = 1/(W\omega^{1/2}) - j/(W\omega^{1/2})$ and C_0, C_R are the oxidised and reduced species surface concentration, respectively. Assuming that only the oxidized form is initially present in the solution, the Nernst equation modifies the expression for W as,

$$W(E) = \frac{RT}{n^2F^2c_0\sqrt{2D_o}}\frac{\left[1+\exp\left[nf(E-E_{1/2})\right]\right]^2}{\exp\left[nf(E-E_{1/2})\right]} \tag{3.13}$$

where $f = F/RT$. The Warburg coefficient has a maximum (Warburg impedance has a minimum) at $E_{1/2}$. The diffusion coefficient can be extracted from this relation by fitting W for various dc bias potential. Likewise, the kinetic rate constant can be obtained from the potential dependent R_{ct} values obtained by fitting the EIS spectra at various voltage and using the equation [65],

$$R_{ct} = \frac{RT}{n^2F^2k_0c_0}\frac{1+\exp\left[nf(E-E_{1/2})\right]}{\varsigma^{\gamma}\exp\left[(1-\gamma)nf(E-E_{1/2})\right]} \tag{3.14}$$

where $\varsigma = D_O/D_R = 1.08$ (from CV). Furthermore, the effective double layer capacitance (C_{eff}) at each voltage can be estimated from constant phase element (CPE) using the following relation [66],

$$C_{eff} = P^{1/N}\left[\frac{1}{R_s} + \frac{1}{R_{ct}}\right]^{(N-1)/N} \tag{3.15}$$

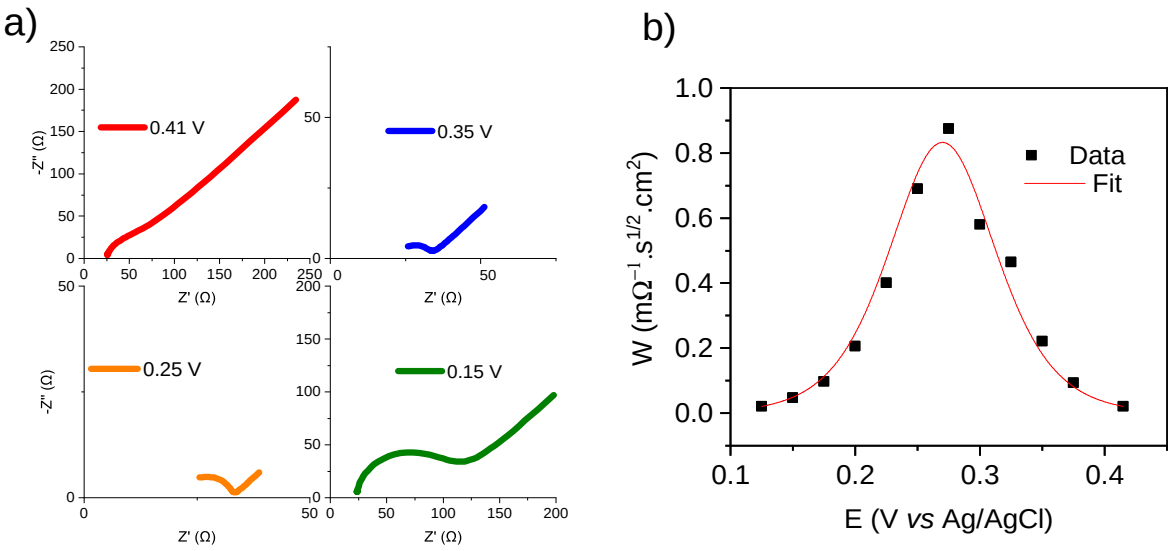

FIGURE 3.19: (a) Impedance spectra at different dc bias voltage of a Pt thin film electrode in 0.2 M $K_3[Fe(CN)_6]$ and 1 M KCl solution and (b) Warburg element extracted from the Randles circuit fit as a function of dc bias voltage.

where P is related to CPE impedance as $Z(f) = 1/[P(j2\pi f)^{\alpha}]$ where f and α are frequency and distribution factors respectively (section 2.1.3.1).

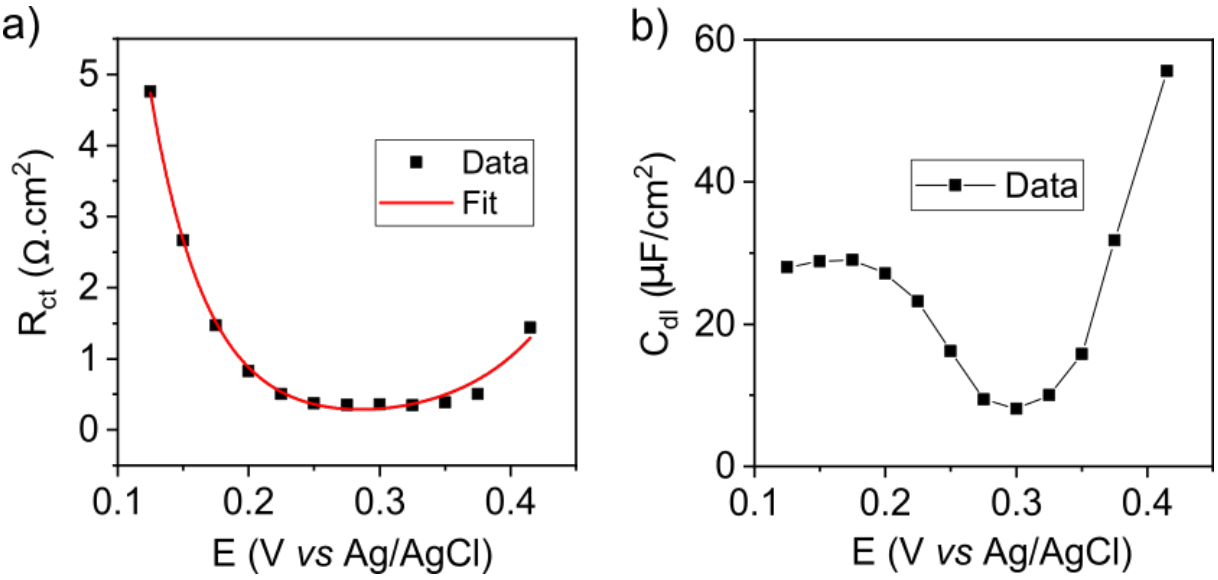

FIGURE 3.20: (a) Charge transfer resistance obtained from Randles circuit fit as a function of dc bias voltage and (b) double layer capacitance estimated using Eqn. 3.15 as a function of DC bias voltage.

Area normalised Warburg element obtained from the impedance fit is plotted against potential (Fig. 3.19b) and is fitted using the Eqn. 3.13. The diffusion coefficient, D, is obtained as $6.08 \pm 0.02 \times 10^{-6}$ cm^2/s which is in good agreement with that of the value calculated using cyclic voltammetry and chronoamperometry. The double layer capacitance is found using the Eqn. 3.15 and its variation with dc bias voltage is shown in Fig. 3.20b. Similar

behaviour of the double layer capacitance has been reported in other model systems like nitrobenzene [19]. The behaviour of capacitance-potential curve can be explained using the Gouy-Chapman-Stern (GCS) model (section 1.1.3.1). According to this model, the V-shape region corresponds to the diffusive double layer capacitance having a minimum near the point of zero charge (PZC), while the voltage independent capacitance at voltage $< 0.175V$ represents the Helmholtz layer.

R_{ct} *vs* potential is fitted using Eqn. 3.14 and the resulting standard kinetic rate constant is found to be $0.88 \pm 0.02 \times 10^{-2}$ cm/s. The k_0 estimated using EIS is 32 % lower than that of the one obtained using cyclic voltammograms. The reason for this difference might be manifold. Even though ferri/ferrocyanide is considered as a model system, many reports suggest that the reaction mechanism is not as simple as expected. Several studies reported the presence of specifically adsorbed intermediates [67], and decomposition of reactants which leads to the formation of Prussian Blue coverage [68]. As the EIS requires a longer time frame compared to the voltammetry, the adsorption and passivation effects can be enhanced in EIS compared to CV measurements. However, multiple EIS measured for 1 hr in an interval of 10 minutes found that spectra is almost stable and reproducible. This suggests that the aforementioned effects might be mostly affecting the electrode surface only in the initial few minutes of measurement.

Technique	10^3 k_0 $\pm$ 0.2 cm/s	10^6 D_R $\pm$ 0.1 cm^2/s
CV	13.0	6.4
CA	–	6.2
EIS	8.8	6.1

TABLE 3.4: Comparison of kinetic rate and diffusion coefficient obtained using different measurement techniques.

3.4 Capping Layer Thickness Dependence on the Electrochemical Activity of Co/Pt Films

Studies of the effects the of the Pt cap layer thickness on the electrochemical activity of Co/Pt thin films allows us to decouple the surface related– and field gradient related– effects. Surface sensitive measurements like X-ray spectroscopy (XPS) and atomic force microscopy (AFM) are incorporated in this discussion in order to explain the electrochemical observations.

In order to investigate the surface purity and reactivity of the films, cyclic voltammograms (CV) at various scan rates are obtained for Co/Pt films with different Pt capping layer thickness. Primarily, Pt and Co/Pt films sputter deposited from HZDR are used for this investigation. All the measurements are performed under an applied out-of-plane field of 400 mT so that the Co/Pt films will be in the saturated state at which the field and field gradient effects will be minimum near the electrode surface. Micro-MHD [25, 69] and edge effects [70] driven stirring can influence the diffusion coefficient values under a surface normal field. But, we will see in section 3.5 that the convective effects are minimum under the field parallel to current configuration. Thus, measurement under 400 mT perpendicular field allows us to compare the reaction rate of monodomain Co/Pt films with that of the Pt films.

From the CV curves (Fig. 3.21), it is found that the peak separation of the Co/Pt CV curves depends on the outer Pt capping layer thickness. At a scan rate 50 mV/s, Co/Pt films with a top Co layer exposed to the solution has a maximum ΔE_p of 137 mV while a 5 nm Pt cap reduced it to 77 mV, comparable to the 75 mV of bulk Pt films (Fig. 3.22a). For a Co/Pt film with outer Pt layer thickness of 3 nm, an intermediate ΔE_p value of 98 mV is observed. Similar behaviour in ΔE_p can be observed irrespective of the scan rate. As discussed in Section 3.3.2.1, ΔE_p is related to the standard kinetic rate constant (Eqn. 3.10). ψ values corresponding to ΔE_p are calculated using Eqn. 3.9 and plotted in Fig. 3.22b. The slope of the curve is proportional to the kinetic rate, with a larger slope for Pt films implying a higher rate constant. Table 3.5 summarises the diffusion and kinetic parameters obtained from CV measurements for all the films under investigation. After testing on many Pt and Co/Pt films, it is found that a minimum of 5 nm Pt cap layer thickness is required for the kinetic rate of the Co/Pt film to be comparable to that of Pt films. The measurement is reproducible, with similar results seen in TCD films. For example, k_0 of TCD Co/Pt films with 2.8 nm outer Pt cap is about 60 % smaller than that of the Pt films. The observed k_0 dependence on the Pt cap layer, being quite reproducible, suggests that it might be related to the surface purity of the films. Furthermore, these results are particularly interesting because a Pt cap layer of 2 – 3 nm is commonly used as a protective layer to avoid oxidation in heterostructure films used for spintronics applications [21–24, 71].

In order to investigate the electrochemically observed Pt cap layer dependence on the kinetics of Co/Pt films, the sample surface is imaged by atomic force microscopy (Fig. 3.23) at room temperature and pressure. Roughness is estimated as the peak position corresponding to the maximum of the Gaussian height distribution. Surface roughness R_A of HZDR

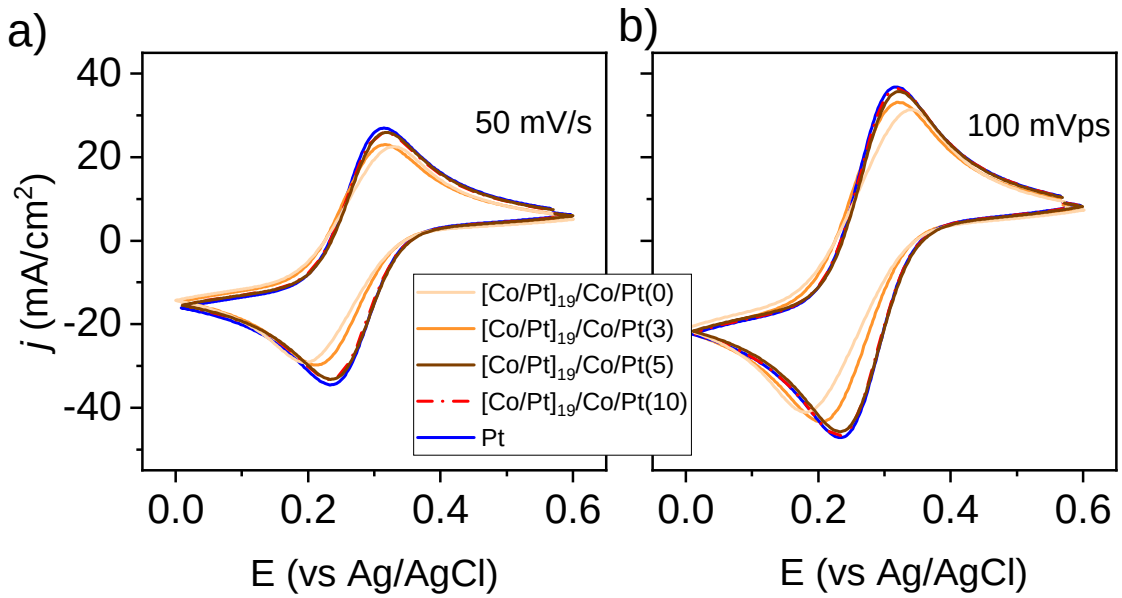

FIGURE 3.21: CV curves of HZDR Co/Pt samples with different Pt cap layer thickness and Pt film at scan rate (a) 50 mV/s and (b) 100 mV/s in solution of 0.2 M potassium ferricyanide and 1 M KCl.

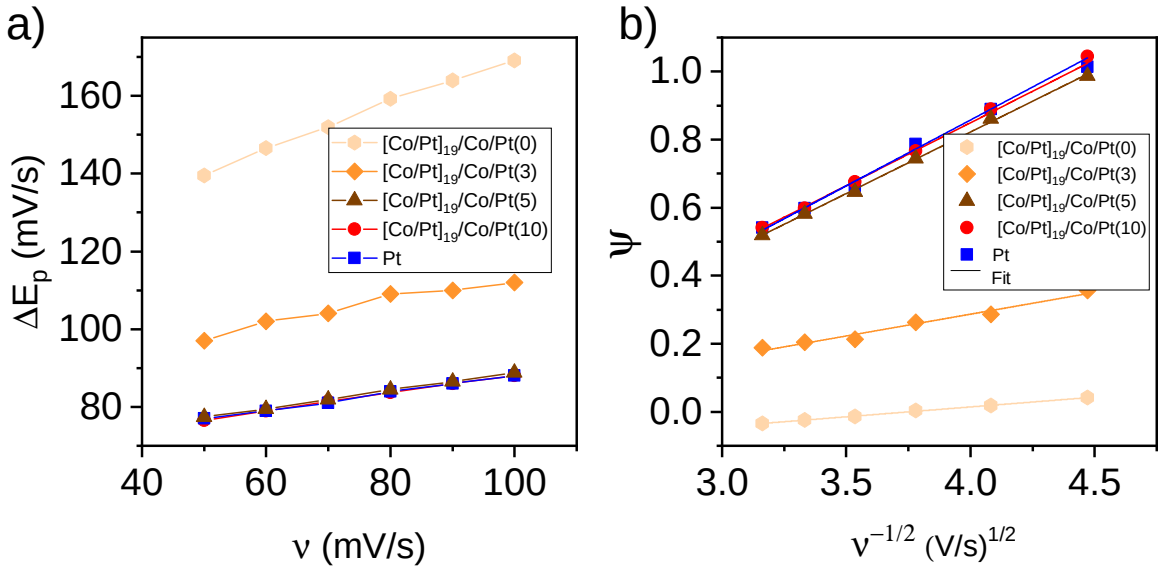

FIGURE 3.22: (a) Peak separation as a function of scan rate and (b) ψ evaluated using Eqn. 3.9 as a function of inverse square root of scan rate for HZDR Pt film and Co/Pt films with different Pt cap layer thickness.

Sample	10^3 k_0 $\pm$ 0.2 cm/s	10^6 D_R $\pm$ 0.1 cm^2/s	10^6 D_O $\pm$ 0.1 (cm^2/s)	SR nm
HZDR samples				
$[Co/Pt]_{19}/Co/Pt(0.0)$	1.1	5.2	4.7	2.7 ± 0.4
$[Co/Pt]_{19}/Co/Pt(3.0)$	3.1	5.8	5.2	2.2 ± 0.3
$[Co/Pt]_{19}/Co/Pt(5.0)$	9.7	6.0	5.5	2.1 ± 0.3
$[Co/Pt]_{19}/Co/Pt(10.0)$	10.0	6.1	5.6	2.1 ± 0.3
Pt	13.0	6.4	5.9	2.2 ± 0.2
TCD samples				
$[Co/Pt]_{19}/Co/Pt(2.8)$	4.5	5.4	5.1	1.4 ± 0.3
Pt film	11.2	5.8	5.4	1.3 ± 0.2

TABLE 3.5: Electrochemical and surface characterization summary of different working electrodes. Pt cap layer thickness in nms.Kinetic rate, k_0, reduction and oxidation diffusion coefficient, D_R and D_O are obtained from CV measurements under an applied out-of-plane magnetic field of 400 mT, and surface roughness, SR is calculated from AFM imaging.

samples is found to be larger than the TCD samples. This is possibly due to the higher sputter deposition rate of the HZDR samples (see Section 3.2.1). The surface roughness of TCD samples is estimated to be lower than 1.5 nm and that of the HZDR samples below 2.5 nm, with the exception of Co exposed Co/Pt sample (Table 3.5).

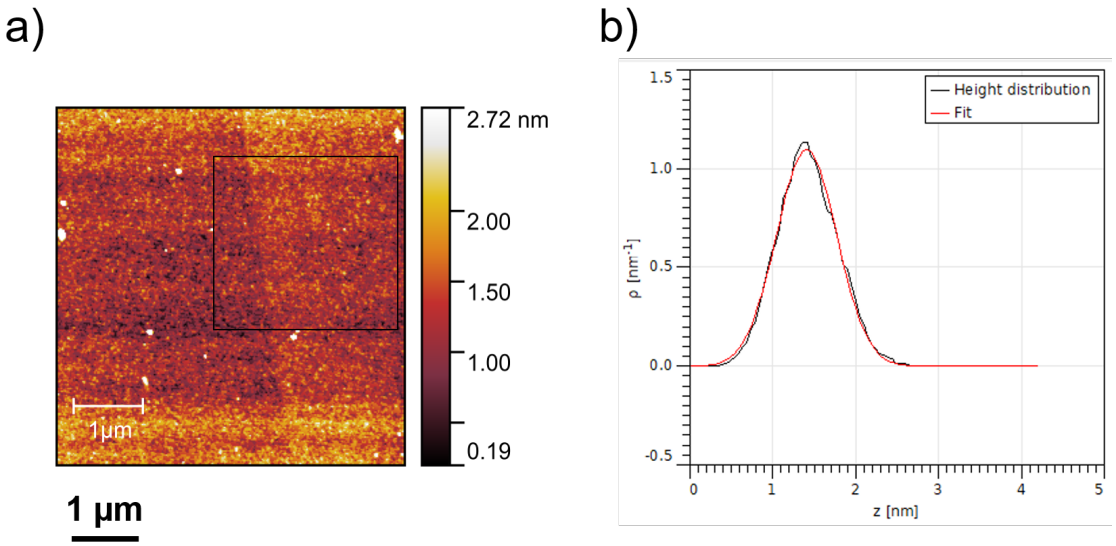

FIGURE 3.23: (a) AFM image of TCD Co/Pt film with 2 nm cap layer, and (b) height distribution and Gaussian fit corresponding to the area enclosed in box as shown in (a)

Angle-resolved X-ray photoelectron spectroscopy (ARXPS) is used to further characterize the chemical properties of the sample surface (Fig. 3.24). The inelastic mean free path of Pt 4f and Co 2p photoelectrons is about 1.5 and 1.2 nm respectively [72] with an expected information depth of 4 nm at the normal emission [18]. Photoemission spectra of Pt 4f and

Co 2p levels are recorded to study the oxidation states at the film surface. In TCD Pt films, the existence of pure Pt at 70.8 ± 0.2eV, Pt^{2+} at 72.9 ± 0.2eV and Pt^{4+} at 74.1 ± 0.2eV is confirmed. For the case of TCD Co/Pt film with an outer 2.8 nm Pt layer, XPS of $2p_{3/2}$ core level reveals the presence of cobalt oxide at the surface. The peak corresponding to metallic Co measured at 777.9 ± 0.2eV, Co^{3+} or Co^{2+} components measured at 780.7± 0.2 eV and the satellite peak of Co^{3+} at 785.0± 0.2eV. At normal emission, the spectra can contain the signal from the buried Co layer, but, the angle resolved measurements confirms the presence of oxides and metallic forms of Co at the sample surface. The inconsistency in the peaks as the angle increases highlights the non-uniformity of both Pt and Co oxides layers [73]. The source of Co or Co oxide in a 2.8 nm Pt capped Co/Pt film might be related to the columnar structure of the multilayer films (section 3.2.1). The columnar structure enhances the roughness and the partial surface coverage at the grain boundary can leave some parts of top Co layer unprotected.

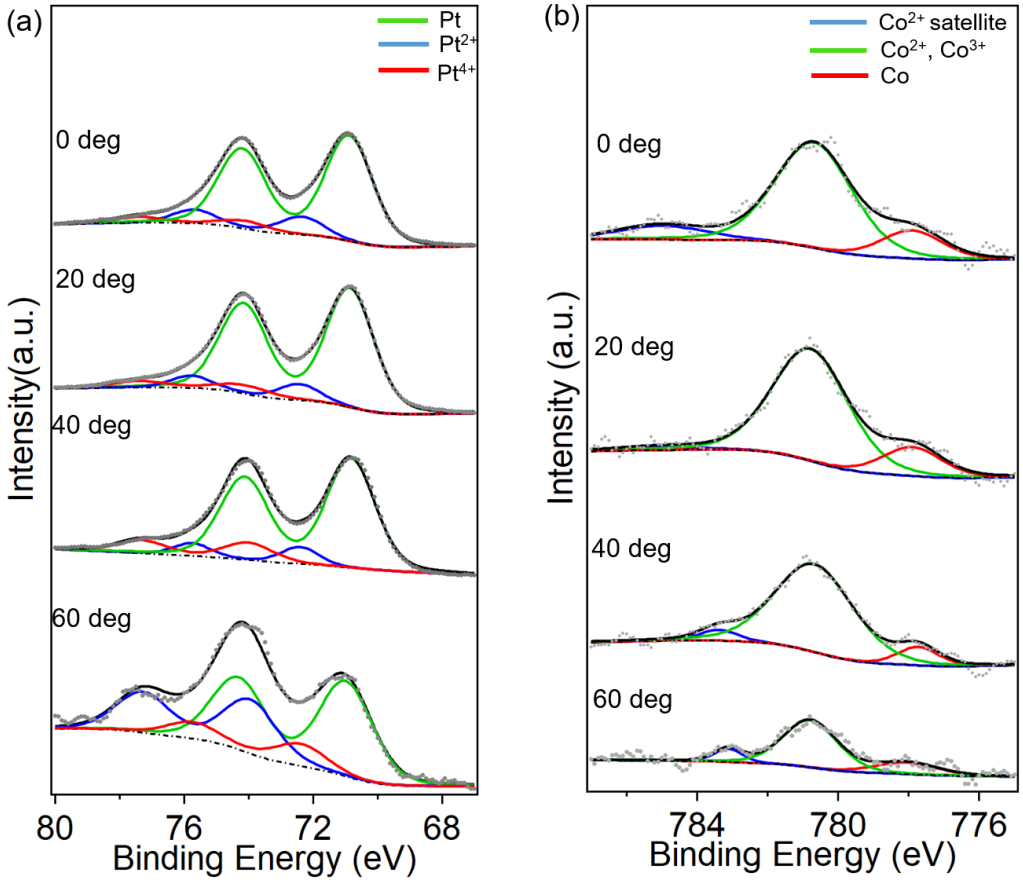

FIGURE 3.24: Angle resolved X-ray photoemission spectra corresponding to (a) Pt $4f_{7/2}$ core level of TCD Pt film and (b) Co $2p_{3/2}$ core level of TCD Co/Pt film. Black line represents the final fit and the coloured lines are the expected spectra for different oxidation states mentioned.

To summarize the capping layer study, it is found electrochemically that the reactivity of Co/Pt electrodes depends on the thickness of outer Pt cap layer. As per the CV measurements, a minimum of 5 nm Pt cap layer is required for Co/Pt multilayer film to be as reactive as Pt films. Surface analysis using AFM technique measure a surface roughness about 1.5 nm for TCD samples and 2.5 nm for HZDR films. To obtain the chemical composition of the film surface, XPS technique is explored. Angle resolved XPS confirm the presence of metallic and oxidised forms of Co at the Co/Pt film surface having 2.8 nm Pt cap layer. Thus, it is shown that electrochemical methods can be used as an alternative for other surface purity analysis. Unlike ARXPS which demands special sample preparation steps, high precision hardwares and high vacuum conditions, the electrochemical technique can be performed at room temperature and pressure, and requires no patterning or special sample preparation.

3.5 Convection Effects - Lorentz Force and Mechanical Stirring

It is known that the Lorentz force influences the mass transport of the system through forced convection near the electrode surface [74–76]. We show in the following section how in-plane field induces MHD stirring equivalent to mechanical stirring by means of cyclic voltammetry and impedance spectroscopy.

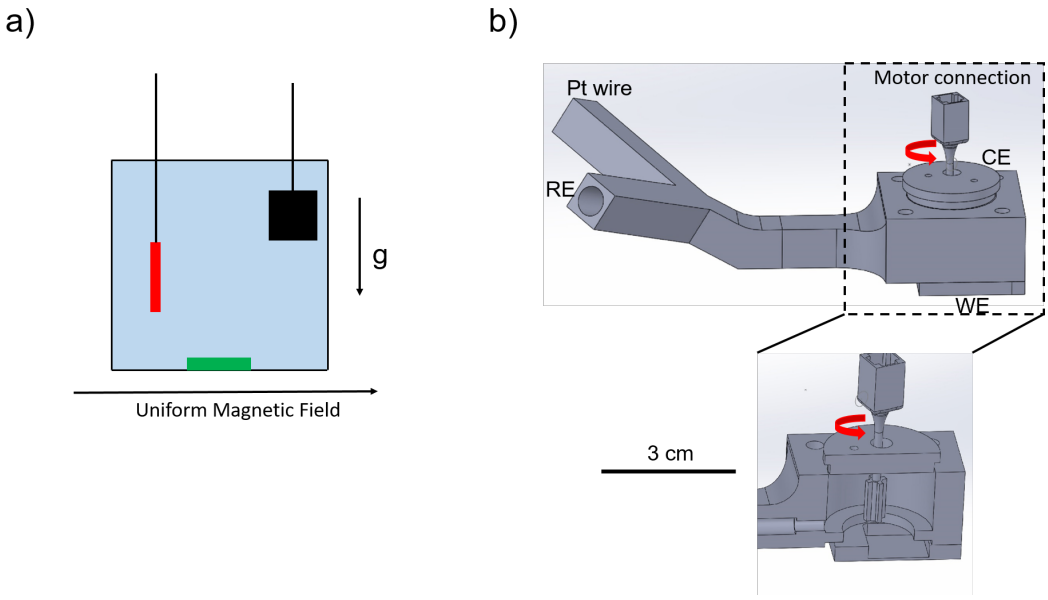

FIGURE 3.25: (a) Schematic of electrode under in-plane magnetic field and (b) electrochemical cell arrangement used for mechanical stirring study.

3.5.1 Lorentz Force

Fig. 3.26 shows how a magnetic field impacts the cyclic voltammetry on Pt and Co/Pt film electrodes for two orientations, (a) the field applied in the plane of the film (IP) or perpendicular to the current, and (b) the field applied out of plane of the film (OP) or parallel to the current as the direction of current is defined normal to the electrode surface. Considering OP alignment (Fig. 3.26a and b), it is observed that convective effects are minimized in this configuration. This would imply that micro-MHD (section 1.2) and edge effects driven convective effects are minimum in the system. For TCD Co/Pt films, a small change in reduction current can be observed with the perpendicular field which might be due to the field gradient effects (detailed discussion in section 3.6). However, no appreciable shift in peak current or peak separation is observed in the OP field geometry.

To probe the Lorentz force induced effects, a uniform magnetic field is applied parallel to the electrode surface. Fig. 3.25a schematically represents the measurement setup. Fig. 3.26c and d shows the MHD effect of both Pt and Co/Pt under IP magnetic field. During the reduction of ferricyanide, Lorentz force effects are negligible in a potential range 0.6 V to 0.25 V which corresponds to the kinetics limited region. As expected, the diffusion limited region is influenced by the in-plane magnetic field. We can also observe from cyclic voltammograms that the Lorentz force effects are asymmetrical on the two reaction peaks which can be explained by the difference in absolute current density values. As the electrolyte consists of ferricyanide solution, the current density is higher in the reduction region (left) compared to the oxidation region (right) resulting the difference in the Lorentz force magnitude. Natural convection also plays a role in the field induced effects based on the density of the species involved [77]. Similar in-plane field behaviour is observed for both Pt and Co/Pt film electrodes and therefore indicates the magnetic domains configuration of the Co/Pt samples does not play a significant role in this field configuration.

Cyclic voltammogram gives qualitative description about the mass transport response to the magnetic field. In order to better understand the Lorentz force effects on the diffusion layer, impedance spectroscopy is further used. A DC bias voltage of 0.15 V is chosen from the CV curves where the reaction is expected to be mass transport limited. Fig. 3.27a shows the evolution of the impedance spectra with the in-plane magnetic field. Spectra are then fitted with a Randles circuit as discussed in Section 3.3.2.3 and the relevant parameters are estimated as a function of field (Fig. 3.27 b,c,d). We found that the Warburg element, related to the diffusion layer, is very sensitive to the field with a power law dependence of $B^{1/3}$, as predicted by Aogaki [78] for the Lorentz force induced magneto-convection. The change

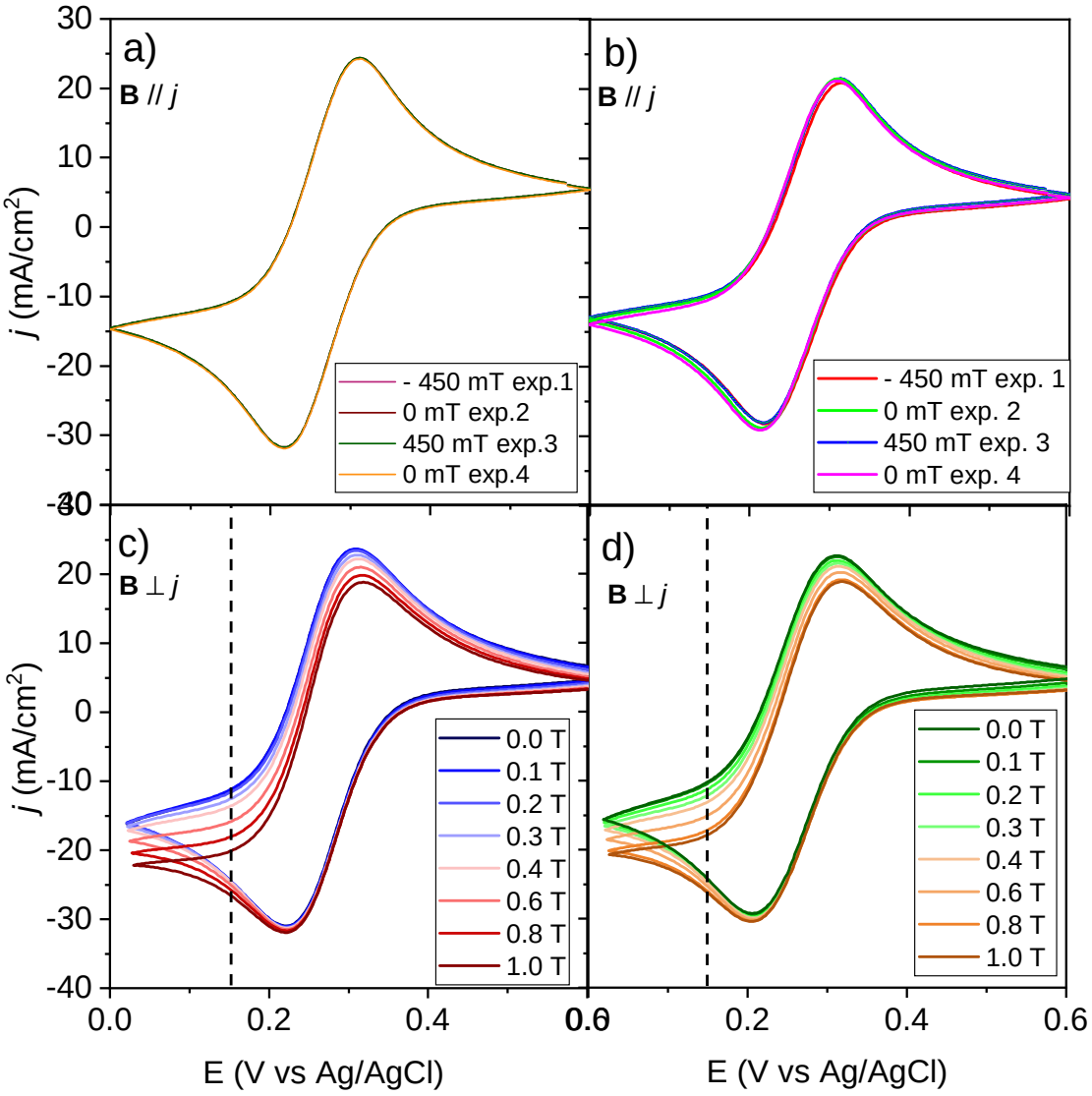

FIGURE 3.26: Cyclic voltammograms of (a) TCD Pt and (b) TCD Co/Pt with 2.8 nm cap layer under different out-of-plane magnetic field. Similar set of c) Pt and d) Co/Pt film under different in-plane magnetic fields. Scan rate of all CV is 50 mV/s.

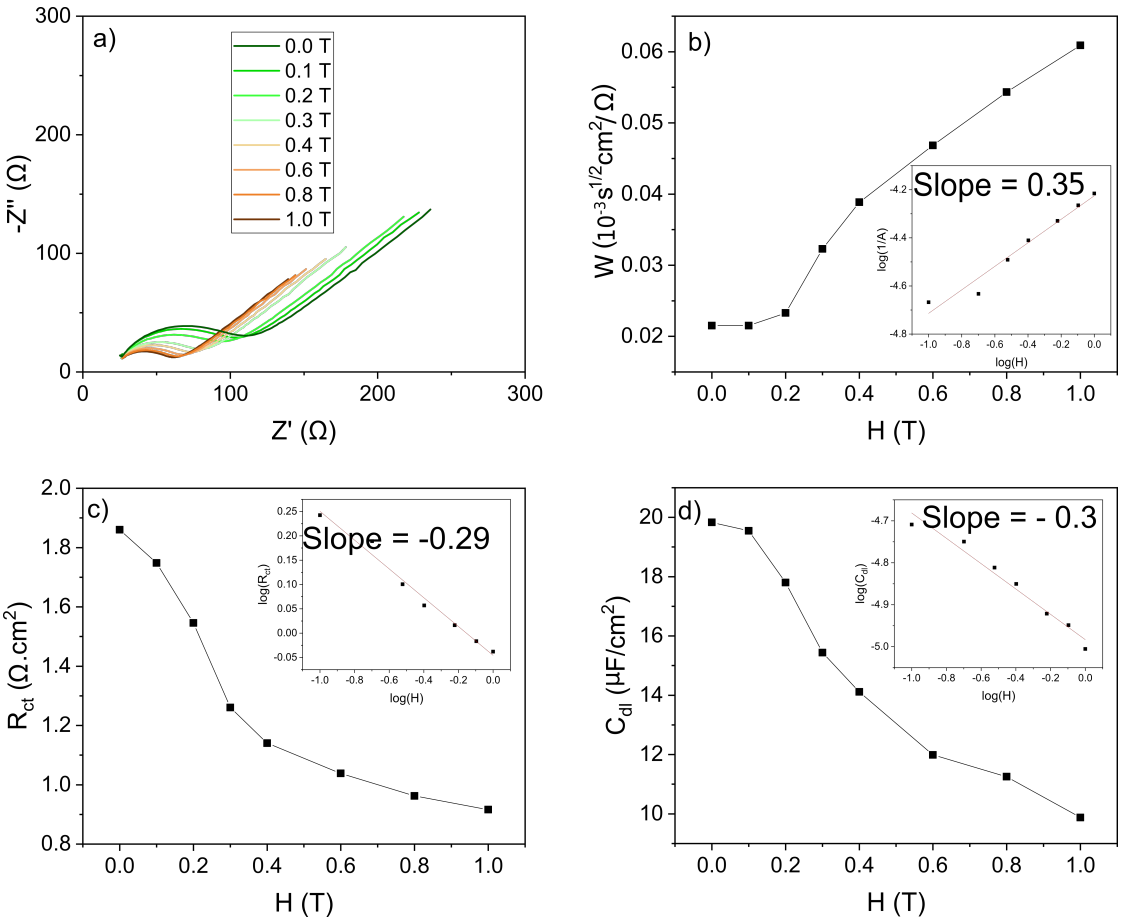

FIGURE 3.27: (a) Evolution of impedance spectra of TCD Co/Pt (2.8 nm Pt cap layer) with in-plane magnetic field at bias voltage 0.15 V. Randles circuit fit parameters (b) inverse of Warburg element, (c) charge transfer resistance and (c) effective capacitance as a function of in-plane field.

of R_{ct} and C_{dl} with the in-plane field suggests that both interfacial and diffusion regions are sensitive to the bulk convection. To confirm that the observed effects originate from the convective effects induced by the Lorentz force, the system is further studied under forced convection induced by mechanical stirring.

3.5.2 Mechanical Stirring

In order to characterize the effect of mechanical stirring, the solution is agitated using the motor as shown in Fig. 3.25b. This setup is different from the rotating disk electrode (RDE) where the working electrode itself act as a pump for flowing.

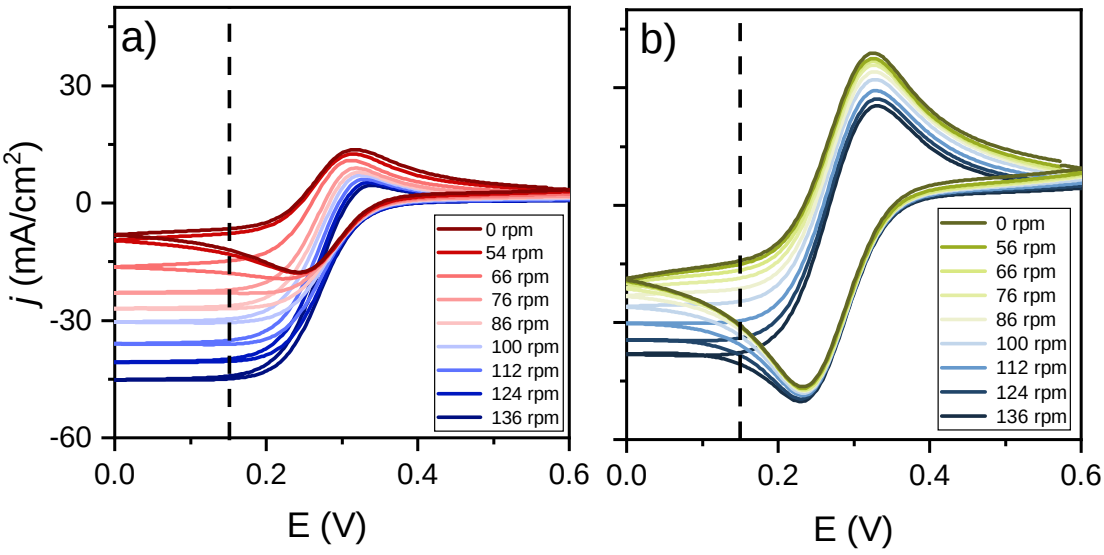

FIGURE 3.28: Cyclic voltammograms of Pt film under mechanical stirring when the voltage sweep rate is a) 10 mV/s and b) 100 mV/s

We expect that mixing the bulk solution sheds some light into the bulk convective effects of the system. Fig. 3.28 shows the response of cyclic voltammograms to the mechanical stirring. CV recorded at slower scan rate is comparatively more sensitive to stirring than the one with higher scan rate. This can be explained by the dependence of diffusion layer thickness on the scan rate. During a slow potential scan rate, the diffusion layer grows thicker as compared to a fast scan rate. Based on our earlier discussion (section 1.2), it is known that the concentration gradient inside the diffusion layer can be influenced by convective effects. Hence, a thicker diffusion layer developed at slower scan rate condition

will be more influenced by the forced convective effects due to stirring, as compared to a thin diffusion layer at larger scan rates.

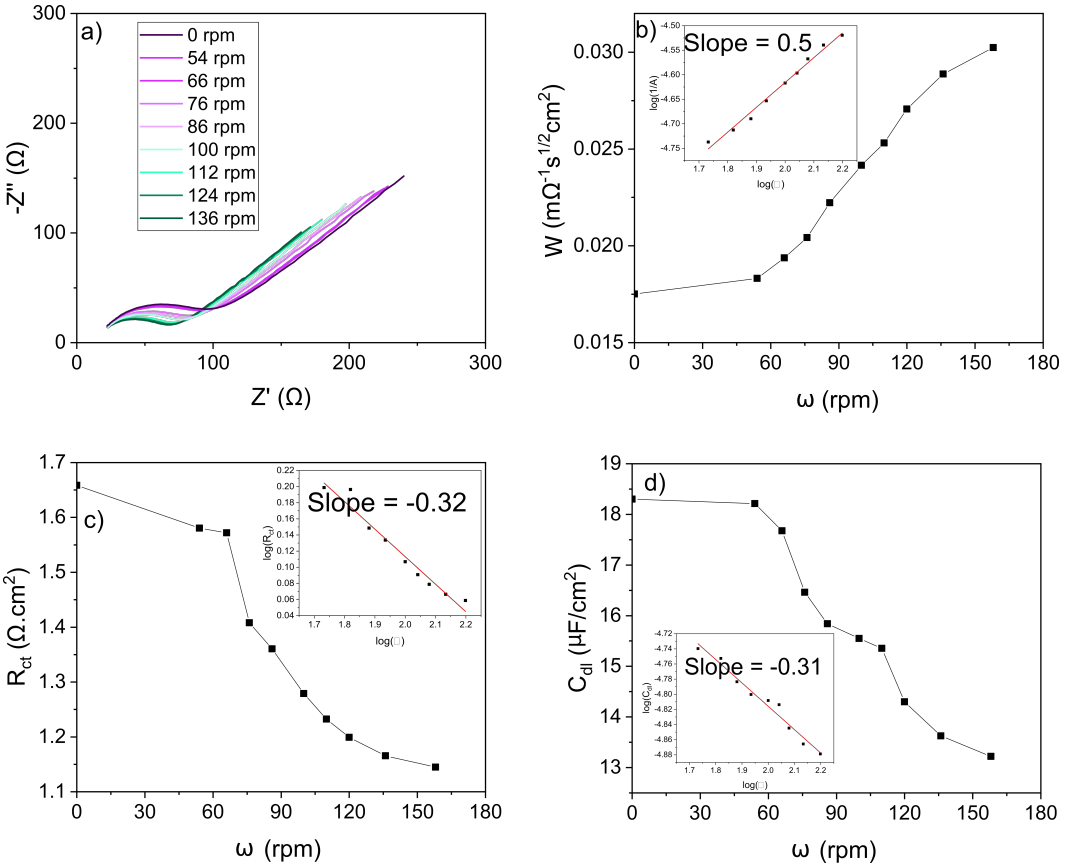

FIGURE 3.29: (a) Evolution of impedance spectra of Pt film with mechanical stirring at bias voltage 0.15 V. Randles circuit fit parameters (b) inverse of Warburg element, (c) charge transfer resistance and (c) effective capacitance as a function of stirring.

Fig. 3.29 shows the impedance spectra and the Randles fit parameters evolution with mechanical stirring. Similar to IP MHD effect, it is found that the mass transport and interface properties are sensitive to the mechanical stirring of the solution. It is estimated that the application of a 0.6 T is equivalent to a rotation of 136 rpm. It is worthwhile to note that this relation can be influenced by several parameters like electrolyte concentration, electrode area, cell volume and motor blade dimensions.

To summarise this section, we found that convective effects are minimum when the field is applied normal to the electrode surface. we also observed that the bulk and interface properties of the reaction is very sensitive to the convective effects induced by Lorentz force in B // j geometry. Additionally, the equivalence of in-plane field driven MHD effect to the mechanically stirring of solution is also shown.

3.6 Effect of large Magnetic Field Gradient at the Electrochemical Interface

In this section, we will study in detail how a large field gradient imposed near to the electrode surface will impact the electrochemical reaction, by means of chronoamperometry and impedance spectroscopy.

3.6.1 Chronoamperometry

Chronoamperometry is used as one of the main methods for detecting steady state effects by the field gradients. It is known that, for a Cottrellian system, the diffusion limited current decreases with time (t) as $t^{-1/2}$ as the current depends on the concentration gradient developed between the electrode-electrolyte interface and the bulk solution. However, at longer timescale, natural convection arising from the density differences in the solution perturbs the concentration gradient and results in a steady-state current. Sugiyama and Aogaki *et al.* [76] theoretically treated the magneto-convection due to non-uniform magnetic field and derived the relation for microelectrode diffusion current density to the field and concentration gradient as

$$j = 0.0969nFD_0\left(\frac{1}{\mu_0 D_0 \varrho}\right)^{1/3}\left(\frac{\partial\chi}{\partial c}\right)^{1/3} \times |\Delta c_s|^{4/3}\left|B\left(\frac{dB}{dz}\right)_{z=0}\right|^{1/3} \tag{3.16}$$

where n is the number of electrons transferred, F is Faraday constant, D_0 is the diffusion coefficient, μ_0 is the magnetic permeability, ϱ is the viscosity, χ is the magnetic susceptibility, and Δc_s is the difference between surface and bulk concentration. This equation assumes magnetic field B and field gradient (dB/dz) in the z-direction. Similar to the discussion in section 1.2.2, Eqn. 3.16 explains the necessity of orthogonal components of both field and susceptibility gradients for the magneto-convection to be active.

In our case, to attain the steady state, a potential of 0.25 V (0.16 V step from the OCP 0.41 V) is applied for 10 minutes. Field is then swept between $\pm$ 400 mT in steps of 10 mT. Once the applied field is stabilized (in $<$ 5 s), the current is measured after waiting for 10 s, implying a delay time of total 15 s between two consecutive current measurements. Fig. 3.30 shows the steady state current hysteresis measurement of ferricyanide reduction with Pt film and HZDR Co/Pt films with different outer Pt cap layer thickness as working electrode. As can be seen, Co/Pt films with up to 5 nm thick Pt cap show a change in current density with applied out-of-plane field, having a maximum magnitude at 0 mT and

a minimum when the field is $> |200|$ mT. When the field is changed from $\pm$ 400 mT to 0 mT, the current density enhancement is about 8, 7 and 5 % for Co/Pt film with outer Pt cap 0.0, 3.0 and 5.0 nm, respectively. On the other hand, no such field dependence on the current density is observed wen the working electrode is a Pt film or a 10 nm thick Pt capped Co/Pt film(Fig. 3.30b).

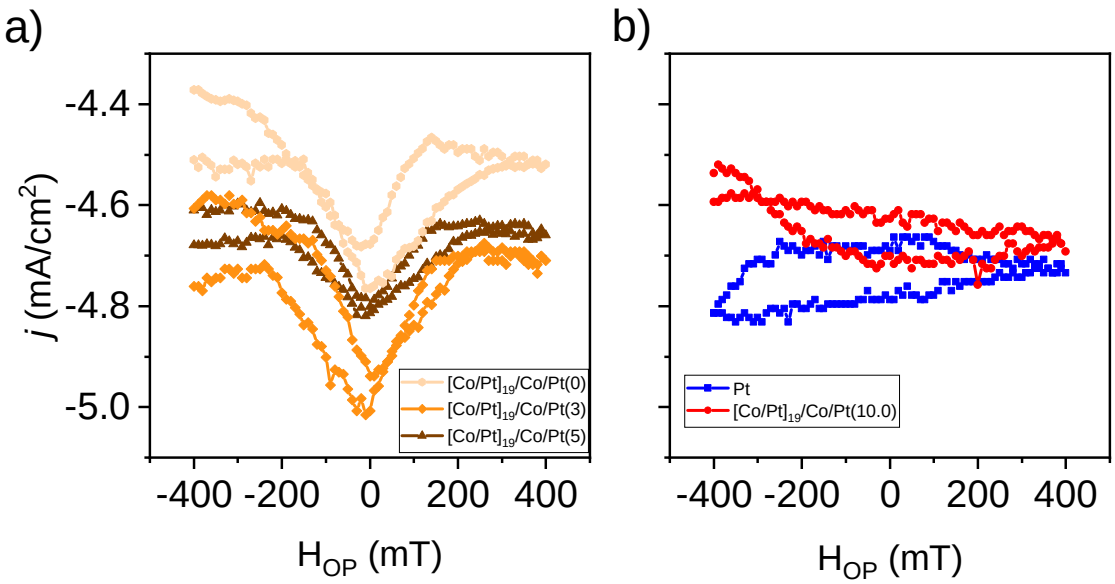

FIGURE 3.30: Steady state current density vs out-of-plane magnetic field at voltage 0.25V (a) for HZDR Co/Pt films with outer Pt cap thickness 0.0, 3 and 5.0 nm, and (b) for Pt film and HZDR Co/Pt film with 10 nm outer Pt cap thickness.

The influence of a magnetic field on electrochemical reactions has been controversially discussed when the field is applied normal to the electrode surface. Lorentz force flows are complex in nature, involving micro-MHD flows generating macro and micro vortexes at the electrode surface. In micro-disk electrodes, MHD stirring due to non-uniform edge current distribution has been reported in the case when the field is applied perpendicular to the surface [53, 79]. Even when the current distribution is uniform, other types of MHD and micro-MHD effects induced convection originating inside the diffusion layer can influence the reaction [69]. During electrodeposition, physical quantities changing with time and location result in non-equilibrium fluctuations. These fluctuations can interact with the field normal to the surface creating characteristic morphologies called the micro-mystery circles [53, 69, 80]. Furthermore, when the field is non-uniform along the direction normal to the surface, the gradient force can induce magneto-convection if the paramagnetic species are involved [53, 81, 82].

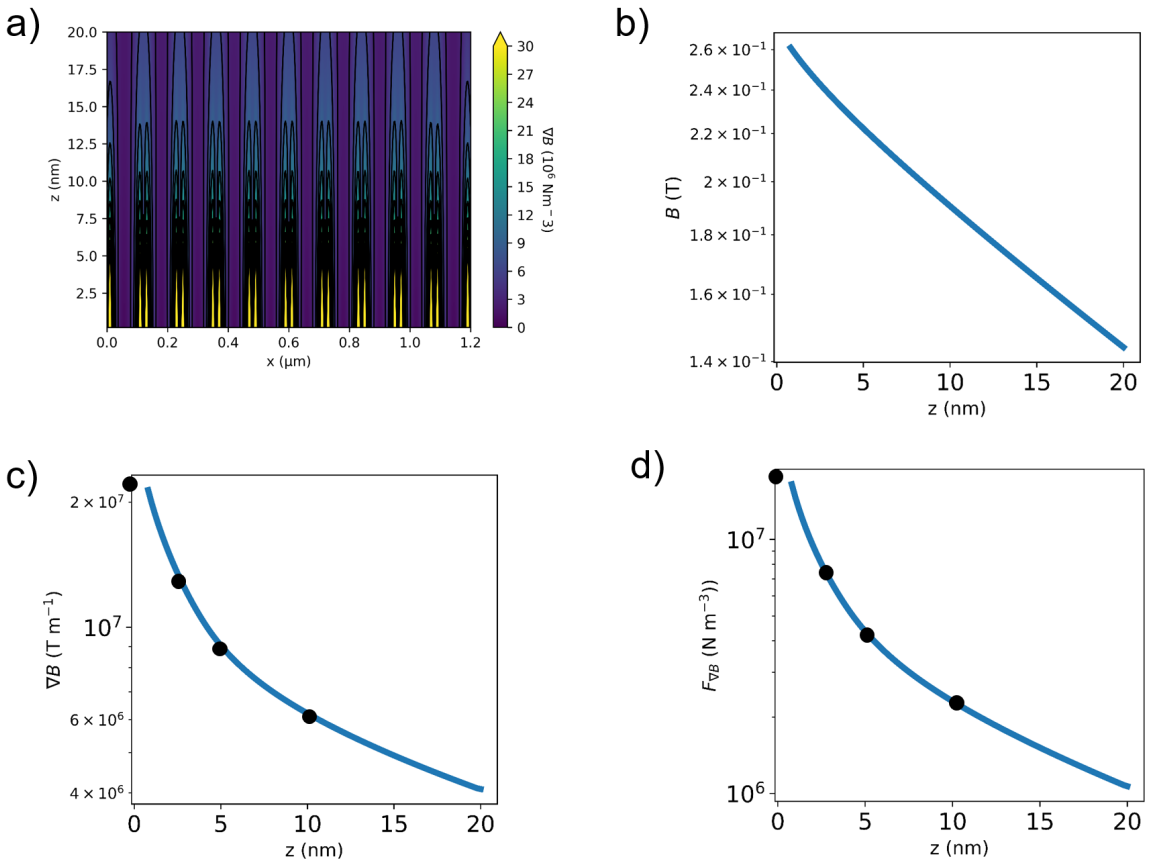

FIGURE 3.31: Force field estimation at the immediate vicinity of thin film obtained using 2D magnetized sheet model. (a) Contour plot of field gradient above the magnetic array having opposite magnetization in the alternate bits. Estimation of (b) magnetic field, (c) field gradient and (d) force field gradient near the electrode surface. The parameters used are magnetic thickness = 20 nm, domain width 0.13 μm, dead layer = 16 %, magnetization= 1.5 T and ferricyanide concentration = 0.1 M.

Returning to the steady current - OP field hysteresis loop, the micro-MHD and edge effect driven convective effects can be assumed to be negligible as no field effects are observed in the Pt and 10 nm capped Co/Pt electrodes. Hence, the external field cannot be considered as a primary source of steady current field dependence in Co/Pt films. Another source of interest is the stray field due to the magnetic multi-domains which is concentrated in the immediate vicinity of the electrode surface. In this few tens of nanometers thin interfacial region, the influence of magnetic field is expected to be negligible as the electrostatic and thermal diffusion driving forces are order of magnitudes higher that of the field induced forces. However, Aogaki *et al.* has reported that the field can in fact induce convection inside the diffusion layer [69] and can influence the morphology of electrodeposits.

To estimate the magnitude of the thin film multi-domain generated force fields involved, the field and field gradient are calculated assuming the thin film as a magnetised 2D sheet. Fig. 3.31 shows the approximated field and gradient field values as a function of distance from the surface of the Co/Pt film. For the Co/Pt film electrode without a Pt cap layer, an average field of 0.26 T is expected at the film surface. As the current density involved is small, the average Lorentz force density at the surface is rather small as 25 N/m^3 (j = 5 mA/cm^2, B = 0.5 T) compare to the force driving natural convection ($\sim 10^3$ N/m^3). On the other hand, the field gradient force can act as driving force of micro-convection. As we already discussed, unlike Lorentz force, the Kelvin force can be enhanced with the reduction of the system size. Hence, field gradient is expected to be maximised in the nano and micro-magnetic objects. From the 2D model of magnetic thin films, it is estimated that the field gradient of the order of 10^7 T/m can be produced at the surface by the multidomain magnetic thin film (Fig. 3.31c). The resultant gradient force density is also of the similar order (Fig. 3.31d) taking $\chi_{mol} = 28.8 \times 10^{-9}$ m^3/mol for potassium ferricyanide, and $c \approx 0.1$ M. The field gradient force can inhibit the convection of paramagnetic species and can locally alter the concentration gradient. A study using CoPt nanowires embedded in an alumina membrane has showed that the oxygen reduction current can be enhanced by the magnetic field gradient driven convective inhibition of paramagnetic radical near electrode surface [11, 12]. Therefore, the large field gradient created by the magnetic multi-domain films at the electrochemical interface is assumed to be the driving force of the observed field effects.

To further confirm the assumption, the OP field dependence of the magnetic multi-domain is compared to the steady state hysteresis behaviour of Co/Pt films. It can be seen from the magnetization curve (Fig. 3.6a) and MOKE imaging (Fig. 3.9) that the Co/Pt films are in multi-domain state when the field is $< |200|$ mT and is saturated at higher fields (at

around|200| mT). As we already discussed, the field gradient due to the Co/Pt film will be maximum in the multi-domain state and will be minimum at the saturated state. The behaviour of steady state current (Fig. 3.30a) follows the evolution of the field gradient due to the Co/Pt film. The dependence of Pt capping layer on the field induced current enhancement can also be explained by the reduction of field gradient with distance from the electrode surface. The current enhancement is maximum in Co/Pt film with no Pt cap and reduces with the Pt cap thickness which eventually vanishes when the cap is 10 nm thick. Similarly, at 10 nm away from the electrode surface, the field gradient reduced by an order of magnitude might be lower than the threshold required for the field-induced microconvection.

3.6.2 Impedance Spectroscopy

Chronoamperometric measurements shows a change in the steady current under the influence of a large field gradient imposed at the electrochemical interface. Electrochemical impedance spectroscopy (EIS) is further used to decouple the influence of field gradient on the interface from bulk properties of the system. As we already discussed, EIS allows to study the fast processes such as kinetics and double layer charging, along with the slow mass transport effects. Pt and Co/Pt films with 3 nm Pt cap are used as working electrodes to compare the field effects. Measurements are carried out under different field applied perpendicular to the film surface. First, a DC bias voltage of 0.25 V is applied for 10 minutes to reach a steady state. Impedance spectra in the frequency range of 100 kHz – 10 Hz are then recorded under different perpendicular magnetic fields. Steady state current response to the applied perpendicular magnetic field is also recorded as a function of time (Fig. 3.32a). From the current response to the magnetic field, about 10 – 20 s current response delay to the applied field is estimated. Hence, all impedance measurements start after a waiting time of 30 s after changing the magnetic field value.

Impedance spectra Fig. 3.32b shows the evolution of the Nyquist plot of a Co/Pt film under various perpendicular magnetic field. The semicircle corresponds to the high frequency charge transfer resistance and double layer capacitance whereas the low frequency straight line on the right side represent the diffusion Warburg impedance. The data is fitted using the Randles circuit to extract the relevant parameters and plotted as a function of magnetic field (Fig. 3.33). The bath resistance R_s is almost invariant with the field as expected (Fig. 3.33d). The low frequency Warburg response is also unaffected by the applied field

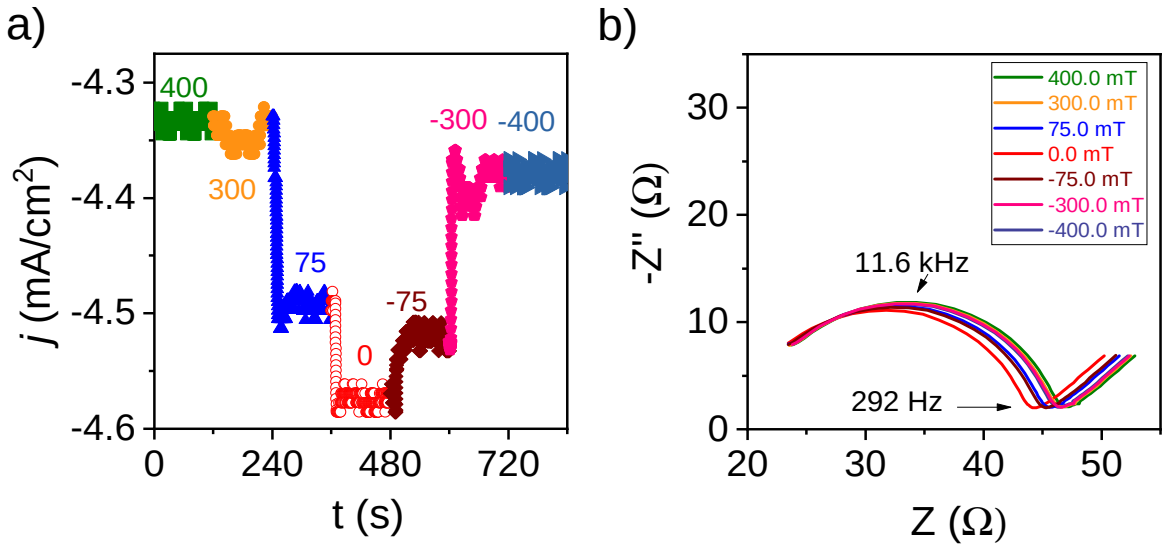

FIGURE 3.32: (a) Chronoamperometry of HZDR Co/Pt (3 nm cap) electrode at potential 0.25 V (vs Ag/AgCl), and (b) impedance spectra at bias potential 0.25 V under different surface normal fields.

(Fig. 3.33c) indicating that the diffusion layer is insensitive to the magnetic field at this bias potential.

The most striking result happens in the high frequency region where the charge transfer resistance (R_{ct}) and double layer capacitance (C_{dl}) shows a clear dependence to the applied magnetic field (Fig. 3.33 a,b). Both quantities are reduced by 5-6 % when the applied field changes from $\pm$ 400 mT to 0 mT. A reduction in R_{ct} is in accordance with the enhancement of current observed in the chronoamperometry measurements (Fig. 3.30a). As the applied DC bias voltage is close to the half potential $E_{1/2}$, the effective double layer capacitance can be treated as a Gouy-Chapman capacitor corresponding to the diffusive double layer region. A change in C_{dl} with the applied field would then imply a change in the concentration of ions in the diffusive double layer region. This matches to our assumption of field gradient driven micro-convection as the origin of current enhancement in Co/Pt films.

For comparison, EIS at different perpendicular field are measured for a pure Pt film, and the relevant parameters are extracted using a similar Randles circuit fit. Fig. 3.34 shows the Nyquist plot and the evolution of the impedance data fitted parameters for a Pt film under different OP magnetic field values. Similarly to the chronoamperometric observations, the Pt film shows no field dependence for the impedance fitted parameters. The average change in the R_{ct} and C_{dl} is about 1 – 2 % per measurement, irrespective of the applied field. This is attributed to the partial surface coverage [68] and specific adsorption effects [67] which has already been reported for ferri/ferrocyanide reactions. However, EIS measurements on Pt

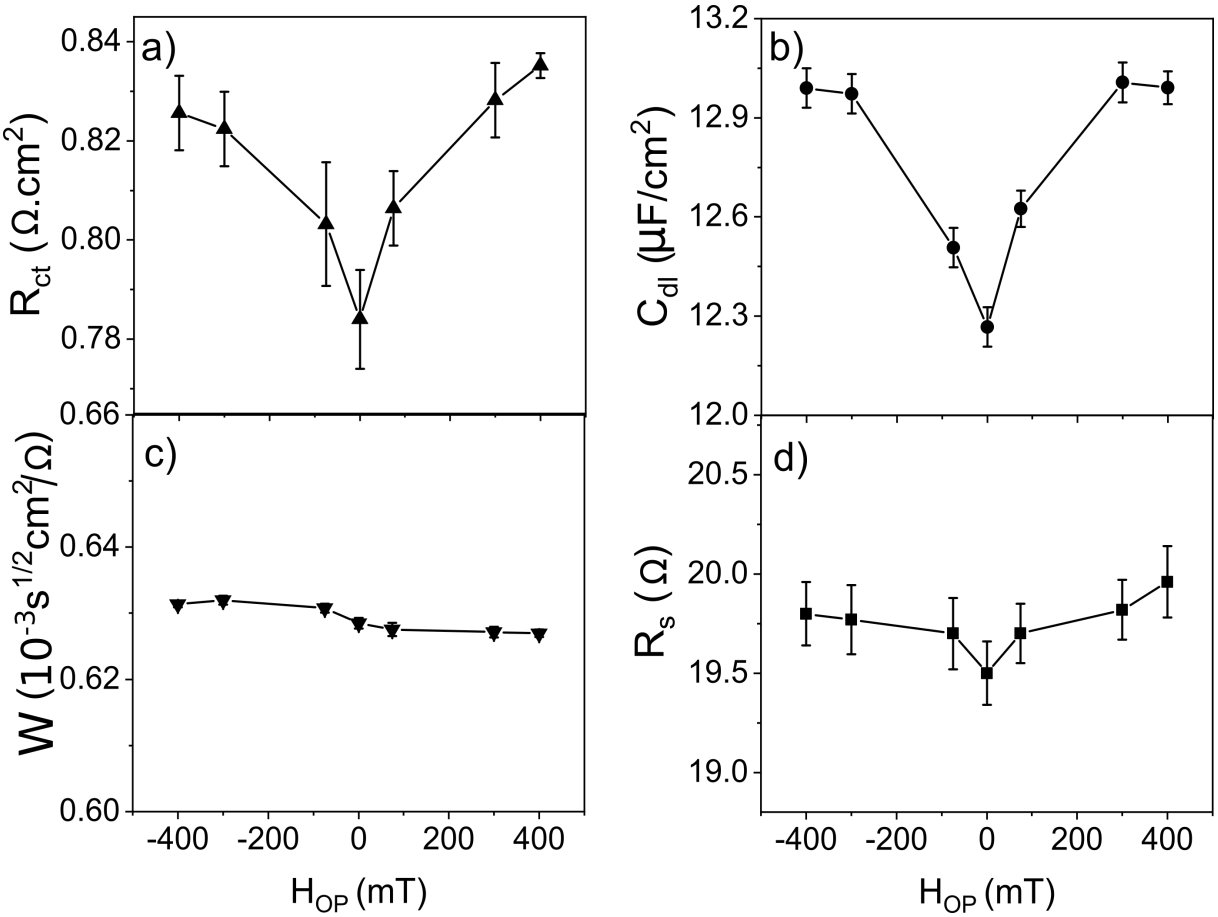

FIGURE 3.33: Randles circuit fitted parameters of Nyquist plots in Fig. 3.32b. (a) charge transfer resistance, (b) double layer capacitance and (c) warburg diffusion impedance and (d) solution resistance evolution as a function of magnetic field applied normal to the Co/Pt film surface. For comparison, y-scale of all plots is chosen such that the total change is around 10%.

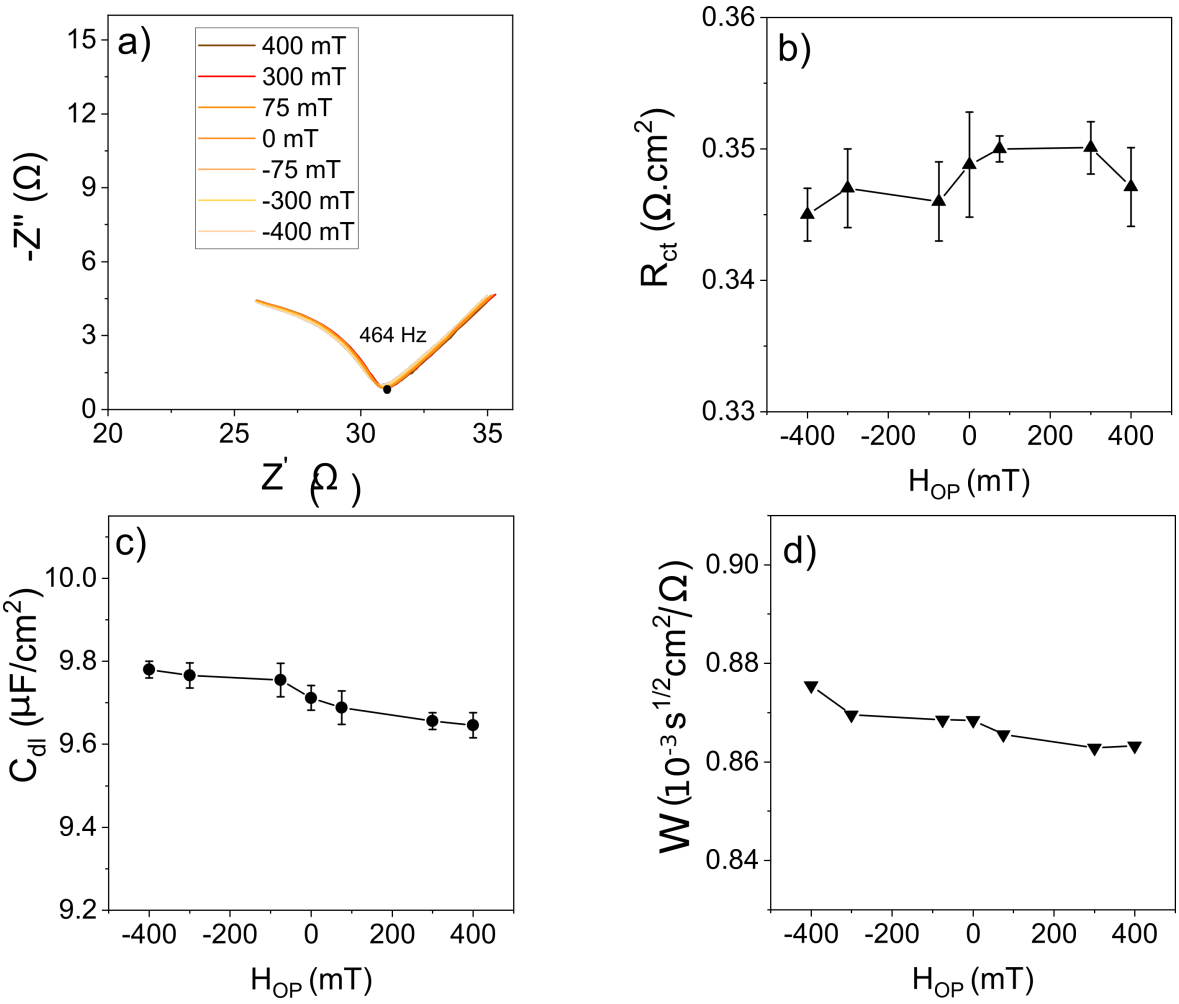

FIGURE 3.34: (a) Nyquist plot of Pt film at dc bias voltage 0.275 V under different magnetic field applied normal to the film surface. (b) charge transfer resistance, (c) double layer capacitance and (d) Warburg diffusion impedance evolution as a function of magnetic field. For comparison, y-scale of b, c and d is chosen such that the total change is around 10%.

films confirms comparatively better reproducibility and stability, and also confirm that the external field induced effects are minimum in the system under investigation.

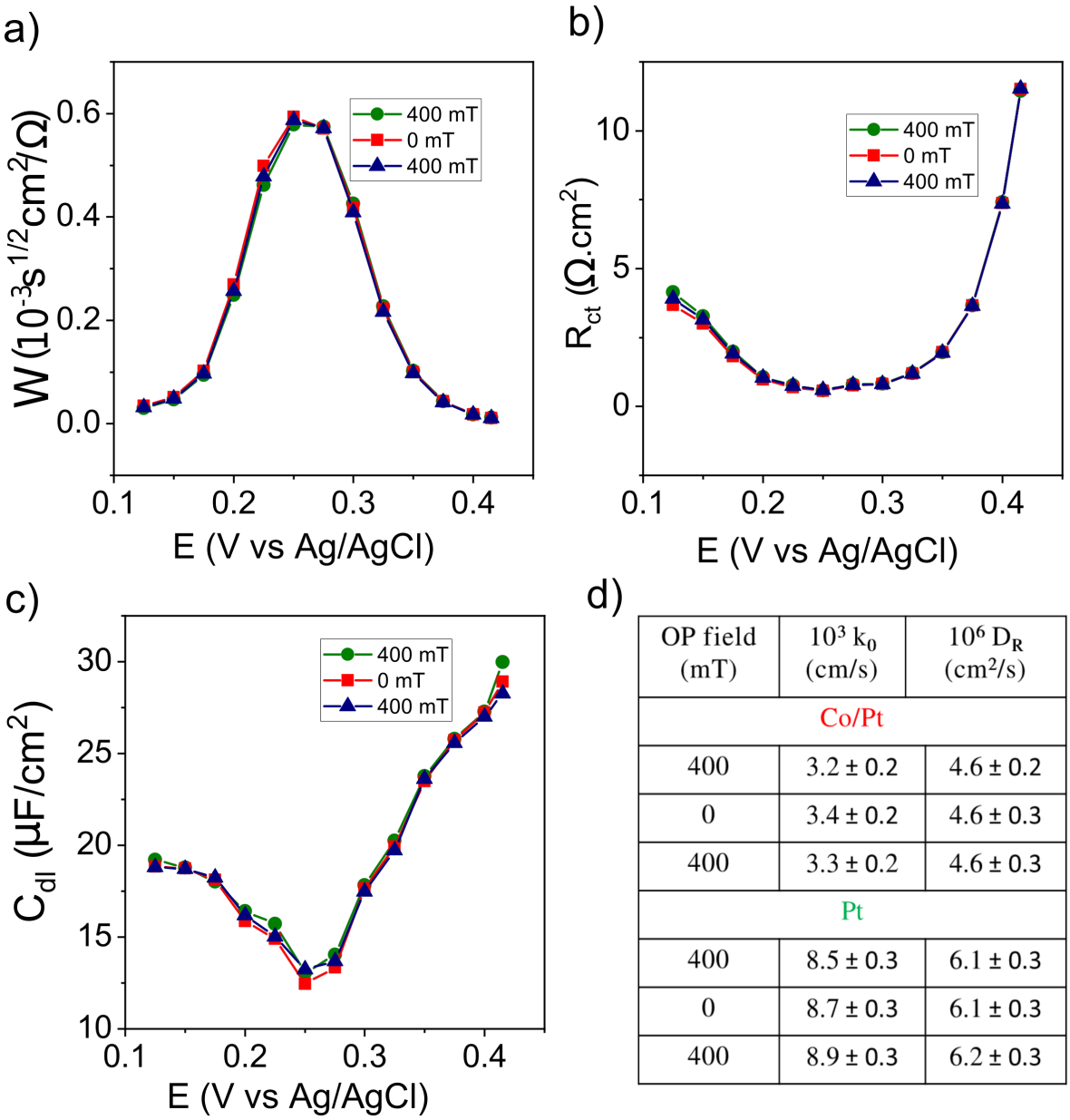

d)

OP field (mT)	10^3 k_0 (cm/s)	10^6 D_R (cm^2/s)
Co/Pt		
400	3.2 ± 0.2	4.6 ± 0.2
0	3.4 ± 0.2	4.6 ± 0.3
400	3.3 ± 0.2	4.6 ± 0.3
Pt		
400	8.5 ± 0.3	6.1 ± 0.3
0	8.7 ± 0.3	6.1 ± 0.3
400	8.9 ± 0.3	6.2 ± 0.3

FIGURE 3.35: Randles circuit fitted parameters of Co/Pt impedance spectra. (a) Warburg diffusion element, (b) charge transfer resistance and (c) double layer capacitance as a function of dc bias voltage under different perpendicular field. (d) Kinetic rate constant and diffusion coefficient calculated for Co/Pt and Pt film under different field conditions.

To better understand the interfacial and bulk effects due to the near electrode large field gradient, multiple impedance spectra are recorded at different DC bias voltages between OCP 0.41 V and the active reduction voltage 0.125 V in steps of 0.025 V. At each DC bias voltage, impedance spectra are recorded under perpendicular fields applied in order: 400 mT, 0 mT and 400 mT. It is worthwhile reminding that, in Co/Pt films, the field gradient due to the multi-domains will be minimum at 400 mT and maximum at 0 mT. Thus, comparison

of impedance spectra recorded for Pt and Co/Pt film in such field configurations should help us to distinguish the field gradient and other surface related effects at different dc bias voltage values. Fig. 3.35 a, b and c show the extracted Randles circuit fit parameters from the impedance spectra of Co/Pt film as a function of potentiostatic conditions for different magnetic fields. As discussed earlier in Section 3.3.2.3, the kinetic rate constant and the reduction diffusion coefficient can be estimated from the potential dependent EIS data using the equations 3.13 and 3.14, and the estimated values for Pt and Co/Pt films are tabulated (Fig. 3.35d). Irrespective of the applied field magnitude, k_0 of Pt shows an increase with respect to the order of measurement but the change is within the standard deviation. In the case of Co/Pt electrode, k_0 increases when the field gradient is maximum (0 mT) but the change with respect to the OP field lies within the standard deviation and cannot be considered as a true shift.

In order to understand the field gradient effect at different voltages, the change in the value of fitted parameters due to the applied field is plotted as a function of bias voltage (Fig. 3.36). The Δ parameter is defined as the percentage change of Randles fit parameter with the field. For example, Δ_{cdl} is defined as,

$$\Delta_{cdl}(\%) = \frac{C_{dl}(B_1) - C_{dl}(B_0)}{C_{dl}(B_0)} \times 100 \tag{3.17}$$

Likewise, Δ_{Rct} and $\Delta_{(W)}$ represents the percentage change in charge transfer resistance (R_{ct}) and Warburg element ($1/W$) with the applied field. Fig. 3.36a(i) shows the percentage change of double layer capacitance (C_{dl}) with the applied perpendicular field at different bias voltage. As can be seen, for Co/Pt electrode, the double layer capacitance is sensitive to the field gradient when the potential is near to the point of zero charge ($E_{PZC} \approx 0.26$ V). This implies that the concentration of ions in the diffusive double layer region has changed due to the field gradient induced micro-convection. The change in C_{dl} is quite reproducible irrespective of the order in which the field is applied (Fig. 3.36a(i) and b(i)). No such change in C_{dl} is observed for Pt electrodes. Far from E_{PZC}, no field dependence to the effective capacitance is observed for either Co/Pt or Pt film electrodes which suggests that the Helmholtz parallel plate like capacitance remain intact and is not sensitive to the field gradient effects. Fig. 3.36a(ii) and b(ii) shows the change in charge transfer resistance (R_{ct}) with the applied perpendicular field at different bias voltage.

For a Co/Pt electrode, R_{ct} changes with the field gradient when the applied potential is

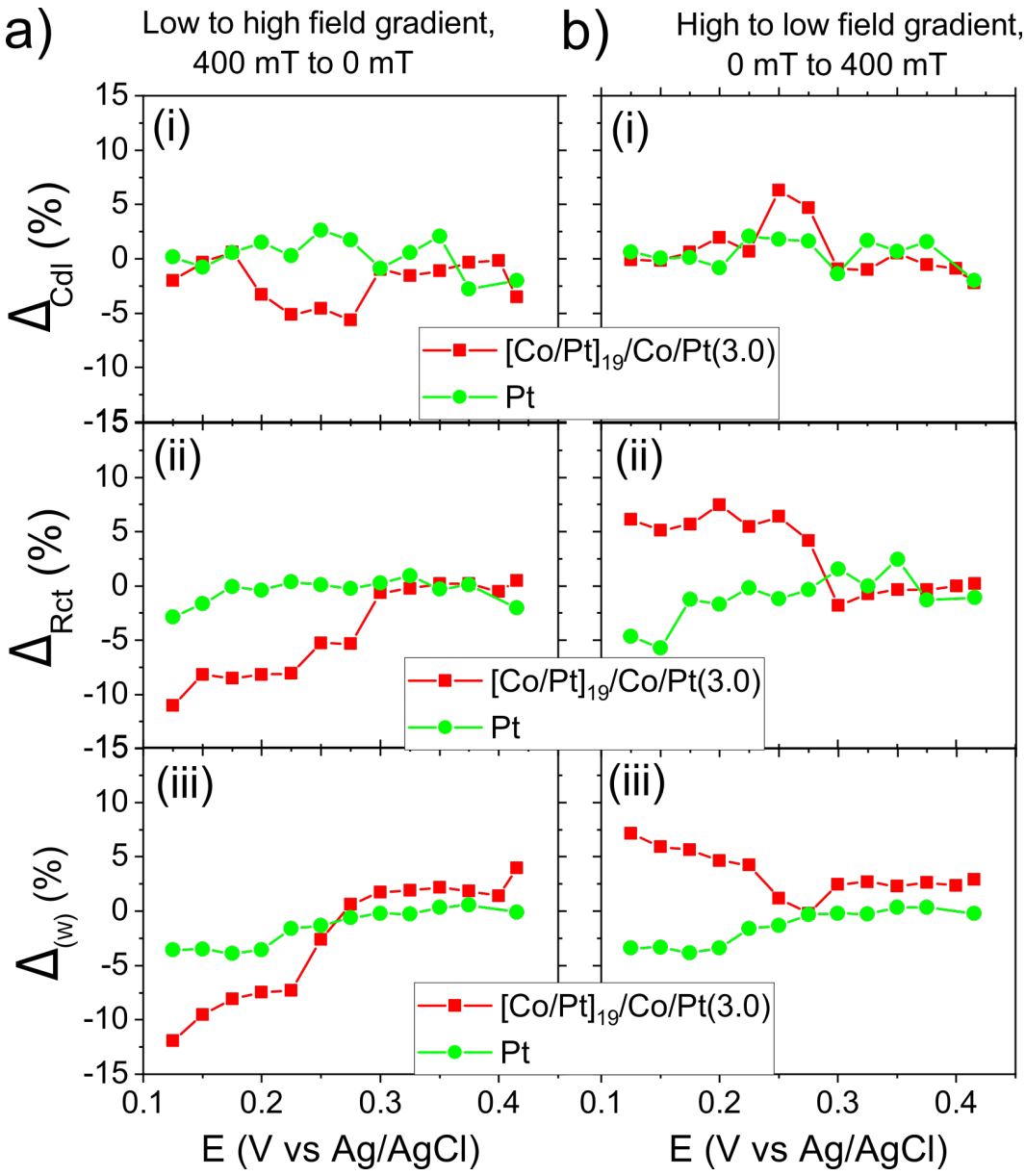

FIGURE 3.36: Percentage change of Randle's circuit fitted parameters of Co/Pt film as a function of dc voltage when applied normal field changes from (a) 400 mT (minimum field gradient)to 0 mT (maximum field gradient) and (b) from 0 mT (maximum field gradient) to 400 mT (minimum field gradient).

$\leq$ 0.275 V. As we already discussed, a concentration gradient is required for the field gradient to induce the convection. When the applied voltage is small (E $< E_{pzc}$), the concentration gradient is assumed to be not large enough for the field gradient effects to be active. Interestingly, the behaviour of Δ_{Rct} changes with the direction of applied field rules out any surface related effects as the source of the observed change and confirms that the observed change is due to the localized field gradient. Lastly, Fig. 3.36a(iii) and b(iii) shows the change in the Warburg diffusion component with the perpendicular field at different bias voltage. Similar to C_{dl} and R_{ct}, no field effect is observed on either Pt and Co/Pt electrode when the applied voltage is small ($E < E_{pzc}$). At the reduction potential 0.275 V, as discussed in the field dependence study (Figs. 3.33), the change in Warburg element for Co/Pt electrode is only 1-2 %, lower than the 5-8 % change in C_{dl} and R_{ct}. However, at more negative potentials, along with the R_{ct} change, the Warburg element also changes with the field gradient. It is already been known from the Lorentz force study (Section 3.5) that the diffusion layer is very sensitive to the convective effects. During active reduction of ferricyanide, the larger concentration gradient and the micro-convection driven by the field gradient can influence the diffusion layer. On the other hand, the applied field has a negligible influence on the Warburg element of the Pt film electrode.

3.7 Conclusion

The influence of a magnetic field on the electrochemical reactions can be explained, in most cases, by means of field influence on the mass transport. When charged species move perpendicular to the field direction, the Lorentz force acts on the species and induce convective flow. A concentration gradient of paramagnetic species orthogonal to the field gradient also has a similar effect and influence the magneto-convection. On the other hand, the field influence on the interfacial region is a controversially discussed topic as the solid/liquid interface is governed by diffusion and electrostatic forces which are orders of magnitude higher than the magnetic forces. Our aim is to investigate the consequence of large field gradient imposed at the interface on the electrochemical reaction.

To create the large field gradient landscape near the immediate vicinity of electrode, magnetic thin films consisting of Co/Pt repeats having perpendicular magnetic anisotropy are sputter deposited. Based on magnetic measurements and imaging techniques, the magnetic multidomains at low applied field are characterised, and the field and field gradient values are estimated by means of 2D magnetised sheet model. Gradient field of the order

of 10^7 T/m is achieved at the film surface. For the electrochemical investigations, a model system of ferri/ferrocyanide reaction is chosen as a standard redox probe. Interfacial and bulk properties of the reaction are pre-characterised using a Pt film as working electrode.

In a separate effort, the influence of Pt cap layer on the electrochemical activity of the Co/Pt multirepeat film is studied. A minimum of 5 nm Pt cap is found to be required for the Co/Pt film to exhibit a reaction rate reaching the one of pure Pt films. The chemical composition on the surface is analysed using angle resolved XPS. For a 3 nm Pt capped Co/Pt film, ARXPS found traces of Co at the surface suggesting an imperfect Pt surface coverage.

To investigate Lorentz force effects, the cyclic voltammetry (CV) and impedance spectroscopy (EIS) are performed under different field applied parallel to the electrode surface. From CV curves, one can evidence the Lorentz force influence on the mass transport limited regime with no indication of impact on the kinetically limited one. Similar observation hold for both Pt and Co/Pt films. Impedance study found that, when the reaction is mass transport limited, the interfacial and bulk properties of the redox reaction are influenced by the Lorentz force. To confirm that the observed effects are indeed due to convection, the equivalence to mechanical stirring is demonstrated.

Lastly, the influence of extreme magnetic fields at the interface between electrode and electrolyte on the electrochemical reaction is characterised. The steady state current shows a clear dependence on the field gradient generated by the multi-domains in Co/Pt films. No field dependence on current is observed for Pt or Co/Pt with 10 nm Pt cap thickness films. The absence of field gradient effect on the 10 nm capped Co/Pt film is attributed to the order of magnitude diminished field gradient. Impedance spectroscopy is further used to study the observed field effect in detail. It is found that, near to the point of zero charge (E_{pzc}) of 0.25 V, the interfacial double layer capacitance (C_{dl}) and charge transfer resistance (R_{ct}) are influenced by the large magnetic field gradient while the diffusion related Warburg impedance (W) isn't. During the active reduction of ferricyanide, at potentials far from from E_{pzc}, interfacial capacitance resembles a tightly packed Helmholtz layer and becomes insensitive to the field gradient. However, in this mass transport limited region, R_{ct} and W shows a dependence to the Kelvin force. The suppression of near-electrode convection of the paramagnetic species is suggested as the mode of action. Thus while there is an enhancement of the effective kinetics, there is no true shift in the underlying kinetics.

Bibliography

[1]L. M. A. Monzon and J. M. D. Coey, "Magnetic fields in electrochemistry: the kelvin force. a mini-review", Electrochemistry Communications **42**, 42–45 (2014).

[2]L. M. A. Monzon and J. M. D. Coey, "Magnetic fields in electrochemistry: the lorentz force. a mini-review", Electrochemistry Communications **42**, 38–41 (2014).

[3]V. Gatard, J. Deseure, and M. Chatenet, "Use of magnetic fields in electrochemistry: a selected review", Current Opinion in Electrochemistry **23**, 96–105 (2020).

[4]J. M. D. Coey, "Magnetism and magnetic materials (cambridge university press)",

[5]R. Aogaki, "Micro-MHD effect on electrodeposition in the vertical magnetic field", Magnetohydrodynamics **39**, ADS Bibcode: 2003MHD....39..453A, 453–460 (2003).

[6]G. Hinds, F. E. Spada, J. M. D. Coey, T. R. Ní Mhíocháin, and M. E. G. Lyons, "Magnetic field effects on copper electrolysis", The Journal of Physical Chemistry B **105**, Publisher: American Chemical Society, 9487–9502 (2001).

[7]H. Liu, L.-m. Pan, H. Huang, Q. Qin, P. Li, and J. Wen, "Hydrogen bubble growth at micro-electrode under magnetic field", Journal of Electroanalytical Chemistry **754**, 22–29 (2015).

[8]P. A. Dunne, J. Hilton, and J. M. D. Coey, "Levitation in paramagnetic liquids", Journal of Magnetism and Magnetic Materials, Proceedings of the Joint European Magnetic Symposia **316**, 273–276 (2007).

[9]P. Dunne and J. M. D. Coey, "Patterning metallic electrodeposits with magnet arrays", Physical Review B **85**, Publisher: American Physical Society, 224411 (2012).

[10]P. Dunne, R. Soucaille, K. Ackland, and J. M. D. Coey, "Magnetic structuring of linear copper electrodeposits", Journal of Applied Physics **111**, Publisher: American Institute of Physics, 07B915 (2012).

[11]N. B. Chaure, F. M. F. Rhen, J. Hilton, and J. M. D. Coey, "Design and application of a magnetic field gradient electrode", Electrochemistry Communications **9**, 155–158 (2007).

[12]N. B. Chaure and J. M. D. Coey, "Enhanced oxygen reduction at composite electrodes producing a large magnetic gradient", Journal of the Electrochemical Society **156**, Publisher: IOP Publishing, F39 (2009).

[13]P. Dunne, T. Adachi, A. A. Dev, A. Sorrenti, L. Giacchetti, A. Bonnin, C. Bourdon, P. H. Mangin, J. M. D. Coey, B. Doudin, and T. M. Hermans, "Liquid flow and control without solid walls", Nature **581**, Number: 7806 Publisher: Nature Publishing Group, 58–62 (2020).

[14]S. Koehler and A. Bund, "Investigations on the kinetics of electron transfer reactions in magnetic fields", The Journal of Physical Chemistry B **110**, Publisher: American Chemical Society, 1485–1489 (2006).

[15]O. Devos, O. Aaboubi, J.-P. Chopart, A. Olivier, C. Gabrielli, and B. Tribollet, "Is there a magnetic field effect on electrochemical kinetics?", The Journal of Physical Chemistry A **104**, Publisher: American Chemical Society, 1544–1548 (2000).

[16]F. A. Garcés-Pineda, M. Blasco-Ahicart, D. Nieto-Castro, N. López, and J. R. Galán-Mascarós, "Direct magnetic enhancement of electrocatalytic water oxidation in alkaline media", Nature Energy **4**, Number: 6 Publisher: Nature Publishing Group, 519–525 (2019).

[17]O. Sambalova, E. Billeter, O. Yildirim, A. Sterzi, D. Bleiner, and A. Borgschulte, "Magnetic field enhancement of electrochemical hydrogen evolution reaction probed by magneto-optics", International Journal of Hydrogen Energy, `10.1016/j.ijhydene.2020.10.210` (2020).

[18]V. Lebedeva, V. Pierron-bohnes, C. Goyhenex, V. Papaefthimiou, S. Zafeiratos, R. Nazmutdinov, V. Da Costa, M. Acosta, L. Zosiak, R. Kozubski, D. Muller, and R. Savinova, "Effect of the chemical order on the electrocatalytic activity of model PtCo electrodes in the oxygen reduction reaction", Electrochimica Acta **108**, 605–616 (2013).

[19]P. Dunne and J. M. D. Coey, "Influence of a magnetic field on the electrochemical double layer", The Journal of Physical Chemistry C **123**, Publisher: American Chemical Society, 24181–24192 (2019).

[20]N. M. Dempsey, D. Le Roy, H. Marelli-Mathevon, G. Shaw, A. Dias, R. B. G. Kramer, L. Viet Cuong, M. Kustov, L. F. Zanini, C. Villard, K. Hasselbach, C. Tomba, and F. Dumas-Bouchiat, "Micro-magnetic imprinting of high field gradient magnetic flux sources", Applied Physics Letters **104**, Publisher: American Institute of Physics, 262401 (2014).

[21]L. Fallarino, A. Oelschlägel, J. A. Arregi, A. Bashkatov, F. Samad, B. Böhm, K. Chesnel, and O. Hellwig, "Control of domain structure and magnetization reversal in thick co/pt multilayers", Physical Review B **99**, Publisher: American Physical Society, 024431 (2019).

[22]O. Hellwig, A. Berger, J. B. Kortright, and E. E. Fullerton, "Domain structure and magnetization reversal of antiferromagnetically coupled perpendicular anisotropy films", Journal of Magnetism and Magnetic Materials **319**, 13–55 (2007).

[23]J. E. Davies, O. Hellwig, E. E. Fullerton, G. Denbeaux, J. B. Kortright, and K. Liu, "Magnetization reversal of $\mathrm{co}\mathrm{pt}$ multilayers: microscopic origin of high-field magnetic irreversibility", Physical Review B **70**, Publisher: American Physical Society, 224434 (2004).

[24]Z. Diao, E. R. Nowak, G. Feng, and J. M. D. Coey, "Magnetic noise in structured hard magnets", Physical Review Letters **104**, Publisher: American Physical Society, 047202 (2010).

[25]Y. Zhang, C. Liang, J. Wu, H. Liu, B. Zhang, Z. Jiang, S. Li, and P. Xu, "Recent advances in magnetic field-enhanced electrocatalysis", ACS Applied Energy Materials, Publisher: American Chemical Society, 10.1021/acsaem.0c02104 (2020).

[26]I. Benguettat-El Mokhtari, A. Mourkas, P. Ntetsika, I. Panagiotopoulos, Y. Roussigné, S. M. Cherif, A. Stashkevich, F. Kail, L. Chahed, and M. Belmeguenai, "Interfacial dzyaloshinskii-moriya interaction, interface-induced damping and perpendicular magnetic anisotropy in pt/co/w based multilayers", Journal of Applied Physics **126**, Publisher: American Institute of Physics, 133902 (2019).

[27]T. Y. Lee, Y. Chan Won, D. Su Son, S. Ho Lim, and S.-R. Lee, "Effects of co layer thickness and annealing temperature on the magnetic properties of inverted [pt/co] multilayers", Journal of Applied Physics **114**, Publisher: American Institute of Physics, 173909 (2013).

[28]B. Böhm, L. Fallarino, D. Pohl, B. Rellinghaus, K. Nielsch, N. S. Kiselev, and O. Hellwig, "Antiferromagnetic domain wall control via surface spin flop in fully tunable synthetic antiferromagnets with perpendicular magnetic anisotropy", Physical Review B **100**, Publisher: American Physical Society, 140411 (2019).

[29]G. J. Kusinski, K. M. Krishnan, D. Weller, B. D. Terris, L. Folks, A. J. Kellock, J. E. E. Baglin, and G. Thomas, "Lorentz transmission electron microscopy investigation of magnetically patterned co/pt multilayers", in *Magnetic storage systems beyond 2000*, edited by G. C. Hadjipanayis, NATO Science Series (Springer Netherlands, Dordrecht, 2001), pp. 157–161.

[30]C. Kittel, "Theory of the structure of ferromagnetic domains in films and small particles", Physical Review **70**, Publisher: American Physical Society, 965–971 (1946).

[31]C. Kittel, "Physical theory of ferromagnetic domains", Reviews of Modern Physics **21**, Publisher: American Physical Society, 541–583 (1949).

[32]C. Kooy, "Experimental and theoretical study of the domain configuration in thin layers of bafe12o19", Publisher:Philips Res. Repts. 15 (1960) 7 (1960).

[33]V. Kamberský, P. de Haan, J. Šimšová, S. Porthun, R. Gemperle, and J. C. Lodder, "Domain wall theory and exchange stiffness in co/pd multilayers", Journal of Magnetism and Magnetic Materials, European Magnetic Materials and Applications Conference **157-158**, 301–302 (1996).

[34]O. Hellwig, G. P. Denbeaux, J. B. Kortright, and E. E. Fullerton, "X-ray studies of aligned magnetic stripe domains in perpendicular multilayers", Physica B: Condensed Matter, Proceedings of the Seventh International Conference on Surface X-ray and Neutron Scattering **336**, 136–144 (2003).

[35]A. Hubert and R. Schafer, "Magnetic domains:the analysis of magnetic microstrutures", Publisher: Springer-Verlag, Berlin, 1998).

[36]E. P. Furlani, "Permanent magnet and electromechanical devices (academic press, san diego, 2001)",

[37]P. Dunne, "Https://zenodo.org/record/4973815/export/json.yiop02jml7b",

[38]J. M. Leal, B. Garcia, and P. L. Domingo, "Outer-sphere hexacyanoferrate(III) oxidation of organic substrates", Coordination Chemistry Reviews **173**, 79–131 (1998).

[39]R. Shimpi, "A review of kinetics of oxidation of organic compounds by hexacyanoferrate(iii)", RJLBPCS 5:164–181, RJLBPCS 5:164–181 (2019).

[40]T. H. Huang, G. Salter, S. L. Kahn, and Y. M. Gindt, "Redox titration of ferricyanide to ferrocyanide with ascorbic acid: illustrating the nernst equation and beer–lambert law", Journal of Chemical Education **84**, Publisher: American Chemical Society, 1461 (2007).

[41]J. J. Van Benschoten, J. Y. Lewis, W. R. Heineman, D. A. Roston, and P. T. Kissinger, "Cyclic voltammetry experiment", Journal of Chemical Education **60**, Publisher: American Chemical Society, 772 (1983).

[42]P. H. Daum and C. G. Enke, "Electrochemical kinetics of the ferri-ferrocyanide couple on platinum", Analytical Chemistry **41**, Publisher: American Chemical Society, 653–656 (1969).

[43]B. N. Figgis, M. Gerloch, R. Mason, and R. S. Nyholm, "The crystallography and paramagnetic anisotropy of potassium ferricyanide", Proceedings of the Royal Society of London. A. Mathematical and Physical Sciences **309**, Publisher: Royal Society, 91–118 (1969).

[44]N. P. C. Stevens, M. B. Rooney, A. M. Bond, and S. W. Feldberg, "A comparison of simulated and experimental voltammograms obtained for the [fe(CN)6]3-/4- couple in the absence of added supporting electrolyte at a rotating disk electrode", The Journal of Physical Chemistry A **105**, Publisher: American Chemical Society, 9085–9093 (2001).

[45]Y. Long, Z. Xu, G. Wang, H. Xu, M. Yang, M. Ding, D. Yuan, C. Yan, Q. Sun, M. Liu, and C. Jia, "A neutral polysulfide/ferricyanide redox flow battery", iScience **24**, 103157 (2021).

[46].

[47]J. Schindelin, I. Arganda-Carreras, E. Frise, V. Kaynig, M. Longair, T. Pietzsch, S. Preibisch, C. Rueden, S. Saalfeld, B. Schmid, J.-Y. Tinevez, D. J. White, V. Hartenstein, K. Eliceiri, P. Tomancak, and A. Cardona, "Fiji: an open-source platform for biological-image analysis", Nature Methods **9**, Number: 7 Publisher: Nature Publishing Group, 676–682 (2012).

[48]C. Beriet and D. Pletcher, "A microelectrode study of the mechanism and kinetics of the ferro/ferricyanide couple in aqueous media: the influence of the electrolyte and its concentration", Journal of Electroanalytical Chemistry, An International Journal Devoted to all Aspects of Electrode Kinetics, Interfacial Structure, Properties of Electrolytes, Colloid and Biological Electrochemistry **361**, 93–101 (1993).

[49]S. A. Campbell and L. M. Peter, "The effect of [k+] on the heterogeneous rate constant for the [fe(CN)6]3/[fe(CN)6]4 redox couple investigated by a.c. impedance spectroscope", Journal of Electroanalytical Chemistry, An International Journal Devoted to All Aspects of Electrode Kinetics, Interfacial Structure Properties of Electrolytes, Colloid and Biological Electrochemistry **364**, 257–260 (1994).

[50]L. M. Peter, W. Dürr, P. Bindra, and H. Gerischer, "The influence of alkali metal cations on the rate of the fe(CN)64/fe(CN)63 electrode process", Journal of Electroanalytical Chemistry and Interfacial Electrochemistry **71**, 31–50 (1976).

[51]V. Sahore, A. Kreidermacher, F. Z. Khan, and I. Fritsch, "Visualization and measurement of natural convection from electrochemically-generated density gradients at concentric microdisk and ring electrodes in a microfluidic system", Journal of The Electrochemical Society **163**, Publisher: IOP Publishing, H3135 (2016).

[52]X. Gao, J. Lee, and H. S. White, "Natural convection at microelectrodes", Analytical Chemistry **67**, Publisher: American Chemical Society, 1541–1545 (1995).

[53]A. Sugiyama, M. Hashiride, R. Morimoto, Y. Nagai, and R. Aogaki, "Application of vertical micro-disk MHD electrode to the analysis of heterogeneous magneto-convection", Electrochimica Acta **28**, 5115–5124 (2004).

[54]J. Lazar, C. Schnelting, E. Slavcheva, and U. Schnakenberg, "Hampering of the stability of gold electrodes by ferri-/ferrocyanide redox couple electrolytes during electrochemical impedance spectroscopy", Analytical Chemistry **88**, Publisher: American Chemical Society, 682–687 (2016).

[55]L. M. Fischer, M. Tenje, A. R. Heiskanen, N. Masuda, J. Castillo, A. Bentien, J. Émneus, M. H. Jakobsen, and A. Boisen, "Gold cleaning methods for electrochemical detection applications", Microelectronic Engineering, MNE '08 **86**, 1282–1285 (2009).

[56]A. J. Bard and L. R. Faulkner., "Electrochemical methods: fundamentals and applications.", 2nd edn. Wiley (2000).

[57]R. S. Nicholson, "Theory and application of cyclic voltammetry for measurement of electrode reaction kinetics.", Analytical Chemistry **37**, Publisher: American Chemical Society, 1351–1355 (1965).

[58]M. Stieble and K. Jüttner, "Surface blocking in the redox system pt/[fe(CN)6]3,[fe(CN)6]4: an ac impedance study", Journal of Electroanalytical Chemistry and Interfacial Electrochemistry **290**, 163–180 (1990).

[59]J. Moldenhauer, M. Meier, and D. W. Paul, "Rapid and direct determination of diffusion coefficients using microelectrode arrays", Journal of The Electrochemical Society **163**, Publisher: IOP Publishing, H672 (2016).

[60]S. J. Konopka and B. McDuffie, "Diffusion coefficients of ferri- and ferrocyanide ions in aqueous media, using twin-electrode thin-layer electrochemistry", Analytical Chemistry **42**, Publisher: American Chemical Society, 1741–1746 (1970).

[61]G. P. Rao and S. K. Rangarajan, "A new relaxation method for studying electrode reactions", Journal of Electroanalytical Chemistry and Interfacial Electrochemistry **41**, 473–489 (1973).

[62]I.-F. Hu, D. H. Karweik, and T. Kuwana, "Activation and deactivation of glassy carbon electrodes", Journal of Electroanalytical Chemistry and Interfacial Electrochemistry **188**, 59–72 (1985).

[63]A. .-. Tran, F. Huet, K. Ngo, and P. Rousseau, "Artefacts in electrochemical impedance measurement in electrolytic solutions due to the reference electrode", Electrochimica Acta, ELECTROCHEMICAL IMPEDANCE SPECTROSCOPY **56**, 8034–8039 (2011).

[64]F. Mansfeld, S. Lin, Y. C. Chen, and H. Shih, "Minimization of high-frequency phase shifts in impedance measurements", Journal of The Electrochemical Society **135**, Publisher: IOP Publishing, 906 (1988).

[65]A. Lasia, "Electrochemical impedance spectroscopy and its applications", in *Modern aspects of electrochemistry*, edited by B. E. Conway, J. O. Bockris, and R. E. White, Modern Aspects of Electrochemistry (Springer US, Boston, MA, 2002), pp. 143–248.

[66]G. J. Brug, A. L. G. van den Eeden, M. Sluyters-Rehbach, and J. H. Sluyters, "The analysis of electrode impedances complicated by the presence of a constant phase element", Journal of Electroanalytical Chemistry and Interfacial Electrochemistry **176**, 275–295 (1984).

[67]A. Więckowski and M. Szklarzyk, "The state of the polycrystalline platinum electrode during the heterogeneous electron-transfer reaction: fe(CN)63+eFe(CN)64", Journal of Electroanalytical Chemistry and Interfacial Electrochemistry **142**, 157–170 (1982).

[68]K. Niwa and K. Doblhofer, "Ir spectroscopic study of adsorbed species formed on electrodes during the fe(cn)346 charge transfer reaction", Electrochimica Acta **31**, 439–443 (1986).

[69]R. Aogaki and R. Morimoto, *Nonequilibrium fluctuations in micro-MHD effects on electrodeposition*, Publication Title: Heat and Mass Transfer - Modeling and Simulation (IntechOpen, Sept. 22, 2011).

[70]D. Fernández and J. M. D. Coey, "Inhomogeneous electrodeposition of copper in a magnetic field", Electrochemistry Communications **11**, 379–382 (2009).

[71]Z. Diao, N. Decorde, P. Stamenov, K. Rode, G. Feng, and J. M. D. Coey, "Magnetization processes in micron-scale (CoFe/pt)n multilayers with perpendicular anisotropy: first-order reversal curves measured by extraordinary hall effect", Journal of Applied Physics **111**, Publisher: American Institute of Physics, 07B538 (2012).

[72]S. Tanuma, C. J. Powell, and D. R. Penn, "Calculations of electron inelastic mean free paths. v. data for 14 organic compounds over the 50–2000 eV range", Surface and Interface Analysis **21**, _eprint: https://onlinelibrary.wiley.com/doi/pdf/10.1002/sia.740210302, 165–176 (1994).

[73]L. Katona, D. Bianchi, J. Brenner, G. Vorlaufer, A. Vernes, G. Betz, and W. S. M. Werner, "Effect of surface roughness on angle-resolved XPS", Surface and Interface Analysis **44**, _eprint: https://onlinelibrary.wiley.com/doi/pdf/10.1002/sia.4886, 1119–1123 (2012).

[74]G. Hinds, J. M. D. Coey, and M. E. G. Lyons, "Influence of magnetic forces on electrochemical mass transport", Electrochemistry Communications **3**, 215–218 (2001).

[75]A. Bund, S. Koehler, H. H. Kuehnlein, and W. Plieth, "Magnetic field effects in electrochemical reactions", Electrochimica Acta, New Developments in Electrode Kinetics:Selection of Papers from the 2nd Gerischer Symposium **49**, 147–152 (2003).

[76]R. Aogaki, K. Fueki, and T. Mukaibo, "Application of magnetohydrodynamic effect to the analysis of electrochemical reactions 1MHD flow of an electrolyte solution in an electrodecell with a short rectangular channel", Denki Kagaku oyobi Kogyo Butsuri Kagaku **43**, 504–508 (1975).

[77]T. Watanabe, Y. Tanimoto, T. Sakata, R. Nakagaki, M. Hiramatsu, and S. Nagakura, "The magnetic field effects on the electrolysis of hexacyanoferrate(II) oxidation and hexacyanoferrate(III) reduction", Bulletin of the Chemical Society of Japan **58**, Publisher: The Chemical Society of Japan, 1251–1254 (1985).

[78]R. Aogaki, K. Fueki, and T. Mukaibo, "Diffusion process in viscous flow of electrolyte solution in magnetohydrodynamic pump electrodes", Denki Kagaku oyobi Kogyo Butsuri Kagaku **44**, 89–94 (1976).

[79]K. M. Grant, J. W. Hemmert, and H. S. White, "Magnetic focusing of redox molecules at ferromagnetic microelectrodes", Electrochemistry Communications **1**, 319–323 (1999).

[80]R. Aogaki, "Magnetic field effects in electrochemistry", Magnetohydrodynamics **37**, 143–150 (2001).

[81]R. N. O'BRIEN and K. S. V. SANTHANAM, "Magnetic field assisted convection in an electrolyte of nonuniform magnetic susceptibility", Journal of Applied Electrochemistry **27**, 573–578 (1997).

[82]M. D. Pullins, K. M. Grant, and H. S. White, "Microscale confinement of paramagnetic molecules in magnetic field gradients surrounding ferromagnetic microelectrodes", The Journal of Physical Chemistry B **105**, Publisher: American Chemical Society, 8989–8994 (2001).

Chapter 4

Electrically Programmable Magnetic Field Gradient Using Focused He^+ Beam Irradiation

In the previous chapter, we discussed how a chemical reaction can be affected by the large field gradient created at the electrochemical interface. Co/Pt multilayers having multi-domains in the remanent magnetic state were used as primary source of the field and field gradient. Such a multilayer allowed the field gradient landscape to be repeatedly switched on and off by applying or removing the external field. However, the domain manipulation by applied field is limited in terms of spatial control and temporal resolution. Recently, it has been reported that the magnetization of nanomagnetic objects can be electrically manipulated within sub-ns time resolution using the technique known as spin orbit torque (SOT) switching. We try to explore the possibilities of this switching process along with the aid of focused light ion irradiation for the spatio-temporal control over the magnetic patterning, while preserving the flat topography of the sample. We discuss the initial results of this long-term project, and shows the pathway through which a model system is created.

4.1 Introduction

Multi-domain states in perpendicular magnetic anisotropy (PMA) thin films can be created either by adjusting the film properties (number of repeats, thickness of magnetic layer), or by patterning using ion irradiation. As compared to the former method, the irradiation assisted patterning is an additional processing step but offers better spatial control of magnetic domains. In order to demonstrate the magnetic patterning and selective magnetization switching in PMA thin films, focused helium ion beam (FIB) is utilized. As compared to other techniques like the focused gallium ion beam and the electron beam, focused helium

ion irradiation offers nanometer precision patterning due to its low scattering and minimal beam divergence in the sample material [1] while keeping limited sample surface damage. Magnetic patterning using broad beam irradiation has been demonstrated using photoresist masks [2–4], but the smallest patterned magnetic bit is mostly determined by the resolution of lithography steps rather than the ion-beam interaction volume [5]. On the contrary, focused helium ion beam allows maskless nanopatterning where the lateral dimensions of the magnetic structures are limited only by the size of collision cascade ($\leq$ 10 nm) [1]. In addition to the nano precision, this approach also preserves the flat topography of the initial magnetic stack [2] which is a major prerequisite for the electrochemical applications we envision [6]. In thin magnetic multilayers, light ion irradiation causes intermixing of the interface atoms which in turn increases the interfacial roughness [7]. This allows control over the interface dependent magnetic properties like magnetization [8] and magnetic anisotropy [2, 9, 10].

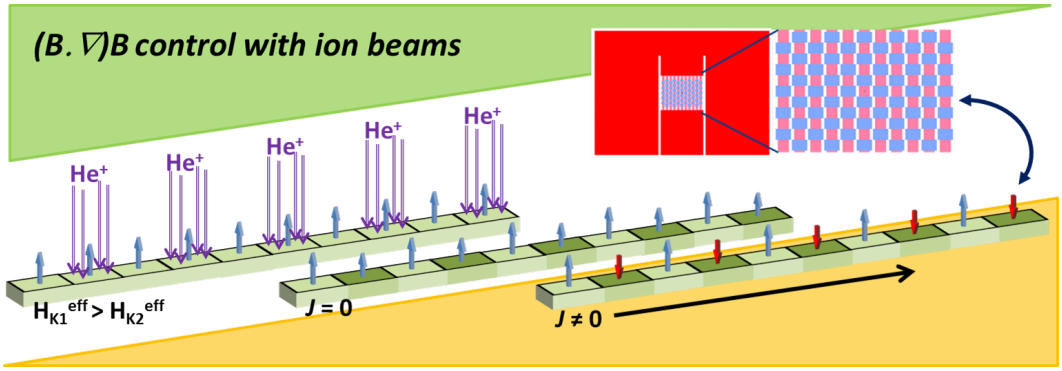

FIGURE 4.1: Spatial control of magnetic anisotropy using light ion irradiation. In the reprogrammable array, selected areas are irradiated with ions causing a reduction in the local magnetic anisotropy field, H_k. The current(J) induced spin-orbit switching will first cause a reversal in areas with reduced H_{eff}, which allows the creation of high magnetic field gradients.

Spin Orbit Torque (SOT) is an efficient way to electrically manipulate the magnetization of nanoscale magnetic objects [11, 12]. As discussed in section 1.4.2.2, the current required to switch the magnetic state ($\pm M_z$) depends on several parameters including saturation magnetization and magnetic anisotropy of the thin film [13], which are difficult to alter locally within a film. It has been recently demonstrated that the photoresist assisted broad beam irradiation can reduce the SOT switching current density [14], tailor the domain wall velocity [15], and even drive the multi-level switching [16] in PMA films. We therefore propose to combine the current driven magnetization switching with the focused ion irradiation technology in order to design ***an electrically reprogrammable magnetic patterns which allows spatial control over the field gradient force density*** *(Fig. 4.1)*. Recent studies have shown that

reversible sub-nanosecond (sub-ns) SOT switching can be achieved in PMA thin films [17, 18]. This is particularly interesting in electrochemcial applications as the ionic atmosphere rearrangement ($\sim$ 10 ns) and solvent dipole reorientation ($\sim$ 10 ps) which occur at the electric double layer prior to heterogeneous electron transfer happen at a similar timescale [19]. Thus, the possibility of ultrafast temporal control of individual magnetic bit states might open the door to experiments providing new insight into the influence of field gradient on the dynamics of fast charge transfer process at the solid/liquid interface.

4.2 Helium Irradiation Assisted Selective Current Driven Magnetization Switching in Magnetic Thin Films

In this section, we demonstrate the selective switching of a 10μm x 10μm region as an initial step towards the realisation of an electrically programmable field gradient landscape. To do so, helium ions are irradiated at the cross of a patterned Hall bar where the evolution of magnetic state can be electrically monitored using the anomalous Hall effect (section 2.3.5). Thin films with desired properties are fabricated and characterized to obtain a better understanding of their electrical and magnetic properties prior to the irradiation studies. Based on this precharacterization, optimum conditions for the irradiation studies are identified. The evolution of magnetic and magneto-transport properties with irradiation dose are studied in detail. Finally, the irradiation mediated selective current driven and field driven magnetic multi-domain states is demonstrated.

4.2.1 Fabrication and micro-patterning of thin films

Magnetic heterostructures having perpendicular magnetic anisotropy (PMA) are fabricated using a DC magnetron sputtering system. Thin films were grown in collaboration with the magnetism and spin electronics team at the Trinity College, Dublin. Silicon(100) wafers with thermally oxidised surface layer of 500 nm are used as substrates over which the films are deposited. Pt, W, Ta and Co are deposited at a rate of 0.016, 0.016, 0.012 and 0.014 nm/s respectively. Deposited samples consists of 1 nm magnetic Co layer sandwiched between heavy metals like Pt, W and Ta. The thickness and structure of films are carefully chosen to obtain an efficient electrical control of the magnetic state [20, 21]. The multilayer stacks are made of:

Si/SiO_2//Ta(5.0)/[Pt(2.0)/Co(1.0)/W(1.5)]/Pt(1.5)/Ta(1.5) and

$Si/SiO_2//Ta(5.0)/[Pt(2.0)/Co(1.0)/Ta(1.5)]/Pt(1.5)/Ta(1.5)$

where all thickness are in nm. These heterostructures will be further referred as [Pt/Co/W] and [Pt/Co/Ta] films respectively. The bottom thick Ta layer acts as seed layer over which heterostructures are deposited. The outer Ta layer is expected to be in the oxidized form TaO_x. For use in electrochemistry, the outer layer has to be replaced with Pt layer. Regardless of the limitations in the optimization, these films can be used as a model system towards the realisation of electrically controllable magnetic multi-domain states.

a)

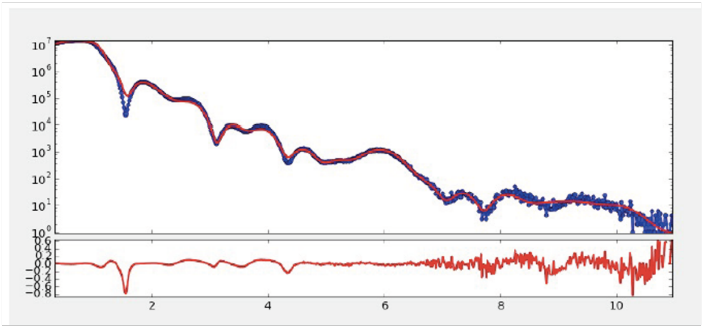

b)

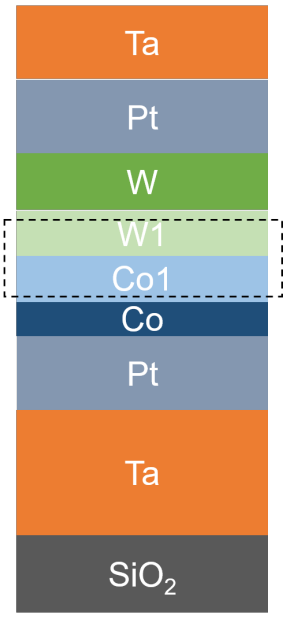

c)

Parameter	Expected thickness nm	Model fit based	
		Thickness ± 0.03 nm	Roughness ± 0.02 nm
Ta	1.5	2.3	0.54
Pt	1.5	2.1	0.33
W	1.5	1.0	0.27
W1	0.0	0.65	0.6
Co1	0.0	0.67	0.43
Co	1.0	0.24	0.22
Pt	2.0	2.1	0.48
SiO_2	Inf	Inf	0.33

FIGURE 4.2: a)X-ray reflectivity data fitted using Genx software for the Pt/Co(1.0)/W film. b) The multilayer structure of the film assumed for the fit and c) the roughness and thickness of individual layers estimated using the fit. Co/W interface is treated as Co/Co1/W1/W where Co1 and W1 are related to the alloy formation.

The deposited samples are characterized using X-ray reflectivity (XRR) measurements to understand the interfacial properties of films (Fig. 4.2). Interface plays a crucial role in the perpendicular magnetic anisotropy (PMA) as well as in the current driven magnetization switching measurement [22]. In order to fit the XRR data[1], a model assuming the alloy formation at the Co/W interface (Co/W $\rightarrow$ Co/Co1/W1/W) is used. Such an assumption can be supported by the alloy formation at Co/W interface reported in several studies [23,

[1]Thanks to Dr. Anna Oleshkevych for her help with XRR fit

24]. Based on the fit analysis, an alloy formation at the Co/W interface, represented as Co1 and W1, could be observed. The Pt/Co interface is also known to alloy [25] but neglected in this model as additional parameters will add more complexity to the fit and the analysis.

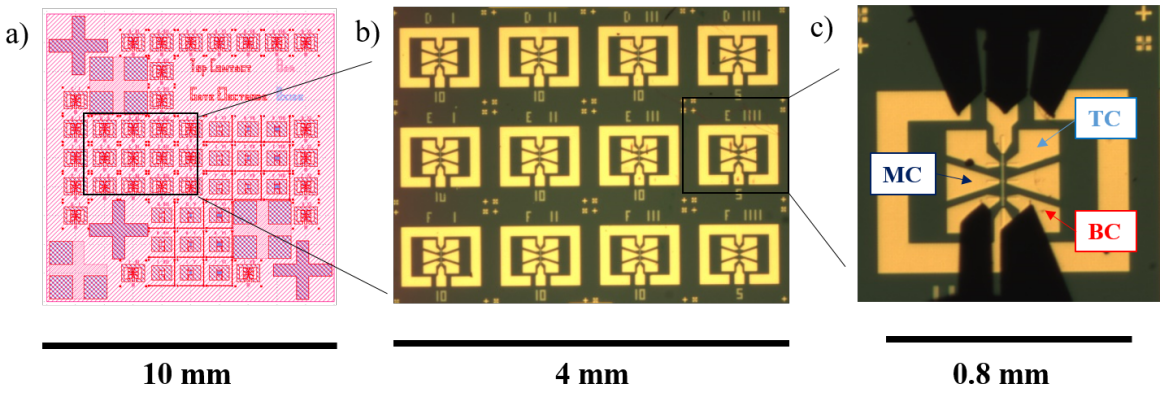

FIGURE 4.3: Lithography pattern. a) Schematic of designed mask. b) Example optical image of patterned Hall bars, and c) electrical contacts on Hall bar using the microtips

Pattering and characterization of these thin films were performed in collaboration with HZDR, Dresden. Micron sized Hall bars were patterned using the combination of UV lithography, Ar+ ion milling and lift-off. A second UV lithography step was performed, and Cr(5.0) /Au(125.0) (numbers in nm) contact pads were deposited on top by thermal evaporation, followed by removal of the photoresist. Design and the optical image of the Hall bar are shown in Fig. 4.3. The bars are 300 µm long, and 10 µm wide. There are three junctions per device, labelled as top cross (TC), middle cross (MC), and bottom cross (BC), contacted using prober microtips to apply current (3 tips at the top) along the Hall bar while recording the transverse voltage (2 tips at the bottom) (Fig. 4.3c).

4.2.2 Pre-characterisation of magnetic thin films

4.2.2.1 Magnetization measurements

Magnetic moment of unpatterned thin films are measured in a commercial SQUID-VSM magnetometer with external field up to 7 T applied both along and normal to the film surface (Fig. 4.4). Robust PMA in both films is confirmed with a saturation magnetization, M_s, 0.84 MA/m and 0.47 MA/m for Pt/Co/W and Pt/Co/Ta films respectively. The obtained M_s value for W-based and Ta-based films are about 42 % and 67 % smaller compared to the bulk magnetization value of hcp Co 1.44 MA/m [26]. We attribute this to the presence of alloy formation at the interface as observed by the XRR measurements (section 4.2.1). The M_s reduction due to the presence of a magnetic dead layer at the Co/W [23] [24] and

Co/Ta [27] interfaces has been previously reported in similar multilayer based systems. The anisotropy field, H_K, is obtained from the in-plane SQUID data and are 1.28 T and 1.2 T for Pt/Co/W and Pt/Co/Ta films respectively, summarized in Table 4.1.

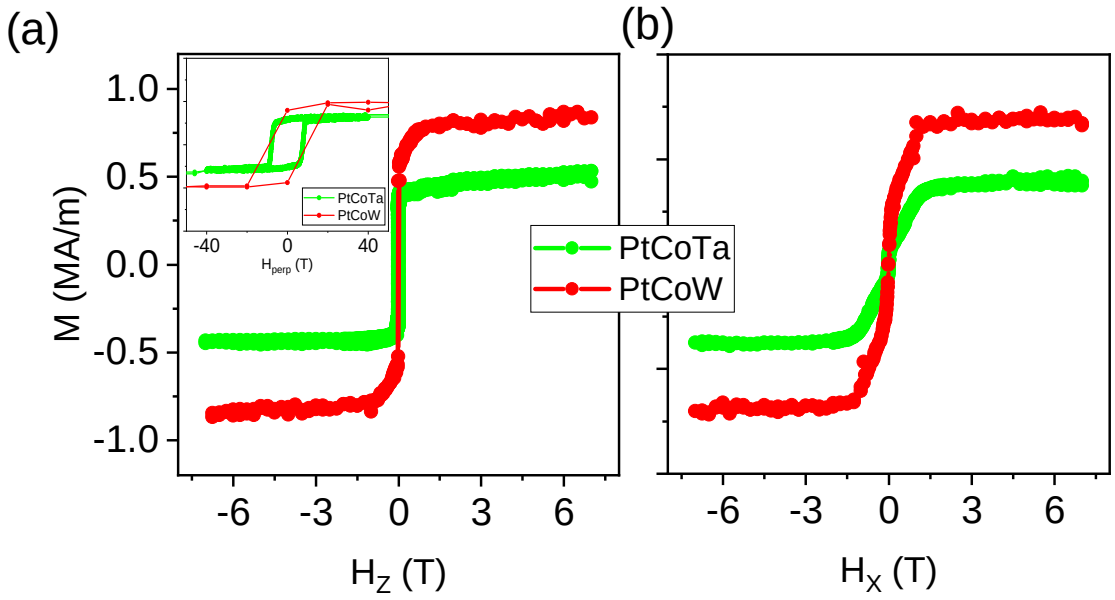

FIGURE 4.4: SQUID measured magnetization curves obtained for Pt/Co/Ta and Pt/Co/W films under a) out-of-plane field and b) in-plane field configurations.

4.2.2.2 Magneto-transport measurements

The anomalous Hall effect(AHE), voltage proportional to the out-of-plane component of the magnetization, is used to study the evolution of magnetic states as a function of current or field applied to the patterned devices.

4.2.2.3 AHE as a function of applied magnetic field

Measurements are performed by applying a DC current of 1 mA and recording the transverse voltage as a function of field. An out-of-plane magnetic field (OP) is swept between + 46 mT and -36 mT with a step size 2 mT. Square hysteresis loops under OP field with unit remanence ratio confirms PMA in both patterned samples (Fig. 4.5a). Under OP field switching, the total change of Hall resistance upon magnetization switching is 1.22 Ω and 1.14 Ω respectively for Pt/Co/W and Pt/Co/Ta devices (Fig. 4.5a). The smaller value for Pt/Co/Ta device is due to its lower magnetization compared to Pt/Co/W (Table 4.1).

AHE based transverse resistance is also measured as a function of in-plane (IP) field applied between +/- 0.9 T with a step of 10 mT. It is interesting to note the change in the shape of the SQUID and AHE curves obtained under IP magnetic field (Fig. 4.4b and Fig. 4.5b).

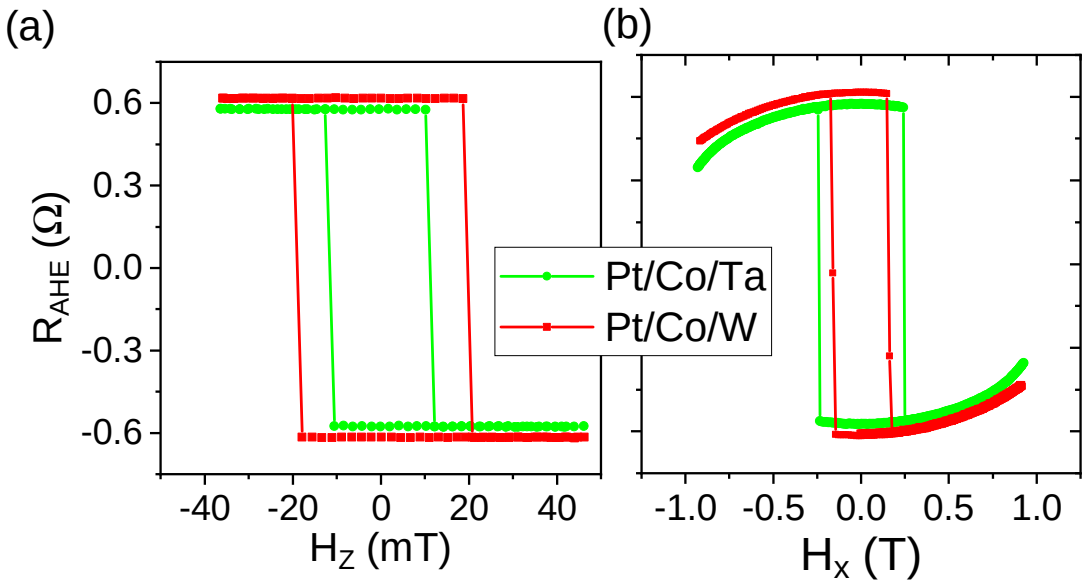

FIGURE 4.5: Anomalous Hall resistance loop as a function of a) out-of-plane and b) in-plane magnetic field

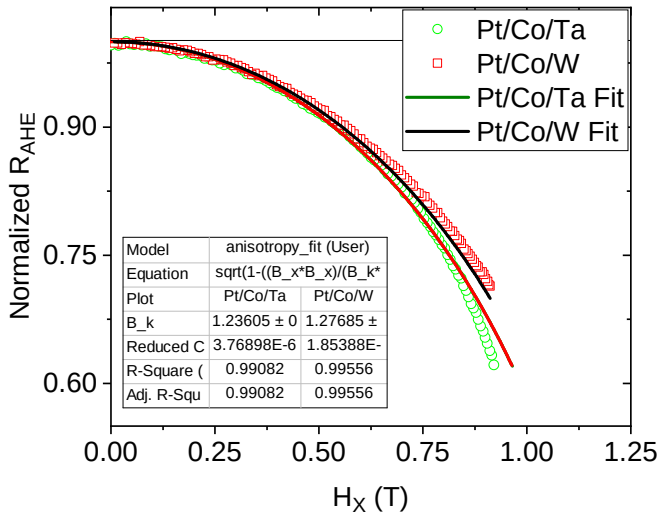

FIGURE 4.6: Normalized Hall resistance (open symbol) of single repeat Pt/Co/W and Pt/Co/Ta thin films as a function of in-plane field and the corresponding anisotropy fit (line)

In SQUID measurements, under IP field, the in-plane component of magnetization (M_x) is measured while AHE is always proportional to the M_z component irrespective of the applied field direction. So, the change in the shape of the curve is related to the difference in the component of magnetization measured in each method.

AHE data under IP field can be used to quantify the anisotropy field of the patterned device. Assuming a coherent rotation for the single domain PMA film under IP field, the magnetic energy can be estimated using the Stoner-Wohlfarth model as [26]

$$E = K_u \sin^2\theta - \mu_0 M H_x \cos(\theta - \pi/2) \tag{4.1}$$

where K_u is the uniaxial anisotropy, θ is the angle between magnetization and surface normal, and H_x is the IP field. Solving Eqn. 4.1 for the energy minimization, and considering the M_z dependence of AHE, we arrive at the relation

$$M_z^{'} = \sqrt{1 - \left(\frac{B_x}{B_k}\right)^2} \tag{4.2}$$

where $M_z^{'}$ is the normalised z component of magnetization, $B_x = \mu_0 H_x$ and $B_k = \mu_0 H_k$ are the applied field and anisotropy field. Fig. 4.6 shows the normalised AHE data in the first quadrant and the anisotropy fit of the samples. The estimated anisotropy field from the fit, 1.27 T for Pt/Co/W and 1.23 T for Pt/Co/Ta, are in good agreement with the obtained values using SQUID: 1.28 T for Pt/Co/W and 1.2 T for Pt/Co/Ta.

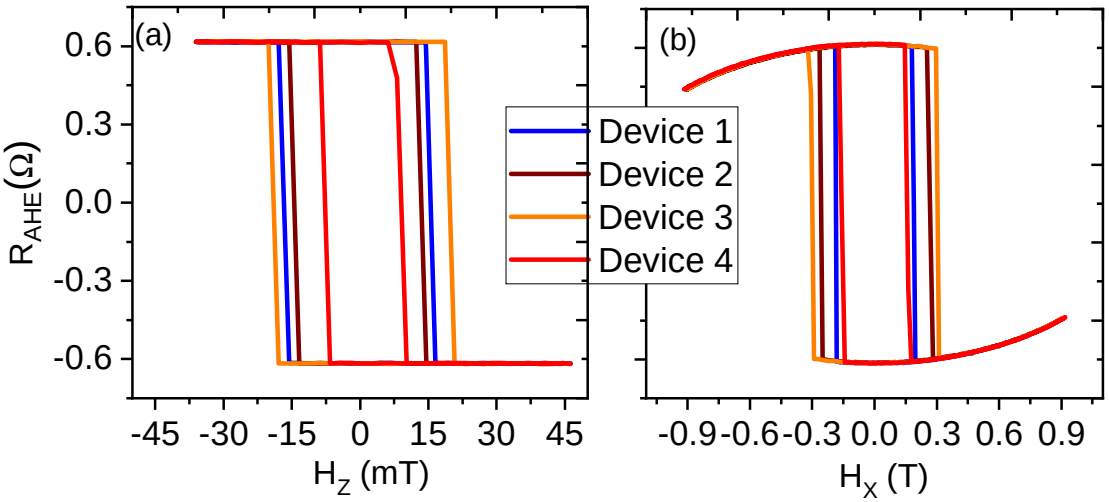

FIGURE 4.7: Distribution of coercivity and anisotropy field of Pt/Co/W devices. Anomalous Hall resistance loop of different Pt/Co/W Hall bars under a) OP applied field and b) IP applied field.

Furthermore, for a better understanding of the coercivity and anisotropy field distribution, magnetic switching under OP and IP field is measured for different Pt/Co/W devices as shown in Fig.4.7(a) and (b). As can be seen in Fig. 4.7a, as expected, the curves overlap under OP field when the R_{AHE} is +/- 0.6 Ω. This implies that the magnetization is saturated along the easy z-axis and its value is invariant irrespective of the Hall bar. However, the coercivity is found to have a 26 % variation, 14 ± 4 mT, which shows its dependence on lithography steps and slight deviations in the Hall bar size, shape and roughness. The lithography based patterning can also induce defects that can act as a source of nucleation/pinning of magnetization reversal which subsequently increases the degree of irreproducibility. On the other hand, from Fig. 4.7b, we find less than 1 % variation in the anisotropy field, 1.27 ± 0.01 T, which suggests its insensitivity to the lithography process and its intrinsic nature determined by the deposition parameters and related thin film properties. Thus, the current induced magnetization reversal, as the switching current mostly depends on intrinsic parameters, can offer advantage in terms of reproducibility of the properties of magnetic bits (detailed discussion in section 4.3.2.2). Moreover, since we tailor the anisotropy directly using irradiation [7], the light ion irradiation can be considered as a robust technique for magnetic patterning.

4.2.2.4 SOT switching

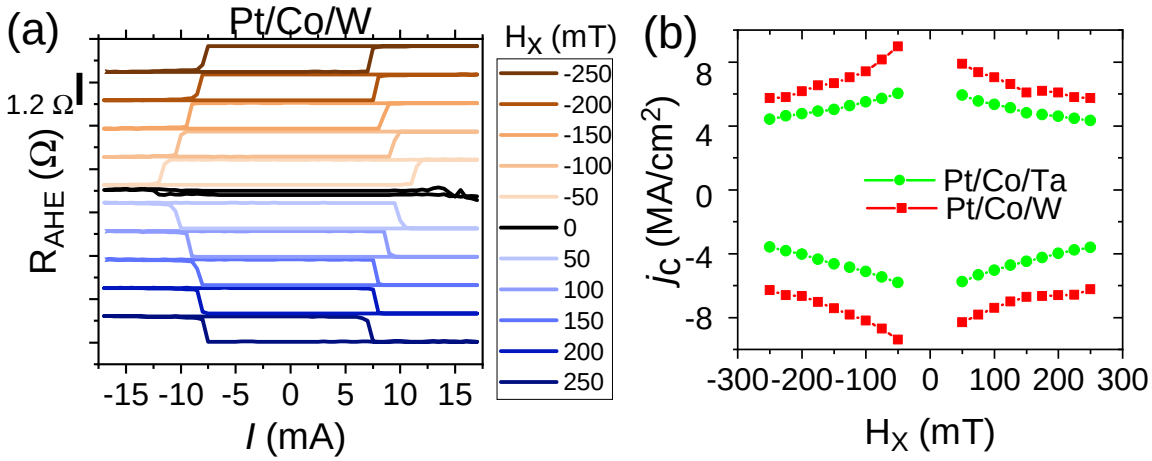

FIGURE 4.8: SOT switching under different bias field. a) current driven switching of single repeat Pt/Co/W device under different in-plane bias field. Data are offset in Y axis for clarity. b) phase diagram of SOT switching current density and bias field verses the magnetic state of Pt/Co/W and Pt/Co/Ta devices.

Current driven magnetization switching measurements are performed by applying current pulses of 2 ms width with a 1 s delay between consecutive pulses, that is, a duty cycle of

0.2 %, which ensures minimal thermal effects in the devices. Based on the macrospin model, the switching current density j_c can be expressed as

$$j_c = \frac{2e\mu_0 M_s t_f}{\hbar\theta_{SH}} \left(\frac{H_k}{2} - \frac{H_x}{\sqrt{2}} \right) \tag{4.3}$$

where e is the electronic charge, M_s is the saturation magnetization, t_f is the magnetic layer thickness, θ_{SH} is the effective spin Hall angle, and H_k, H_x are the anisotropy and bias fields. Measurements are performed under several different bias magnetic field values ranging between $\pm$ 250 mT applied along/opposite to the longitudinal current line as shown in Fig. 4.8a. Deterministic current driven magnetization switching is achieved in both devices with a non-zero bias field of magnitude higher than 50 mT. Under a bias field of 150 mT, the average switching current density (j_c) is 6.0 MA/cm^2 for Pt/Co/W and 5.2 MA/cm^2 for Pt/Co/Ta device. As expected from the macrospin model of SOT switching (Eqn. 4.3), j_c for Pt/Co/W is higher than that of Pt/Co/Ta as the former has a comparatively higher saturation magnetization and slightly higher anisotropy field (table 4.1). For both devices, the current required to switch the magnetization increases with decreasing bias field as shown in Fig. 4.8b. No switching is observed at zero bias field.

4.2.2.5 Second harmonic Hall measurement

Harmonic Hall measurements are used to quantify the spin-orbit effective field in the Pt/Co/W thin film. Measurements are performed by applying a sinusoidal ac current (frequency 1234.56 Hz) having amplitude in the range of 1 mA (0.8 MA/cm^2) to 4 mA(3.2 MA/cm^2). The first (V_ω) and second ($V_{2\omega}$) harmonic Hall voltages are detected using a lock-in amplifier while sweeping the field in longitudinal (H_X) and transverse (H_Y) directions. Prior to measurements, the device is magnetized by applying an out-of-plane field of 0.45 T, large enough to saturate the sample. Fig.4.9 shows the harmonic Hall data under longitudinal and transverse field configurations measured under current of 2 mA. Assuming low Joule heating, uniaxial anisotropy and small magnetization tilt, the current induced effective field, ΔH_{SL} and ΔH_{FL}, can be obtained using the expression:

$$\Delta H_{SL} \approx -2 \left\{ \frac{\partial V_{2\omega}}{\partial H_x} \Big/ \frac{\partial^2 V_\omega}{\partial H_x^2} \right\} \text{ and } \Delta H_{FL} \approx -2 \left\{ \frac{\partial V_{2\omega}}{\partial H_y} \Big/ \frac{\partial^2 V_\omega}{\partial H_y^2} \right\} \tag{4.4}$$

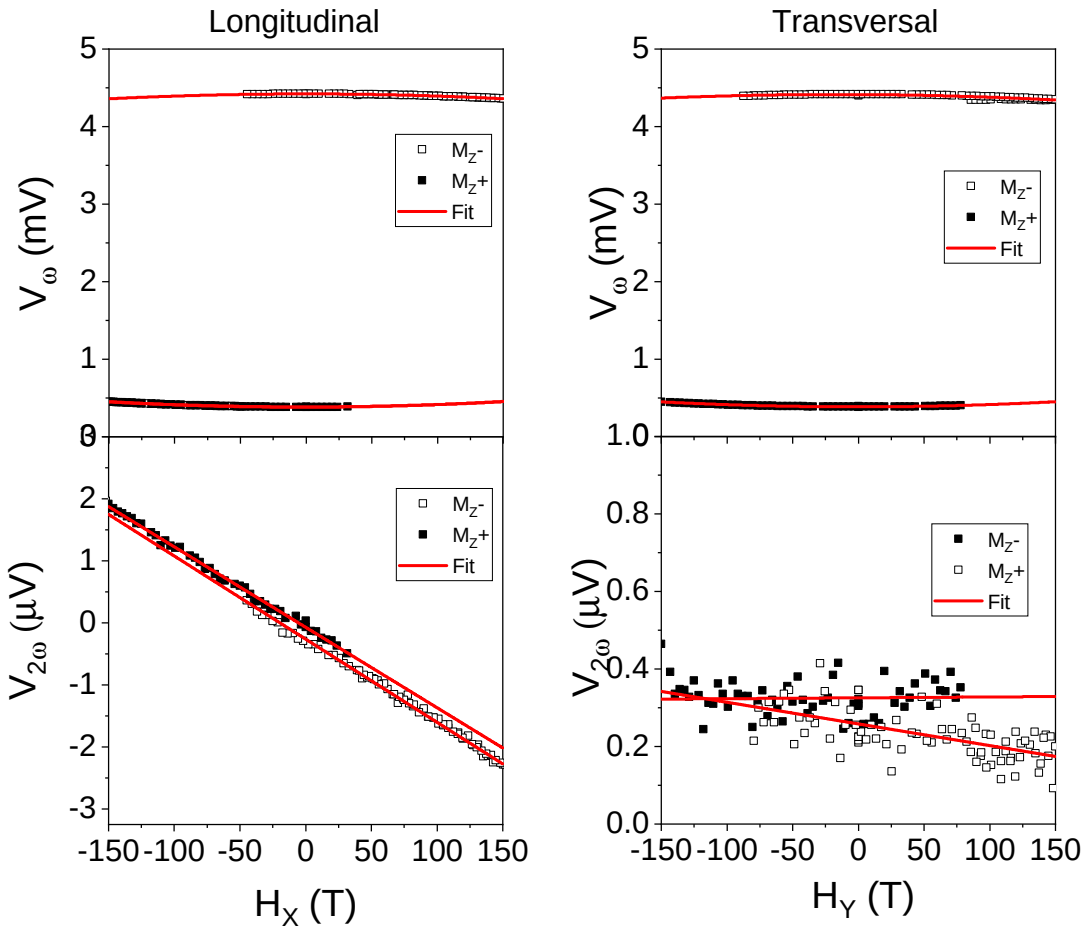

FIGURE 4.9: First and second harmonic Hall measurement of Pt/Co/W device under magnetic field applied longitudinal and transverse to the current channel. The effective current density through the device is 1.6 MA/cm^2

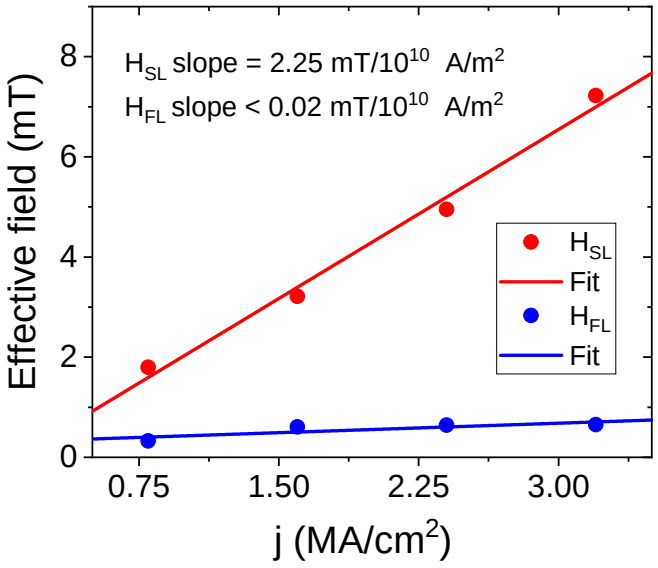

FIGURE 4.10: Damping-like ΔH_{SL} and field-like ΔH_{FL} effective field as a function of current density for the Pt/Co/W device.

V_ω and $V_{2\omega}$ are fitted using quadratic and linear function respectively to obtain the current induced effective field. The linear dependence of the effective field with current indicates a negligible effect of Joule heating in the measured current range (Fig. 4.10). The obtained value of H_{SL}/j is 2.25 mT/ 10^{10}A/m^2 and H_{FL}/j is < 0.02 mT/ 10^{10}A/m^2. The order of magnitude difference between the effective fields indicate the dominant role of damping like torque on the current induced magnetization switching in Pt/Co/W device. It is known that planar Hall effect (PHE) also contributes to the harmonic signal when its value is comparable to AHE ($\xi = {}^{\Delta R_{PHE}}/_{\Delta R_{AHE}} > 0.5$). However, in similar Pt/Co/W systems, ξ is found to be as small as 0.05 [28]. Therefore, we also assume a weak PHE contribution in the Pt/Co/W film and neglect its effect in further analysis. Based on the drift-diffusion model [29], the damping like torque is derived from the bulk spin Hall effect where the spin current generated due to bulk spin-orbit coupling diffuses through a transparent heavy metal/ferromagnet interface and exerts a torque. In such a case, the effective spin Hall angle of the heterostructure, θ_{SHA}, can be estimated as,

$$\theta_{SHA} = \frac{2e}{\hbar}\frac{\mu_0 H_{SL} M_s t_{FM}}{j} \tag{4.5}$$

where t_{FM} is the ferromagnetic layer thickness and j is the total current density passing through the multilayer stack. Using M_s = 0.84 MA/m obtained from SQUID and the magnetic layer thickness t_{Co} = 1.0 nm, we obtain the effective θ_{SHE} = 0.43 for the Pt/Co/W device. The obtained value is comparable to the values that has reported for similar heavy metal sandwiched magnetic layer based heterostrutures, 0.35 for Pt/Co/Ta [30], 0.45 for Pt/Co-Ni/W [31] and 0.41 for Pt/Co/Cr/Ta [32] thin films. The θ_{SHE} of Pt is $\sim$ +0.07 [12] [33] and the one of β-phase W is -0.3 [21], lower than that of the Pt/Co/W film. The enhanced damping like torque and θ_{SHE} in the current device is attributed to the dissimilar metals with opposite spin Hall angles on opposite sides of the ferromagnet [30, 31, 34].

It is important to note that an Oersted field, $H_{oersted}$, generated by the current flowing through the top and bottom heavy metals, can also affect the efficiency of SOT switching [35] as it has the similar symmetry to the field-like current-induced field. As the Hall bar width (10 μm) is significantly larger than its thickness (12.5 nm), the current flowing device can be approximated as flowing through an infinitely long sheet and from Ampere's law, $H_{oersted} \approx \mu_0 \frac{j_{HM} t_{HM}}{2}$. For t_{HM}= 5 nm, the Oersted field is found to be 0.03 mT/10^{10} A/m^2 which is negligible compared to the damping like field.

Table 4.1 summarises the obtained properties of Pt/Co/W and Pt/Co/Ta samples. Even

Samples	M_s $\pm$ 0.03 MA/m	H_K $\pm$ 0.02 T	K_{eff} kJ/m^3	Δ	j_c^{av} $\pm$ 0.4 MA/cm^2
Pt/Co/W	0.84	1.27	537 $\pm$ 27	133 $\pm$ 7	6.0
Pt/Co/Ta	0.47	1.23	289 $\pm$ 23	72 $\pm$ 3	4.6

TABLE 4.1: Summary of initial characterisation of Pt/Co/W and Pt/Co/Ta thin films. M_s is obtained from SQUID. All other parameters are obtained from magneto-transport measurement

though both samples have similar anisotropy field, the higher M_s value hints on a better interface quality in Pt/Co/W film compared to Pt/Co/Ta film. The effective anisotropy energy, $K_{eff} = M_s H_K/2$, is also found to be lower in Pt/Co/Ta devices. The average SOT switching current density, j_c^{av}, is found to be higher in Pt/Co/W compared to the Pt/Co/Ta device which is related to the higher M_s value of the former device and can be explained by the macrospin model. The thermal stability factor is defined as $\Delta = K_{eff} V / k_B T$, where V is the magnetic element volume, k_B is the Boltzman constant and T is the temperature. Δ is a measure of the amount of magnetic energy required to stabilize the magnetic bits compared to the thermal energy. For both devices, Δ, calculated for a high data density 32 nm sided magnetic bit [36] with 1 nm magnetic layer thickness, is found to be > 60, which is the criterion for 10 years stable storage [37].

4.2.3 Focused He^+ ion irradiation

A Carl Zeiss Orion Nanofab helium ion microscope is used to locally irradiate the Hall bar. The spot size of the beam at the sample surface is below 4 nm, and the beam voltage is held at 25kV. The beam current is measured on the beam blanker before each exposure and is typically 0.6 pA. A 0.1 pA current is occasionally used when lower dose rates are needed. Using four Kleindiek MM3A micromanipulators inside the chamber, it is possible to monitor, in real time, the evolution of the anomalous Hall resistance with irradiation dose (Fig. 4.11a). A Keithley 2400 source meter is used to provide a continuous 1 mA DC transverse current and measure the corresponding longitudinal voltage evolution with junction irradiation under zero applied magnetic field (Fig. 4.11b). This *in situ* electrical characterization along with the possibility of interface engineering using ion irradiation offers high flexible, high spatial resolution, and high precision magnetic patterning for fundamental and application based studies.

Fig. 4.11b shows the evolution of the Hall resistance with irradiation of both Pt/Co/W and Pt/Co/Ta Hall bar crosses. The size of the irradiated cross is 10 µm x 10 µm. In the case

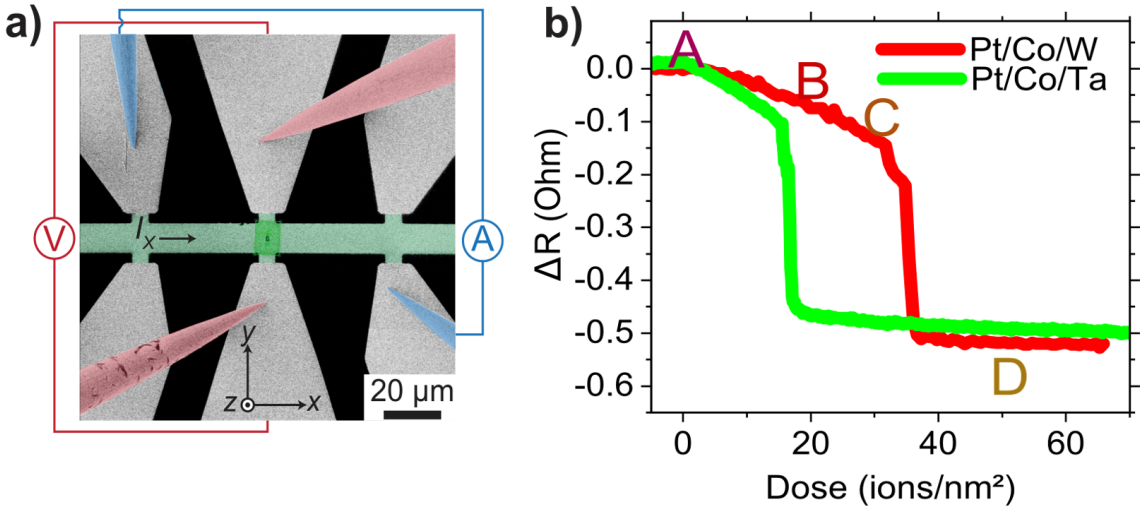

FIGURE 4.11: Focused ion beam irradiation and in situ characterization . a) False coloured helium microscope image of the patterned Hall bar b) real time in situ evolution of anomalous Hall resistance with irradiation dose.

of Pt/Co/W film , R_{AHE} gradually reduces until a critical dose of 35 ions/nm^2 is reached, after which a sharp drop is observed. This reduction in the Hall resistance is ascribed to the decreased perpendicular magnetic anisotropy due to the irradiation induced interface mixing. When the ion dose is greater than a critical value, the magnetization undergoes a sharp transition from out-of-plane to in-plane which corresponds to the sharp drop in the AHE measurement curve. The total deflection in the Hall resistance during the irradiation is 0.52 Ω which is close to the half of the 1.22 Ω Hall resistance change under the OP field driven switching. The offset of $\sim$ 0.1 Ω is due to the sensitivity of AHE to the unirradiated region close to the Hall cross.

In situ irradiation studies are also performed on the Pt/Co/Ta samples (Fig. 4.11b). The critical dose of this film is found to be 16 ions/nm^2 which is comparatively lower than that of Pt/Co/W films. This might be due to the previously observed poor interface of the heterostructure. Thus, the *in situ* irradiation measurements can also be used as a complementary method to indirectly study the interface quality. All the irradiation experiments and further characterization are limited to Pt/Co/W based samples owing to its better interface quality compared to the Pt/Co/Ta sample.

Resistivity of the heavy metal layer adjacent to the magnetic layer can modulate the SOT switching efficiency [38–40]. Change in the bulk resistivity of Pt enhances the spin orbit coupling effects and improve the spin current generation. However, this increased resistivity can adversely affect the power efficiency as well cause current shunting effects in the FM layer [41]. Therefore, an understanding of the resistivity evolution with irradiation

is required to describe the physical origin of the irradiation effects on the SOT switching. We thus measured the change in the nominal resistivity as a function of irradiation dose *in situ* using the 4-probe method(Fig. 4.12). The nominal resistivity changes from 214 μΩ.cm for unirradiated sample to 224 μΩ.cm for 30 ions/nm^2 dose. Such a small change (5%) might be due to the interface modification rather than a bulk effect. Nevertheless, this small change is incorporated in the SOT efficiency calculation which will be discussed in the next section.

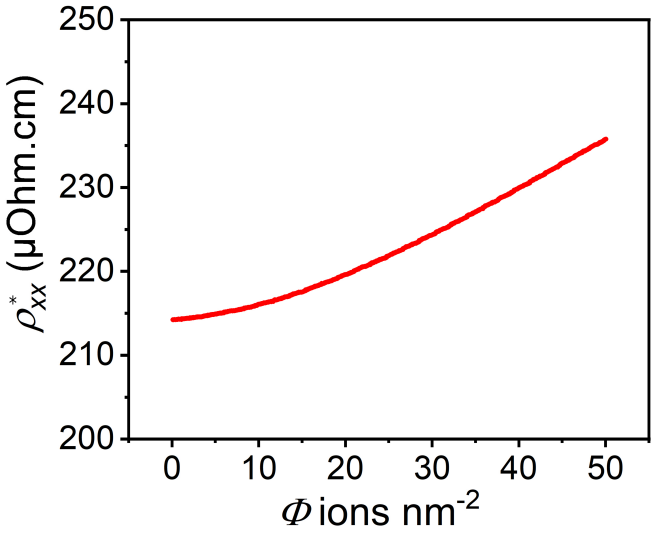

FIGURE 4.12: *In-situ* nominal longitudinal resistivity ρ^*_{xx} evolution of Pt/Co/W thin film with helium irradiation. The resistivity estimation not taken into account the sample thickness change with irradiation.

4.2.4 Irradiation induced effects in the Pt/Co/W device

In order to study the helium irradiation effects on the magnetic and current driven magnetization switching, four doses noted A, B, C, D are chosen along the irradiation curve (Fig. 4.11b) of the Pt/Co/W film. Irradiation effects on the Hall resistance hysteresis under the OP and IP magnetic field are shown in Fig. 4.13. Except for 1 ion/nm^2 in Fig. 4.13a, coercivity diminishes with irradiation, but this finding should be treated with caution as we already discussed the strong dependence of coercivity on the lithography pathway. Any effect of irradiation on coercivity might possibly be due to the reduction in the interfacial strain and the creation of nucleation centers. It is previously reported that broad beam He$^+$ ion irradiation facilitates interface intermixing and alloy formation at the Co/Pt interface [7] which results in a decrease of coercivity [2]. Furthermore, a reduction in the saturation resistance is observed with the irradiation dose, related to the irradiation induced reduction of saturation magnetization of thin film due to alloying of the interfaces. Under the IP and

OP applied fields, several steps are observed in the Hall loop when the irradiation dose is $\geq$ 30 ions/nm^2. The additional steps are due to the Hall sensitivity to the unirradiated regions adjacent to the irradiated one as well as the multi-domain nature of the switching . When the device is irradiated with a dose of 50 ions/nm^2, exceeding the critical dose of 35 ions/nm^2, PMA is lost as can be seen from the Hall loop under OP applied field.

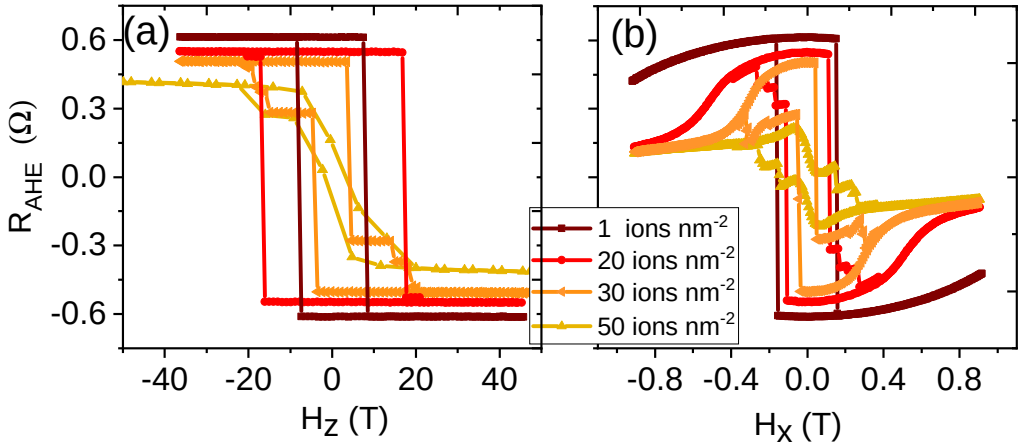

FIGURE 4.13: Ex situ anomalous Hall resistance loop of Pt/Co/W devices irradiated with different doses under a) out-of-plane and b) in-plane magnetic field

To estimate the anisotropy field of the irradiated crosses, normalized magnetization data under IP applied field is fitted using Eqn. 4.2 and is shown in Fig. 4.14a. After irradiating the sample with dose $\geq$ 20 ions/nm^2, a significant deviation from the macrospin coherent rotation based fit can be observed, which is likely due to the formation of magnetic domain structures. The saturation magnetization change with dose (Fig. 4.14b) is determined from the relative change in the *ex situ* saturation Hall resistance under OP applied field (Fig. 4.13a). Upon irradiating the film with near critical dose of 35 ions/nm^2, the anisotropy field is reduced from 1.27 T to 0.41 T, that is a reduction of 67 % from the initial value. The saturation magnetization, on the other hand, is less sensitive to the irradiation and only reduces by 13.7 % from the unirradiated film initial value.

The macrospin model for SOT switching (Eqn. 4.3) implies that both H_k and M_s plays an important role in determining the current density for magnetization switching. Fig. 4.15a shows the evolution of SOT switching under a bias field of 150 mT. Irradiation does not impact significantly the switching current until a dose of 20 ions/nm^2 is reached with j_c^- reducing from -6.0 to -5.0 MA/cm^2 (Table 4.2). Upon irradiation with a near critical dose of 30 ions/nm^2, the average switching current density drastically reduces by 70 % when compared to the unirradiated samples initial value. This reduction is consistent with the

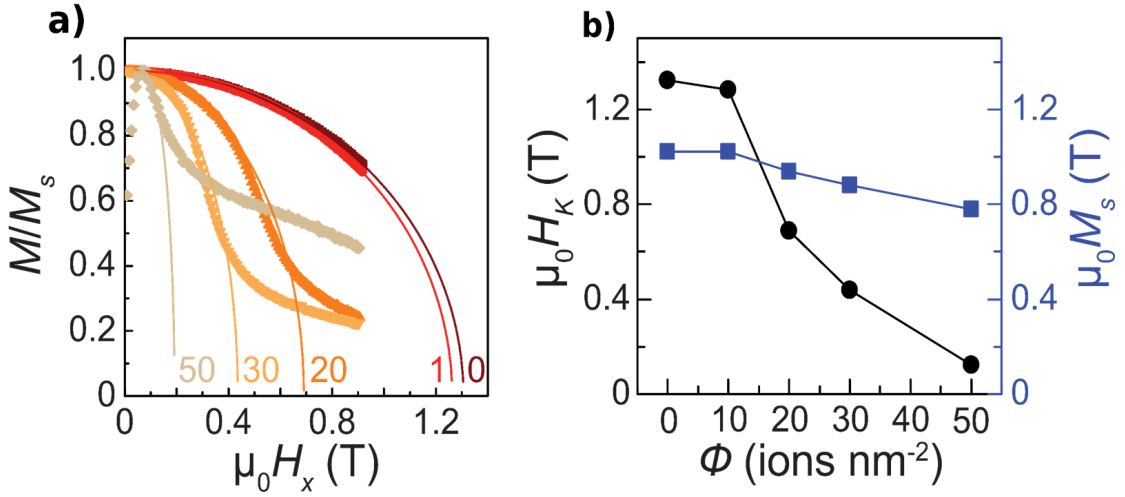

FIGURE 4.14: Magnetic characterization of irradiated Hall bars. (a) normalized magnetization under IP applied field for different irradiation doses and the corresponding anisotropy fit represented as solid lines. (b) Anisotropy field and saturation magnetization as a function of irradiation dose

67% reduction in the anisotropy field of 30 ions/nm^2 irradiated sample. For an overexposed dose of 50 ions/nm^2 irradiated sample, a small Hall loop which corresponds to the switching of adjacent unirradiated region is observed.

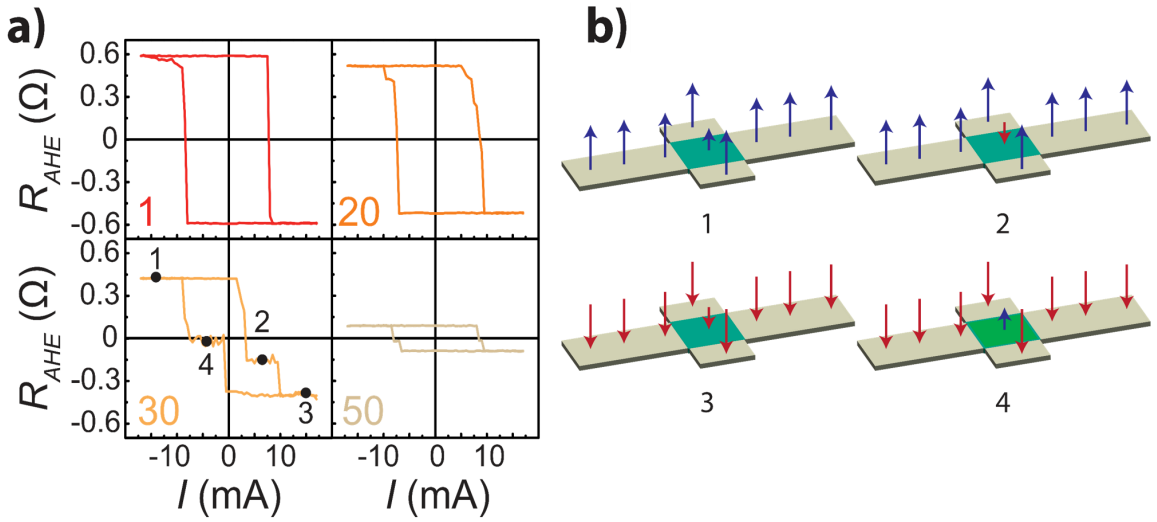

FIGURE 4.15: Current driven switching of irradiated Pt/Co/W films under bias field 150 mT. (a) SOT switching at different irradiation dose and (b) schematics of different magnetic states achievable through SOT switching, numbered 1-4 in 30 ions/nm^2 from sub panel of (a)

In order to further understand the physical origin for the switching current reduction in the irradiated films, harmonic Hall measurements are performed. Both bulk spin Hall effect and the spin transparency at the heavy metal/ferromagnetic interface can be altered

due to the light ion irradiation. As discussed earlier in section 4.2.2.5, harmonic Hall measurements in irradiated devices quantify the effective damping like field as a function of applied current (Fig. 4.16a). We found no appreciable change in the θ_{SHE} with irradiation dose (Fig. 4.16b), which suggests that the spin current generated in the bulk of heavy metal remains unchanged under irradiation. It is important to note that the obtained θ_{SHE} is not corrected for planar Hall effect (PHE) contribution which arises from the in-plane magnetization components. We already observed that the z-component of magnetization is less sensitive to the irradiation compared to the magnetic anisotropy (Fig. 4.14) and it is assumed that PHE contribution is weak in the Pt/Co/W irradiated devices. Moreover, negligible change in the bulk resistivity of the device (Fig. 4.12) also hints that bulk magnetic properties are relatively insensitive to the light ion irradiation as compared to the interface dependent properties like the anisotropy field [38–40].

a)

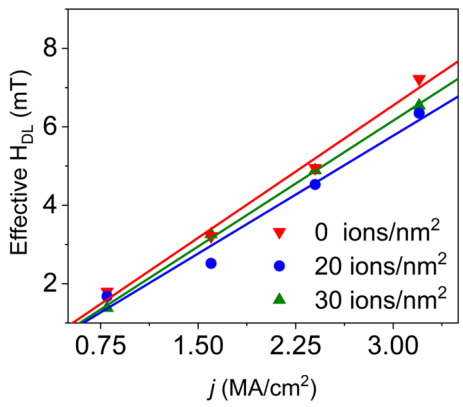

b)

Dose Ions/nm^2	θ_{SHE}
0.0	0.43 ± 0.04
20.0	0.36 ± 0.05
30.0	0.41 ± 0.03

FIGURE 4.16: a)Damping like ΔH_{SL} current induced field for different dose irradiated Pt/Co/W devices obtained from the harmonic Hall measurement as a function of applied current and b) spin Hall angle, θ_{SHE} extracted for different irradiation doses.

For a quantitative comparison between different systems, it is useful to define an approximate figure of merit for the SOT switching efficiency. We define a SOT switching efficiency parameter, η, which scales the magnetic switching energy by the electric power injected in the multilayer stack. It can be expressed in unit of seconds as,

$$\eta = \frac{K_{eff} t_f}{Pd} \tag{4.6}$$

where the numerator is the magnetic energy barrier (K_{eff}) per unit area of the magnetic free layer of thickness t_f and the denominator is the electrical power (P) per unit area (in the entire stack thickness d) required to switch the magnetic state. Substituting for the K_{eff}

(under bias field H_x), and the switching power, the efficiency becomes

$$\eta = \frac{\mu_0 M_s (H_k - H_x) t_f}{2 J_c^2 \rho d} \tag{4.7}$$

where ρ is the longitudinal resistivity of the device. If the minimum pulse duration for the deterministic switching is known, then it can be divided with η to get a dimensionless switching efficiency. Either way a larger η implies a magnetically more stable element that requires less electric power to switch the magnetization. j_c can be further approximated using the macrospin model under the condition $H_x << H_k$ to define an intrinsic efficiency

$$\eta_i = \frac{\hbar^2 \theta^2}{2\mu_0 M_s H_k e^2 \rho d t_f} \tag{4.8}$$

It is important to understand the difference between the two SOT efficiencies, η and η_i. η is a preferable efficiency comparator between different systems as it is calculated from experimentally obtained parameters. On the other hand, it is challenging to make accurate comparisons between different reports in the literature which do not always include all relevant details. In that case, η_i, which depends solely on the intrinsic material properties, can be considered as a better figure of merit for comparisons between systems. Thus Eqn. 4.8 can be considered as a theoretical guideline for developing power efficient magnetically stable material designs. Its drawback is that it is based on the macrospin approximation, which cannot fully describe the current induced magnetization reversal in large samples, and therefore overestimates the current density by a factor of 10-100.

Dose ions/nm^2	K_{eff} kJ/m^3	Δ	ρ $\mu\Omega$.cm	j_c^- MA/cm^2	j_c^+ MA/cm^2	j_c^{th} MA/cm^2	η ps	η_i fs
0	537	133	214	-6.0	6.0	459	7.1	1.2
1	521	129	214	-6.0	6.0	442	6.9	1.2
20	257	64	219	-5.0	6.0	184	4.3	2.5
30	153	39	224	-0.8	2.7	85	86	4.2
50	38	9	235	-	-	-	-	-

The properties listed are effective anisotropy K_{eff}, thermal stability parameter Δ, negative and positive experimental critical current densities J_c^-, J_c^+, the theoretical critical current density j_c^{th} determined using macrospin model (section 1.4.2.2) with B_x = 150 mT, the switching efficiency η calculated from Eqn. 4.7, and intrinsic efficiency η_i using Eqn. 4.8. Note that for 50 ions/nm^2, only switching of adjacent unirradiated regions is detected.

TABLE 4.2: Magnetic properties of the Pt/Co/W thin film at various irradiation doses

Table 4.2 summarises the ion irradiation dependence of the magnetic and current driven properties of the Pt/Co/W thin films. Experimental efficiency, η, of unirradiated film is

Stack	j_c^a MA/cm^2	B_x mT	θ_{SH}^b	Δ^c	η ps	η_i fs	ref
Pt 3/Co 0.6/AlO_x 1.6	78	47.5	0.07	74	0.02	0.09	[42]
Ta 3/Pt 5/Co 0.6/Cr 2/Ta 5	2.70	20	0.41	106	28	2.02	[32]
Ta 3/Pt 5/Co 0.8/W 3/TaO_x 2	2.30	5	0.24	136	69	0.78	[43]
Ta 5/CoFeB 1.1/MgO 2/Ta 2	3.09	20	0.08	56	14	0.19	[44]
Bi_2Se_3 7.4e/CoTb 4.6/SiN_x 3	3.0	100	0.16	73	6.2	0.23	[45]
Pt 4/Co 0.4/Ni 0.2/Co 0.4/Pt 2^g	7.1	0	0.07	13	0.74	0.72	[46]
Pt 5/Ba$Fe_{12}O_{19}$3^f	5.7	123	0.07	232	18	0.04	[47]

^{a} If $J_c \neq J_c^+$, then the smaller of the two values is taken. ^{b} When not reported, literature values of θ_{SH}, are taken from [48]; for multilayers with adjacent layers of opposite θ_{SH}, the magnitude of the larger one is chosen. ^{c}Calculated for $H_x = 0$. ^{d}When not reported, calculated using bulk resistivity values from ref [49] and then corrected using the M-S model [50]. ^{e}Topological insulator used for spin injection. ^{f}Ferromagnetic insulator. ^{g}Zero-field switching device, moving between a remnant state $m_z = 0$, and a downward pointing m_z state.

TABLE 4.3: SOT switching efficiency comparison

7.1 ps which reduces to 4.3 ps for irradiation dose 20 ions/nm^2. This reduction is due to the greater reduction of thermal stability factor compared to the switching current density decrease. However, at 30 ions/nm^2, η improves by an order of magnitude upon the virgin state to a maximum value of 86 ps. Meanwhile, intrinsic efficiency, η_i, steadily increases from 1.2 fs for dose 1 ions/nm^2 to 4.2 fs for near critical dose 30 ions/nm^2. The difference in the η and η_i variation with dose is due to the macrospin approximation used to calculate the latter. Table 4.3 lists the switching efficiency of some relevant magnetic stacks found in the literature. Large efficiency of 69 ps is observed for Ta/Pt/Co/w/Ta thin films while topological insulator Bi_2Si_3 based film and magnetic insulator $BaFe_12O_19$ on Pt films have lower efficiencies.

Thermal stability (Table 4.2) of the magnetically patterned devices is important for both electrochemical as well as magnetic memory based applications. $\Delta = 60$ is the magnetic recording criterion for 10 years stable storage [37]. In our case, for a 1 nm thick and 32 nm sided element of Pt/Co/W film, $\Delta = 60$ for 20 ions/nm^2 dose which makes it a good candidate for magnetic storage. However, for 30 ions/nm^2, Δ reduces to 38, which is equivalent of 95 % data retention for 16 days [51]. Unlike the magnetic storage applications, electrochemical experiments don't require long term stability of the magnetic films. A few days of stable magnetic configuration is enough to fully characterize the magnetic field effects in a specific reaction. Moreover, weakly bistable devices also find applications in spin Hall oscillators [52], probabilistic computing [53] or random number generator [54].

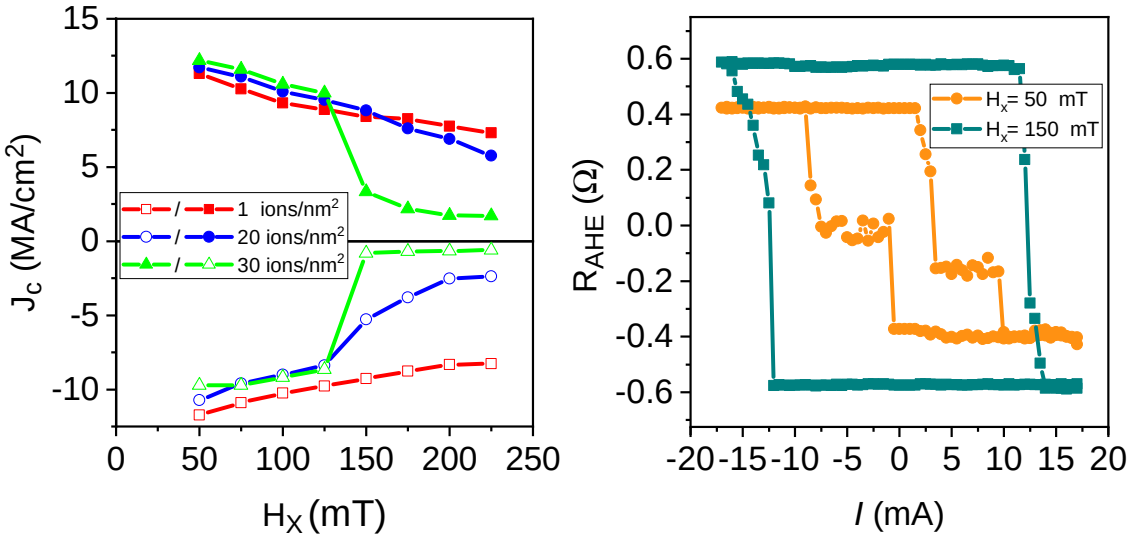

FIGURE 4.17: a) SOT working diagram of the switching current density and bias field versus magnetic state of device at different doses b) SOT switching of 30 ions/nm^2 irradiated device under low and high bias field.

To elucidate the electrically controlled magnetic multi-domain states, we revisit the current induced magnetization reversal curves of the device irradiated with 30 ions/nm^2 (sub panel of Fig. 4.15a). When the current is swept from 17 mA to -17 mA under a bias field of 150 mT, the first step with 0.4 Ω change in R_{AHE} is measured at a current of -0.4 mA (-800 kA/cm^2). With further increase in current magnitude, a second step with similar R_{AHE} change is observed at -10 mA (-6.0 MA/cm^2), a value similar to the one on unirradiated sample. Hence, the first step in the switching curve is expected to be due to the magnetization reversal of the irradiated region while the second step corresponds to the switching of the adjacent peripheral region of the Hall cross. Thus the irradiated region, which requires a lower current density for the magnetization switching, can be be selectively switched if the current is swept between +/- 3 mA. Hence, the independent selective switching of irradiated region makes the helium ion patterned film a 4-state magnetic device which can be programmed by electric current.

In-plane bias field also plays an important role in the realisation of current driven selective switching of the magnetization. Fig. 4.17a shows how the switching current evolves with the bias field for different irradiation doses. It is observed that at low bias field ($<$ 150 mT) j_c does not change significantly with the irradiated dose. In other words, no selective switching of irradiated region can be expected under this condition. Similar bias field dependence on switching current density in irradiated devices is observed in recent studies [55]. It is showed that, under small in-plane bias field, SOT switching proceeds via

multiple nucleation centers rather than the macrospin like behaviour, therefore makes the switching process less sensitive to anisotropy gradient. On the other hand, when the bias field is higher, the switching proceeds via domain wall propagation from limited nucleation points where the anisotropy gradient imposed by irradiation can affect the switching process. Nevertheless, the phase diagram (Fig. 4.17a) help us to define the working conditions for selective switching through anisotropy patterning.

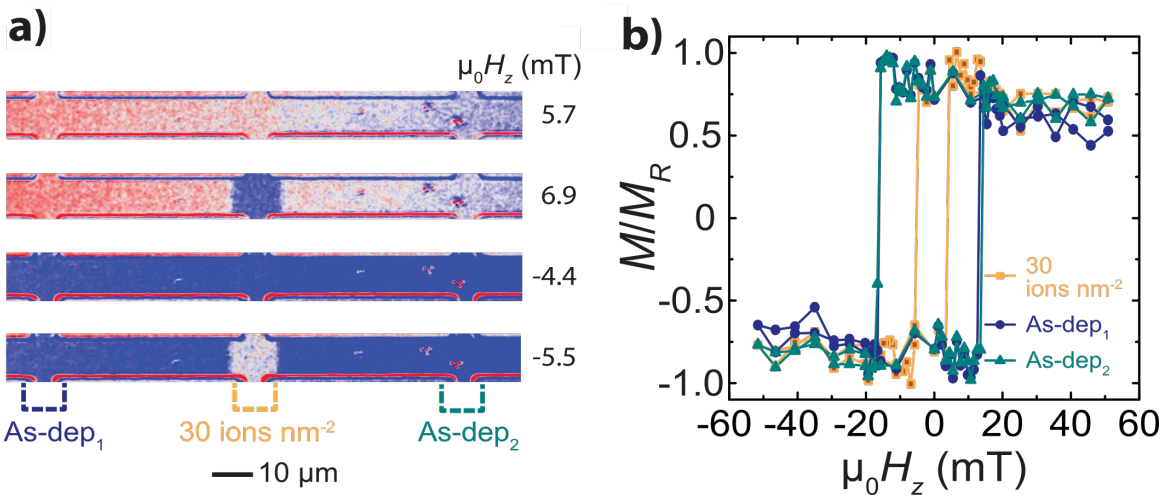

FIGURE 4.18: a) MOKE images of 30 ions/nm^2 irradiated device under different OP magnetic field b) Hysteresis loop of irradiated and non irradiated region in the same Hall bar extracted from MOKE image contrast analysis.

Magneto-optical-Kerr effect (MOKE) imaging under magnetic field normal to the film surface is performed to visualize the irradiation mediated selective switching of the Hall cross. Fig. 4.18a shows the MOKE images of the 30 ions/nm^2 Hall cross irradiated device under different OP magnetic field configuration. It is evident that the coercive field for the irradiated and non irradiated regions are different, which leads to the independent switching of regions under OP magnetic field. Fig. 4.18b shows the hysteresis loop of the irradiated and non irradiated region (as dep$_1$, as dep$_2$) extracted from the MOKE images. As expected from the previous ion induced interface roughness studies [3] [56], irradiated region has a reduced coercivity of 5 mT compared to the 16 mT of the non irradiated region. The change in coercivity of different regions in the same Hall bar provide a better confirmation to the irradiation induced effects in PMA thin films.

4.2.5 Irradiation induced surface modifications

In this section, we will discuss about a late addition to this work, which is the irradiation induced surface modification determined using atomic force microscopy (AFM). To estimate

the surface etching due to irradiation, we looked at the surface analysis of one sample (single repeat of Pt/Co(1.2)/W) at one dose (37 ions/nm^2) shown in Fig. 4.19a . From the AFM linescan analysis, it is found that up to 4 nm of material is removed from the top of the sample (Fig. 4.19b).

Upon irradiating the single repeat Pt/Co(1.2)/W device with a near critical dose of 37 ions/nm^2, the cross sectional area reduces by about 30 %. We will discuss how this change in area would propagate through the equation and would affect the estimation of relevant properties of the irradiated device. If we assume a uniform current distribution, the switching current density would expect to be 30 % higher. Based on Eqn.4.5, the spin Hall angle would be lowered by 30 %. Including the changes in the resistivity and total layer thickness into Eqn. 4.7, we found that the switching efficiency, η, would change from 86 ps to 42 ps, about 50 % reduction from the initial value. The irradiation induced surface modification is expected to modify the values of other doses, but would not invalidate the current results, e.g. 30 % reduction in thickness, is still smaller than the 70 % nominal change in j_c that is observed for the near critical dose irradiated device. Thus, even if the the thickness change is taken into account, there will be still an improvement in the switching current density, but it's just not as impressive as before. Moreover, recent studies based on broad beam irradiation using photoresist overlayer has been reported that the intermixing of the layers is what causes the switching current improvement [57, 58].

The sputtering rate has a logarithmic dependency to the irradiation dose [10], and the other doses irradiated samples need to be measured, but weren't possible to do before. Therefore, I am not in a position to modify the thickness/current densities in this section of my thesis, and instead to show the general trend the nominal sample thicknesses is retained for all data analysis.

In order to avoid the sample surface etching and to preserve the flat topography of the irradiated samples, we propose to coat the sample with photoresist prior to the irradiation (Fig. 4.19c). The resist should be thin enough to allow the focused helium ion beam to pass through but also thick enough to avoid the sample surface etching.

4.3 Irradiation Effects in Single And Three Repeat Pt/Co/W films

In the previous section, the electrical and magnetic control of magnetic multi-domain formation in pseudo-single domain multilayer devices were discussed. Magnetic gradient force density is proportional to the gradient as well as to the magnitude of the magnetic field.

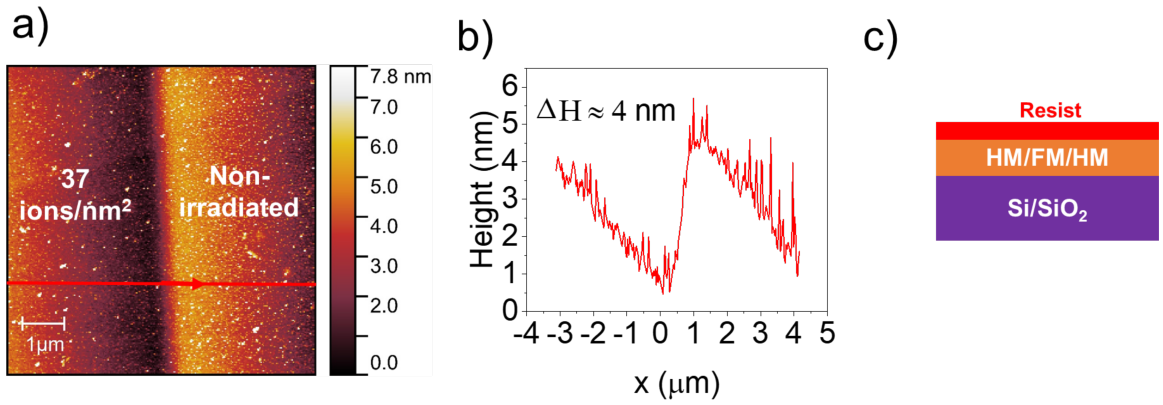

FIGURE 4.19: a) AFM acquired image showing the topography of single repeat Pt/Co(1.2)/W device irradiated with dose 35 ions/nm^2 and unirradiated region. b) The AFM linescan vs distance along the horizontal red line in a). c) Proposed resist assisted magnetic patterning for conserving the flat topography of the sample surface.

Increasing the volume of magnetic material that can be controllable by means of electric current will be advantageous in terms of the enhanced field gradient force as well as the improved thermal stability of magnetic states. The magnetic volume of a heterostructure film can be increased either by increasing the thickness of the magnetic layer or by increasing the number of FM/HM bilayer repeats. Based on our earlier discussion (section 1.3), in PMA films, the thickness of magnetic layer is constrained by the balance between surface and shape anisotropy. However, increasing the number of repeats up to a certain limit can preserve the PMA and pseudo-single domain magnetic state of the film. SOT switching efficiency (Eqn. 4.7), is proportional to the ratio of magnetic layer thickness to the total thickness, so it can also be improved by this approach.

Thin films having single and three Pt/Co(t)/W repeats with different magnetic layer thicknesses are fabricated. Samples are precharacterized by magnetic and magneto-transport measurements prior to irradiation studies. Based on the initial characterization, a single and three repeats samples with optimum magnetic layer thickness are identified for subsequent irradiation studies.

4.3.1 Sample fabrication and micro-patterning

DC magnetron sputtering machine discussed in section 2.2.1 is used for the thin film deposition. Between the deposition of thin film samples discussed in the previous section and the current set of thin films, there is a one year gap due to the machine build. However, deposition parameters are almost unchanged. Thin film samples consists of Pt/Co/W repeats

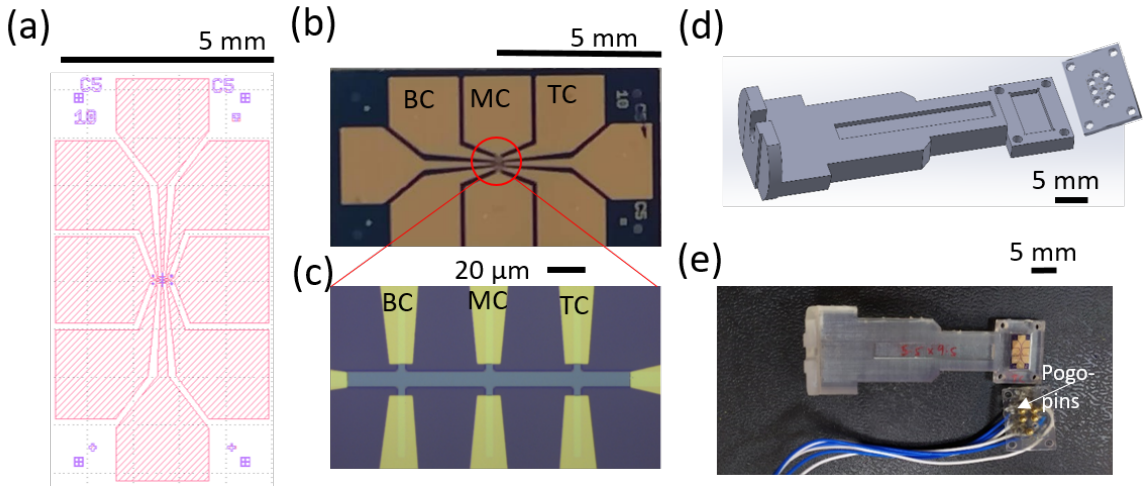

FIGURE 4.20: Lithography pattern and sample connection. a) Schematic of designed mask. b) Example optical image of patterned Hall bars c) Enlarged view of Hall bar d) schematics of 3d-printed parts for sample connection e) 3D printed pogo-pins attached sample holder with sample.

with different Co thickness and the full heterostructure is:

$$Si/SiO2//Ta(5.0)/Pt(2.0)/[Co(t_{Co})/W(1.5)/Pt(1.5)]_N/Ta(1.5)$$

where t_{Co} = 1.0, 1.2 and 1.5 nm (all thickness in nm), and N = 1 and 3. Such a heterostructure ensures that, irrespective of the number of repeats, Co is always sandwiched between heavy metals of opposite spin Hall angle with Pt layer at the bottom and W layer at the top.

Measurements and device patterning are performed at IPCMS. Thin films are patterned using direct laser writing lithography in combination with the e-beam evaporator for etching. Hall bars of width 10 μm, and length 300 μm are patterned with three crosses, which we call top cross (TC), middle cross (MC), and bottom cross (BC)(Fig. 4.20a). The lateral distance between Ti(3.0)/Au(47.0) contact pads on the crosses is 20 μm, and 180 μm longitudinally. Compared to the previous design used in section 4.2.1, the current design consists of comparatively larger contact pads which can be then contacted using specially designed 3D-printed sample holder and pogo-pins as shown in Fig. 4.20 (b) and (e). This way of contacting made the connections more robust and reproducible compared to the conventional silver paste or microtips based contacts..

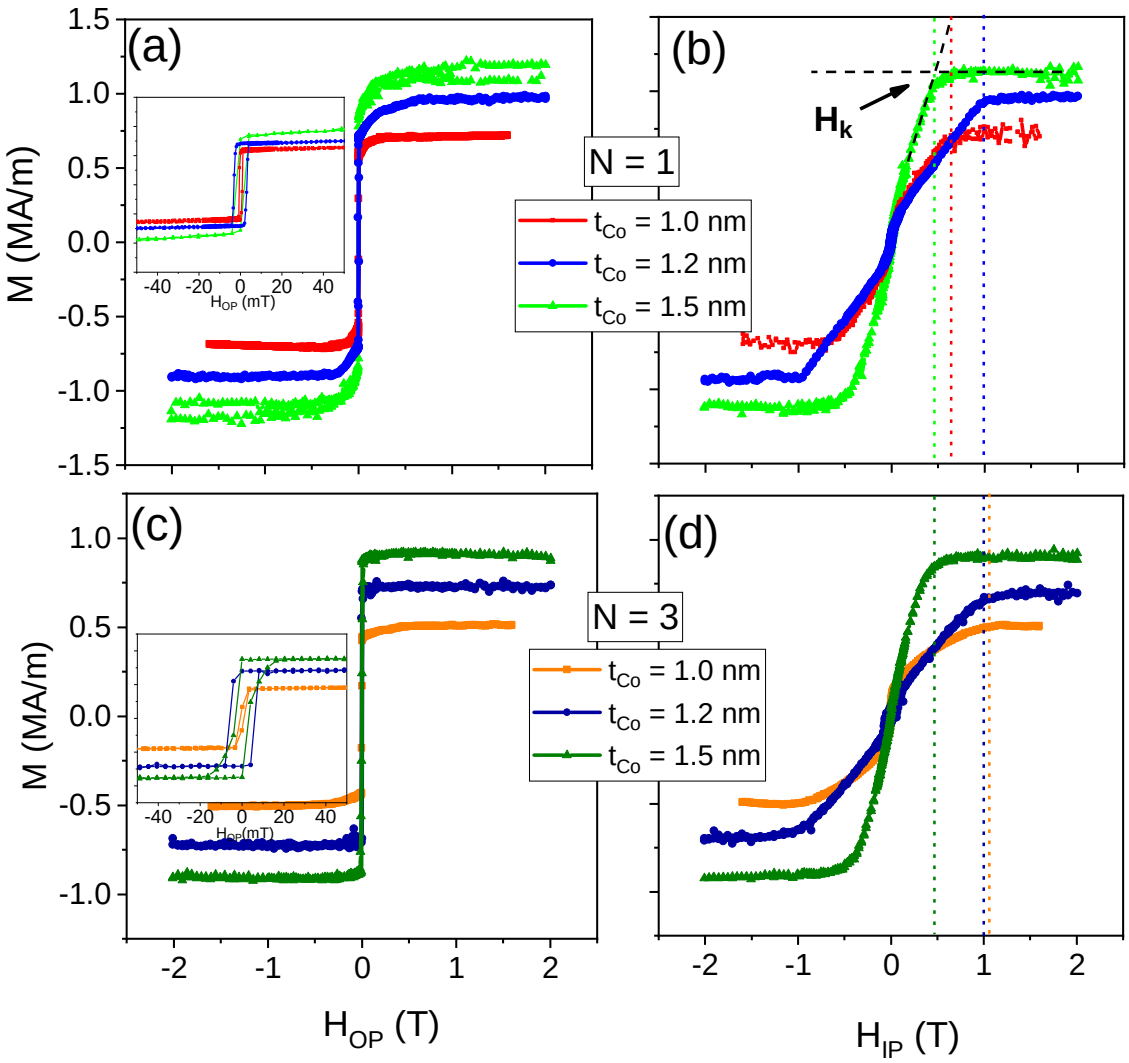

FIGURE 4.21: SQUID magnetization of single repeat Pt/Co(t)/W devices under a) out-of-plane field and b) in-plane field. Magnetization data for three repeat $[Pt/Co(t)/W]_3$ devices under a) out-of-plane field and b) in-plane field

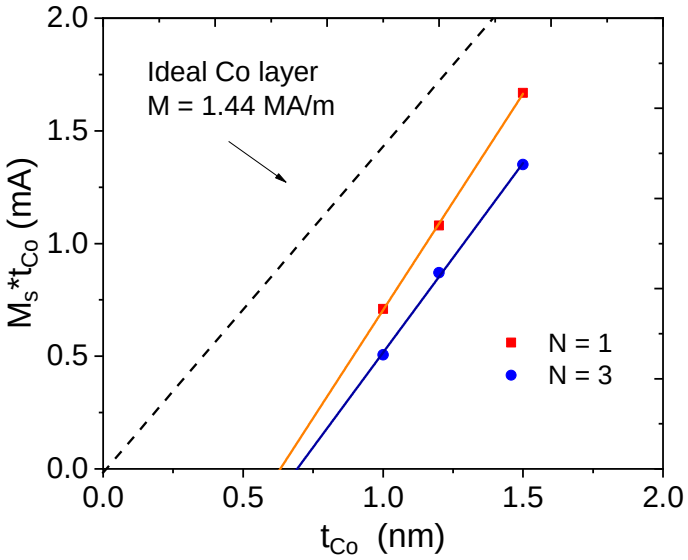

FIGURE 4.22: Saturation magnetization times Co thickness vs Co thickness for single and three repeats of Pt/Co/W film. Symbols represent the SQUID-VSM data and solid line corresponds to the fit.

4.3.2 Initial characterization of magnetic films

4.3.2.1 Magnetization data

In order to fully characterize single and three repeats of Pt/Co/W thin films, magnetization of the unpatterned thin films are measured using SQUID magnetometer under in-plane (IP) and out-of-plane (OP) applied fields. Fig. 4.21 shows the magnetization data for all samples. The observed OP easy axis of magnetization confirms that all the films posses perpendicular magnetic anisotropy. Volume magnetization of each sample is obtained by dividing the magnetic moment by the total magnetic Co layer volume. The anisotropy field H_k can be estimated as the IP field required to saturate the magnetization (Table 4.4). Single and three repeats of 1.2 nm ultrathin Co film are found to have almost similar anisotropy field values. Upon further increase in the Co thickness to 1.5 nm, irrespective of N, a decrease of H_K is found. For both N=1 and N=3 samples, M_s is observed to increase with the Co thickness. For same Co thickness, M_s of N=3 is always smaller than N=1. In addition, the obtained M_s values for all the films exhibit a significant reduction compared to Co bulk magnetization 1.44 MA/m. All these observations can be attributed to the presence of a magnetic dead layer in the film. It has already been reported that heavy W atoms deposited on Co layer causes intermixing at the Co/W interface [59–61] and subsequently reduces the effective Co thickness [23, 24]. Dead layer thickness is quantified from the linearized M_s plot shown

in Fig. 4.22 and is found to be 0.63 nm for single repeat and 0.7 nm (per layer) for three repeats films comparable to the values reported for ultrathin Co films [23, 61]. The dead layer calculation matches with the XRR fit based on the model of alloy formation at Co/W interface (section 4.2.1).

4.3.2.2 Magneto-transport measurements

Thin films are patterned into Hall bars for measuring the local modifications resulting from focused light ion irradiation. Magnetic field and current driven magnetization switching are characterized using AHE measurements.

Magneto-transport measurements of single and three repeat Pt/Co/W samples under OP and IP field are shown in Fig 4.23. The change of R_{AHE} under OP field for single repeat Pt/Co/W devices with Co thickness 1.0, 1.2 and 1.5 nm is 1.4, 1.46 and 1.76 Ω and for the three repeats is 0.7, 1.25 and 1.24 Ω, respectively. This change in Hall signal is in accordance with the change in the M_s value of the samples (Table 4.4) as the Hall signal is proportional to the magnetization. A slight reduction in the ΔR_{AHE} for N=3, t_{Co} = 1.5 nm device might be due to the shape anisotropy induced magnetization tilt from OP axis as this film contains larger magnetic volume. In N=3 devices, several steps can be observed in the switching curves under OP field (Fig. 4.23a) which relate to the individual layers switching.

The evolution of AHE under IP field for single and three repeats Pt/Co/W devices is shown in Fig. 4.23(b) and (d). The anisotropy field, calculated from the AHE in-plane field data (Eqn. 4.2), is in good agreement with the values deduced from SQUID data (Table 4.4). Compared to all devices, the three repeats patterned device with 1.5 nm Co thickness (Fig. 4.23b) shows a much lower H_k and the AHE behavior under IP field does not match a macrospin model, likely due to the multi-domain formation and stray field effects. These results are reproducible from sample to sample.

Current induced magnetization switching measurements are performed in all the devices at bias field 150 mT (Fig. 4.24). Hysteresis loops are observed in all devices except for $[Pt/Co(1.5)/W]_3$ which is surprising considering its comparatively low anisotropy field. Switching current density and SOT efficiency are listed in Table 4.4. j_c of single and three repeats of [Pt/Co(1.0)/W] device is comparatively lower, which is in good agreement with the j_c dependence to M_s, H_K and t_{Co} based on the macrospin model [13] [62]. In view of the dead layer thickness, and using the anisotropy field and the SOT switching efficiency as a selection criteria, single and three repeats of Pt/Co(**1.2**)/W devices are chosen for further characterization and irradiation studies.

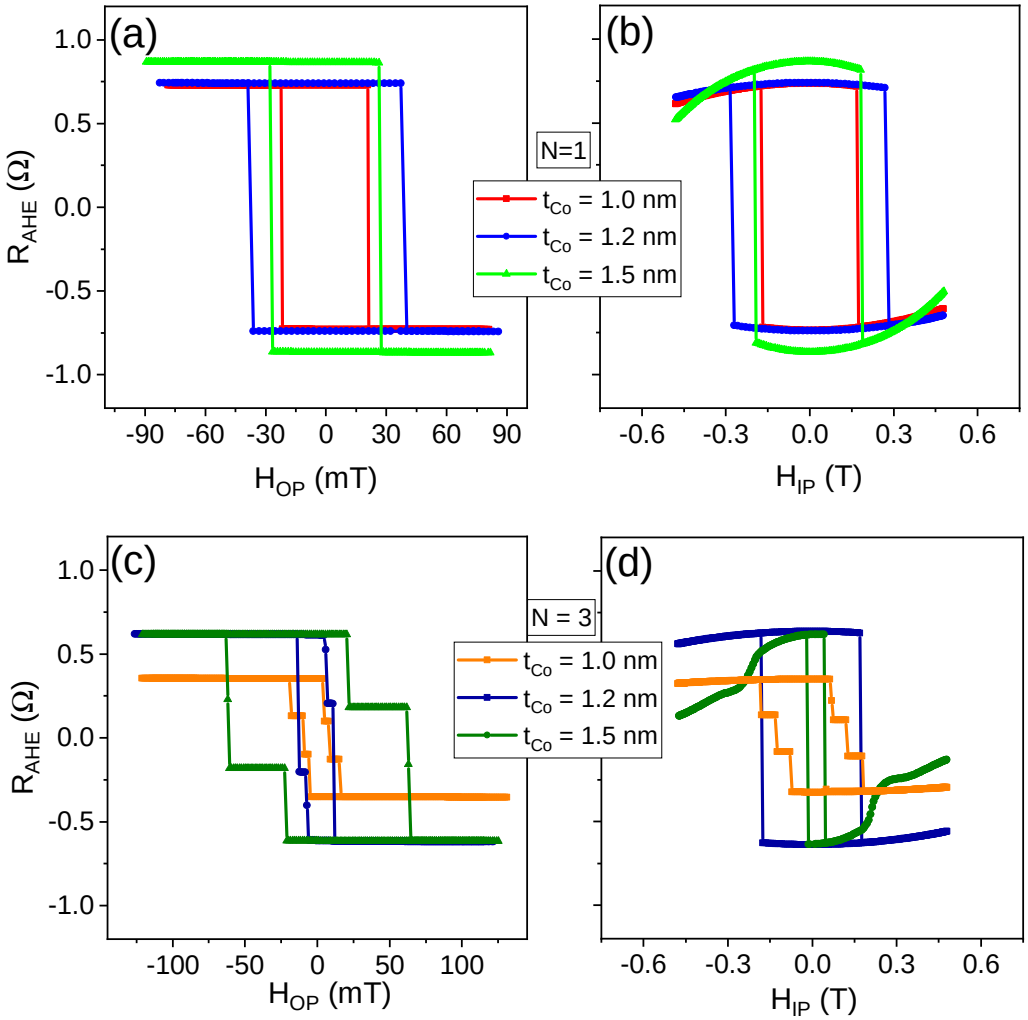

FIGURE 4.23: Anomalous Hall loop of [Pt/Co/W] device with various Co thickness under a) out-of-plane field and b) in-plane field. Similar loop for $[Pt/Co/W]_3$ device under c)out-of-plane field and d) in-plane field

t_{Co}	N	M_s	H_{KS}	H_{KA}	K_{eff}	Δ	j_c^{av}	η
		$\pm$ 0.03	$\pm$0.02	$\pm$0.01			$\pm$ 0.4	
nm		MA/m	T	T	kJ/m^3		MA/cm^2	ps
1.0	1	0.71	0.74	0.74	302 $\pm$ 21	75 $\pm$ 5	3.2	25 $\pm$ 8
1.2	**1**	**0.92**	**1.02**	**1.12**	**482 $\pm$ 24**	**143 $\pm$ 7**	**8.1**	**9 $\pm$ 2**
1.5	1	1.11	0.51	0.52	289 $\pm$ 19	107$\pm$ 7	7.6	6 $\pm$ 1
1.0	3	0.54	1.34	1.24	310 $\pm$ 23	230 $\pm$ 17	3.5	57 $\pm$ 17
1.2	**3**	**0.72**	**1.02**	**1.05**	**378 $\pm$ 23**	**336 $\pm$20**	**7.75**	**14 $\pm$ 2**
1.5	3	0.93	0.42	0.35	182 $\pm$ 16	202 $\pm$ 18	-	-

M_s and H_{KS} obtained from SQUID measurement, and H_{KA} obtained from AHE data. Average switching current density,j_c^{av}, and H_k estimated from AHE IP data is used for efficiency, η, calculation.

TABLE 4.4: Summarized magnetic and magneto-transport properties of unirradiated Pt/Co/W films with different Co thickness and number of repeats N.

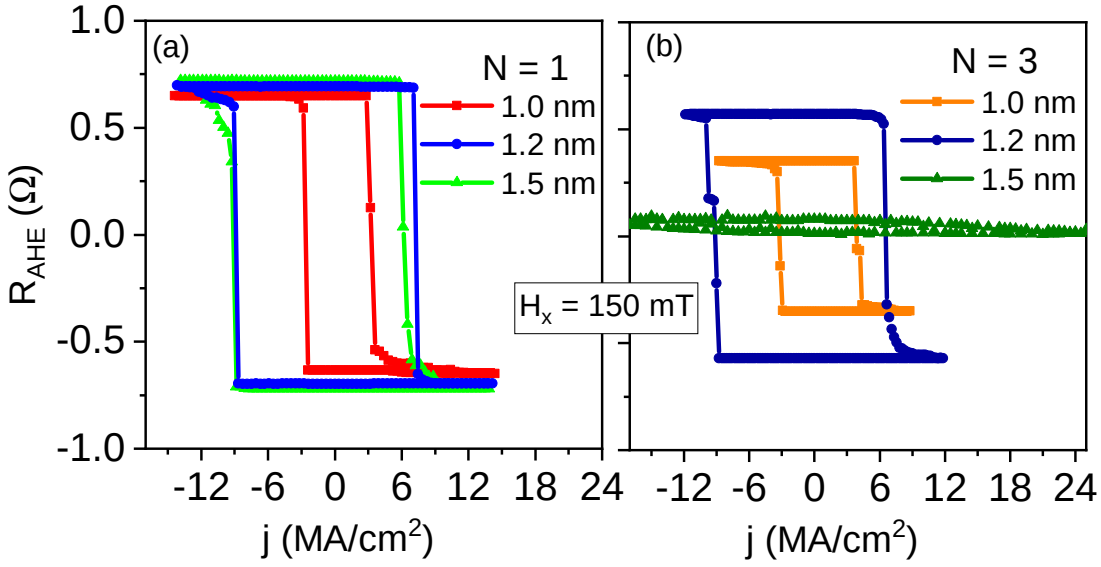

FIGURE 4.24: SOT switching under bias field 150 mT of a) single repeat Pt/Co/W and b) three repeat Pt/Co/W device.

We already discussed the sensitivity of coercivity and the robustness of anisotropy field to the lithography steps (section 4.2.2.3). To illustrate this in the case of N=3 repeats devices, AHE based hysteresis loop under OP and IP magnetic field is measured on multiple samples (Fig. 4.25 a and b). Under the OP field, single and multi-level switching are observed with a 22 % variation in the onset field, 32 $\pm$ 7 mT. On the other hand, we find less than 1 % variation in the anisotropy field, 1.12 $\pm$ 0.01 T. Based on the macrospin model [13], SOT switching current density is not dependent on the coercivity but to the film intrinsic properties: the anisotropy field and saturation magnetization. In order to confirm the results of the previous section, illustrating how SOT is much more robust approach for magnetization switching than applying an external magnetic field, SOT switching is performed in Pt/Co(1.2)/W and $[Pt/Co(1.2)/W]_3$ devices (Fig. 4.25 c and d). We find less than 10 % variation in the switching current density, irrespective of the number of repeats. Even without taking into consideration the uncertainty in the Hall bar cross sectional area, the SOT switching current density variation is found to be lower than the coercivity variation. Thus, compared to magnetic field driven switching, current induced switching can be considered as a superior technique in terms of precision and robustness.

In order to get a better spatial and temporal understanding of the current induced magnetization switching, high resolution polar Kerr microscopy is used to visualize the magnetic domain evolution. Simultaneous AHE measurement and the Kerr imaging of current induced magnetization switching allows one-to-one mapping between Kerr images and the

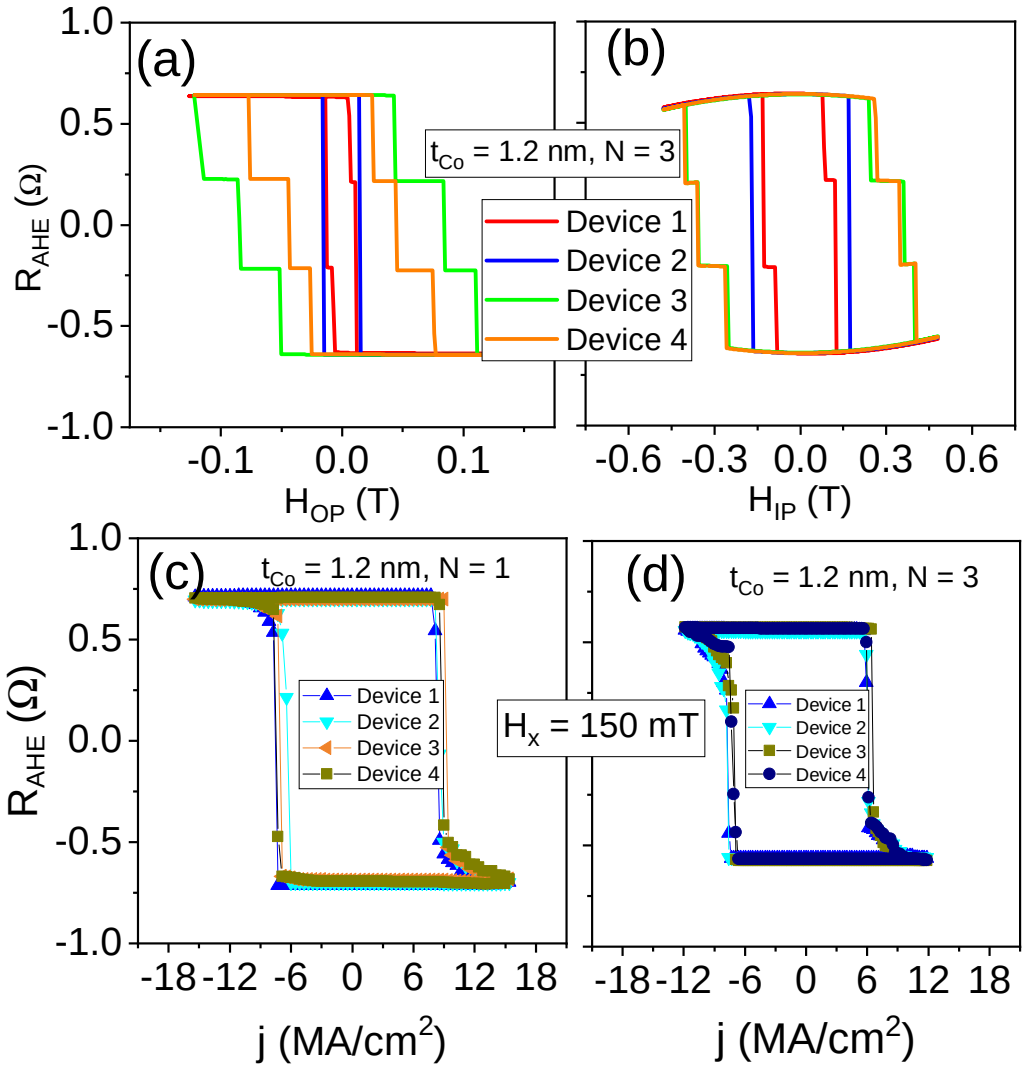

FIGURE 4.25: Distribution of a) coercivity and b) anisotropy field in multiple devices with N = 3 repeat and Co thickness 1.2 nm. Irrespective of the multi-levels of switching under OP field, the starting point of field (onset field) is considered for uncertainity calculation. Distribution of SOT switching currents under bias field 150 mT in multiple a) Pt/Co(1.2)/W and b) $[Pt/Co(1.2)/W]_3$ devices.

data points in the AHE switching loop. In the experiment, 1 ms current pulses of varying magnitude are applied under a constant bias field with AHE resistance and Kerr images recorded 1 s after each pulse. Prior to each switching measurements, devices are magnetized in one direction with a large perpendicular magnetic field of 0.45 T. Processed Kerr images of SOT switching of the single repeat Pt/Co/W with the current looped between 21 mA and -21 mA under bias field 100 mT are shown in Fig. 4.26. At state (1), the device is saturated along one direction. Upon sweeping the current from 21 mA to -21 mA, at -14 mA (11 MA/cm^2), reverse domain nucleation starts at one side of the device. AHE data

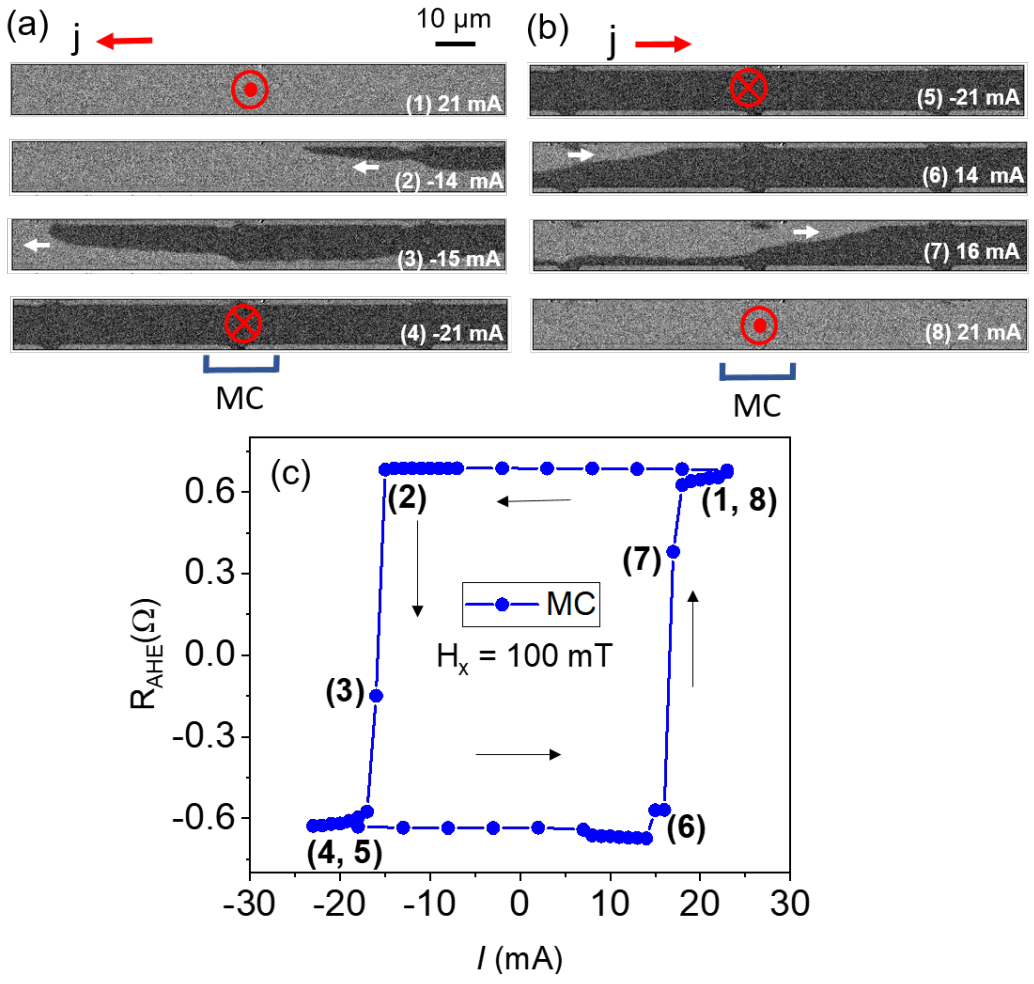

FIGURE 4.26: MOKE imaging of SOT switching of single repeat Pt/Co/W device under bias field 100 mT (a) current pulses 21 mA to -21 mA b) reverse current sweep from -21 mA to 21 mA and c) *in-situ* anomalous Hall resistance measurement.

is not sensitive to this nucleation as it is only sensitive to the M_Z changes at the MC junction. Upon further increase in current magnitude, at -15 mA(11.8 MA/cm^2), the domain wall (DW) propagates and reaches the MC junction detected as state (3) in the AHE curve. The magnetization completely switches with further increase in current. When the current is reversed, a DW nucleates at the other edge of the device and propagates in the opposite direction. Thus, the Kerr imaging suggests that, rather than the multiple random nucleation sites initiated switching [63], the DW propagation is the determining factor of SOT switching in the Pt/Co/W device at high bias field. For the [Pt/Co(1.2)/W]$_3$ device, similar switching images are observed.

4.3.3 Comparison of irradiation effects in Pt/Co/W and [Pt/Co/W]$_3$ devices

Pre-characterized Pt/Co(1.2)/W and [Pt/Co(1.2)/W]$_3$ devices are used for irradiation studies. It is understood from the previous irradiation study that the adjacent unirradiated region's magnetization contributes to the Hall signal for an irradiated 10 μm x 10 μm area at the Hall cross (section 4.2.4). In order to avoid this complication from the unirradiated region, devices are irradiated in larger 20 μm x 20 μm region at the Hall cross. Fig.4.27 shows the *in-situ* evolution of the AHE resistance with irradiation for single and three repeats of Pt/Co(1.2)/W devices. Like previous studies, for [Pt/Co(1.2)/W] device, the AHE resistance initially decreases with irradiation until a critical dose of 44 ions/nm^2 and then a sharp drop is observed. The resistance drop which corresponds to the spin transition from out-of-plane to in-plane orientation is complete at 46.7 ions/nm^2. The total deflection in resistance is 0.67 Ω which is almost equal to the half of full deflection under OP magnetic field, 1.46 Ω. On the other hand, the *in-situ* Hall resistance of Pt/Co(1.2)/W]$_3$ device exhibit multiple level under increasing irradiation dose. After the initial decrease in the R_{AHE}, a resistance drop of 0.2 Ω occurred around 29 ions/nm^2 followed by a 0.4 Ω drop around 42 ions/nm^2. The total change, 0.6 Ω, is almost equal to the half of full deflection under OP magnetic field, 1.26 Ω. The multi-steps in the irradiation curve can be explained as individual layers change of magnetic orientation. With increase in the number of repeats, the interface roughness increase and consequently reduces the interface quality [64]. If we assume that each magnetic layer contributes almost equally to the Hall voltage, the resistance drop around 29 ions/nm^2 can be considered as the transition of a single magnetic layer while at 44 ions/nm^2 trigger the transition of the remaining two layers.

In order to study the ion irradiation effects on the intrinsic magnetic properties, devices

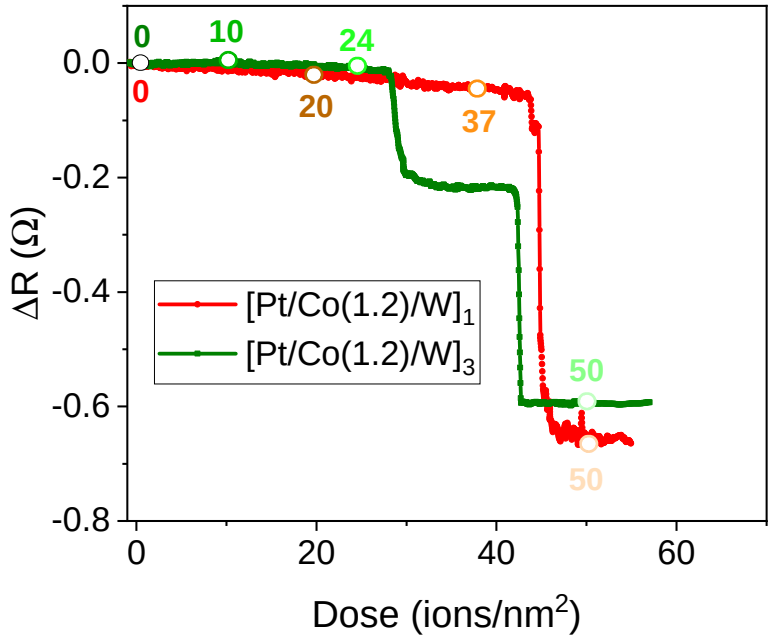

FIGURE 4.27: *In-situ* Hall resistance evolution with helium irradiation for [Pt/Co/W] and $[Pt/Co/W]_3$ Hall bars.

are irradiated with different doses chosen from the irradiation curve (Fig. 4.27). The irradiation induced change in the anisotropy field and the saturation magnetization of the Pt/Co(1.2)/W and $[Pt/Co(1.2)/W_3$ devices are shown in Fig. 4.28 a and b. As discussed earlier, H_K is estimated by the anisotropy fit to the AHE data under IP field and M_s is determined from the relative change in the *ex situ* saturation Hall resistance under OP field. For the Pt/Co(1.2)/W device, H_K reduces from 1.1 T to 0.31 T, a 72 % reduction from the initial value upon irradiation with a near critical dose of 37 ions/nm^2. Meanwhile, for $[Pt/Co(1.2)/W_3$ device under 24 ions/nm^2, H_K reduces from 1.07 T to 0.4 T, ie, 62.6 % reduction from the initial value. On the other hand, M_s of Pt/Co(1.2)/W and $[Pt/Co(1.2)/W_3$ reduces only by 7.7 % and 4 % from the initial value of 0.9 MA/m and 0.72 MA/m. The M_s change is larger for single repeat as it is irradiated with a higher dose than three repeats film. The change in H_K and M_s is attributed to the ion induced intermixing at the interface [7].

Current induced magnetization switching measurements are performed in the irradiated samples to characterize the SOT switching properties of the irradiated single and three repeats films. Fig. 4.29a shows the SOT switching measurements of the Pt/Co(1.2)/W device irradiated with different doses under a bias field of 100 mT. When the device is irradiated with a near critical dose of 37 ions/nm^2, the average switching current j_c is reduced from

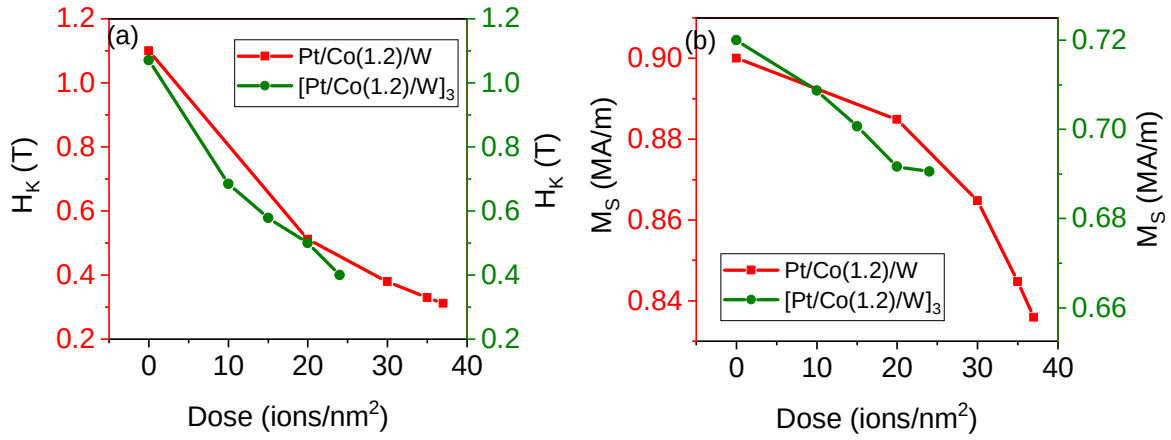

FIGURE 4.28: Ex situ a) anisotropy field and b) saturation magnetization evolution with the irradiation dose for Pt/Co(1.2)/W and $[Pt/Co(1.2)/W]_3$ films.

8.6 MA/cm^2 to 2.0 MA/cm2^2, ie a reduction of 76 % from that of the initial value (Table 4.5). Based on the macrospin model, this j_c reduction is in agreement with the 72 % reduction in the anisotropy field. The similar SOT switching curves for the $[Pt/Co(1.2)/W]_3$ device is shown in Fig. 4.29b. As can be seen, upon irradiation with a near critical dose of 24 ions/nm^2, the switching current density substantially reduces from 8.3 MA/cm^2 to 4.0 MA/cm^2, a 52 % reduction. For both devices, no switching is observed at the junction irradiated with a high dose of 50 ions/nm^2. However, contrary to the previous study on 10 μm x 10 μm irradiated Hall cross(section 4.2.4), no multi-level switching can be observed, which implies that the Hall signal is insensitive to the switching of adjacent non-irradiated regions of 20 μm x 20 μm irradiated Hall cross. Table 4.5 summarizes the relevant properties of irradiated N=1 and N=3 repeats Pt/Co(1.2)/W devices. For near critical dose irradiated devices, the N=3 device has higher thermal stability compared to N=1, due to the improved magnetic volume. But, the switching efficiency η of three repeats sample is found to be lower than the single repeat, due to the differences in the switching current density.

Polar Kerr microscopy is used to image the current induced magnetic domain evolution in the irradiated devices. Fig.4.30a shows the MOKE images of a Pt/Co(1.2)/W device at current pulses swept between $\pm$ 35 mA to -35 mA under 100 mT bias field. Three different regions in the Hall bar are defined, 'A' is the unirradiated region in between two irradiated regions, 'B' is the irradiated Hall cross as region and unirradiated region with only its left border defined by irradiation. Prior to measurements, thin film magnetization is saturated by applying an out-of-plane field of 0.45 T, confirmed by the Kerr image at 35 mA. At -2 mA, the nucleation of a reversed domain starts at the irradiated region 'B', followed by the

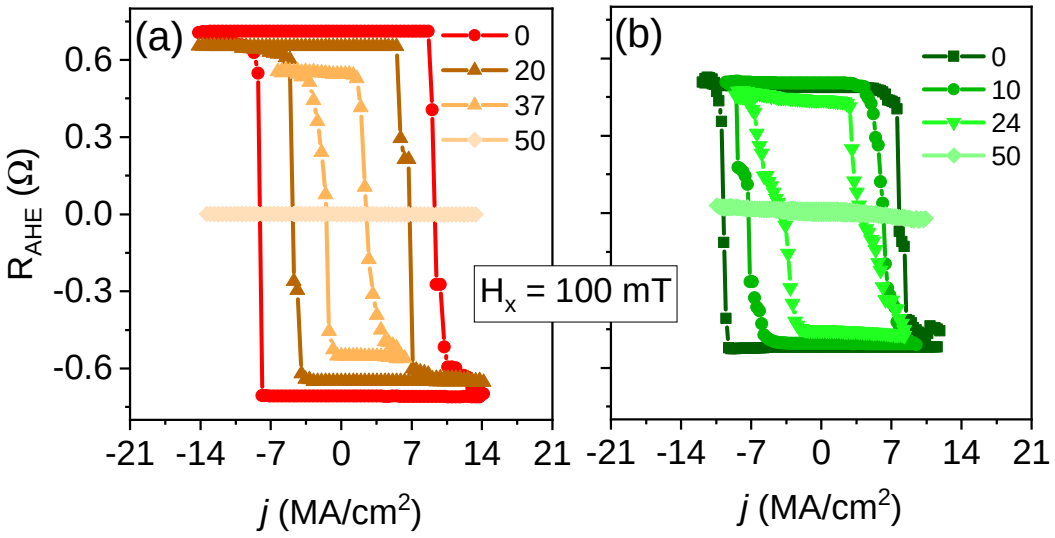

FIGURE 4.29: Current driven switching under in-plane bias field 100 mT of irradiated a) Pt/Co(1.2)/W and b) $[Pt/Co(1.2)/W]_3$ device.

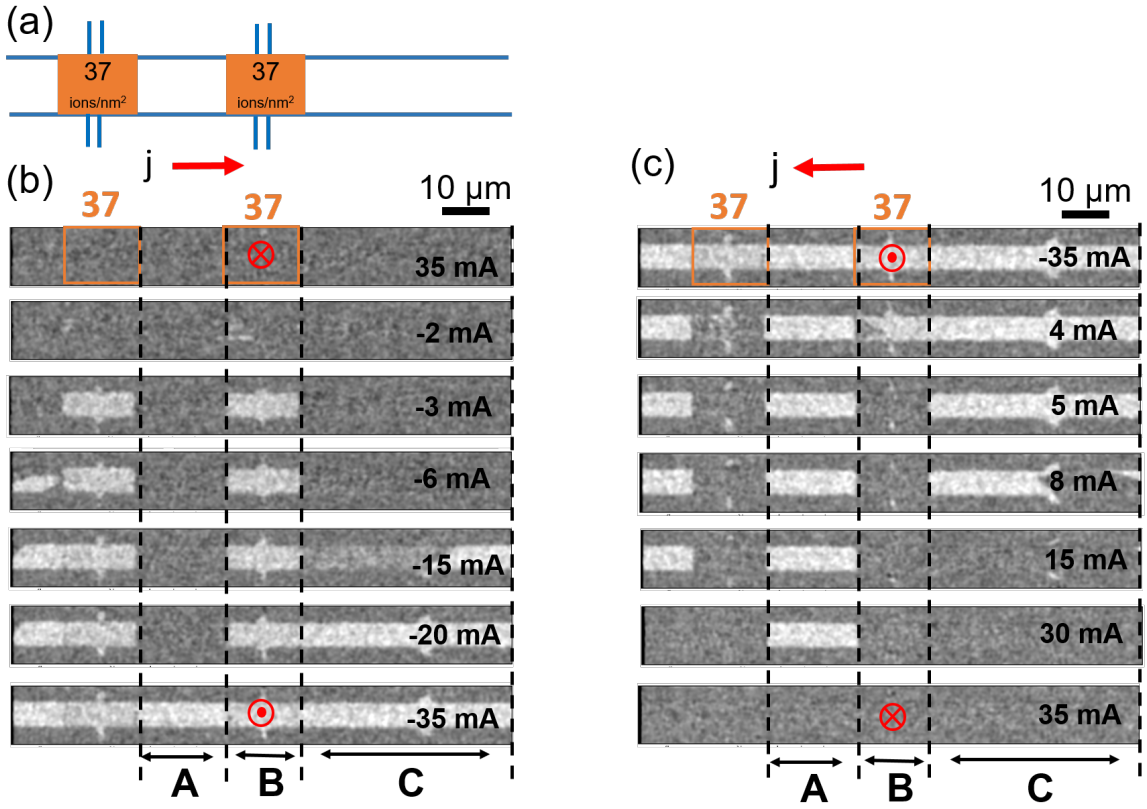

FIGURE 4.30: MOKE images of SOT switching of 37 ions/nm^2 irradiated Pt/Co(1.2)/W film under bias field of 100 mT. a) Schematics of the Hall bar highlighting irradiated regions. b) Current induced switching during the current sweep from 35 mA to -35 mA and b) similar switching images when the current is reversed.

Dose ions/nm^2	K_{eff} kJ/m^3	Δ	j_c^- MA/cm^2	j_c^+ MA/cm^2	j_c^{av} MA/cm^2	η ps	η_i fs
N=1. t_{Co}=1.2 nm							
0	405	134	-8.1	+ 9.1	8.6	4	2
20	180	70	-4.9	+6.7	5.7	5	4
37	94	40	-1.5	+2.5	2	30	6.4
N=3. t_{Co}=1.2 nm							
0	342	320	-9.8	+7.8	8.3	5	0.5
10	218	210	-7.3	+6.3	6.8	6	0.8
24	134	136	-4.0	+4.0	4.0	12	1.2

The properties listed are effective anisotropy K_{eff}, thermal stability parameter Δ, negative, positive and average experimental critical current densities J_c^-, J_c^+, J_c^{av}, bias field B_x = 100 mT, the switching efficiency η calculated from Eqn. 4.7, and intrinsic efficiency η_i using Eqn. 4.8. Note that for N=3 samples complete switching is assumed and the onset current of switching is considered as switching current.

TABLE 4.5: Relevant properties of N=1 and N=3 Pt/Co(1.2)/W thin film at various irradiation doses

complete switching through rapid domain wall propagation at -3 mA. At this current, the irradiated region is selectively switched and the DW propagation stopped at the boundary between irradiated and non-irradiated areas. The domains remain stable under further increase in the current, which is attributed to the anisotropy gradient imposed by light ion irradiation [65]. For a current further increased to -15 mA, nucleation and domain wall propagation in the region 'C' is initiated, and the complete switching is realized at -20 mA. It is worthwhile to note that compared to all the regions in the Hall bar, the region 'A', having the irradiation induced anisotropy gradient at the right and left borders, requires the largest switching current $>$ 30 mA. This is ascribed to the fact that the domains at the left and right border of the region 'C' are pinned by the irradiation which further inhibits the nucleation and domain wall propagation [5] [16]. Fig.4.30b shows the Kerr images when the current is reversed. It can be seen that, irrespective of current sweep direction, the magnetization switch initially in the irradiated region 'B' followed by region 'C' and finally at region 'A'. Thus, Kerr imaging confirms how one can selectively switch - by means of electric current-areas defined by their irradiation history.

Current driven magnetization switching of near critical dose irradiated [Pt/Co(1.2)/W]$_3$ devices is also imaged using polar Kerr microscopy (Fig. 4.31 a and b). As seen in Fig. 4.31a, reverse domain nucleation and DW propagation are initiated in the irradiated region when a current of -10 mA is applied to the device. With further increase in current to -19 mA, the

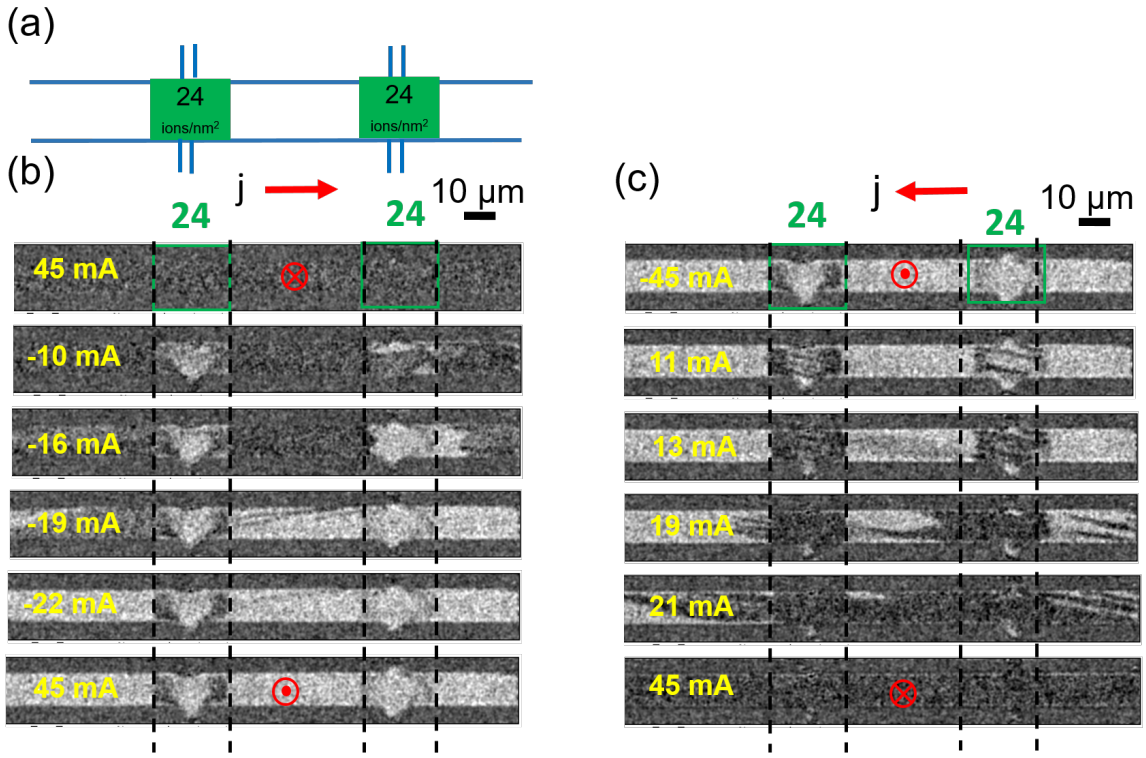

FIGURE 4.31: MOKE images of SOT switching of 24 ions/nm^2 irradiated $[Pt/Co(1.2)/W]_3$ film under bias field of 100 mT. a) Schematics of the irradiation design on the Hall bar. b) Current induced switching during the current sweep from 45 mA to -45 mA and c) similar switching images when the current is reversed.

irradiated region is partially switched along with the unirradiated region. Multi-domain states with stripe domains are also observed along the switching process. At high current of -45 mA, the irradiated region remains in the multidomain state while the non-irradiated regions are completely switched. It should also be noted that the multi-domain formation is difficult to deduce from the *ex situ* SOT curves of $[Pt/Co(1.2)/W]_3$ device (Fig. 4.29b) due to the limited spatial sensitivity of the Hall voltage. The formation of multi-domains state in the irradiated region might be due to the reduced interface anisotropy compared to the demagnetising field. The influence of the shape of the irradiated area on the multi-domain formation has to be further validated. However, even though multi-domain states are achieved through current pulses, we might need to further improve the $[Pt/Co(1.2)/W]_3$ device in order to achieve a fully controlled magnetic field gradient switching device by electrical means.

4.4 FIB Patterning for Multi-level Current Induced Magnetization Switching

Until now, we have demonstrated the irradiation assisted selective switching of Hall cross in single and three repeat Pt/Co/W devices. In the previous studies, the number of intermediate force field states are limited only to a binary high and a low field gradient condition. In order to access more intermediate multi-domain states, pattern designs can be further improved by irradiating with several different doses multiple zones in the same sample. Multi-step switching also finds application in the field of memory applications. Deterministic multi-level switching has been realized by changing the number of FM/HM repeats [66], changing the thickness of individual FM layer in multilayer stacks [67],and using broad-beam irradiation [58]. Compared to the mentioned techniques, the current induced multi-state magnetization switching via focused helium ion irradiation offers advantage in terms of the simplicity and the spatial resolution of the magnetic patterning.

In this section, the current driven switching of the Hall cross patterned for multi-level switching is discussed. Such a design not only improves the field gradient and access more intermediate force field states but also helps to understand the relevant parameters which ultimately allow us to pattern nanomagnetic electrically controllable arrays. Already precharacterized Pt/Co(1.2)/W devices are used to demonstrate the multi-level current driven irradiation assisted magnetization switching. The required doses are carefully chosen from the irradiation curve (Fig. 4.32).

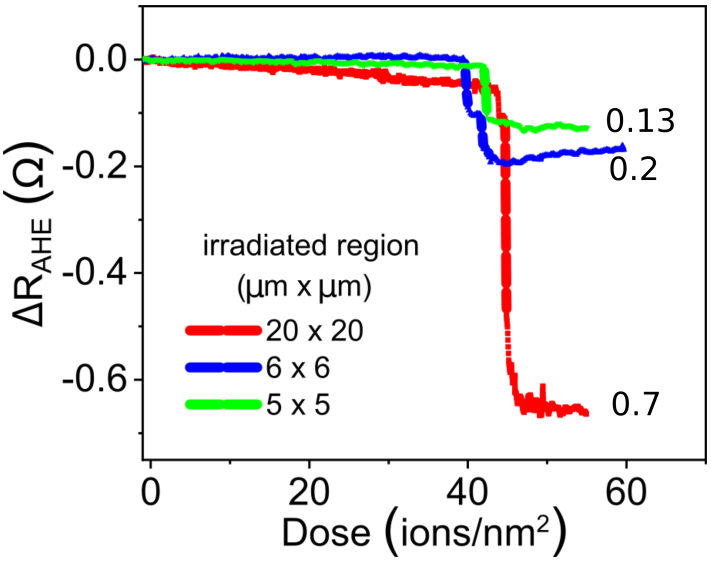

FIGURE 4.32: in situ anomalous Hall resistance evolution of Pt/Co(1.2)/W device with different irradiation area at the Hall cross.

To realise the multi-level magnetization switching, an understanding about the spatial sensitivity at the Hall cross is crucial. For this purpose, *in situ* anomalous Hall resistance as a function of irradiation dose for different exposed area of Pt/Co(1.2)/W Hall cross are measured (Fig. 4.32). Similar to our previous results, irrespective of irradiation area, a reduction in the Hall resistance is observed with the irradiation until a critical dose of 42.5 $\pm$ 2 ions/nm^2 followed by a sharp drop where the easy axis changes from out-of-plane to in-plane magnetization. The critical dose is almost unaffected by the choice of area of irradiation, which makes the FIB robust towards the lithography steps. When decreasing the area of irradiation, similar decrease in the total Hall resistance change upon irradiation is noted. When the irradiated region is 20 μm x 20 μm, fully covering the Hall cross, the total fall in Hall resistance is 0.7 Ω , almost equal to the half of the full deflection of R_{AHE} 1.46 Ω corresponding to magnetization switching under OP field (Fig. 4.23). The full R_{AHE} deflection is 0.2 Ω for 6 μm x 6 μm and 0.13 Ω for 5 μm x 5 μm irradiated Hall cross. The dependence of Hall resistance change on the irradiated area confirms the high spatial sensitivity of R_{AHE} in the two-dimensional Hall cross structures [68]. This makes the Hall bar as the method of interest to investigate the evolution of complex magnetic states upon partial junction irradiation using focused light ion beam.

Fig.4.33a shows the schematics of the Hall bar, highlighting the irradiated region and doses used to study the current driven 4-level magnetization switching. Based on our earlier observation of domain wall pinning by ion irradiation (Fig. 4.30), a 5 μm x 10 μm area on both sides of the Hall cross is irradiated with a near critical dose of 35 ions/nm^2 so that

the regions with a Hall cross has a well-defined anisotropy gradient frontier that inhibits the nucleation of the reversal away from the region of interest. In order to implement the two-level magnetization switching, Hall crosses are irradiated with an intermediate dose of 23 ions/nm^2 and near critical dose of 35 ions/nm^2 chosen from the irradiation curve (Fig. 4.27). 'Cross A' is defined as the Hall cross without a non-irradiated gap between the different dose irradiated regions while 'cross B' has a 1 μm gap separating the irradiated regions. Current induced magnetization switching of 'cross B' characterized by the Hall

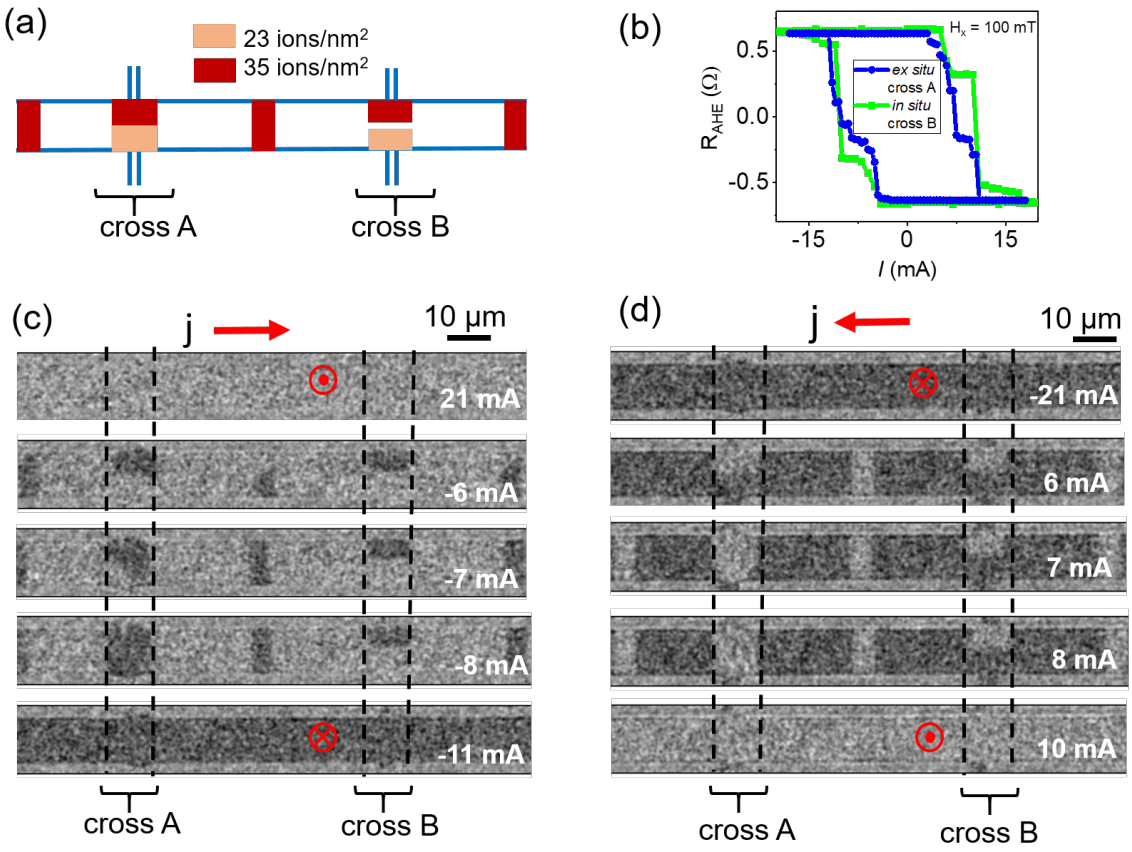

FIGURE 4.33: 4-level switching demonstration in Pt/Co(1.2)/W device. a) Schematics of the irradiation pattern with doses represented in colour code. b) Hall resistance based SOT switching loops under bias field 100 mT. Cross B with gap is measured in situ during MOKE imaging and cross A is measured ex situ. Kerr images of SOT switching under similar bias field a) when the current is swept from 21 mA to -21 mA and b) when the current is reversed.

response *in situ* measured during the Kerr imaging is shown in Fig. 4.33b. As can be seen from the SOT switching curve, the Hall cross with the gap between irradiated regions has a well defined intermediate state, in contrast to the cross without gap. In order to further validate the observation, Kerr microscope images of the SOT switching are analysed (Fig. 4.33 c and d). When the current is swept from 21 mA to -21 mA (Fig. 4.33c), at -6 mA, domain nucleation and propagation starts at the regions irradiated with 35 ions/nm^2. Compared to

the -3 mA switching current of a full cross irradiation with the similar dose (Fig. 4.33), the higher switching current for the switching of a partially irradiated cross is assigned to the smaller area of irradiation and the resulting reduction in the nucleation sites and domain propagation. Returning to 4-level switching, with a small increment 1 mA, at -7 mA, the 23 ions/nm^2 irradiated region without gap at 'cross A' starts switching, with complete reversal achieved at at -8 mA. On the other hand, the switching of 23 ions/nm^2 irradiated region with gap at 'cross B' remain unaffected up to -11 mA, at which a full reversal of the Hall bar is realized. Similar switching behaviour is observed when the current is reversed (Fig. 4.33d). The requirement of a required gap between the irradiated regions for well-defined 4-level switching indicate how it is essential to create anisotropy barriers, acting as a reversal domain wall pinning, in order to stabilize a difference of the switching critical currents of two areas with different local magnetic anisotropy.

To further enhance the field gradient and increase the intermediate switching states, Hall crosses are irradiated with 4 different doses in smaller regions of size 4.5 μm x 4.5 μm, while keeping a gap of 1 μm in between the irradiated regions. Doses are chosen based on the irradiation curve (Fig. 4.27) and frontiers of the Hall crosses are irradiated with 35 ions/nm^2 for well defined anisotropy gradient boundaries (Fig. 4.34a). MOKE images of selective SOT switching is obtained at different current values (Fig. 4.34c and d) and the electrical hysteresis loop is extracted (Fig. 4.34b). Like previous experiments, the thin film is presaturated by applying out-of-plane field of 0.45 T. Under bias field of 100 mT, independent selective current induced magnetization switching of irradiated regions can be visualized using Kerr microscopy. As expected, the order of switching follows the irradiation doses. The switching of regions follows the similar order even when the current is reversed (Fig. 4.34d), making possible 6-levels memory deterministic writing. Table 4.6 summarizes the switching current density corresponding to the 4 different doses in the 6-level switching. As can be seen, the switching current follows the irradiation dose but the values are higher than that of the corresponding 20 μm x 20 μm irradiated region (Table 4.5), which is attributed to the well-defined irraddiation assisted anisotropy gradient frontier that inhibits the nucleation of reversal domains in the former samples.

4.5 Conclusion

Magnetic thin films having a magnetic layer sandwiched between heavy metals of opposite spin Hall angle were fabricated. Magnetic and magneto-transport measurements confirmed

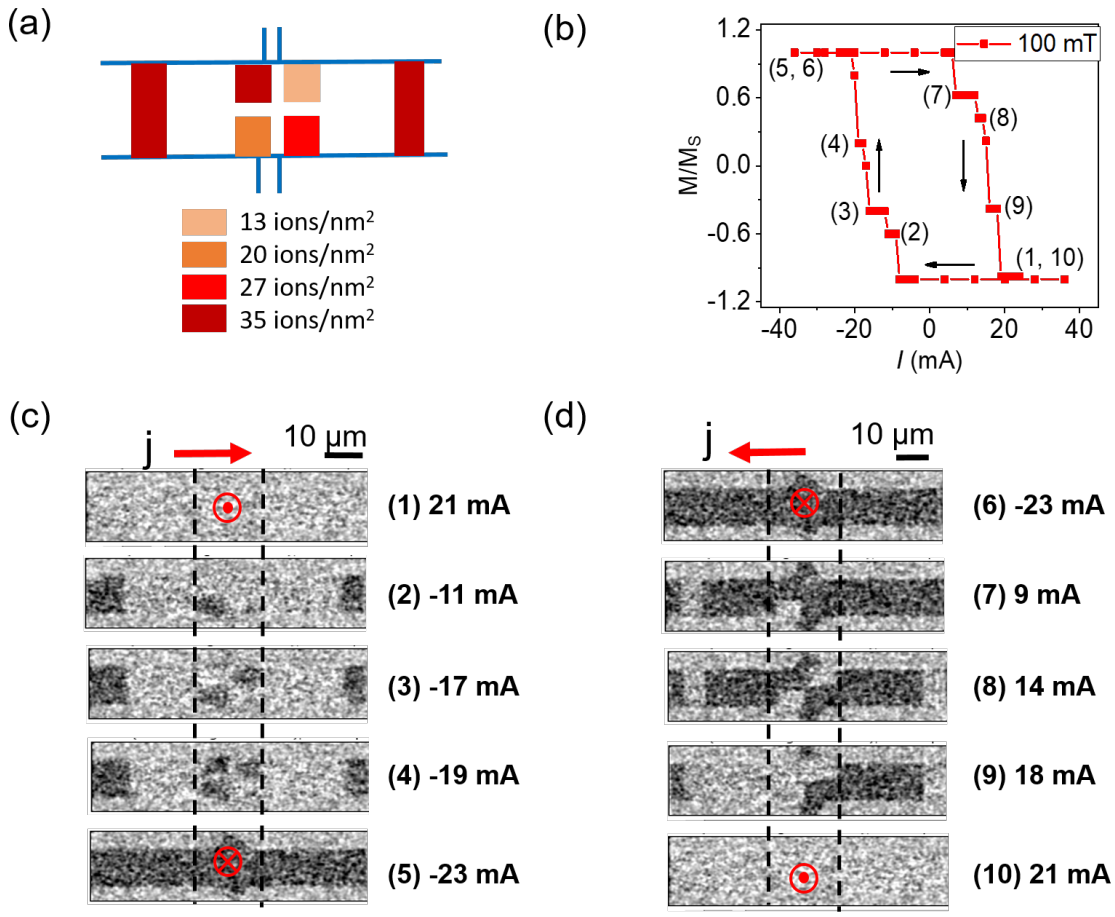

FIGURE 4.34: The current induced 6-level switching demonstration in Pt/Co(1.2)/W device. a) Schematics of the irradiation pattern with doses represented in colour code. b) MOKE-acquired SOT switching loops of irradiated Hall cross under bias field 100 mT. States corresponding to the Kerr images are highlighted. Kerr images of SOT switching under similar bias field a) when the current is swept from 21 mA to -23 mA and b) when the current is reversed.

Dose ions/nm^2	j_c^- MA/cm^2	j_c^+ MA/cm^2
13	-15.7	14.2
20	-12.6	11
27	-8.6	9.4
35	6.3	4.7

TABLE 4.6: Switching current density of a 6-level irradiated device as a function of irradiation dose.

intact PMA in the as-deposited and the patterned Pt/Co/W and Pt/Co/Ta based thin films. Deterministic SOT switching was realised with the help of symmetry breaking bias field applied collinear to the current. The switching current density obtained for Pt/Co/Ta lower than that of the Pt/Co/W devices was attributed to the higher interface diffusion in the former sample. Harmonic Hall measurement found estimates of the effective spin Hall angle of the Pt/Co/W based device in good agreement with the literature values. Furthermore, the damping-like torque was found to be the dominating term in the current induced magnetization switching of Pt/Co/W devices.

Focused helium ion irradiation was used to magnetically pattern the single repeat Pt/Co/W based perpendicular anisotropy thin films. Maskless light ion irradiation can locally control the interface dependent intrinsic magnetic properties, more specifically their magnetic anisotropy and saturation magnetization. *In situ* electrical measurement allowed us to control in real-time the evolution of anisotropy with irradiation. The obtained irradiation curve guided the choice of the proper dose for the detailed study on ion induced effects on the current driven magnetization switching. Following the dependence of the anisotropy field, the switching current density of near critical dose irradiated region was also reduced by about 70 % as compared to the unirradiated region. No appreciable change in the spin Hall angle and longitudinal resistivity were observed with irradiation, suggesting its insensitivity to the bulk properties. Thus, the selective switching of irradiated cross from the rest of the Hall bar was achieved and electrically controllable multi-domain state is demonstrated.

In an attempt to increase the amount of magnetic material and therefore improve the field gradient, helium irradiation effects on the three repeats of Pt/Co/W films were compared with that of single repeat films. Films with different Co layer thickness were fabricated and characterized using magnetic and magneto-transport measurements. Dead layer formation was observed in all films. Based on the initial characterization, single and three repeats of Pt/Co/W film with 1.2 nm Co were chosen for the irradiation studies. Independent magnetic layer switching in three repeat films can be observed in the *in situ* irradiation curve. Complex multi-domain states which cannot be fully controllable by electric current were observed in the irradiated three repeat film.

We also showed how one can deterministically access more intermediate multi-domain states by means of irradiating smaller adjacent domains using several different doses inferred from the calibration *in situ* irradiation dose. Magneto-optical Kerr (MOKE) imaging was used to visualize the domain evolution with the current pulses. Along with the electrical measurement, Kerr imaging made us realize the importance of irradiation gap between

irradiated regions for a well-defined multi-level switching, ascribed to the domain wall pinning and anisotropy gradient.

To conclude, electrically tunable magnetic multi-domain state is demonstrated in a model system. In order to attain the ultimate goal, more optimization is required in terms of the magnetic volume, structure of the multilayer, domain size and space between irradiated bits, temporal control of the magnetization, and the surface roughness. However, we showed the power of an original methodology to realize the development of electrically reconfigurable nanomagnetic arrays for dynamic magnetic patterns on flat materials.

Bibliography

[1]G. Hlawacek, V. Veligura, R. van Gastel, and B. Poelsema, "Helium ion microscopy", Journal of Vacuum Science & Technology B **32**, 020801 (2014).

[2]C. Chappert, H. Bernas, J. Ferré, V. Kottler, J.-P. Jamet, Y. Chen, E. Cambril, T. Devolder, F. Rousseaux, V. Mathet, and H. Launois, "Planar patterned magnetic media obtained by ion irradiation", Science **280**, 1919–1922 (1998).

[3]T. Devolder, "Light ion irradiation of Co/Pt systems: Structural origin of the decrease in magnetic anisotropy", Physical Review B **62**, 5794–5802 (2000).

[4]M. Urbaniak, P. Kuświk, Z. Kurant, M. Tekielak, D. Engel, D. Lengemann, B. Szymański, M. Schmidt, J. Aleksiejew, A. Maziewski, A. Ehresmann, and F. Stobiecki, "Domain-Wall Movement Control in Co/Au Multilayers by ${\mathrm{He}}^{+}$-Ion-Bombardment-Induced Lateral Coercivity Gradients", Physical Review Letters **105**, 067202 (2010).

[5]T. Devolder, C. Chappert, Y. Chen, E. Cambril, H. Bernas, J. P. Jamet, and J. Ferré, "Sub-50 nm planar magnetic nanostructures fabricated by ion irradiation", Applied Physics Letters **74**, 3383–3385 (1999).

[6]M. J. Gira, K. P. Tkacz, and J. R. Hampton, "Physical and electrochemical area determination of electrodeposited Ni, Co, and NiCo thin films", Nano Convergence **3**, 6 (2016).

[7]J. Fassbender, D. Ravelosona, and Y. Samson, "Tailoring magnetism by light-ion irradiation", Journal of Physics D: Applied Physics **37**, R179–R196 (2004).

[8]F. Röder, G. Hlawacek, S. Wintz, R. Hübner, L. Bischoff, H. Lichte, K. Potzger, J. Lindner, J. Fassbender, and R. Bali, "Direct Depth- and Lateral- Imaging of Nanoscale Magnets Generated by Ion Impact", Scientific Reports **5**, 16786 (2015).

[9]J. H. Franken, M. Hoeijmakers, R. Lavrijsen, and H. J. M. Swagten, "Domain-wall pinning by local control of anisotropy in Pt/Co/Pt strips", Journal of Physics: Condensed Matter **24**, 024216 (2011).

[10]C. Fowley, Z. Diao, C. C. Faulkner, J. Kally, K. Ackland, G. Behan, H. Z. Zhang, A. M. Deac, and J. M. D. Coey, "Local modification of magnetic anisotropy and ion milling of Co/Pt multilayers using a He$\mathplus$ion beam microscope", Journal of Physics D: Applied Physics **46**, 195501 (2013).

[11]I. M. Miron, K. Garello, G. Gaudin, P.-J. Zermatten, M. V. Costache, S. Auffret, S. Bandiera, B. Rodmacq, A. Schuhl, and P. Gambardella, "Perpendicular switching of a single ferromagnetic layer induced by in-plane current injection", Nature **476**, 189–193 (2011).

[12]L. Liu, T. Moriyama, D. C. Ralph, and R. A. Buhrman, "Spin-Torque Ferromagnetic Resonance Induced by the Spin Hall Effect", Physical Review Letters **106**, 036601 (2011).

[13]K.-S. Lee, S.-W. Lee, B.-C. Min, and K.-J. Lee, "Threshold current for switching of a perpendicular magnetic layer induced by spin Hall effect", Applied Physics Letters **102**, 112410 (2013).

[14]J. Yun, Y. Zuo, J. Mao, M. Chang, S. Zhang, J. Liu, and L. Xi, "Lowering critical current density for spin-orbit torque induced magnetization switching by ion irradiation", Applied Physics Letters **115**, 032404 (2019).

[15]X. Zhao, B. Zhang, N. Vernier, X. Zhang, M. Sall, T. Xing, L. H. Diez, C. Hepburn, L. Wang, G. Durin, A. Casiraghi, M. Belmeguenai, Y. Roussigné, A. Stashkevich, S. M. Chérif, J. Langer, B. Ocker, S. Jaiswal, G. Jakob, M. Kläui, W. Zhao, and D. Ravelosona, "Enhancing domain wall velocity through interface intermixing in W-CoFeB-MgO films with perpendicular anisotropy", Applied Physics Letters **115**, 122404 (2019).

[16]X. Zhao, Y. Liu, D. Zhu, M. Sall, X. Zhang, H. Ma, J. Langer, B. Ocker, S. Jaiswal, G. Jakob, M. Kläui, W. Zhao, and D. Ravelosona, "Spin–orbit torque driven multi-level switching in He+ irradiated W–CoFeB–MgO Hall bars with perpendicular anisotropy", Applied Physics Letters **116**, 242401 (2020).

[17]K. Jhuria, J. Hohlfeld, A. Pattabi, E. Martin, A. Y. Arriola Córdova, X. Shi, R. Lo Conte, S. Petit-Watelot, J. C. Rojas-Sanchez, G. Malinowski, S. Mangin, A. Lemaître, M. Hehn, J. Bokor, R. B. Wilson, and J. Gorchon, "Spin–orbit torque switching of a ferromagnet with picosecond electrical pulses", Nature Electronics **3**, 680–686 (2020).

[18]C. O. Avci, "Picosecond switching in a ferromagnet", Nature Electronics **3**, 660–661 (2020).

[19]C. M. A. Brett and A. M. Oliveira-Brett., "Electrochemistry: principles, methods, and applications", Oxford University Press, Oxford, New York, Tokyo (2000).

[20]I. Benguettat-El Mokhtari, A. Mourkas, P. Ntetsika, I. Panagiotopoulos, Y. Roussigné, S. M. Cherif, A. Stashkevich, F. Kail, L. Chahed, and M. Belmeguenai, "Interfacial dzyaloshinskii-moriya interaction, interface-induced damping and perpendicular magnetic anisotropy in pt/co/w based multilayers", Journal of Applied Physics **126**, Publisher: American Institute of Physics, 133902 (2019).

[21]C.-F. Pai, L. Liu, Y. Li, H. W. Tseng, D. C. Ralph, and R. A. Buhrman, "Spin transfer torque devices utilizing the giant spin Hall effect of tungsten", Applied Physics Letters **101**, 122404 (2012).

[22]R. Wang, Z. Xiao, H. Liu, Z. Quan, X. Zhang, M. Wang, M. Wu, and X. Xu, "Enhancement of perpendicular magnetic anisotropy and spin-orbit torque in Ta/Pt/Co/Ta multilayered heterostructures through interfacial diffusion", Applied Physics Letters **114**, 042404 (2019).

[23]S. Mendisch, G. Žiemys, V. Ahrens, Á. Papp, and M. Becherer, "Pt\Co\W as a candidate for low power nanomagnetic logic", Journal of Magnetism and Magnetic Materials **485**, 345–350 (2019).

[24]A. Petford-Long, P. Grundy, and J. Jakubovics, "Structure and magnetic properties of Co-based multilayers", IEEE Transactions on Magnetics **26**, 2733–2735 (1990).

[25]J. S. Tsay and C. S. Shern, "Diffusion and alloy formation of co ultrathin films on pt(111)", Journal of Applied Physics **80**, Publisher: American Institute of Physics, 3777–3781 (1996).

[26]J. M. D. Coey, *Magnetism and magnetic materials* (Cambridge University Press, 2010).

[27]S. Woo, M. Mann, A. J. Tan, L. Caretta, and G. S. D. Beach, "Enhanced spin-orbit torques in Pt/Co/Ta heterostructures", Applied Physics Letters **105**, 212404 (2014).

[28]Z. A. Bekele, K. Meng, J. Miao, X. Xu, and Y. Jiang, "The dominancy of damping like torque for the current induced magnetization switching in Pt/Co/W multilayers", Solid State Communications **274**, 41–45 (2018).

[29]P. M. Haney, H.-W. Lee, K.-J. Lee, A. Manchon, and M. D. Stiles, "Current induced torques and interfacial spin-orbit coupling: Semiclassical modeling", Physical Review B **87**, 174411 (2013).

[30]S. Woo, M. Mann, A. J. Tan, L. Caretta, and G. S. D. Beach, "Enhanced spin-orbit torques in Pt/Co/Ta heterostructures", Applied Physics Letters **105**, 212404 (2014).

[31]J. Yu, X. Qiu, W. Legrand, and H. Yang, "Large spin-orbit torques in Pt/Co-Ni/W heterostructures", Applied Physics Letters **109**, 042403 (2016).

[32]B. Cui, S. Chen, D. Li, J. Yun, X. Guo, K. Wu, X. Zhang, Y. Wang, Y. Zuo, M. Gao, and L. Xi, "Current-induced magnetization switching in Pt/Co/Ta with interfacial decoration by insertion of Cr to enhance perpendicular magnetic anisotropy and spin–orbit torques", Applied Physics Express **11**, 013001 (2017).

[33]S. Emori, U. Bauer, S.-M. Ahn, E. Martinez, and G. S. D. Beach, "Current-driven dynamics of chiral ferromagnetic domain walls", Nature Materials **12**, 611–616 (2013).

[34]J. Yu, X. Qiu, Y. Wu, J. Yoon, P. Deorani, J. M. Besbas, A. Manchon, and H. Yang, "Spin orbit torques and Dzyaloshinskii-Moriya interaction in dual-interfaced Co-Ni multilayers", Scientific Reports **6**, 32629 (2016).

[35]M. Jiang, H. Asahara, S. Sato, S. Ohya, and M. Tanaka, "Suppression of the field-like torque for efficient magnetization switching in a spin–orbit ferromagnet", Nature Electronics **3**, 751–756 (2020).

[36]J.-M. Hu, Z. Li, L.-Q. Chen, and C.-W. Nan, "High-density magnetoresistive random access memory operating at ultralow voltage at room temperature", en, Nature Communications **2**, Number: 1 Publisher: Nature Publishing Group, 553 (2011).

[37]R. F. L. Evans, R. W. Chantrell, U. Nowak, A. Lyberatos, and H.-J. Richter, "Thermally induced error: Density limit for magnetic data storage", Applied Physics Letters **100**, 102402 (2012).

[38]J. W. Lee, Y.-W. Oh, S.-Y. Park, A. I. Figueroa, G. van der Laan, G. Go, K.-J. Lee, and B.-G. Park, "Enhanced spin-orbit torque by engineering pt resistivity in Pt/Co/AlO_x structures", Phys. Rev. B **96**, 064405 (2017).

[39]E. Sagasta, Y. Omori, S. Vélez, R. Llopis, C. Tollan, A. Chuvilin, L. E. Hueso, M. Gradhand, Y. Otani, and F. Casanova, "Unveiling the mechanisms of the spin hall effect in ta", Phys. Rev. B **98**, 060410 (2018).

[40]L. Wang, R. J. H. Wesselink, Y. Liu, Z. Yuan, K. Xia, and P. J. Kelly, "Giant room temperature interface spin hall and inverse spin hall effects", Phys. Rev. Lett. **116**, 196602 (2016).

[41]K. Meng, J. Miao, X. Xu, Y. Wu, J. Xiao, J. Zhao, and Y. Jiang, "Modulated switching current density and spin-orbit torques in MnGa/Ta films with inserting ferromagnetic layers", Scientific Reports **6**, 38375 (2016).

[42]I. Mihai Miron, G. Gaudin, S. Auffret, B. Rodmacq, A. Schuhl, S. Pizzini, J. Vogel, and P. Gambardella, "Current-driven spin torque induced by the Rashba effect in a ferromagnetic metal layer", Nature Materials **9**, 230–234 (2010).

[43]X. Zhang, J. Mao, M. Chang, Z. Yan, Y. Zuo, and L. Xi, "Current-induced magnetization switching in Pt/Co/W and Pt/Co/W0.82Pt0.18 structures with perpendicular magnetic anisotropy", Journal of Physics D: Applied Physics **53**, 225003 (2020).

[44]S. K. Li, X. T. Zhao, W. Liu, Y. H. Song, L. Liu, X. G. Zhao, and Z. D. Zhang, "Interface effect of ultrathin W layer on spin-orbit torque in Ta/W/CoFeB multilayers", Applied Physics Letters **114**, 082402 (2019).

[45]J. Han, A. Richardella, S. A. Siddiqui, J. Finley, N. Samarth, and L. Liu, "Room-Temperature Spin-Orbit Torque Switching Induced by a Topological Insulator", Physical Review Letters **119**, 077702 (2017).

[46]K. Cai, M. Yang, H. Ju, S. Wang, Y. Ji, B. Li, K. W. Edmonds, Y. Sheng, B. Zhang, N. Zhang, S. Liu, H. Zheng, and K. Wang, "Electric field control of deterministic current-induced magnetization switching in a hybrid ferromagnetic/ferroelectric structure", Nature Materials **16**, 712–716 (2017).

[47]P. Li, T. Liu, H. Chang, A. Kalitsov, W. Zhang, G. Csaba, W. Li, D. Richardson, A. DeMann, G. Rimal, H. Dey, J. S. Jiang, W. Porod, S. B. Field, J. Tang, M. C. Marconi, A. Hoffmann, O. Mryasov, and M. Wu, "Spin–orbit torque-assisted switching in magnetic insulator thin films with perpendicular magnetic anisotropy", Nature Communications **7**, 12688 (2016).

[48]J. Sinova, S. O. Valenzuela, J. Wunderlich, C. H. Back, and T. Jungwirth, "Spin hall effects", Rev. Mod. Phys. **87**, 1213–1260 (2015).

[49]W. M. Haynes, ed., *CRC handbook of chemistry and physics*, 95th ed. (CRC Press, Boca Raton, June 30, 2014), 2704 pp.

[50]A. F. Mayadas and M. Shatzkes, "Electrical-resistivity model for polycrystalline films: the case of arbitrary reflection at external surfaces", Phys. Rev. B **1**, 1382–1389 (1970).

[51]D. Weller and A. Moser, "Thermal effect limits in ultrahigh-density magnetic recording", IEEE Transactions on Magnetics **35**, 4423–4439 (1999).

[52]H. Fulara, M. Zahedinejad, R. Khymyn, A. A. Awad, S. Muralidhar, M. Dvornik, and J. Åkerman, "Spin-orbit torque–driven propagating spin waves", Science Advances **5**, eaax8467 (2019).

[53]W. A. Borders, A. Z. Pervaiz, S. Fukami, K. Y. Camsari, H. Ohno, and S. Datta, "Integer factorization using stochastic magnetic tunnel junctions", Nature **573**, 390–393 (2019).

[54]H. Lee, F. Ebrahimi, P. K. Amiri, and K. L. Wang, "Design of high-throughput and low-power true random number generator utilizing perpendicularly magnetized voltage-controlled magnetic tunnel junction", AIP Advances **7**, 055934 (2017).

[55]S. An, E. Baek, J.-A. Kim, K.-S. Lee, and C.-Y. You, *Improved Spin-orbit Torque Induced Magnetization Switching Efficiency by Helium Ion Irradiation*, Jan. 2022.

[56]C. Vieu, J. Gierak, H. Launois, T. Aign, P. Meyer, J. P. Jamet, J. Ferré, C. Chappert, T. Devolder, V. Mathet, and H. Bernas, "Modifications of magnetic properties of Pt/Co/Pt thin layers by focused gallium ion beam irradiation", Journal of Applied Physics **91**, 3103–3110 (2002).

[57]J. Yun, Y. Zuo, J. Mao, M. Chang, S. Zhang, J. Liu, and L. Xi, "Lowering critical current density for spin-orbit torque induced magnetization switching by ion irradiation", Applied Physics Letters **115**, Publisher: American Institute of Physics, 032404 (2019).

[58]X. Zhao, Y. Liu, D. Zhu, M. Sall, X. Zhang, H. Ma, J. Langer, B. Ocker, S. Jaiswal, G. Jakob, M. Kläui, W. Zhao, and D. Ravelosona, "Spin–orbit torque driven multi-level switching in he+ irradiated w–CoFeB–MgO hall bars with perpendicular anisotropy", Applied Physics Letters **116**, Publisher: American Institute of Physics, 242401 (2020).

[59]S. Bandiera, R. C. Sousa, B. Rodmacq, and B. Dieny, "Asymmetric Interfacial Perpendicular Magnetic Anisotropy in Pt/Co/Pt Trilayers", IEEE Magnetics Letters **2**, 3000504–3000504 (2011).

[60]M. Spasova, U. Wiedwald, R. Ramchal, M. Farle, M. Jergel, E. Majkova, S. Luby, and R. Senderak, "Magnetization and Magnetic Anisotropy of Co/W Multilayers", physica status solidi (b) **225**, 449–457 (2001).

[61]A. G. Kolesnikov, A. V. Ognev, M. E. Stebliy, L. A. Chebotkevich, A. V. Gerasimenko, and A. S. Samardak, "Nanoscale control of perpendicular magnetic anisotropy, coercive force and domain structure in ultrathin Ru/Co/W/Ru films", Journal of Magnetism and Magnetic Materials **454**, 78–84 (2018).

[62]D. Zhu and W. Zhao, "Threshold Current Density for Perpendicular Magnetization Switching Through Spin-Orbit Torque", Physical Review Applied **13**, 044078 (2020).

[63]J. Cao, Y. Chen, T. Jin, W. Gan, Y. Wang, Y. Zheng, H. Lv, S. Cardoso, D. Wei, and W. S. Lew, "Spin orbit torques induced magnetization reversal through asymmetric domain wall propagation in Ta/CoFeB/MgO structures", Scientific Reports **8**, 1355 (2018).

[64]I. Benguettat-El Mokhtari, A. Mourkas, P. Ntetsika, I. Panagiotopoulos, Y. Roussigné, S. M. Cherif, A. Stashkevich, F. Kail, L. Chahed, and M. Belmeguenai, "Interfacial Dzyaloshinskii-Moriya interaction, interface-induced damping and perpendicular magnetic anisotropy in Pt/Co/W based multilayers", Journal of Applied Physics **126**, 133902 (2019).

[65]J. H. Franken, M. Hoeijmakers, R. Lavrijsen, J. T. Kohlhepp, H. J. M. Swagten, B. Koopmans, E. van Veldhoven, and D. J. Maas, "Precise control of domain wall injection and pinning using helium and gallium focused ion beams", Journal of Applied Physics **109**, 07D504 (2011).

[66]K.-F. Huang, D.-S. Wang, M.-H. Tsai, H.-H. Lin, and C.-H. Lai, "Initialization-Free Multilevel States Driven by Spin–Orbit Torque Switching", Advanced Materials **29**, _eprint: https://onlinelibrary.wiley.com/doi/pdf/10.1002/adma.201601575, 1601575 (2017).

[67]Y. Sheng, Y. C. Li, X. Q. Ma, and K. Y. Wang, "Current-induced four-state magnetization switching by spin-orbit torques in perpendicular ferromagnetic trilayers", Applied Physics Letters **113**, Publisher: American Institute of Physics, 112406 (2018).

[68]M. Alexandrou, P. W. Nutter, M. Delalande, J. de Vries, E. W. Hill, F. Schedin, L. Abelmann, and T. Thomson, "Spatial sensitivity mapping of Hall crosses using patterned magnetic nanostructures", Journal of Applied Physics **108**, 043920 (2010).

Chapter 5

Conclusions and Outlook

5.1 Conclusions

We investigated the behaviour of an electrochemical reaction under the presence of a large magnetic field gradient at the solid-liquid interface. Considering the size independent nature of the magnetic field, a nanomagnetic thin film having a multi-domain magnetic state was envisioned as an appropriate source which can generate intense stray fields and field gradients at the immediate vicinity of the film surface. Two strategies were pursued to create a magnetic multi-domain configuration where the force field can be switched on or off by an external magnetic field or by an electric current.

To magnetically control the evolution of force the field landscape, Co/Pt multilayers having perpendicular magnetic anisotropy (PMA) were fabricated. From a combination of magnetic measurements and magnetic domains imaging techniques, an intense nanoscale field gradient of the order of 10^7 T/m was estimated using 2D analytical field calculations. In order to investigate the field effects on electrochemical reactions, a model ferri/ferrocyanide reaction was chosen as a standard redox probe, where the complications due to the electrode surface modification and the bubble evolution can be avoided. Initially, we studied the dependence of Pt cap layer thickness on the electrochemical activity of the Co/Pt multirepeat film. We found that a minimum of 5.0 nm Pt cap was required to ensure a reaction rate reaching that of pure Pt films, whereas the surface analysis on a thinner Pt (2.8 nm) capped Co/Pt multilayer confirmed traces of cobalt and cobalt oxide. The columnar growth of the multilayer was suggested as a possible explanation for the imperfect Pt surface coverage. In a separate effort, the Lorentz force effects were investigated by applying a magnetic field parallel to the electrode surface. No evidence of the influence of Lorentz force on the kinetically limited region was observed. On the other hand, in the mass transport limited region, both interfacial and bulk parameters of the reaction were found to be influenced by the Lorentz force effects. Furthermore, we showed that the Lorentz force driven magnetic

stirring was equivalent to mechanical stirring using a rotating blade.

The impact on the redox reaction by the application of intense stray fields and field gradients at the electrode-electrolyte interface was studied. About 6 - 8% enhancement of the steady state current was observed in response to the nanoscale Kelvin force density imposed by Co/Pt multilayers covered with no more than 5.0 nm Pt. As the current measured for the Pt film and thick Pt capped (10.0 nm) Co/Pt multilayer showed no dependence to the field, we ruled out the external magnetic field as a primary source of the observed effect. The field effects were studied in more detail using ac impedance technique and revealed that the interfacial parameters such as double layer capacitance (C_{dl}) and charge transfer resistance (R_{ct}) were sensitive to the field gradient, for applied potential near to the point of zero charge (E_{pzc}) 0.25 V. Furthermore, during the active reduction of ferricyanide, at potentials far from from E_{pzc}, both interfacial and bulk parameters were found to be influenced by the intense nanoscale field gradient. The suppression of near-electrode convection of the paramagnetic species was suggested as the mode of action. Thus, while there is an enhancement of the effective kinetics, there was no evidence of modifications of the underlying kinetics.

Additionally, we achieved electrically controllable magnetic multi-domain state in thin film PMA heterostructures. These consisted of magnetic layer sandwiched between heavy metals of opposite spin Hall angles (Pt/Co/W and Pt/Co/Ta) and were characterised using the magnetometry and magneto-transport measurements. Spin-orbit torque switching was realized on patterned Hall bars with the aid of a small symmetry breaking bias field. The PMA thin films were magnetically patterned using focused helium ion irradiation which allowed us to locally control the interface dependent properties such as magnetic anisotropy and saturation magnetization. *In situ* electrical measurements allowed us to real-time monitor the anisotropy changes under irradiation. Furthermore, *ex situ* measurements were performed on samples irradiated with specific doses. About 70 % reduction in both anisotropy field and switching current density of the irradiated region as compared to the unirradiated region was observed. Thus, SOT driven selective magnetization switching or an electrically tunable magnetic multi-domain state was demonstrated.

Systematic studies to improve the field gradient were carried out by increasing the number of repeats as well as by reducing the size of irradiated regions. Irradiation of multi-magnetic layer repeats (N=3) gave rise to complex magnetic multi-domain states, which were not fully switcahble by electric currents. On the other hand, controllable intermediate multi-domain states were attained by irradiating regions with different doses. Kerr microscopy in combination with magneto-transport measurements revealed the importance

of keeping a gap between irradiated regions for a selective independent switching of an irradiated region.

To conclude, nanomagnetic PMA thin films having multidomain magnetic states were realised as a source of nanoscale intense magnetic field gradient. Two strategies are employed to create a multi-domain magnetic thin film. As a comparatively known approach, Co/Pt based multilayers were prepared, where multi-domain state in the as prepared state can be manipulated using an external magnetic field. The intense nanoscale field gradient generated by the thin film is found to improve the efficiency of the electrochemcial reaction. Another sophisticated approach based on the combination of spin-orbit torque (SOT) and the ion irradiation was exploited to create an electrically tunable magnetic multi-domain states.

5.2 Outlook

In this research, we focused on studies of the electrochemical response of a model redox system to a large field gradient imposed at the nanoscale. In terms of applications, it would be interesting to investigate the influence of the Co/Pt multilayer based thin film electrodes on other electrochemical reactions, for example on the efficiency of the oxygen reduction reaction (ORR). ORR is one of the most important and well studied reaction because of its major role in the energy conversion process, in particular in the field of fuel cells [1]. Owing to the paramagnetic nature of the oxygen molecules, the Kelvin field gradient force has been reported to accelerate the ORR efficiency [2, 3] through the enhanced mass transport in diffusion layer. Upon imposing a larger field gradient near to the electrode surface, the field gradient could further inhibit the convection of the intermediate paramagnetic HO_2^- radical resulting in an enhanced reduction of oxygen molecules.

In addition, it has been reported that the release size and residence time of bubbles are sensitive on magnetic forces [4]. For example, when the magnetic field driven local convective effects acts in favour of the buoyancy force, it reduces the average size of detaching bubbles and also shorten their lifetime on the electrode surface, resulting in an enhancement in the efficiency of the reactions. As we already discussed, multidomain Co/Pt based thin films can create a non-uniform local magnetic field and large field gradient near their immediate surface. Hence, a study related to the effect of local field and field gradient conditions on bubble growth would be interesting as it can find applications in energy storage related reactions like oxygen evolution reaction (OER) and hydrogen evolution reaction (HER).

As far as electrical control of magnetic domain states was concerned, there is still room for improvements in terms of the focused ion beam (FIB) patterning as well as the optimization of spin orbit torque (SOT) switching. The minimum size of the FIB patterned region during this research work is a 2 μm sided square. With the focused He+ beam, structures of the order of a few nanometers can be patterned, which is difficult to achieve using photoresist based lithography techniques. As the field gradient increases by reducing the domain size, we can expect a larger gradient force field in the immediate vicinity of the nanopatterned device. On the other hand, the edge effects, the demagnetising field and the thermal energy are expected to be relevant parameters at this length scale in determining the efficiency of current induced switching. In our study, we observed the critical role of a gap between irradiated regions to selectively switch the irradiated regions. Hence, a further study changing the gap between irradiated regions will be interesting for tuning the interaction between irradiated regions. In order to incorporate the electrically reprogrammable magnetic arrays into the electrochemical setup, a flat surface of the magnetic film is a prerequisite. It is observed that a few nanometers of sample surface is etched due to the maskless FIB patterning [5]. A photoresist coating, thin enough for the He+ beam to pass through but thick enough to avoid sample etching, is a possible solution to obtain an irradiated film with negligible surface damage. Further optimizations related to the beam interaction with the photoresist will be interesting to optimize the process of a maskless FIB patterning with minimal specimen surface damage.

The spin-orbit torque (SOT) driven magnetization switching in combination with the irradiation induced magnetic patterning can be explored to obtain not only sub-μm spatial resolution but also sub-ns temporal control of magnetization dynamics. It has been reported that, owing to the negligible incubation time and the immediate response to the SOT effective fields, the current induced magnetization switching occurs in the GHz frequency range [6, 7]. Hence, a further study to optimize the switching time of the specifically irradiated magnetic bits would be interesting to realise a magnetic force field landscape which can be switched on or off in an ultrafast time scale, which would provide novel insights into the magnetic field effects in electrochemical reactions.

Bibliography

[1]Y. Zhang, C. Liang, J. Wu, H. Liu, B. Zhang, Z. Jiang, S. Li, and P. Xu, "Recent advances in magnetic field-enhanced electrocatalysis", ACS Applied Energy Materials, Publisher: American Chemical Society, 10.1021/acsaem.0c02104 (2020).

[2]N. B. Chaure, F. M. F. Rhen, J. Hilton, and J. M. D. Coey, "Design and application of a magnetic field gradient electrode", Electrochemistry Communications **9**, 155–158 (2007).

[3]N. B. Chaure and J. M. D. Coey, "Enhanced oxygen reduction at composite electrodes producing a large magnetic gradient", Journal of the Electrochemical Society **156**, Publisher: IOP Publishing, F39 (2009).

[4]D. Li, B. Cui, T. Wang, J. Yun, X. Guo, K. Wu, Y. Zuo, J. Wang, D. Yang, and L. Xi, "Effect of inserting a non-metal c layer on the spin-orbit torque induced magnetization switching in pt/co/ta structures with perpendicular magnetic anisotropy", Applied Physics Letters **110**, Publisher: American Institute of Physics, 132407 (2017).

[5]C. Fowley, Z. Diao, C. C. Faulkner, J. Kally, K. Ackland, G. Behan, H. Z. Zhang, A. M. Deac, and J. M. D. Coey, "Local modification of magnetic anisotropy and ion milling of Co/Pt multilayers using a He$\mathplus$ion beam microscope", Journal of Physics D: Applied Physics **46**, 195501 (2013).

[6]K. Garello, C. O. Avci, I. M. Miron, M. Baumgartner, A. Ghosh, S. Auffret, O. Boulle, G. Gaudin, and P. Gambardella, "Ultrafast magnetization switching by spin-orbit torques", Applied Physics Letters **105**, Publisher: American Institute of Physics, 212402 (2014).

[7]K. Jhuria, J. Hohlfeld, A. Pattabi, E. Martin, A. Y. Arriola Córdova, X. Shi, R. Lo Conte, S. Petit-Watelot, J. C. Rojas-Sanchez, G. Malinowski, S. Mangin, A. Lemaître, M. Hehn, J. Bokor, R. B. Wilson, and J. Gorchon, "Spin–orbit torque switching of a ferromagnet with picosecond electrical pulses", Nature Electronics, Publisher: Nature Publishing Group, 1–7 (2020).

Appendix A

Appendix A

A.1 Domain Theory of Magnetic Stripe Domains

The domain formation and the domain width variation with magnetic layer thickness in perpendicular anisotropy Co/Pt and Co/Pt multilayers can be well understood within the model of periodic stripe domains in an infinite sheet with uniaxial perpendicular anisotropy originally suggested by Kittel [1, 2] and further improved by Kooy and Enz [3]. In this model, the energies of interest are the domain wall energy and magnetostatic energy due to demagnetizing field. Domain formation reduces the latter at the expense of wall energy. Hence, periodic parallel stripe domain pattern is determined by the balance between the demagnetizing energy reduction versus domain wall energy increase.

In the limit of thick films $t >> \mathrm{D}$, any interaction between the field created at both surface are neglected.The magnetostatic energy is then given as

$$E_{demag} = 0.85 M_s^2 D \tag{A.1}$$

The total domain wall energy can be estimated as [4, 5]

$$E_{wall} \approx \frac{4\sqrt{AK_u}.t}{D} \tag{A.2}$$

where $\sigma = 4\sqrt{AK}$ is the wall energy per unit area and t/D is the total domain wall area. Upon Minimizing the energy, it can be seen that the domain width grows as $\mathrm{D} \sim \sqrt{t}$ which follows the prediction by Kittel [1].

In the limit of thin film $t < D$, the two surfaces interact magnetostatically. For a one-dimensional stripe domains of width D, the demagnetisation energy can be now be estimated as [6]

$$E_{demag} = \frac{16 M_s^2 D}{\pi^2} \sum_{n}^{odd} \frac{1}{n^3} \left[1 - \exp(-n\pi.t/D)\right] \tag{A.3}$$

Solving for the energy minimization with respect to the magnetic layer thickness t, domain wall width now increases as $D \sim t\exp(1/t)$. The minimum domain size is denoted as characteristic domain size characteristic domain size D_0 given as $D_0 = \sigma_w/2\pi M_s$ for $t \sim D_0$ (Fig A.1b). This typical behaviour of domains for perpendicular thin films have been reported by several studies [1–5].

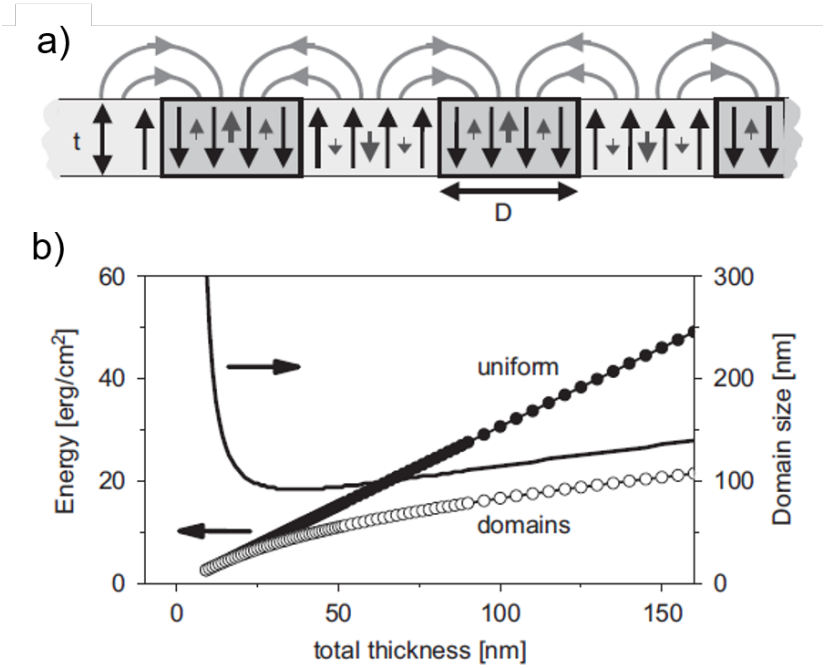

FIGURE A.1: a)Illustration of perpendicular anisotropy stripe domains having domain width D. b) Total magnetic energy (left axis) for uniform magnetization and stipe domains and domain width variation (right axis, solid line) with the magnetic film thickness [5].

Bibliography

[1]C. Kittel, "Theory of the structure of ferromagnetic domains in films and small particles", Physical Review **70**, Publisher: American Physical Society, 965–971 (1946).

[2]C. Kittel, "Physical theory of ferromagnetic domains", Reviews of Modern Physics **21**, Publisher: American Physical Society, 541–583 (1949).

[3]C. Kooy, "Experimental and theoretical study of the domain configuration in thin layers of bafe12o19", Publisher:Philips Res. Repts. 15 (1960) 7 (1960).

[4]A. Hubert and R. Schäfer, "Domain theory", in *Magnetic domains: the analysis of magnetic microstructures*, edited by A. Hubert and R. Schäfer (Springer, Berlin, Heidelberg, 1998), pp. 99–335.

[5]O. Hellwig, A. Berger, J. B. Kortright, and E. E. Fullerton, "Domain structure and magnetization reversal of antiferromagnetically coupled perpendicular anisotropy films", Journal of Magnetism and Magnetic Materials **319**, 13–55 (2007).

[6]Z. Málek and V. Kamberský, "On the theory of the domain structure of thin films of magnetically uni-axial materials", Cechoslovackij fiziceskij zurnal **8**, 416–421 (1958).

Jinu KURIAN

Design of a high intensity magnetic force field source and studies of its impact on electrochemical reaction at the liquid-solid interface.

Résumé

L'influence d'un champ magnétique sur l'électrochimie, dans la plupart des cas, peut être expliquée par les effets de convection dans la couche de diffusion induits par la force de Lorentz et/ou la force de Kevin. Cependant, les effets du champ à l'interface électrochimique sont un sujet controversé. Nous étudions comment les forces magnétiques exaltées à l'échelle nanométrique, agissant à l'interface électrode/électrolyte, peuvent avoir un impact sur la réaction électrochimique. Deux stratégies ont été suivies pour créer une configuration magnétique multi-domaines où le champ de force peut être activé ou désactivé par le champ magnétique externe ou par un courant électrique. Des multicouches de films Co/Pt présentant une anisotropie magnétique perpendiculaire nous ont permis de réaliser des configurations générant des champs de force contrôlable magnétiquement. Des études électrochimiques utilisant des films de Co/Pt sur le système modèle du couple redox ferri/ferrocyanure ont révélé l'influence d'un champ de force à l'échelle nanométrique sur le processus électrochimique. En outre, la commutation de magnétisation induite par le couplage spin-orbite en combinaison avec la technologie d'irradiation par ions hélium focalisés est explorée pour créer des bits magnétiques reprogrammables électriquement. Un système modèle a été exploré, dans lequel la résolution spatio-temporelle de la génération du champ de force peut être utilisée pour obtenir de nouvelles informations sur les effets du champ dans les réactions électrochimiques. En outre, en raison de la nature omniprésente des molécules paramagnétiques dans les réactions, le champ de force intense à l'échelle nanométrique pourrait ouvrir de nouvelles voies pour améliorer l'efficacité de réactions technologiquement pertinentes.

Mots clés : Films minces magnétiques, anisotropie magnétique perpendiculaire, force Kelvin à l'échelle nanométrique, processus électrochimique, couplage spin-orbite, microscopie à ions hélium focalisés.

Résumé en anglais

The influence of a magnetic field on the electrochemistry, in most cases, can be explained by the convective effects in the diffusion layer induced by the Lorentz force and/or the Kevin force. However, the field effects at the electrochemical interface is a controversial topic. We study how large magnetic forces, enhanced at the nanoscale and acting at an electrode/electrolyte interface can impact the electrochemical reaction. Two strategies were pursued to create a magnetic multi-domain configuration where the force field can be switched on or off by the external magnetic field or by an electric current. Co/Pt multilayer films having perpendicular magnetic anisotropy allowed us to realize the magnetically controllable force field landscape. Electrochemical investigations using Co/Pt films on the model system of ferri/ferrocyanide redox couple revealed the influence of large nanoscale force field on the electrochemical process. Furthermore, spin-orbit torque induced magnetization switching in combination with focused helium ion irradiation technology is explored to demonstrate electrically reprogrammable magnetic bits. A model system is achieved, where the spatio-temporal resolution of the force field generation could be explored to obtain novel insights into the field effects on electrochemical reactions. In addition, owing to the ubiquitous nature of the paramagnetic molecules in the reactions, the nanoscale intense force field could open new pathways to improve the efficiency of technologically relevant reactions.

Keywords: Magnetic thin films, perpendicular magnetic anisotropy, nanoscale Kelvin force, electrochemical process, spin-orbit torque, focused helium ion microscopy.